UNIVERSITY OF OKLAHOMA

GRADUATE COLLEGE

THE STRUCTURAL CHARACTERIZATION OF THE INTERACTIONS OF MYOGLOBIN, HEMOGLOBIN, *C. DIFFICILE* NITROREDUCTASE AND CYTOCHROME P450 WITH N-CONTAINING COMPOUNDS

A DISSERTATION

SUBMITTED TO THE GRADUATE FACULTY

in partial fulfillment of the requirements for the

Degree of

DOCTOR OF PHILOSOPHY

By

SAMANTHA MALIA POWELL
Norman, Oklahoma
2019

THE STRUCTURAL CHARACTERIZATION OF THE INTERACTIONS OF MYOGLOBIN, HEMOGLOBIN, *C. DIFFICILE* NITROREDUCTASE AND CYTOCHROME P450 WITH N-CONTAINING COMPOUNDS

A DISSERTATION APPROVED FOR THE
DEPARTMENT OF CHEMISTRY AND BIOCHEMISTRY

BY

Dr. George B. Richter-Addo, Chair

Dr. Ann H. West

Dr. Christina Bourne

Dr. Adam Duerfeldt

Dr. Anne K. Dunn

Acknowledgements

I would not have been able to accomplish any of this work without the help and support of many people. First and foremost, I'd like to thank my family for their support and encouragement. Navigating graduate school is not an easy task, but my family has continuously been there cheering me on and pushing me to reach my goal of becoming a PhD scientist. Additionally, I thank my family for being so patient with me as I learn how to better communicate my research in a way that won't make all of their eyes glaze over. To my grandparents, I truly cherish all of the support and wisdom they've provided me with. To my parents, I thank them for raising me to be such an independent and hard-worker and for always reminding me that I can do whatever I set my mind to. A special thanks to my dad, who has been there for me and my sister through everything. To my sister, my little Boo, thank you for being my rock. I am incredibly grateful that I have a sibling that I can also call my friend. And to all of my friends, especially Josh, Gabby, Andrew, Camry, Taryn and Jordan, thank you for helping make the journey to my PhD a little easier.

I'd like to give a big thanks to my PhD advisor, Dr. George B. Richter-Addo. During my time at OU, he has been a very supportive mentor both in my research and career goals. I'm very grateful for all the opportunities, such as conferences and internships, that I've had thanks to him. I'd also like to thank my advisory committee for their help and support over the past five years, Dr. Ann H. West, Dr. Christina Bourne, Dr. Adam Duerfeldt, and Dr. Anne K. Dunn.

Much of the work in this dissertation would not have been accomplished without the amazing support staff that we have in our department. Thank you to Dr. Fares Najar for

his help with bioinformatics, Dr. Philip Bourne for his help with protein purification and Melanie Norris for her help with travel and purchasing accounts. I'd especially like to thank Dr. Leonard M. Thomas for teaching me and assisting me with X-ray crystallography. Additionally, I'd like to thank all of those involved in the Michael Price Family Foundation *C. difficile* project. Thank you to the OU team, Neda Hessami, Dr. Smita K. Menon, Jamie R. Sykes, Dr. Skyler D. Hebdon, Dr. Elizabeth A. Karr and Dr. Catherine E. Bishop. And thank you to our collaborators at Albert Einstein College of Medicine, Drs. Steve Almo, James Love, and Vern Schramm.

Finally, I'd like to thank all of the GBRA group members, both past and present. When I first joined the GBRA lab, Dr. Bing Wang trained and mentored me. I will forever be thankful for our friendship and all that he taught me about biochemistry and X-ray crystallography. I'd also like to thank Dr. Jun (Eva) Yi, for teaching me the basics of hemoglobin. Thank you to Viridiana Herrera for her help and friendship as we have struggled and, more importantly, succeeded in our research. A big thanks to the very dedicated undergraduates in our lab, Kiana Prather and Nancy Nguyen, who have been a huge help in completing my experiments. Thank you to Dr. Erwin Abucayon who helped me with synthesis and NMR. And to the other GBRA group members, Dr. Ye Guan, Dr. Dennis Awasabisah, Jeremy Zink, and Jennifer Londoño Salazar, thank you for making our lab the best lab to be a part of!

Funding

We are grateful to the National Science Foundation (Grant CHE-1566509 to GBR-A) for funding for this work. Proteins were in part purified in the OU Protein Production Core and X-ray data was obtained in the OU Macromolecular Crystallography Laboratory, which are supported by an Institutional Development Award (IDeA) from the National Institute of General Medical Sciences of the National Institutes of Health under grant number P20GM103640. We thank the Price Family Foundation for funding our *C. difficile* research. Use of the Stanford Synchrotron Radiation Lightsource, SLAC National Accelerator Laboratory, is supported by the U.S. Department of Energy, Office of Science, Office of Basic Energy Sciences under Contract No. DE-AC02-76SF00515. The SSRL Structural Molecular Biology Program is supported by the DOE Office of Biological and Environmental Research, and by the National Institutes of Health, National Institute of General Medical Sciences (including P41GM103393). The contents of this publication are solely the responsibility of the authors and do not necessarily represent the official views of NIGMS or NIH.

Table of Contents

List of Tables

List of Figures

Abbreviations

1-EtIm	1-ethylimidazole
1-MeIm	1-methylimidazole
1,2-diMeIm	1,2-dimethylimidazole
2-Et-4-MeIm	2-ethyl-4-methylimidazole
2-EtIm	2-ethylimidazole
2-MeIm	2-methylimidazole
3-MePhHZ	3-methylphenylhydrazine
4-ClPhHZ	4-chlorophenylhydrazine
4-MeIm	4-methylimidazole
ACM	acetamide
AmphNHOH	*N*-hydroxyamphetamine
βME	β-mercaptoethanol
CAMNO	nitrosochloramphenicol
CDI	*C. difficile* infection
DNase	deoxyribonuclease I
EDTA	ethylenediaminetetraacetic acid
EtNO	nitrosoethane
FMN	flavin mononucleotide
FMT	fecal microbiota transplant
Hb	hemoglobin
hhMb	horse heart myoglobin
Im	imidazole

iPrNO	2-nitrosopropane
Mb	myoglobin
MeNHOH	*N*-methylhydroxylamine
MeNO	nitrosomethane
Mtz	metronidazole
NAD(P)H	nicotinamide adenine dinucleotide (phosphate)
NB	nitrobenzene
NMR	nuclear magnetic resonance
NR	nitroreductase
NTZ	nitazoxanide
OU MCL	University of Oklahoma Macromolecular Crystallography Lab
OU PPC	University of Oklahoma Protein Production Core
P450 BM3-HD	heme domain of cytochrome P450 from *Bacillus megaterium*
P450s	cytochromes P450
PDB	Protein Data Bank
PhHZ	phenylhydrazine
PhNHOH	*N*-phenylhydroxylamine
PhNO	nitrosobenzene
PMSF	phenylmethylsulfonyl fluoride
PrNO	1-nitrosopropane
RMSD	root mean square deviation
RNase	ribonuclease A
RNHOH	hydroxylamine-compound, R=alkyl or aryl

RNO	nitroso-compound, R=alkyl or aryl
SDS-PAGE	sodium dodecyl sulfate polyacrylamide gel electrophoresis
SNO	*S*-nitrosothiol
swMb	sperm whale myoglobin
t-BuNHOH	*N*-tertbutylhydroxylamine
wt	wild type

Abstract

The overall goal of my work was to probe the structural biology of drug metabolite protein interactions and to correlate this with the negative side effects associated with many prescription drugs. More specifically, the focus was on the interactions of myoglobin (Mb), hemoglobin (Hb), a *Clostridioides difficile* nitroreductase (NR), and cytochrome P450 BM3-HD with N-containing compounds. Using a combination of spectroscopy and X-ray crystallography, I was able to accomplish this goal.

In **Chapter 2**, the focus was on the formation of heme-nitroso adducts of Mb and Hb generated through oxidative and reductive pathways. While I initially predicted that heme-nitroso adducts would result from the reaction of Mb and Hb with nitro- and hydroxylamine-containing compounds, what actually resulted was the determination of a variety of products in addition to the predicted *N*-bound nitroso adducts. X-ray crystal structures of these products revealed that some of the compounds evaluated can indeed damage Hb through the formation of hemichromes that can be correlated with early stages of heme loss, which, downstream, may cause anemia. Additionally, we observed, for the first time, that two of the compounds evaluated are capable of *S*-nitrosating Hb at the βCys93 residue, an important contributor to the transportation of NO throughout the body. And finally, one of the X-ray crystal structures displays a ligand trapped in a Xe pocket, further demonstrating how large ligands can travel through the pockets within both Mb and Hb to reach the heme active site. The work presented in this chapter thus demonstrates a wide range of products that can result from the reaction of Mb and Hb with nitro- and hydroxylamine-containing compounds.

In **Chapter 3**, the focus was on *C. difficile* NRs responsible for metabolizing the antibiotic Mtz. Using UV-vis spectroscopy, I confirmed that a putative NR from *C. difficile* does in fact function as a Type I NR. Additionally, I solved its X-ray crystal structure, one of the first two reported from the hypervirulent *C. difficile* strain. The X-ray crystal structure also revealed a putative binding site for Mtz. The work in this chapter provides one of the first expression, purification, characterization and crystallization of a NR from the hypervirulent *C. difficile* strain.

The focus of **Chapter 4** was on the interaction of cytochrome P450 BM3-HD with RNOs, imidazoles and arylhydrazines. Using spectroscopy, I showed that the interaction of RNOs with P450 BM3-HD result in *N*-bound products and the extent of product formation was dependent on alkyl group size. Imidazoles were found to bind through their N-atoms in a type II fashion. And finally, arylhydrazines were observed to initially bind in a type II manner, but with exposure to air, they formed σ-bonded aryl-iron complexes. The work in this chapter elucidates the identity of the products in the reaction of P450 BM3-HD with RNOs, imidazoles and arylhydrazines.

Together, the work presented in **Chapters 2-4**, shows how N-containing compounds and their metabolites interact with Mb, Hb, NRs and P450 BM3-HD.

Chapter 1. Introduction

Nitrogen is one of the most abundant elements on Earth, making up ~78% of the Earth's atmosphere (in the form of N_2), and it is the fourth most abundant element in the human body.[1] Nitrogen is an important component of many endogenous compounds, such as DNA bases, amino acids, protein cofactors like flavin mononucleotide (FMN) and heme. Unsurprisingly, it is also found in many exogenous compounds and many of these are known to cause diseases or inhibit the natural functions of the proteins within the human body, emphasizing the relevance and importance of focusing on the interactions of these N-containing compounds with proteins.

When a person is prescribed a medication, it is assumed that it is going to improve their health, however, most medications have minor and/or major side effects. As drugs are metabolized, their metabolites can interact with off-target proteins accounting for some of the side effects associated with them. For example, Adderall is prescribed for the treatment of attention deficit hyperactivity disorder (ADHD) and narcolepsy. A major component of Adderall is amphetamine, a N-containing compound. Amphetamine is metabolized in the liver by cytochromes P450 (P450s) and its metabolites are able to travel through the bloodstream, interacting with proteins such as hemoglobin (Hb) and myoglobin (Mb). Amphetamine metabolites have been shown to inhibit both P450s[2-6] and a mutant form of Mb.[7] Another N-containing drug, Chloramphenicol, is widely prescribed for the treatment of bacterial infections, but it has been shown to irreversibly interact with P450s and can displace O_2 from Hb.[8, 9]

To combat the negative side effects associated with many prescription drugs, it is necessary to understand the biological chemistry of the drug metabolites. In **Chapter 2,** I

investigate the interactions of Hb and Mb with N-containing compounds. In **Chapter 3**, I characterize a new bacterial protein that metabolizes N-containing compounds. And finally, in **Chapter 4**, I study the products of the interactions of a model P450 with a series of N-containing compounds.

1.1 Heme protein interactions with N-containing compounds

Simple nitrogen oxides (NO_x) play an important role in the global nitrogen cycle (**Figure 1.1**).[1] Various metalloproteins are involved in NO_x interconversions, a major component of which are heme proteins (*** in Figure 1.1**). A substantial gap in knowledge is the structural biology of heme protein-NO_x interactions.

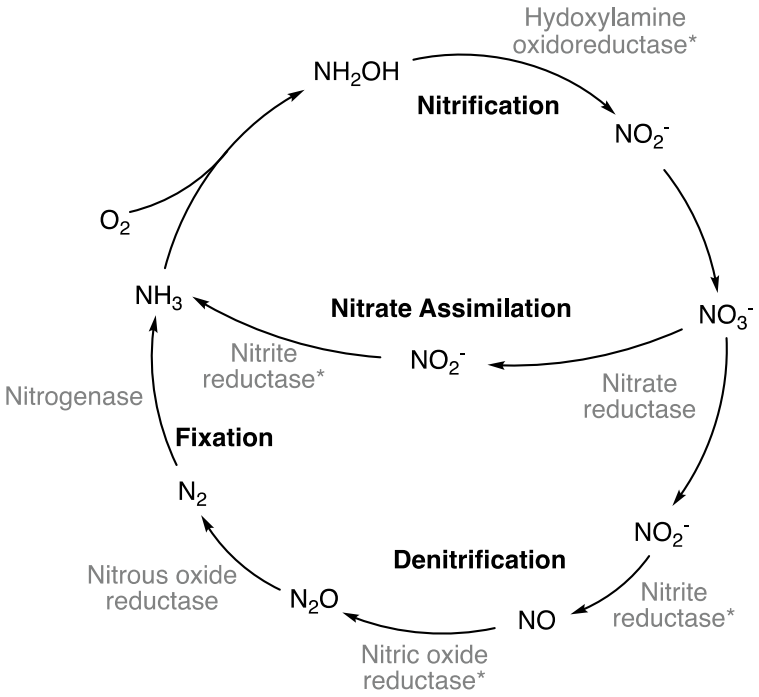

Figure 1.1. The nitrogen cycle and the enzymes (*heme proteins) involved (noted in grey).

Myoglobin (Mb) and hemoglobin (Hb) are both mono heme-containing proteins found in the muscles (Mb) and blood (Hb). The primary role of Hb and Mb is dioxygen transport and storage, respectively. This role can be disrupted by the binding of other compounds, such as NO_x derivatives, to the heme-Fe centers of these proteins. Nitroso (RNO, R=alkyl or aryl) compounds are NO_x derivatives, and they can form in vivo through

two potential routes – through the oxidation of amines (RNH_2) and hydroxylamines (RNHOH) or through the reduction of nitro-containing (RNO_2) compounds (**Figure 1.2**).[10]

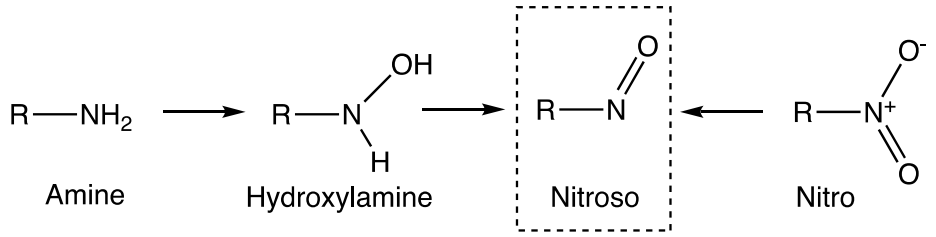

Figure 1.2 The oxidative metabolism (left) of amines and hydroxylamines, and the reductive metabolism (right) of nitro compounds resulting in the nitroso derivatives where R = alkyl or aryl.

Chapter 2 focuses on the structural biology of heme protein-nitroso derivatives. The metabolism of many commonly prescribed amine-containing (such as Adderall) and nitro-containing drugs (such as chloramphenicol) to their respective RNO derivatives are known, but much is still unknown about the nature of the resulting inhibitory heme-RNO interaction. The goal of this work was to characterize heme-RNO products generated by both the reductive and oxidative pathways. Presented in this work is the spectroscopic and crystallographic characterization of the products of the reactions between Mb and Hb with nitro- and hydroxylamine-containing compounds. I have determined high-resolution X-ray crystal structures of eight unique Mb/Hb-RNO complexes and collectively, these results illustrate the inhibitory and/or damaging effects that the formation of heme-nitroso complexes can have in mammalian biology.

1.2 *Clostridioides difficile* nitroreductase

Metronidazole (Mtz), a nitro-containing drug, is prescribed for a multitude of bacterial infections, including *Clostridioides difficile* infection (CDI). CDI is caused by *C. difficile*, a bacterium that infects the lower gastrointestinal tract. According to the Center for Disease Control, each year, CDI causes ~29,000 deaths and costs the United States $1 billion in excess medical costs.[11] Mtz has remained the number-one recommended drug for the treatment of CDI, despite the recent emergence of Mtz-resistant *C. difficile* strains.[12-18] If nothing is done to combat this resistance, the death tolls and costs linked with CDI will continue to rise.

In *C. difficile*, the nitroreductase (NR) enzymes are responsible for the metabolism of nitro-containing compounds including Mtz. Mtz is actually a prodrug that must be biochemically reduced for it to elicit its bactericidal effects. It is thought that the hydroxylamine metabolite is responsible for the bactericidal effects of Mtz, by inducing DNA breaks.[19] Unlike Mb and Hb, which utilize a metal-containing heme to reduce nitro-containing compounds, NRs utilize a non-metal-containing flavin mononucleotide (FMN) cofactor to reduce nitro-containing compounds (**Figure 1.3**).

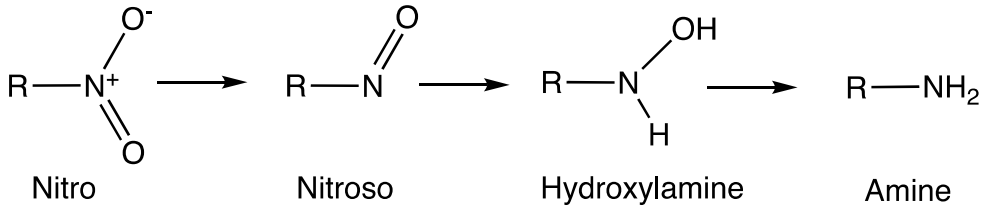

Figure 1.3 Reduction pathway of nitro compounds by Type I (air-insensitive) NRs.

Mtz resistance has been associated with NRs in both *Bacterocides fragilis* and *Helicobacter pylori*. [19-23] Additionally, in *C. difficile*, a mutation resulting in a truncation of a NR was found in both a resistant strain and sensitive strain with reduced susceptibility to Mtz, implicating NRs in Mtz resistance in *C. difficile*.[24] Despite the importance of *C. difficile* NRs, no NRs from a pathogenic strain in *C. difficile* had been characterized prior to our work.[25] In **Chapter 3**, I present the characterization of one of the first NRs from a pathogenic strain (CDR20291) of *C. difficile* using UV-vis spectroscopy and X-ray crystallography.

1.3 Cytochrome P450 BM3-HD

In humans, cytochromes P450 (P450s) are the primary protein responsible for metabolizing xenobiotics, making them an important family of proteins to study.[26] P450s are a class of heme-containing mono-oxygenases that perform a multitude of functions, however they are best known for their role in drug metabolism.[26, 27] Most human P450s are membrane-bound, making them difficult to work with and often necessitating the use of a model system. The P450 from *Bacillus megaterium* (P450 BM3) is commonly used as a model for human P450s, as it is not membrane-bound and is readily solubilized.[28] P450 BM3 possesses both a heme domain and a reductase domain. For the purposes of my study, only the heme domain was used (P450 BM3-HD).

In Mb and Hb, the heme is coordinated by a proximal His, but in P450s, the heme is coordinated by a proximal Cys. Additionally, the active site of P450 BM3-HD, while similar to that of Mb and Hb, is significantly larger in volume. This large difference in volume accounts, in large part, for a much greater diversity of substrates (based on size) that can bind within the active site.

The interaction of P450 BM3-HD with three different N-containing ligand sets (RNOs, imidazoles and arylhydrazines) is presented in **Chapter 4**. As shown in **Figure 1.2**, RNOs are produced either through oxidative or reductive metabolism, and these RNOs can inhibit P450s by binding at their Fe centers.[5, 29, 30] Imidazole groups are a common moiety in P450-targeted drugs, due to the high affinity of imidazoles for heme proteins.[31, 32] Arylhydrazines ($ArNHNH_2$, Ar = aryl), components of drugs such as isoniazid, an antibiotic prescribed for tuberculosis, and hydralazine, a medication used to treat high

blood pressure and heart failure, can cause adverse health effects in humans such as cancer, liver damage, hemolytic anemia and reticulocytosis.[33, 34] Much is still unknown about the nature of the products of the reactions between P450 BM3-HD and the above sets of compounds. My work presented in this chapter, using primarily UV-vis spectroscopy, helps to elucidate the identity of these products.

1.4 References

[1] Atkins, P. W., Overton, T. L., Rourke, J. P., Weller, M. T., and Armstrong, F. A. (2010) *Shriver and Atkins' Inorganic Chemistry*, 5 ed., Oxford University Press, Great Britain.

[2] Franklin, M. R. (1974) Complexes of metabolites of amphetamines with hepatic cytochrome P-450, *Xenobiotica 4*, 133-142.

[3] Franklin, M. R. (1974) The formation of a 455 nm complex during cytochrome P-450-dependent *N*-hydroxyamphetamine metabolism, *Mol Pharmacol 10*, 975-985.

[4] Jonsson, J., and Lindeke, B. (1976) On the formation of cytochrome P-450 product complexes during the metabolism of phenylalkylamines, *Acta Pharm Suec 13*, 313-320.

[5] Mansuy, D., Rouer, E., Bacot, C., Gans, P., Chottard, J. C., and Leroux, J. P. (1978) Interaction of aliphatic N-hydroxylamines with microsomal cytochrome P450: Nature of the different derived complexes and inhibitory effects on monoxygenases activities, *Biochem Pharmacol 27*, 1229-1237.

[6] James, R. C., and Franklin, M. R. (1975) Comparisons of the formation of cytochrome P-450 complexes absorbing at 455 nm in rabbit and rat microsomes, *Biochem Pharmacol 24*, 835-838.

[7] Wang, B., Powell, S. M., Guan, Y., Xu, N., Thomas, L. M., and Richter-Addo, G. B. (2017) Nitrosoamphetamine binding to myoglobin and hemoglobin: Crystal structure of the H64A myoglobin-nitrosoamphetamine adduct, *Nitric Oxide 67*, 26-29.

[8] Halpert, J. (1981) Covalent modification of lysine during the suicide inactivation of rat liver cytochrome P-450 by chloramphenicol, *Biochem Pharmacol 30*, 875-881.

[9] Eyer, P., Lierheimer, E., and Schneller, M. (1984) Reactions of nitrosochloramphenicol in blood, *Biochem Pharmacol 33*, 2299-2308.

[10] Lee, J., Chen, L., West, A. H., and Richter-Addo, G. B. (2002) Interactions of organic nitroso compounds with metals, *Chem Rev 102*, 1019-1066.

[11] Centers for Disease Control and Prevention. (2013) Antibiotic resistance threats in the United States, http://www.cdc.gov/drugresistance/threat-report-2013/pdf/ar-threats-2013-508.pdf.

[12] World Health Organization (2017) WHO Model List of Essential Medicines, 20th ed.

[13] Leffler, D. A., and Lamont, J. T. (2009) Treatment of *Clostridium difficile*-associated disease, *Gastroenterology 136*, 1899-1912.

[14] Musher, D. M., Aslam, S., Logan, N., Nallacheru, S., Bhaila, I., Borchert, F., and Hamill, R. J. (2005) Relatively poor outcome after treatment of *Clostridium difficile* colitis with metronidazole, *Clin Infect Dis 40*, 1586-1590.

[15] Nair, S., Yadav, D., Corpuz, M., and Pitchumoni, C. S. (1998) *Clostridium difficile* colitis: factors influencing treatment failure and relapse--a prospective evaluation, *Am J Gastroenterol 93*, 1873-1876.

[16] Baines, S. D., O'Connor, R., Freeman, J., Fawley, W. N., Harmanus, C., Mastrantonio, P., Kuijper, E. J., and Wilcox, M. H. (2008) Emergence of reduced susceptibility to metronidazole in *Clostridium difficile*, *J Antimicrob Chemother 62*, 1046-1052.

[17] Huang, H., Weintraub, A., Fang, H., and Nord, C. E. (2009) Antimicrobial resistance in *Clostridium difficile*, *Int J Antimicrob Agents 34*, 516-522.

[18] Jin, S. J., Seo, K. H., and Wi, Y. M. (2018) The effect of concomitant use of systemic antibiotics in patients with *Clostridium difficile* infection receiving metronidazole therapy, *Epidemiol Infect 146*, 558-564.

[19] Sisson, G., Jeong, J. Y., Goodwin, A., Bryden, L., Rossler, N., Lim-Morrison, S., Raudonikiene, A., Berg, D. E., and Hoffman, P. S. (2000) Metronidazole activation is mutagenic and causes DNA fragmentation in *Helicobacter pylori* and in *Escherichia coli* containing a cloned *H. pylori* rdxA+ (nitroreductase) gene, *J Bacteriol 182*, 5091-5096.

[20] Gal, M., and Brazier, J. S. (2004) Metronidazole resistance in *Bacteroides* spp. carrying nim genes and the selection of slow-growing metronidazole-resistant mutants, *J Antimicrob Chemother 54*, 109-116.

[21] Reysset, G. (1996) Genetics of 5-nitroimidazole resistance in *Bacteroides* species, *Anaerobe 2*, 59-69.

[22] Schapiro, J. M., Gupta, R., Stefansson, E., Fang, F. C., and Limaye, A. P. (2004) Isolation of metronidazole-resistant *Bacteroides fragilis* carrying the nimA nitroreductase gene from a patient in Washington State, *J Clin Microbiol 42*, 4127-4129.

[23] Jeong, J. Y., Mukhopadhyay, A. K., Dailidiene, D., Wang, Y., Velapatino, B., Gilman, R. H., Parkinson, A. J., Nair, G. B., Wong, B. C., Lam, S. K., Mistry, R., Segal, I., Yuan, Y., Gao, H., Alarcon, T., Brea, M. L., Ito, Y., Kersulyte, D., Lee, H. K., Gong, Y., Goodwin, A., Hoffman, P. S., and Berg, D. E. (2000) Sequential inactivation of rdxA (HP0954) and frxA (HP0642) nitroreductase genes causes moderate and high-level metronidazole resistance in *Helicobacter pylori*, *J Bacteriol 182*, 5082-5090.

[24] Lynch, T., Chong, P., Zhang, J., Hizon, R., Du, T., Graham, M. R., Beniac, D. R., Booth, T. F., Kibsey, P., Miller, M., Gravel, D., Mulvey, M. R., and Canadian Nosocomial Infection Surveillance, P. (2013) Characterization of a stable, metronidazole-resistant *Clostridium difficile* clinical isolate, *PLoS ONE 8*, e53757.

[25] Wang, B., Powell, S. M., Hessami, N., Najar, F. Z., Thomas, L. M., Karr, E. A., West, A. H., and Richter-Addo, G. B. (2016) Crystal structures of two nitroreductases from hypervirulent *Clostridium difficile* and functionally related interactions with the antibiotic metronidazole, *Nitric Oxide 60*, 32-39.

[26] Guengerich, F. P. (2015) Human cytochrome P450 enzymes, In *Cytochrome P450: Structure, Mechanism, and Biochemistry* (Ortiz de Montellano, P. R., Ed.) 4 ed., Kluwer Academic/Plenum Publishers, New York.

[27] Hannemann, F., Bichet, A., Ewen, K. M., and Bernhardt, R. (2007) Cytochrome P450 systems - biological variations of electron transport chains, *Biochim Biophys Acta 1770*, 330-344.

[28] Munro, A. W., Leys, D. G., McLean, K. J., Marshall, K. R., Ost, T. W. B., Daff, S., Miles, C. S., Chapman, S. K., Lysek, D. A., Moser, C. C., Page, C. C., and Dutton, P. L. (2002) P450 BM3: the very model of a modern flavocytochrome, *Trends Biochem Sci 27*, 250-257.

[29] Delaforge, M., Jaouen, M., and Mansuy, D. (1983) Dual effects of macrolide antibiotics on rat liver cytochrome P-450, *Biochem Pharmacol 32*, 2309-2318.

[30] Bensoussan, C., Delaforge, M., and Mansuy, D. (1995) Particular ability of cytochromes P450 3A to form inhibitory P450-iron-metabolite complexes upon metabolic oxidation of aminodrugs, *Biochem Pharmacol 49*, 591-602.

[31] Hackett, J. C., Kim, Y.-W., Su, B., and Brueggemeier, R. W. (2005) Synthesis and characterization of azole isoflavone inhibitors of aromatase, *Bioorg Med Chem 13*, 4063-4070.

[32] Recanatini, M., Cavalli, A., and Valenti, P. (2002) Nonsteroidal aromatase inhibitors: Recent advances, *Med Chem Res 22*, 282-304.

[33] Choudhary, G., and Hansen, H. (1998) Human health perspective of environmental exposure to hydrazines: A review, *Chemosphere 37*, 801-843.

[34] Jonen, H. G., Werringloer, J., Prough, R. A., and Estabrook, R. W. (1982) The reaction of phenylhydrazine with microsomal cytochrome P-450. Catalysis of heme modification, *J Biol Chem 257*, 4404-4411.

Chapter 2. Heme-nitroso adducts produced via the reductive and oxidative pathways

2.1 Introduction

In mammals, the muscle protein myoglobin (Mb) and the blood protein hemoglobin (Hb) are associated with dioxygen (O_2) storage and transport, respectively, by binding O_2 at their heme sites. Nitroso compounds (RNO; R = alkyl or aryl) can bind complementarily to the heme Fe since they are valence isoelectronic with O_2.[1] RNO derivatives are produced either through oxidative metabolism of amines and hydroxylamines, or reductive metabolism of nitro compounds (**Figure 2.1**).

Once present, RNO derivatives can bind to the Fe centers of the heme cofactors of various heme proteins and upon binding, can inhibit their normal functions. In fact, it has been shown that Hb has a higher affinity for RNOs than O_2.[2] Although many amine- and nitro-containing drugs are commonly prescribed for various medical uses, and their

---

*Reproduced in part, with permission, from (i) "Nitrosoamphetamine binding to myoglobin and hemoglobin: Crystal structure of the H64A myoglobin-nitrosoamphetamine adduct," B. Wang, S.M. Powell, Y. Guan, N. Xu, L.M. Thomas, G.B. Richter-Addo. *Nitric Oxide* **2017**, *67*, 26-29 © 2017 Elsevier Inc. (ii) "Nitrosyl myoglobins and their nitrite precursors: Crystal structural and quantum mechanics and molecular mechanics theoretical investigations of preferred Fe–NO ligand orientations in myoglobin distal pockets," B. Wang, Y. Shi, J. Tejero, S.M. Powell, L.M. Thomas, M.T. Gladwin, S. Shiva, Y. Zhang, G.B. Richter-Addo. *Biochemistry* **2018**, *57*, 4788−4802. © 2018 American Chemical Society.

metabolism to nitroso (RNO) derivatives are known, much is still unknown about the resulting heme-RNO interactions, increasing the importance of this work.

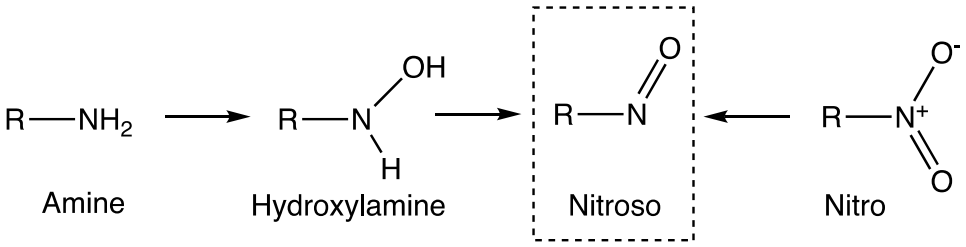

Figure 2.1. The oxidative metabolism of amines/hydroxylamines and the reductive metabolism of nitro compounds resulting in the nitroso derivatives (R = alkyl or aryl).

Mb is a ~17 kDa monomeric heme-containing protein located in the muscles of animals and its primary function is to store O_2.[3] Human adult Hb, on the other hand, is a ~64 kDa tetrameric protein consisting of two α and two β subunits, which is present in the blood and functions as an O_2 transporter.[3] Each Hb subunit is ~16 kDa and contains a single heme cofactor. Although the α and β subunits of human adult Hb have only 43% sequence identity, their active site residues are conserved. Additionally, the globular shapes of the α and β subunits are quite similar as well with an RMSD of 0.861 Å. Mb and the α subunit of Hb have only 25% sequence identity, but Mb and the β subunit of Hb have no significant sequence identity. Despite these low sequence identities, the overall globular folds of Mb and Hb consisting of α-helices are highly conserved with an RMSD of 1.085 Å (for α) and 1.139 Å (for β) (**Figure 2.2**).

Much of the reason for the similarity in the interactions between substrates with Mb and Hb at their Fe centers can be correlated with their highly conserved active sites (**Figure 2.3**). The proximal His in the F helix (H93 in Mb, H87 in α Hb and H92 in β Hb)

coordinates with the heme-Fe, holding it in place. The distal His in the E helix (H64 in Mb, H58 in α Hb and H63 in β Hb) has been shown to play an important role in the interaction of and entry of substrates and subsequent stabilization of binding to the heme.[4-6]

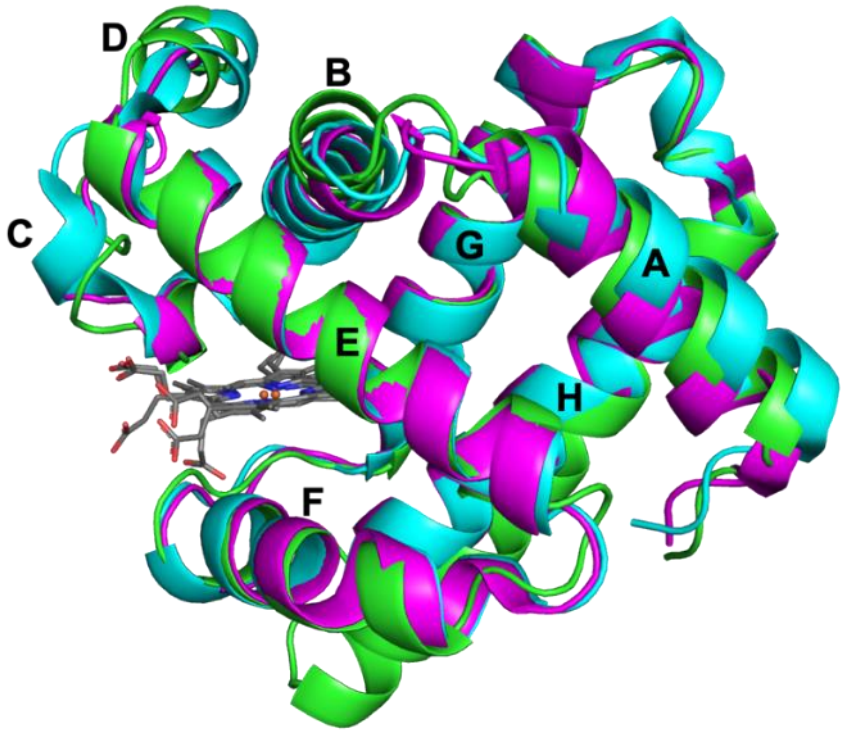

Figure 2.2. Overlay of swMb (green, PDB id: 2MBW) with the α (magenta) and β (cyan) subunits of Hb (PDB id: 3P5Q).

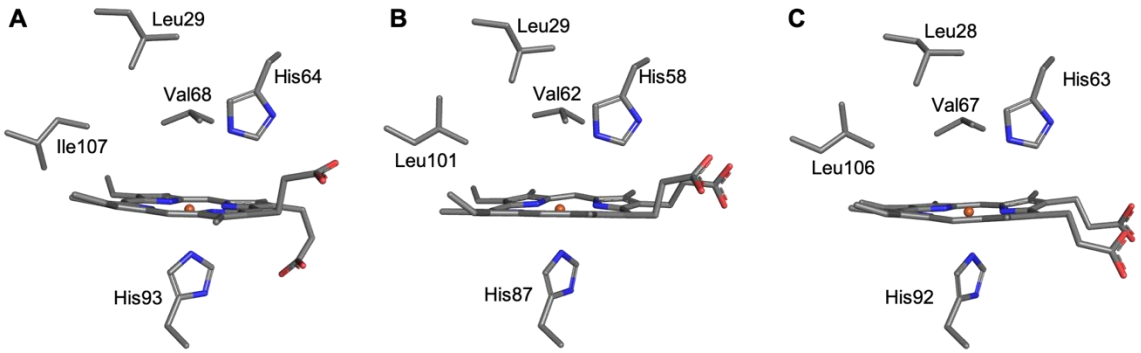

Figure 2.3. Active site comparison of (A) swMb (PDB id: 2MBW) with (B) the Hb α subunit and (C) the Hb β subunit (PDB id: 3P5Q).

Due to the importance of the distal His residue and the hydrogen bonding stabilization it provides, our lab commonly uses four different Mb mutants – H64V, H64A, H64Q and V68A/I107Y (AY), to further examine its role in ligand binding and entry. In the H64V and H64A mutants, the bulky His residue is replaced with a smaller residue incapable of providing a hydrogen bond. Many species of mollusks[7-9] and nematodes[10] have a hydrophobic residue (Val or Leu) at this site in their wild-type (wt) Mbs. The H64Q mutant introduces a more flexible residue that is capable of hydrogen bonding (both as an acceptor and donor). Some species of elephants[11, 12], worms[13, 14] and sharks[15-17] have a Gln at this same position in their wt Mbs. The AY double mutant provides a second hydrogen-bonding site in the interior region of the active site.

The goal of this study was to characterize representative nitroso adducts of Mb and Hb and to evaluate their potential physiological consequences. This was achieved by employing both the reductive and oxidative pathways for the generation of the nitroso products (**Figure 2.1**). For the reductive pathway, inorganic nitrite (NO_2^-) and the organic nitro compounds metronidazole (Mtz) and chloramphenicol (CAM) were used (**Figure 2.4, left**). For the oxidative pathway, the organic hydroxylamine (RNHOH) compounds *N*-phenylhydroxylamine (PhNHOH), *N*-hydroxyamphetamine (AmphNHOH), *N*-tertbutylhydroxylamine (*t*-BuNHOH) and *N*-methylhydroxylamine (MeNHOH) were used (**Figure 2.4, right**).

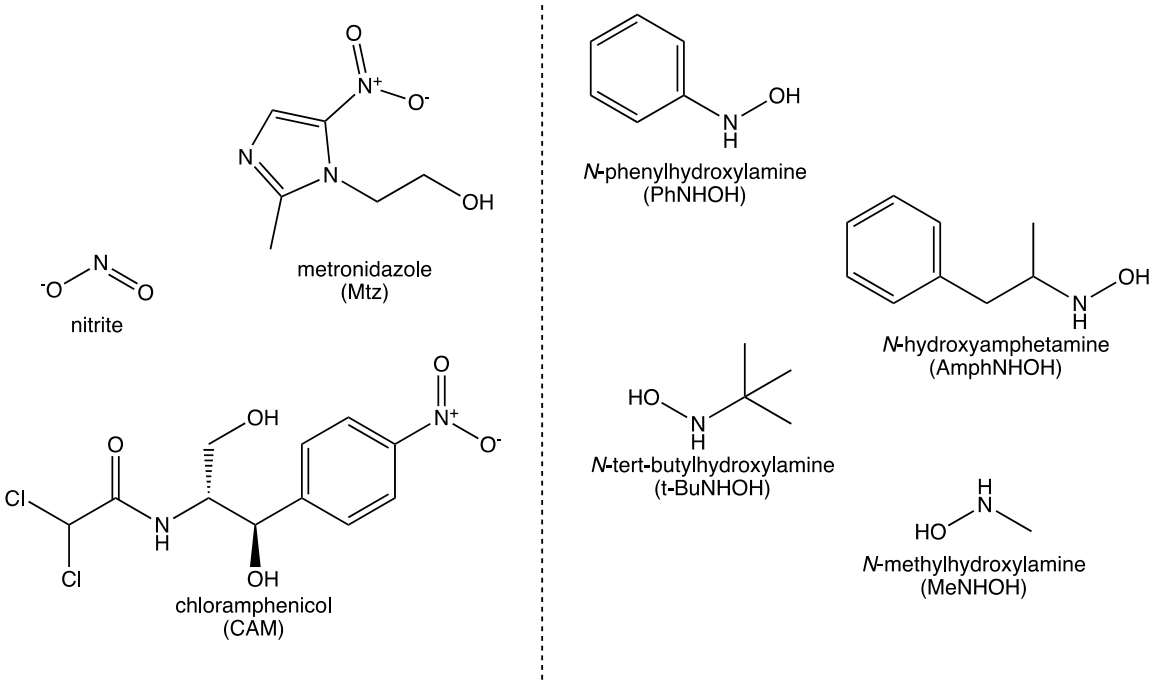

Figure 2.4. Nitro-containing substrates (left) and hydroxylamine-containing substrates (right) used in this study.

Nitrite has long been known to interact with Mb.[18] Its role in meat curing[19, 20], nitrification and the global nitrogen cycle[21], and vasodilation[22-24] have made it an important compound to study. While there is a large body of work on the chemistry of nitrite, prior to our group's work, there had not been a systematic study of what factors influence the binding mode of nitrite in heme proteins such as Mb and Hb.[4] Presented here is a study of the interaction of nitrite with the H64V mutant of sperm whale Mb (swMb). The related interaction with horse heart Mb (hhMb) was reported earlier by our group.[5] Both sw and hhMb are used since they are easily obtained and high a high sequence identity with human Mb (84 - 88%).

CAM and Mtz are widely prescribed antibiotics for the treatment of bacterial infections. CAM has been shown to interact irreversibly with cytochromes P450 (P450s)

and can displace O_2 from Hb.[25, 26] Interactions of CAM with Mb had not yet been reported and there were no crystal structures of any heme protein with CAM prior to my work in this area. Mtz is used in the treatment of *C. difficile* infections and is typically metabolized by the bacterial nitroreductase enzymes (See Chapter 3). Mtz has been detected in blood samples of treated patients and its metabolites are known to be excreted through the liver.[27] This latter observation sparked my interest in the interaction of Mtz with heme proteins. I note that the interaction of Mtz with any heme protein had not been reported prior to this work.

Aniline ($PhNH_2$) is a widely used chemical in industrial settings and its toxic effects are well-documented.[28-30] P450s are known to oxidatively metabolize aniline into PhNHOH. It has been confirmed that PhNHOH is the toxic form of aniline, and its presence leads to blood disorders such as methemoglobinemia and hemolytic anemia.[31, 32] This is thought to be caused by the formation of nitrosobenzene (PhNO) upon reaction of PhNHOH with heme proteins.[30] PhNO can also be formed from the nitrobenzene ($PhNO_2$) precursor under reducing conditions.[33] Given the importance of PhNHOH in human health, I became interested in further defining the products that result from its reactions with swMb and human Hb.

Some commonly prescribed medications contain amphetamine (Amph), methamphetamine (methAmph), or a form of either. For example, Adderall®, a drug used to treat attention deficit hyperactivity disorder (ADHD) and narcolepsy, is a combination of Amph and dextroamphetamine (d-Amph). Desoxyn® is a prescription methAmph for the treatment of obesity and ADHD. Despite their high medicinal value, Amph derivatives are known to have high potential for abuse.[34] Because of this, Amph and methAmph are

classified by the U.S. Drug Enforcement Agency as Schedule II substances, meaning the drug has high potential for abuse and use may lead to severe dependence.[34] Interactions of Amph and methAmph with heme proteins are an important component of their metabolism. Amph is oxidatively metabolized by P450s to generate AmphNHOH and other products[1], while methAmph is oxidatively metabolized by P450s via aromatic hydroxylation and/or *N*-demethylation to generate Amph and AmphNHOH.[35] Amph and AmphNHOH can also react with P450s to form inhibitory complexes[36-40] as a result of the nitrosoamphetamine (AmphNO) metabolite forming an Fe-AmphNO complex.[39, 41] AmphNHOH has been isolated as a metabolic intermediate of Amph in animals[42], but surprisingly, formation of heme-AmphNO derivatives for Mb or Hb had not yet been reported prior to our lab's work.[43] Interestingly, it has been suggested by others that Mb- and Hb-AmphNO derivatives were unlikely to form due to the large size of AmphNO and the smaller-size heme distal pocket cavity in these proteins.[44, 45]

The *t*-BuNHOH and benzaldehyde compounds result from the decay of PBN (α-phenyl-*N*-*t*-butyl nitrone), a compound that has been shown to delay senescence in human lung fibroblasts, reverse the decay of mitochondria in rat livers and exert a neuroprotective effect in gerbils and rats.[46] Atamna et al. used *t*-BuNHOH, MeNHOH and PhNHOH to show that PBN is unnecessary to exert these effects and that it is actually the *N*-hydroxylamine metabolite of PBN that is responsible for these effects. They found that all *N*-hydroxylamines tested could exert these effects.[46] Additionally, MeNHOH is used in the synthesis of biologically active azetidinones and isoxazoles, which make up the core of many prescription drugs.[47] The interaction of *N*-hydroxylamines such as *t*-BuNHOH and MeNHOH with heme proteins has been studied in Mb and Hb[48] as well as in

microperoxidase 8.[44] MeNHOH has also been used to probe the reaction mechanism of P450s.[49, 50] Prior to this work, however, there were no three-dimensional X-ray crystal structures characterizing the products of the interactions between Hb and *t*-BuNHOH and MeNHOH.

The work presented in this chapter provides both a spectroscopic and structural analysis of the heme-nitroso products of Mb and Hb formed through both the reductive and oxidative pathways in reaction with nitro and hydroxylamine compounds, respectively.

2.2 Materials and Methods

2.2.1 Cloning of swMb

The plasmid (pET-28a-wt) containing the gene for recombinant wild-type sperm whale myoglobin (wt swMb) was obtained from Professor Mario Rivera from the University of Kansas. The wt recombinant protein expressed from this plasmid as compared to native wt swMb, has an additional N-terminus Met and a mutation (D122N).[6]

All mutagenesis was performed in our lab by Dr. Bing Wang, using the Quick-Change method (Stratagene), and transformed into *E. coli* DH5α competent cells. All mutants were confirmed by sequencing at Oklahoma Medical Research Foundation (OMRF) at the University of Oklahoma Health Sciences Center (OUHSC).

2.2.2 Expression and purification of swMb proteins

The swMb proteins (wt and mutants) were expressed in *E. coli* BL21 (DE3). The proteins were purified as described by Springer and Sligar[51] with slight modifications. The resuspended cells were lysed using an Emulsiflex in a buffer made up of 50 mM Tris, 1 mM EDTA, pH 7.4 containing appropriate amounts of DNase, RNase and PMSF. A 60% ammonium sulfate precipitation was used first to remove contaminating proteins. This was followed by a 95% ammonium sulfate precipitation to obtain swMb. Overnight dialysis in a 1:9 glycerol to low salt buffer (100 mM potassium phosphate, 40 mM NaCl, pH 6) was used to remove ammonium sulfate. After centrifugation, the supernatant was loaded onto a CM52 cation exchange column equilibrated with low salt buffer. The sample was eluted using a linear salt gradient (40 mM – 1 M NaCl). Fractions containing the protein of interest (as judged by SDS-PAGE) were pooled for use in subsequent steps.

It is common to obtain a mixture of apo and heme-bound protein from this procedure. Therefore, to obtain a homogenous mixture, heme reconstitution was performed following ion exchange column chromatography. Specifically, an excess of heme (15 mM dissolved in 0.1 M NaOH) was added dropwise into the pooled protein and the solution was left to stir overnight at 4 °C.

After centrifugation, the supernatant was concentrated using an Amicon ultra filter with a cutoff of 10 kDa (Millipore) and loaded onto a G75 gel filtration column equilibrated with 20 mM Tris, 1 mM EDTA, at pH 7.4. Pure protein fractions (as judged by SDS-PAGE) were pooled and concentrated to either ~20 mg/mL for hanging drop crystallization or ~60 mg/mL for batch method crystallization. Protein concentration of wt and mutant (H64A, H64Q, V68A/I107Y) swMb was estimated using the absorbance of the heme (Soret band at λ 408 nm) using the extinction coefficient of ferric Mb^{III}-H_2O (188 $mM^{-1}cm^{-1}$). The exception to this is ferric H64V $swMb^{III}$ which has a characteristic peak at 395 nm in the Soret band with a corresponding extinction coefficient of 103 $mM^{-1}cm^{-1}$ at this wavelength.[52]

If the resulting protein contained a mixture of oxidized (i.e., ferric) and reduced (i.e., ferrous) species typically indicated by a shoulder in the absorbance peak in the Soret region, an excess of potassium ferricyanide was added to fully oxidize the protein. The mixture was vortexed and then loaded onto a G25 desalting column to remove any excess potassium ferricyanide. Following this, the protein was again concentrated for use in further studies.

2.2.3 Isolation and purification of human Hb

Human blood was obtained, with permission, from the Blood Bank at the University of Oklahoma Health Science Center in the form of packed cells. The bag of packed cells (~400 mL) was immediately placed on ice without direct contact in order to avoid degradation of the cells. OxyHb (ferrous Hb^{II}-O_2) was isolated from the packed cells and purified following published protocols.[3, 53] The concentration of the final, purified ferrous Hb^{II}-O_2 was measured by UV-vis spectroscopy using its extinction coefficient of 13.8 $mM^{-1}cm^{-1}$ at 541 nm and 14.6 $mM^{-1}cm^{-1}$ at 577 nm. The protein was flash frozen and stored at -80 °C until needed.

Prior to use, to ensure that all ferrous Hb^{II}-O_2 was converted to metHb (ferric Hb^{III}-H_2O), 1.5 molar excess of potassium ferricyanide was added to thawed ferrous Hb^{II}-O_2. After the solution turned from red to brown, indicating the reaction had taken place, the sample was loaded onto a G25 size exclusion column equilibrated with 50 mM sodium phosphate, pH 7.4 to remove any excess potassium ferricyanide. Brown-colored fractions were collected and combined. The concentration of ferric Hb^{III}-H_2O was measured by UV-vis spectroscopy using its extinction coefficient of 9.1 $mM^{-1}cm^{-1}$ at 500 nm and 3.8 $mM^{-1}cm^{-1}$ at 630 nm.[3]

For all anaerobic experiments, the sample of Hb^{II}-O_2 in buffer was degassed by bubbling nitrogen gas through it for ~30 min and transferred into an anaerobic MBraun chamber. After 4-5 days in the chamber, the ferrous Hb^{II}-O_2 had converted to deoxyHb (ferrous Hb^{II}) as verified by UV-vis spectroscopy. The concentration of ferrous Hb^{II} was determined by UV-vis spectroscopy using its extinction coefficient of 133 $mM^{-1}cm^{-1}$ at 430 nm and 12.5 $mM^{-1}cm^{-1}$ at 555 nm.[3]

2.2.4 Protein characterization

All swMb proteins (wt and mutants) were expressed in *E. coli*. The wt and mutant proteins, except for the double mutant V68A/I107Y, were expressed in high yields (~100 mg/L). The double mutant V68A/I107Y was expressed in significantly lower yields (~10 mg/L). Following the CM52 column chromatography purification step, some impurities remained in the sample, but the final G75 column chromatography purification step removed these impurities. All swMb proteins were obtained in high purity (>90%) as evaluated by SDS-PAGE. Human oxyHb was also obtained at high purity following purification.

2.2.5 UV-vis spectroscopy

UV-vis measurements were carried out using a Hewlett-Packard 8453 spectrophotometer. Quartz cuvettes (Starna Cells) equipped with screw caps were used for all experiments. All spectroscopy was carried out aerobically, unless otherwise noted.

2.2.6 Synthesis of nitrosochloramphenicol

Nitrosochloramphenicol (CAMNO) was synthesized with the assistance of Dr. Erwin Abucayon following a published protocol.[54, 55] The purity was checked by ^{1}H NMR spectroscopy. The final product was dissolved in methanol for use in UV-vis studies.

^{1}H NMR (400 MHz, CD_3OD, 25 °C, δ ppm): 7.77 (m, aromatic C-H), 6.16 (s, Cl_2C-H), 5.06 (d, benzylic C-H), 4.62 (br, N-H), 4.10 (m, HCN-H), 3.70 (m, O-H), 4.78 and 3.52 (residual CH_3OH).

2.2.7 Synthesis of N-hydroxyamphetamine

N-hydroxyamphetamine (AmphNHOH) was synthesized with the assistance of Dr. Erwin Abucayon following a published protocol.[56] The purity was checked by ^{1}H NMR spectroscopy, and the final product was dissolved in methanol for use in UV-vis studies.

^{1}H NMR (400 MHz, $CDCl_3$, 25 °C, δ ppm): 7.30 (m, 2H), 7.26 (s, residual $CHCl_3$), 7.19 (m, 3H), 6.23 (s, 1H), 5.13 (s, 1H), 3.22 (m, 1H), 2.85 (m, 1H), 2.63 (m, 1H), 1.10 (m, 3H).

2.2.8 Materials

Nitro compounds, sodium nitrite, CAM and Mtz, were purchased from Sigma Aldrich, Aldrich, and Fluka, respectively. Hydroxylamine compounds, PhNHOH, MeNHOH hydrochloride and *t*-BuNHOH hydrochloride, were purchased from Aldrich. All chemicals were used as received.

2.2.9 UV-vis spectroscopy of swMb and Hb with nitro-containing compounds

2.2.9.1 H64V swMb with nitrite

UV-vis spectroscopy was used to monitor the reaction of H64V Mb and nitrite. An initial reading was taken of the starting ferric H64V Mb^{III} (10 μL of 20 mg/mL) in 2.5 mL of 0.1 M sodium phosphate buffer at pH 7.4. 5 μL of sodium nitrite (1M) was then added to the cuvette to produce the ferric H64V Mb^{III}-NO_2 spectrum. Similar methods were followed to generate the spectrum of ferrous H64V Mb^{II}-NO from the addition of 5 μL of sodium dithionite (1M) to the ferric protein followed by the addition of sodium nitrite.

2.2.9.2 swMb and ferric Hb with Mtz and CAM

UV-vis spectroscopy was used to monitor the reaction of ferric $swMb^{III}$-H_2O (wt and mutants) and ferric Hb^{III}-H_2O with Mtz and CAM. An initial reading was taken of the starting ferric Mb^{III}-H_2O (5 μL of 20 mg/mL) or ferric Hb^{III}-H_2O (10 μL of 25 mg/mL) in 2.5 mL of 0.1 M sodium phosphate buffer at pH 7.4. 5 μL of sodium dithionite (1 M) was added to the cuvette to fully reduce the protein to ferrous deoxyMb^{II}, and a reading was taken. 10-15 μL of substrate (50 mg/mL CAM or 20 mM Mtz) was then added to the cuvette. Readings were taken at different time points during the course of the reaction to monitor its progress.

2.2.9.3 deoxyHb with CAMNO

UV-vis spectroscopy was used to monitor the anaerobic reaction of ferrous deoxyHb^{II} with CAMNO. All buffers were degassed by bubbling nitrogen gas through them for ~30 min and brought into an anaerobic MBraun chamber prior to use.

Additionally, the cuvettes were capped prior to their transfer to the spectrometer in the main lab to prevent entry of O_2. An initial reading was taken of the starting ferrous deoxyHb^{II} (10 μL of 25 mg/mL) in 2.5 mL of 0.1 M sodium phosphate buffer at pH 7.4. 10 μL of CAMNO (dissolved in methanol) was then added to the cuvette. Readings were taken at different time points during the course of the reaction to monitor its progress.

2.2.10 UV-vis spectroscopy of swMb and ferric Hb with hydroxylamines

2.2.10.1 swMb and ferric Hb with AmphNHOH

UV-vis spectroscopy was used to monitor the reaction of ferric swMb^{III}-H_2O (wt and mutants) and ferric Hb^{III}-H_2O with AmphNHOH. An initial reading was taken of the starting ferric Mb^{III}-H_2O (10 μL of 20 mg/mL) or ferric Hb^{III}-H_2O (10 μL of 30 mg/mL) in 2.5 mL of 0.1 M sodium phosphate buffer at pH 7.4. Next, 10 μL of AmphNHOH (200 mM) was added. Readings were taken at different time points during the course of the reaction to monitor its progress. The anaerobic reaction of ferrous deoxyHb^{II} with AmphNHOH was also performed following the same procedures; however, the cuvette was sealed, and all reagents were degassed by bubbling nitrogen gas through them for ~30 min prior to use and added in an MBraun anaerobic chamber.

In order to monitor the reversal of this reaction, ferric Mb^{III}-H_2O (in 0.1 M sodium phosphate buffer at pH 7.4) and solid AmphNHOH were mixed until the ferrous Mb^{II}-AmphNO complex formed. 5 μL of this reaction solution was added to 2.5 mL of 0.1 M sodium phosphate buffer at pH 7.4. Finally, 5 μL of potassium ferricyanide (100mM) was then added to the cuvette to oxidize the protein. This procedure was also performed for ferrous Hb^{II}-AmphNO.

2.2.10.2 Ferric Hb with PhNHOH, t-BuNHOH and MeNHOH

UV-vis spectroscopy was used to monitor the reaction of ferric Hb^{III}-H_2O with PhNHOH, *t*-BuNHOH and MeNHOH. An initial reading was taken of the starting ferric Hb^{III}-H_2O (15 μL of 30 mg/mL) in 2.5 mL of 0.1 M sodium phosphate buffer at pH 7.4. 20 μL of substrate (200 mM in the same buffer) was then added to the cuvette. Readings were taken at different time points during the course of the reaction to monitor its progress.

2.2.10.3 wt swMb with PhNHOH

UV-vis spectroscopy was used to monitor the reaction of ferric wt $swMb^{III}$-H_2O (in 0.1 M sodium phosphate buffer at pH 7.4) with PhNHOH. An initial reading was taken of the starting ferric wt Mb^{III}-H_2O (10 μL of 20 mg/mL) in 2.5 mL of 0.1 M sodium phosphate buffer at pH 7.4. 10 μL of substrate (200 mM in the same buffer) was then added to the cuvette. Readings were taken at different time points during the course of the reaction to monitor its progress. In order to monitor the reversal of this reaction, wt Mb^{III}-H_2O and solid PhNHOH were mixed for 10 min to generate ferrous wt Mb^{II}-PhNO. 5 μL of this reaction solution was then added to 2.5 mL of 0.1 M sodium phosphate buffer at pH 7.4. 5 μL of potassium ferricyanide (100mM) was then added to the cuvette to oxidize the protein.

2.2.11 Crystallization

2.2.11.1 H64V swMb-nitrite

Crystals of ferric H64V swMb^{III} were grown as described by Phillips et al.[57] Well solutions containing 2.52-3.2 M ammonium sulfate, 100 mM Tris-HCl, 1 mM EDTA, pH 7.4 or 9.0 were used for the hanging drop vapor diffusion method. The drops contained a 1:1 ratio of protein (28 mg/ml) to well solutions. The drops were seeded with crushed ferric H64A swMb^{III}-H_2O crystals after an equilibration period of 8 h. The best crystals grew using 2.6-2.8 M ammonium sulfate at pH 9.0 after two weeks. Crystals were looped and placed into a 4 μL drop of well solution containing 10% glycerol, and the drop was covered with mineral oil. A few grains of solid sodium nitrite were added into the drop and allowed to soak for up to 1 h. Crystals were harvested at different time points (15, 20, 25 and 30 min) for X-ray diffraction data collection.

2.2.11.2 H64Q swMb with Mtz

The co-crystallization method was utilized. 75 μL of ferric H64Q swMb^{III}-H_2O (20 mg/mL in 0.1 M sodium phosphate buffer at pH 7.4) was mixed with a few grains of solid Mtz and allowed to react for 15 min. A small of amount of solid sodium dithionite was then added to the mixture. Completion of the reaction was confirmed using UV-vis spectroscopy. Crystals were grown using the hanging drop vapor diffusion method as described by Phillips et al.[57] The wells contained 2.56-2.76 M ammonium sulfate, 100 mM Tris-HCl, 1 mM EDTA, pH 7.4 or 9.0 and the drops contained a 1:1 ratio of protein-reaction to well solution. The drops were seeded with crushed ferric H64A swMb^{III}-H_2O crystals after an equilibration period of 6 h.

2.2.11.3 deoxyHb with CAMNO

Anaerobic co-crystallization was utilized to crystallize [α-Fe^{II}][β-Fe^{II}-SNO]$_{\{CAMNO\}}$. In an MBraun anaerobic chamber, 2.5 mL of deoxyHb^{II} (30 mg/mL in 50 mM sodium phosphate, pH 7.4) was mixed with a few grains of solid CAMNO and allowed to react for 20 min. Completion of the reaction was confirmed using UV-vis spectroscopy. Crystals were grown using the batch method as described by Safo and Abraham.[53] 10.25x64 mm Monoject blood collection tubes (COVIDIEN) were used, and the tubes contained 0.5 M Fe citrate, 200 μL of the deoxyHb^{II}-CAMNO mixture and varying ratios of 3.6 M ammonium phosphate/sulfate.

2.2.11.4 wt swMb with PhNHOH

Crystallization of ferric wt swMb^{III}-H_2O was performed using the hanging drop vapor diffusion method following the method of Phillips et al.[57] Wells containing 2.52-3.2 M ammonium sulfate, 100 mM Tris-HCl, 1 mM EDTA, pH 7.4 or 9.0 were used. The drops contained a 1:1 ratio of protein (20 mg/ml in 0.1 M sodium phosphate buffer at pH 7.4) to well solutions and were seeded after an equilibration period of 8 h. The best crystals grew using 2.56 M ammonium sulfate at pH 7.4. Crystals were looped into a 4 μL drop of well solution containing 10% glycerol and the drop was covered with mineral oil. A small amount of solid PhNHOH was added into the drop and allowed to soak for up to 1 d. Crystals were harvested at different time points (30 min, 1 h, 2 h, 4 h, 6 h and 1 d).

2.2.11.5 Ferric Hb with PhNHOH, MeNHOH, t-BuNHOH and AmphNHOH

Co-crystallization was utilized to obtain crystals of the products resulting from the reactions of ferric Hb^{III}-H_2O with PhNHOH, MeNHOH, *t*-BuNHOH and AmphNHOH. The reactions were carried out in solution, and reaction completion was verified using UV-vis spectroscopy prior to crystallization. For $[\alpha\text{-}Fe^{III}(H_2O)][\beta\text{-}Fe^{III}(His)_2\text{-}SNO]_{\{PhNO\}}$, 2.5 mL of ferric Hb^{III}-H_2O (30 mg/ml 50 mM sodium phosphate, pH 7.4) was mixed with 0.5 mL of PhNHOH (200 mM in water) for 15 min prior to setting up crystallization. For $[\alpha\text{-}Fe^{III}(H_2O)][\beta\text{-}Fe^{II}(MeNO)]$, 7.5 mL of ferric Hb^{III}-H_2O (30 mg/ml in 50 mM sodium phosphate, pH 7.4) was mixed with a few grains of solid MeNHOH for a total of 48 h; crystallization was set up at 2 h, 24 h, and 48 h. For $[\alpha\text{-}Fe^{III}(H_2O)][\beta\text{-}Fe^{III}(His)_2]_{\{t\text{-}BuNHOH\}}$, 7.5 mL of ferric Hb^{III}-H_2O (30 mg/ml in 50 mM sodium phosphate, pH 7.4) was mixed with a few grains of solid *t*-BuNHOH for a total of 5 d; crystallization was set up at 24 h, 48 h and 5 d. For $[\alpha\text{-}Fe^{III}(H_2O)][\beta\text{-}Fe^{II}(AmphNO)]$, 2 mL of ferric Hb^{III}-H_2O (30 mg/ml in 50 mM sodium phosphate, pH 7.4) was mixed with 0.5 mL AmphNHOH (90 mM in methanol) and allowed to react for one week prior to setting up crystallization. Crystals were grown using the batch method as described by Safo and Abraham.[53] 10.25x64 mm Monoject blood collection tubes (COVIDIEN) were used, and they contained 3.2 M Na/K phosphate buffer (pH 6.30, 6.47 or 6.81), 5 μL toluene, and varying ratios of buffer to protein reaction solutions.

2.2.12 X-ray data collection

The diffraction data for all X-ray crystal structures, except that for [α-$Fe^{III}(H_2O)$][β-$Fe^{III}(His)_2$-SNO]$_{\{PhNO\}}$, were collected at the University of Oklahoma Macromolecular Crystallography Lab (OU MCL) using a home source Rigaku MicroMax 007HF microfocus X-ray generator coupled to a PILATUS 200K detector. The data was collected at 100 K with Cu Kα radiation (λ = 1.54178 Å) from the generator operated at 40 kV/30 mA. The diffraction data for [α-$Fe^{III}(H_2O)$][β-$Fe^{III}(His)_2$-SNO]$_{\{PhNO\}}$was collected at the Stanford Synchrotron Radiation Lightsource (SSRL) on beamline 9-2 (λ = 0.98 Å) equipped with a PILATUS 6M PAD detector.

2.2.13 Data processing, structure solution and refinement

The X-ray diffraction data for all structures were processed using *HKL3000*[58] and the resulting *sca* files were converted to *mtz* using *Scalepack2mtz* in the CCP4 program suite.[59] *PHASER MR* (CCP4)[60] was used to determine the initial phases. The model used for molecular replacement for all Mb structures (except H64V swMb-nitrite) was wt swMb (ferric Mb^{III}-H_2O) at 1.5 Å resolution (PDB ID: 2MBW) with the heme, water molecules and ligands removed from the structure. The model used for molecular replacement for all Hb structures was ferric *R*-state human aquomethemoglobin (ferric Hb^{III}-H_2O) at 2.0 Å resolution (PDB ID: 3P5Q) with the heme, water molecules, toluene and ligands removed from the structure. All refinements were performed using *Refmac5* (CCP4).[61] Models were rebuilt using *COOT*[62] and validated using *MolProbity*[63] to check for unusual residue conformations and contacts. Each structure is detailed below.

The figures for each structure were generated using *Pymol.*[64] $2F_o$-F_c electron density maps were calculated by *Fast Fourier Transform* (FFT; CCP4).[65] F_o-F_c electron density maps were generated by first deleting all ligands from the final *pdb* file of each structure. This *pdb* file was used to create a new F_c *mtz* file using *SFall* (CCP4). The F_c *mtz* file was used to generate the F_o-F_c electron density map using *FFT*. The resulting *FFT map* files were converted to *ccp4* files and displayed in *Pymol*.

2.2.13.1 Ferric H64V swMb^{III}-nitrite

The model used for molecular replacement was wt swMb (ferric Mb^{III}-H_2O) at 2.0 Å resolution (PDB ID: 2MGJ) with the heme, water molecules, and ligands removed from the structure. Ten initial cycles of restrained refinement were run with *Refmac5*, and the *R* factor decreased from 0.330 to 0.262. Ligands and water were added to the model based on the F_o-F_c electron density maps in the subsequent refinement cycles. Two sulfate anions, three glycerol and four nitrite anions (ligand id: NO2) were added to the model. Two conformations for the sidechain Val68 were modeled with 50% occupancy each. The final *R* factor and R_{free} were 0.171 and 0.204, respectively. The final structure was deposited in the PDB with PDB accession number 6CF0.

2.2.13.2 Ferrous H64Q swMb^{II}-acetamide

Ten initial cycles of restrained refinement were run with *Refmac5*, and the *R* factor decreased from 0.361 to 0.276. Ligands and water were added to the model based on the F_o-F_c electron density maps in the subsequent refinement cycles. Two sulfate anions, two glycerol and one acetamide (ligand id: ACM) were added to the model. The *N*-terminal

Met and the *C*-terminal residues Q152 and G153 were omitted due to lack of electron density. Two conformations for the sidechains Val68 and Lys133 were modeled with 50% occupancy each. The final *R* factor and R_{free} were 0.204 and 0.221, respectively.

2.2.13.3 [α-Fe^{II}][β-Fe^{II}-SNO]$_{\{CAMNO\}}$

Ten initial cycles of restrained refinement were run with *Refmac5*, and the *R* factor decreased from 0.451 to 0.331. Ligands and water were added to the model based on the F_o-F_c electron density maps in the subsequent refinement cycles. Four glycerol, eight sulfates and one CAMNO (ligand id: 5NF) were added to the model. The model for CAMNO was built in *Phenix* using *REEL*.[66] The coordinates in a new *pdb* file and the topologies in a monomer library *cif* file were produced using *eLBOW*.[67] CAMNO was modeled in with two different conformations of the terminal NO group at 50% occupancy each. Additional electron density around the -SH groups of the βCys93 residues were best modeled as *S*-nitroso moieties in these new *S*-nitrosocysteine derivatives (ligand id: SNC) and were modeled with two conformations at 50% occupancy each. The *N*-terminal residues Val1 and Lys2 in both β chains were omitted due to lack of electron density. Two conformations (50% occupancy each) were modeled for the sidechains Val96, Leu106 and Ser131 in α1, for Ser84, Val96, Lys99 and Ser131 in α2, for Thr12, Leu32, Leu68, Leu78, Lys95, Asn108, and Asn139 in β1 and for Thr12, Glu26, Lys95, and Asn139 in β2. The final *R* factor and R_{free} were 0.153 and 0.205, respectively.

2.2.13.4 Ferrous wt swMb^{II}-PhNO

Ten initial cycles of restrained refinement were run with *Refmac5*, and the *R* factor decreased from 0.418 to 0.307. Ligands and water were added to the model based on the F_o-F_c electron density maps in the subsequent refinement cycles. One PhNO (ligand id: NBE) and one sulfate anion were added to the model. The *N*-terminal Met and the *C*-terminal residues Asn152 and Gly153 were omitted due to lack of electron density. The final *R* factor and R_{free} were 0.233 and 0.274, respectively. The final structure was deposited in the PDB with accession number 6M9N.

2.2.13.5 [α-Fe^{III}(H$_2$O)][β-Fe^{III}(His)$_2$-SNO]$_{\{PhNO\}}$

Ten initial cycles of restrained refinement were run with *Refmac5*, and the *R* factor decreased from 0.349 to 0.291. Ligands and water were added to the model based on the F_o-F_c electron density maps in the subsequent refinement cycles. Five PhNO (ligand id: NBE) and one glycerol were added to the model. Additional electron density around the -SH groups of the βCys93 residues were best modeled as *S*-nitroso moieties in these new *S*-nitrosocysteine derivatives (ligand id: SNC) and were modeled with two conformations at 50% occupancy each. Two conformations for each of the sidechains of β1-Glu26, β1-Asp94, β1-His117, β2-Glu26, β2-His117 were modeled with 50% occupancy each. The *C*-terminal residues 144-146 in both β chains were omitted due to lack of electron density. The final *R* factor and R_{free} were 0.201 and 0.248, respectively. The final structure was deposited in the PDB with accession number 6M9O.

2.2.13.6 [α-$Fe^{III}(H_2O)$][β-Fe^{II}(MeNO)]

Ten initial cycles of restrained refinement were run with *Refmac5*, and the *R* factor decreased from 0.275 to 0.245. Ligands and water were added to the model based on the F_o-F_c electron density maps in the subsequent refinement cycles. Two MeNO ligands (ligand id: NSM), four glycerol, and two toluene molecules were added to the model. The *C*-terminal residues 140-141 in both α chains were omitted due to lack of electron density. Two conformations for the sidechains Thr38 in both α chains and Arg40 in both β chains were modeled with 50% occupancy each. The final *R* factor and R_{free} were 0.185 and 0.241, respectively.

2.2.13.7 [α-$Fe^{III}(H_2O)$][β-$Fe^{III}(His)_2$]$_{\{t\text{-}BuNHOH\}}$

Ten initial cycles of restrained refinement were run with *Refmac5*, and the *R* factor decreased from 0.314 to 0.264. Ligands and water were added to the model based on the F_o-F_c electron density maps in the subsequent refinement cycles. Four glycerol and four *t*-BuNHOH molecules (ligand id: S9V) were added to the model. The model for *t*-BuNHOH was built in *Phenix* using *REEL*.[66] The coordinates in a new *pdb* file and the topologies in a monomer library *cif* file were produced using *eLBOW*.[67] The *C*-terminal residues 143-146 in both β subunits were omitted due to lack of electron density. The final *R* factor and R_{free} were 0.211 and 0.288, respectively.

2.2.13.8 [α-$Fe^{III}(H_2O)$][β-Fe^{II}(AmphNO)]

Ten initial cycles of restrained refinement were run with *Refmac5*, and the *R* factor decreased from 0.353 to 0.273. Ligands and water were added to the model based on the

F_o-F_c electron density maps in the subsequent refinement cycles. Two AmphNO ligands (ligand id: 3QM), one AmphNHOH molecule (ligand id: K7M) and one glycerol molecule were added to the model. The model for AmphNHOH was built in *Phenix* using *REEL*.[66] The coordinates in a new *pdb* file and the topologies in a monomer library *cif* file were produced using *eLBOW*.[67] The *C*-terminal residues R141 in α1, 140-141 in α2 and 146 in β2, as well as the *N*-terminal residues 1 in β1, and 1-2 in β2, were omitted due to lack of electron density. The final *R* factor and R_{free} were 0.216 and 0.287, respectively. The final structure was deposited in the PDB with accession number 6M9P.

2.2.14 UV-vis spectroscopy of crystals used in data collection

In order to characterize the redox state of the crystals used to determine the crystal structures and to determine if X-ray exposure altered the redox state, UV-vis spectra of crystals were obtained after data collection. Specifically, after data collection, the crystal was removed from the goniometer and placed into a drop of 2-5 μL of 100 mM sodium phosphate buffer at pH 7.4. Once the crystal was fully dissolved, the UV-vis spectrum was obtained using a Synergy HTX (Biotek) instrument.

2.3 Results

2.3.1 Interaction of H64V swMb and nitrite

2.3.1.1 UV-vis of H64V swMb and nitrite

Upon mixing ferric H64V swMb^{III} (0.1 M sodium phosphate at pH 7.4) with nitrite, no significant changes were observed in the UV-vis spectrum of the protein in either the Soret or Q regions. The peak in the Soret band remained at 395 nm and the peak in the Q band remained at 507 nm (**Figure 2.5A**). These results are consistent with the weak binding interaction between ferric H64A swMb^{III}-H_2O and nitrite.[4]

Dithionite was added to ferric H64V swMb^{III} to reduce the protein to its deoxy form (ferrous deoxyMb^{II}) and as a result, a shift in the Soret band from 395 nm to 433 nm (**Figure 2.5B, C**), and in the Q region from 506 nm to 559 nm (**inset of Figure 2.5C**) was observed. Next, nitrite was added and over time, a disappearance of the 433 nm peak and an appearance of a peak at 422 nm was observed in the Soret region (**Figure 2.5B, C**). Disappearance of the 559 nm peak and the appearance of two peaks at 548 nm and 584 nm within the Q band region also occurred (**inset of Figure 2.5C**). The reaction reached completion after ~35 min (**inset of Figure 2.5B**). These shifts are consistent with those observed for the reaction of nitrite with the ferrous deoxyMb^{II} form of wt and the H64A, H64Q, and V68A/I107Y swMb mutants.[4]

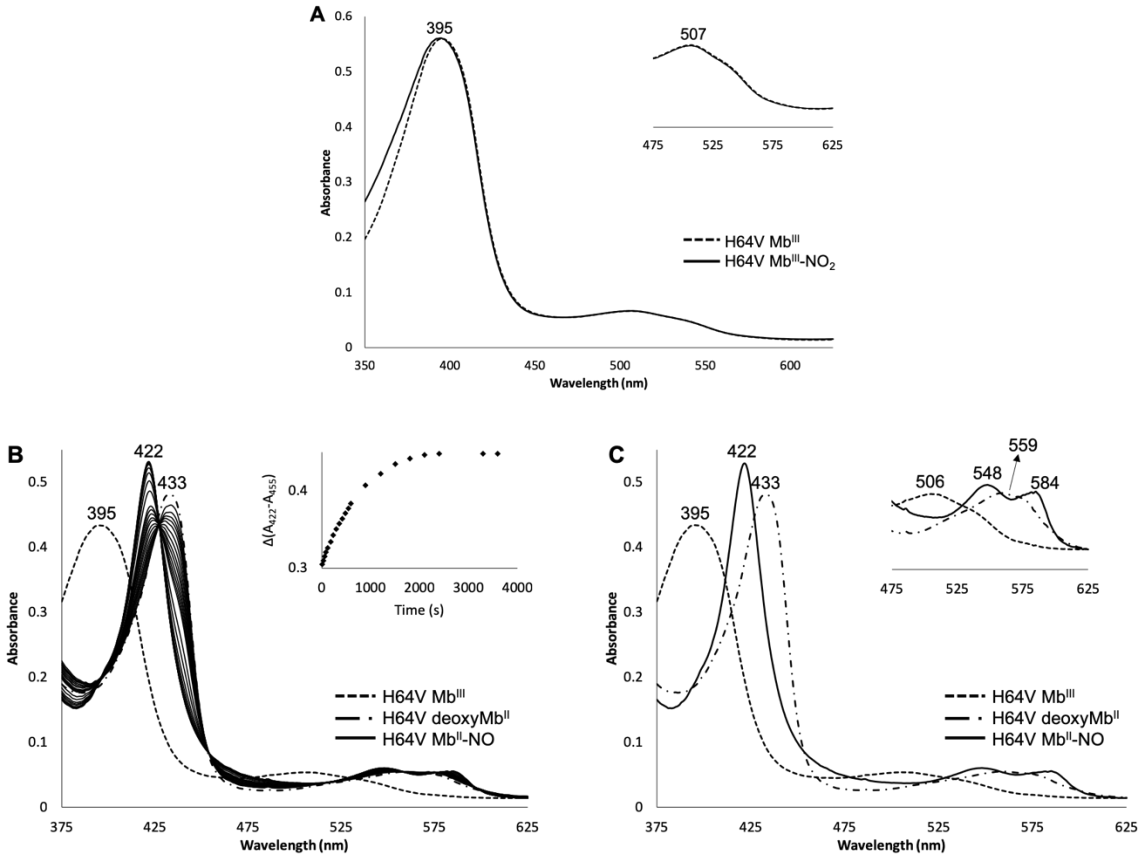

Figure 2.5. UV-vis spectroscopy of the reaction between ferric H64V swMb^{III} and nitrite. (A) Changes 30 min after the addition of nitrite. (B) Changes after the addition of dithionite followed by the addition of nitrite, additionally, a plot of ΔAbs(422-455) versus time. (C) UV-vis spectra of the three forms observed during the reaction of H64V swMb with nitrite, additionally, a zoomed in picture of the Q band region. Conditions: 0.1 M phosphate buffer pH 7.4, 4.5 μM Mb, 2 mM nitrite, and (B and C) 2 mM dithionite.

2.3.1.2 X-ray crystal structure of H64V swMb^{III}-NO$_2$

Crystals of ferric H64V swMb^{III}-NO$_2$ were obtained by soaking ferric H64V swMb^{III} crystals with nitrite (See Section 2.2.8.1). Crystals were harvested at 15, 20, 25, and 30 min time points. The best crystal for structure determination was obtained from a crystal harvested at the 30 min time point. The X-ray crystal structure of ferric H64V swMb^{III}-NO$_2$ was solved to 1.64 Å resolution. Data collection and refinement statistics are displayed in **Table 2-7**. As shown in **Figure 2.6**, the nitrite is *N*-bound to the heme-Fe. This matches the ferric H64V hhMb^{III}-NO$_2$ structure (See Discussion).[4] Note that Val68 is modeled in two orientations (50% occupancy each).

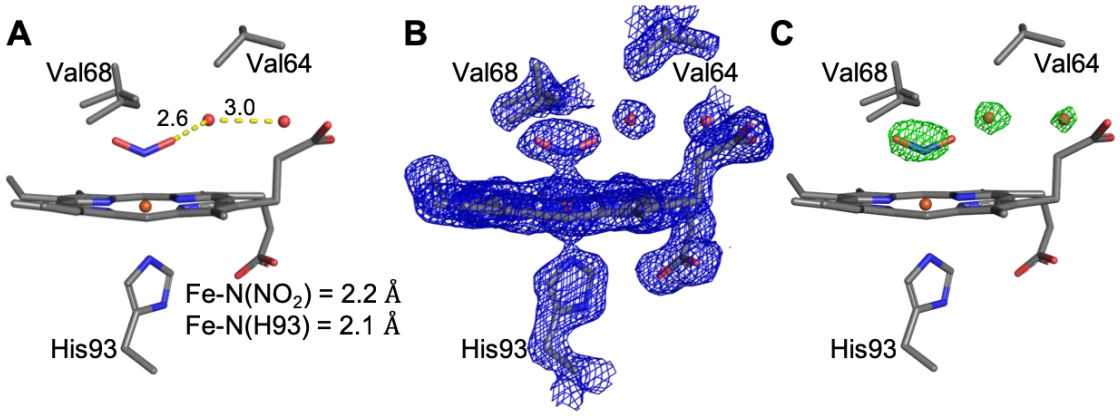

Figure 2.6. X-ray crystal structure of ferric H64V swMb^{III}-NO$_2$ showing only the active site. (A) Final model. (B) $2F_o$-F_c map (contoured at 1 σ). (C) F_o-F_c omit map (contoured at 2.5 σ).

2.3.2 Interactions of swMb and Hb with metronidazole and chloramphenicol

2.3.2.1 UV-vis spectroscopic monitoring of the reactions of swMb with Mtz and CAM

In all cases (wt and mutant), an initial reading was taken of ferric swMb^{III}-H_2O. Dithionite was added to reduce the protein to its ferrous deoxyMb^{II} form and as a result, shifts in the Soret band from ~409 to ~433 nm were observed for all proteins (**Figure 2.7**).

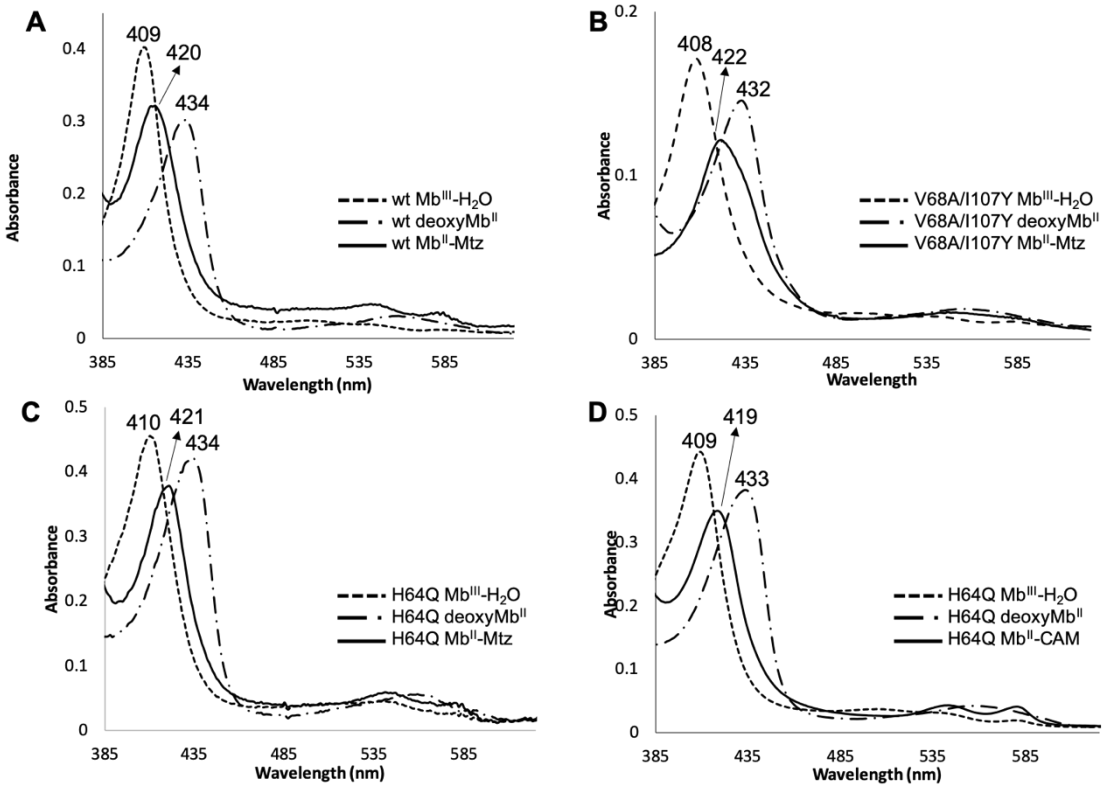

Figure 2.7. UV-vis spectral changes during the reactions of (A) wt Mb with Mtz, (B) V68A/I107Y Mb with Mtz, (C) H64Q Mb with Mtz, and (D) H64Q Mb with CAM. Conditions: 0.1 M phosphate buffer, pH 7.4, [protein] = 2.0 µM, [dithionite] = 2 mM, [Mtz] = 350 µM or [CAM] = 600 µM.

Mtz or CAM was then added to the reduced protein. In the case of ferric wt Mb^{III}-H_2O in its reaction with Mtz, the peak in the Soret band shifted from 434 nm for the reduced

protein (ferrous deoxyMb^{II}) to 420 nm (**Figure 2.7A**) and the reaction was complete after ~20 min. Similar shifts were seen in the Soret bands for both ferric V68A/I107Y (432 to 422 nm) and H64Q Mb^{III}-H_2O (434 to 421 nm) in their reactions with Mtz (**Figure 2.7B-C**). The reaction of the H64Q Mb mutant with Mtz was complete after ~5 min, but the reaction with the V68A/I107Y Mb mutant took ~75 min to reach completion. Ferric H64Q Mb^{III}-H_2O was the only form of swMb that reacted with CAM, resulting in shifts in the Soret band from 434 to 419 nm (**Figure 2.7D**). This reaction was complete after ~10 min. The data in **Table 2-1** summarizes the UV-vis spectral observations. The plots are not shown for the reactions that did not occur as the spectrum remained the same as the deoxyMb^{II} spectrum.

Table 2-1. Summary of the interaction of swMb with Mtz and CAM.

Ligand	**wtMb**	**H64A**	**H64Q**	**H64V**	**V68A/I107Y**
Mtz	420 nm at 20 min	No rxn	421 at 5 min	No rxn	422 at 75 min
CAM	No rxn	No rxn	419 nm at 10 min	No rxn	No rxn

2.3.2.2 UV-vis spectroscopic monitoring of the reactions of Hb with CAM, Mtz and CAMNO

The reactions of ferric Hb^{III}-H_2O with CAM and Mtz was performed and monitored with UV-vis spectroscopy, however no changes in the UV-vis spectra were observed, indicating lack of reaction. Previous work by Eyer, Lierheimer and Schneller[26] demonstrated that Hb interacts with the nitroso derivative of CAM, namely nitrosochloramphenicol (CAMNO), under *anaerobic* conditions. Therefore, UV-vis spectroscopy was used to probe the anaerobic interaction between ferrous deoxyHb^{II} and CAMNO.

After ~5 min, the Soret peak[3] of ferrous deoxyHb^{II} at 430 nm shifted to 422 nm (**Figure 2.8**), likely indicating the generation of a derivative with an Fe-bound ligand. The peak at 422 nm was stable for ~20 min. After that time, the peak slowly shifted to 406 nm, indicative of the formation of ferric Hb^{III} implying limited stability of the Hb(CAMNO) derivative.

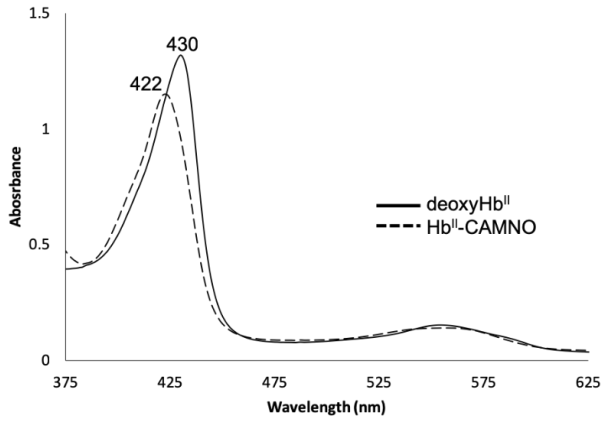

Figure 2.8. UV-vis spectral changes during the reaction of ferrous deoxyHb^{II} with CAMNO. Conditions: 0.1 M phosphate buffer at pH 7.4, [Hb] = 2.0 µM, final [CAMNO] = 600 µM.

2.3.2.3 The X-ray crystal structure of H64Q swMb with ACM

Ferric H64Q swMb^{III}-H_2O co-crystallized with Mtz yielded a product whose X-ray crystal structure did not match that of an Mtz-bound species. Instead, the new electron density at the heme site best matched that of acetamide ($CH_3C(=O)NH_2$; ACM). This structure was solved to 1.76 Å resolution at our home source (**Figure 2.9**). Data collection and refinement statistics are shown in **Table 2-7**. The diffraction data was obtained from crystals that grew in 2.60 M ammonium sulfate (see section 2.2.8.2). The crystallization conditions also contained Mtz and dithionite which resulted in the ring cleavage of Mtz, producing ACM (see later). As can be seen in **Figure 2.9**, ACM is bound to the Fe-center, and is best modeled as an O-bound species (see later).

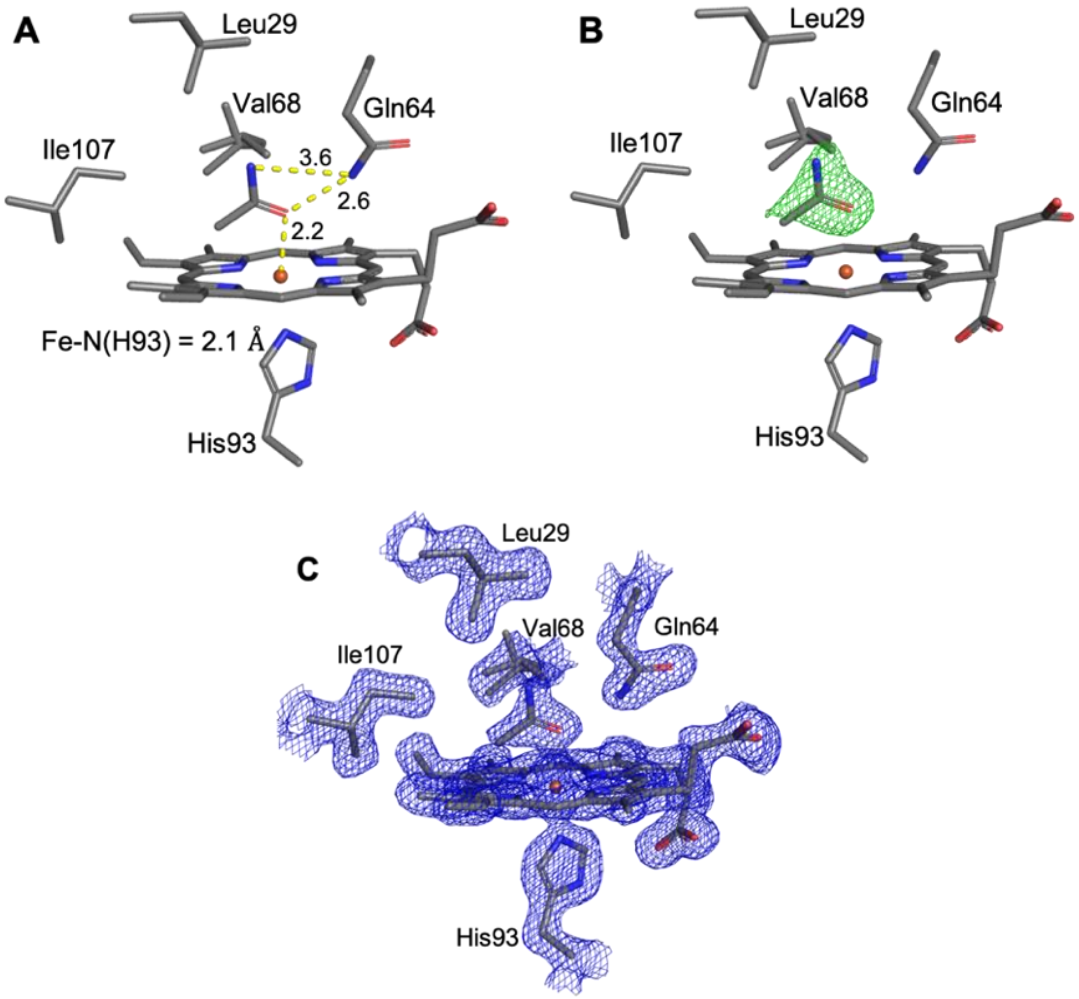

Figure 2.9. X-ray crystal structure of ferrous H64Q swMb^{II}-ACM showing only the active site. (A) Final model of the active site. (B) F_o-F_c omit map (contoured at 1.5 σ). (C) $2F_o$-F_c map (contoured at 1.0 σ).

2.3.2.4 The X-ray crystal structure of the product resulting from reacting ferrous deoxyHb^{II} with CAMNO

The X-ray crystal structure of ferrous [α-Fe^{II}][β-Fe^{II}-SNO]$_{\{CAMNO\}}$, resulting from the reaction of ferrous deoxy Hb^{II} and CAMNO, was solved to 1.75 Å resolution from diffraction data collected at our home source. Data collection and refinement statistics are displayed in **Table 2-7**. The diffraction data was obtained from crystals grown in final concentrations of 10.2 mM Fe citrate and 2.79 M ammonium phosphate/sulfate (See Section 2.2.8.3). The final tetrameric model as well as the active sites of one α and one β subunit are shown in **Figure 2.10**. The α active site contains a fixed water molecule; however, the water does not lie perfectly above the Fe in the pocket and it is not coordinated with the Fe as it is too far away to form a direct Fe-H_2O bond (3.5 Å, **Figure 2.10B**). This fixed water molecule is stabilized by hydrogen bonding with His58 (2.7 Å). On the other hand, the β subunit does not contain any ligands or fixed waters (**Figure 2.10C**).

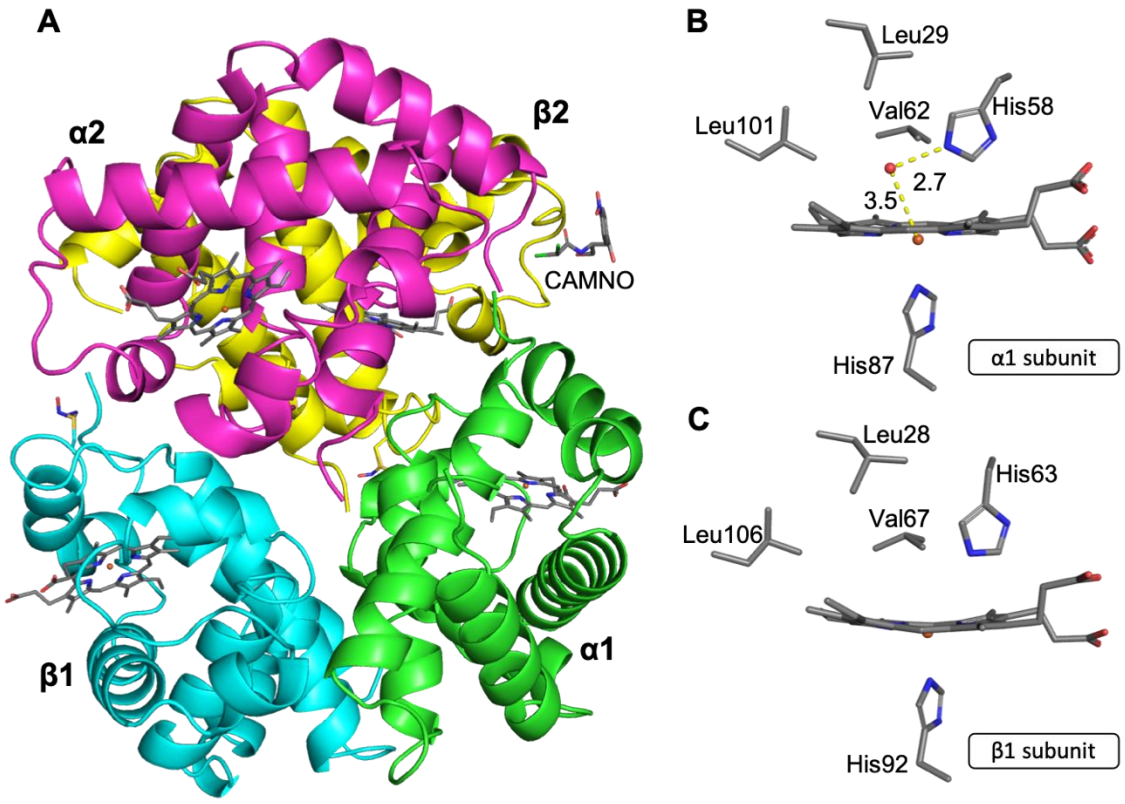

Figure 2.10. X-ray crystal structure of [α-Fe^{II}][β-Fe^{II}-SNO]$_{\{CAMNO\}}$. (A) Overall tetrameric form. Final model of the active site of the α1 (B) and β1 subunit (C).

In both active sites, the heme plane is not flat and is slightly distorted with the Fe center below the heme plane, indicating that the protein structure is likely in the T-state conformation. To further investigate this, we compared the β2 FG and α1 C interface, referred to as the signature "switch" region, of [α-Fe^{II}][β-Fe^{II}-SNO]$_{\{CAMNO\}}$ and of a known T-state Hb structure (PDB id: 1B86).[68] The overall RMSD between the two structures is 0.381 Å and their switch regions align well, indicating that [α-Fe^{II}][β-Fe^{II}-SNO]$_{\{CAMNO\}}$ is in the T-state conformation (**Figure 2.11**). Additionally, both the α and β active sites of T-state deoxyHb match those of [α-Fe^{II}][β-Fe^{II}-SNO]$_{\{CAMNO\}}$.

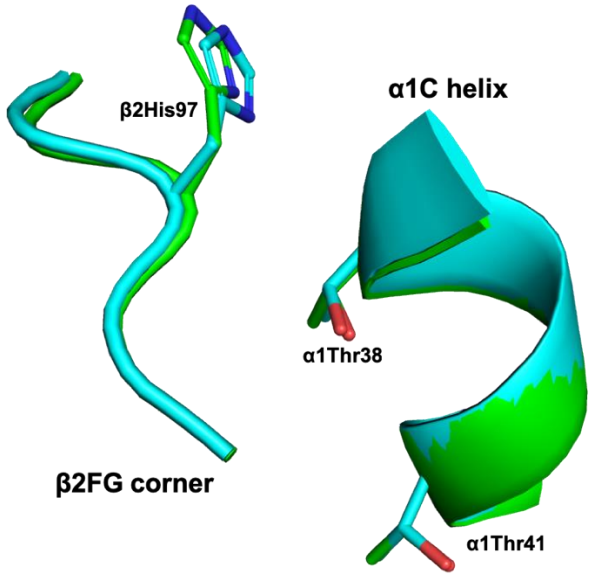

Figure 2.11. Comparison of the α1β2 interface of [α-Fe^{II}][β-Fe^{II}-SNO]$_{\{CAMNO\}}$ (green) and T-state deoxyHb (cyan; PDB id: 1B86). Analysis of the representative key residues show that the [α-Fe^{II}][β-Fe^{II}-SNO]$_{\{CAMNO\}}$ structure presented in this work is in the T-state conformation.

UV-vis spectral data were collected on the crystal used for the diffraction data collection to determine if any oxidation state changes had occurred during data collection. After X-ray data collection, the crystal was dissolved in 0.1 M sodium phosphate at pH 7.4, and a UV-vis spectrum was obtained (**Figure 2.12**). A peak at 430 nm in the Soret region and a peak at 555 nm in the Q band region were observed. These peaks match the spectrum for ferrous deoxyHb^{II} confirming that the [α-Fe^{II}][β-Fe^{II}-SNO]$_{\{CAMNO\}}$ complex was in the ferrous form.

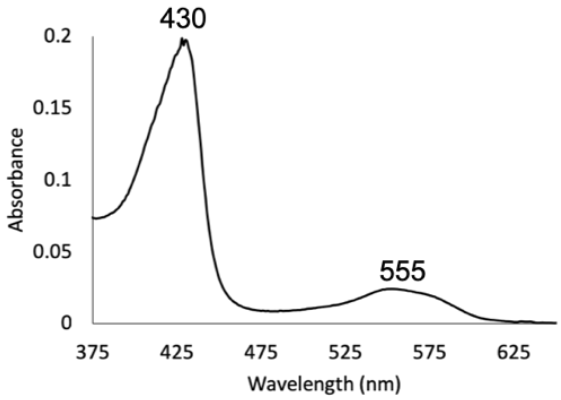

Figure 2.12. UV-vis spectroscopy of the dissolved crystal of [α-Fe^{II}][β-Fe^{II}-SNO]$_{\{CAMNO\}}$ after X-ray diffraction data collection.

Unfortunately, CAMNO was not observed in the active site of deoxyHb, but was found outside of the protein in the solvent region between the β2 and α2 subunits of the same tetramer (**Figure 2.10A**). The terminal nitroso group was modeled in two conformations (50% occupancy each). The CAMNO molecule is held in place through a series of hydrogen bonding interactions with fixed water and nearby sidechains (**Figure 2.13**).

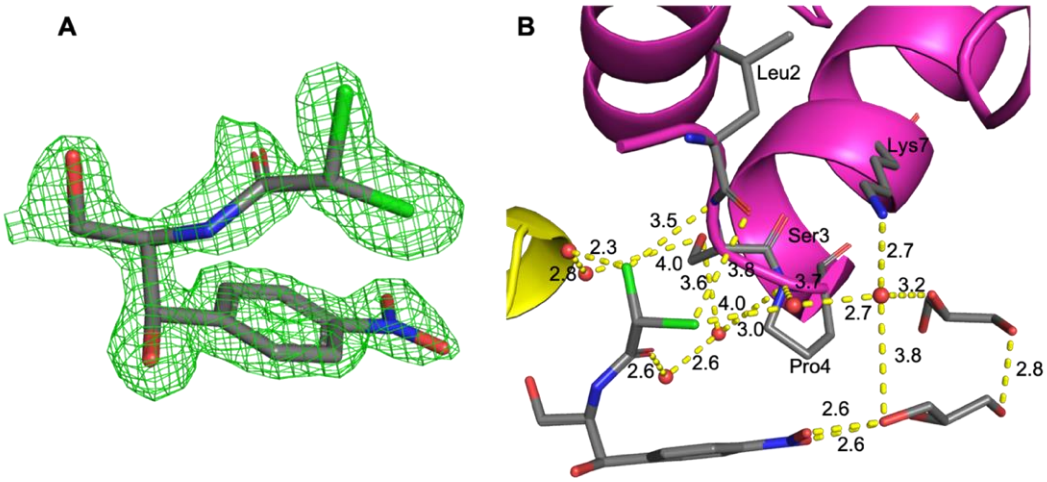

Figure 2.13. (A) F_o-F_c omit map of the CAMNO molecule (contoured at 2.5 σ). (B) The CAMNO hydrogen bonding network.

Intriguingly, I found that βCys93 had been nitrosated in both β subunits (**Figure 2.14**), resulting in *S*-nitrosothiol (SNO) derivatives. Unrestrained refinement was used to model in SNO in place of the -SH group of Cys93, and the SNO was modeled in two different conformations at 50% occupancy each. In both subunits, the two conformations are stabilized through hydrogen-bonding interactions with fixed waters and the nearby Asp94, His97, His146 and Lys144 residues (**Figure 2.15**).

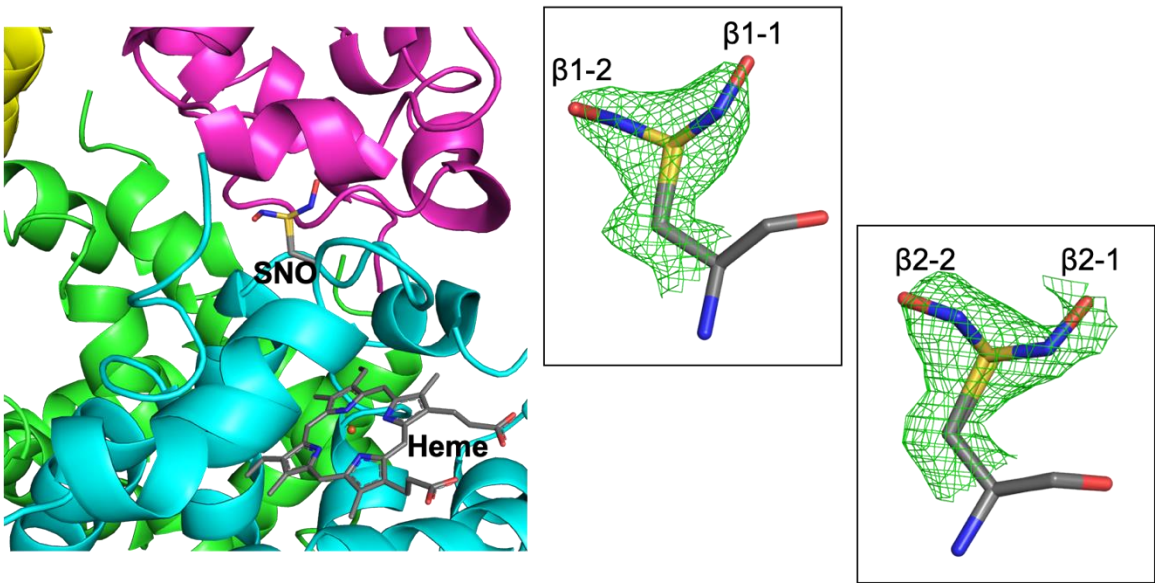

Figure 2.14. The environment surrounding the -SNO moiety in the overall [α-Fe^{II}][β-Fe^{II}-SNO]$_{\{CAMNO\}}$ crystal structure and the F_o-F_c omit maps (contoured at 2.0 σ) for the -SNO groups in both β subunits.

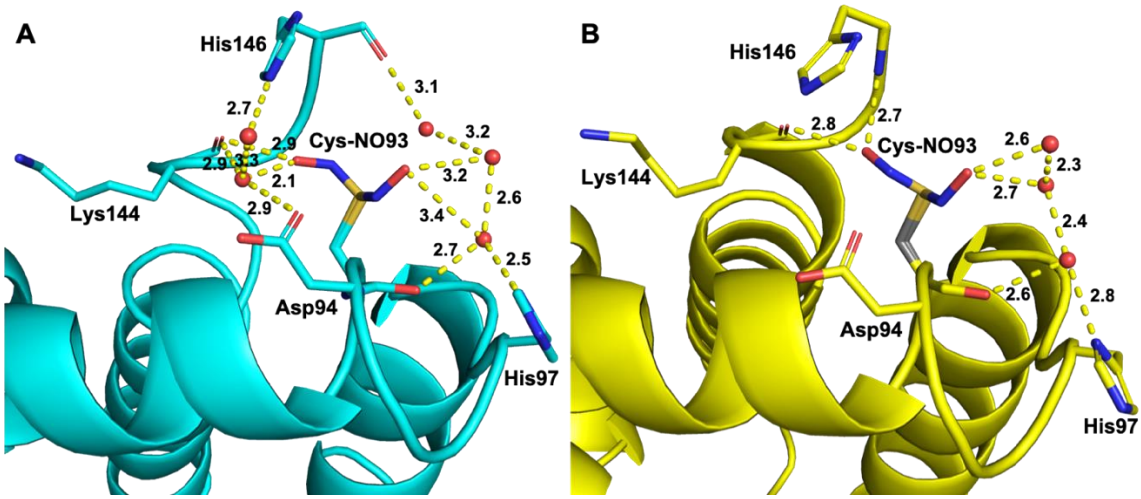

Figure 2.15. Cys93-NO H-bonding interactions in the (A) β1 and (B) β2 subunits.

Macromolecular crystallography is not normally able to distinguish between various forms of *S*-nitrosation. Hence, computational studies have been performed by others to predict bond lengths and bond angles of all the possible -SNO species (**Table 2-2**).[69-73] **Table 2-3** displays the geometric parameters for the SNO groups present in [α-Fe^{II}][β-Fe^{II}-SNO]$_{\{CAMNO\}}$. These measurements are in agreement with calculations performed by Zhao and Houk[69] that show within this crystal structure, conformation 1 of the nitrosated Cys93 is most likely the *trans*-SNO species and conformation 2 is most likely the thionitroxide radical (Cys-S-NH-O•).

Table 2-2. Geometrical parameters of RSNO species as calculated by Zhao and Houk.[69] Bond distances are measured in Å and angles are measured in °.

	N-O	**S-N**	**C-S**	**∠SNO**	**∠CSN**	**∠CSNO**
***cis*-RSNO**	1.194	1.791	1.804	118	104	0
***trans*-RSNO**	1.192	1.799	1.811	116	97	180
RS-N•-OH	1.395	1.696	1.812	106	97	180
RS-NH-O•	1.272	1.733	1.733	123	100	72
RS-NH-OH	1.447	1.721	1.721	113	105	64

Table 2-3. [α-Fe^{II}][β-Fe^{II}-SNO]$_{\{CAMNO\}}$ SNO parameters. Bond distances are measured in Å and angles are measured in °.

	N-O	**S-N**	**C-S**	**∠SNO**	**∠CSN**	**∠CCS**	**∠CSNO**
β1-1	1.25	1.56	1.84	121	107	111	163
β1-2	1.21	1.52	1.82	120	101	114	65
β2-1	1.25	1.58	1.83	122	112	116	173
β2-2	1.21	1.52	1.82	117	114	114	76

2.3.3 Interactions of wt swMb with PhNHOH

2.3.3.1 UV-vis spectroscopy of wt swMb with PhNHOH

Upon mixing ferric wt swMb^{III}-H_2O with PhNHOH, changes in both the Soret and Q bands regions were observed using UV-vis spectroscopy. The peak in the Soret region shifted from 409 to 424 nm (**Figure 2.16A-B**). Additionally, the Q band peaks shifted from 503 and 625 to 543 and 561 nm (**inset of Figure 2.16B**). These shifts are indicative of the formation of a ferrous derivative with an Fe-bound ligand. The reaction was essentially complete after ~15 min (**inset of Figure 2.16A**). To test the chemical reversibility of the reaction between ferric Mb^{III} and PhNHOH, the oxidant potassium ferricyanide was added to the ferrous product Mb^{II}-PhNO in buffer (0.1 M sodium phosphate at pH 7.4). The original peaks in the Soret band and in the Q band were regenerated, indicating a return to the ferric form of Mb (**Figure 2.16C**).

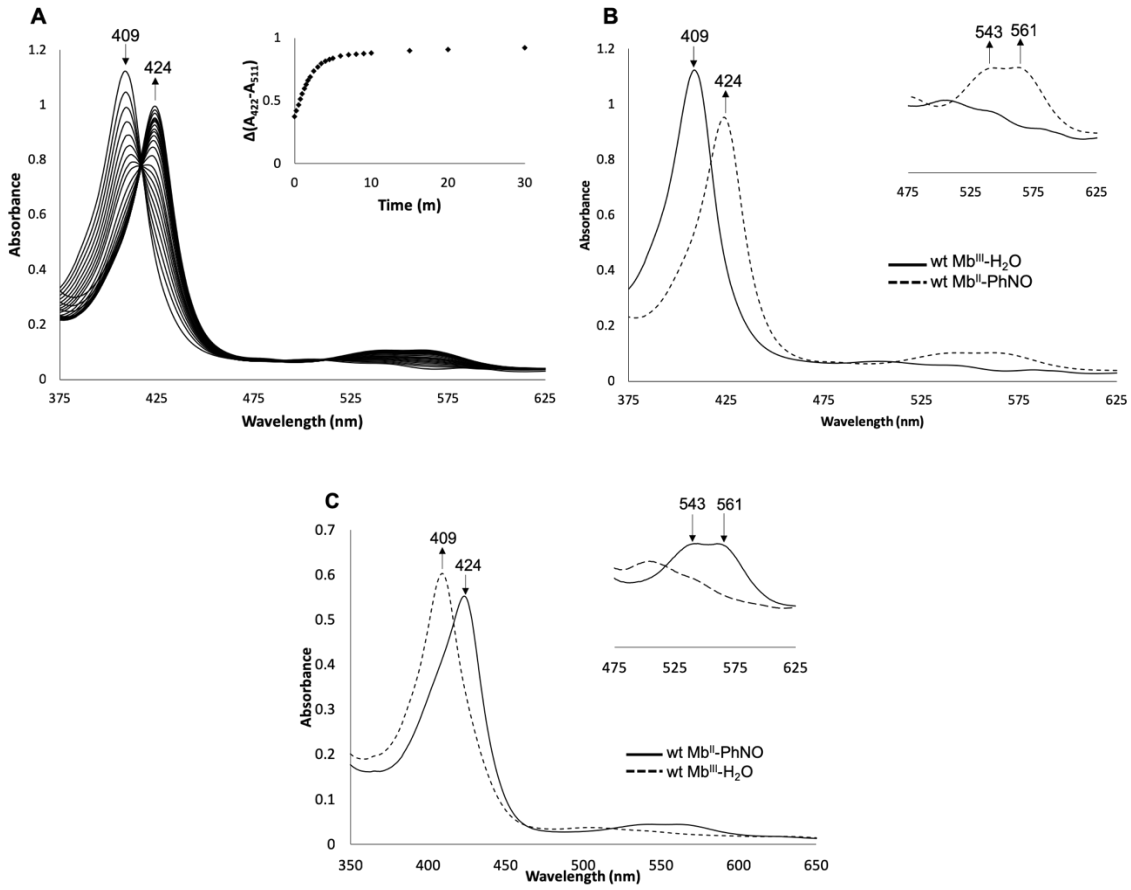

Figure 2.16. Reactions of the ferric wt swMb^{III}-H_2O with PhNHOH. (A) Changes after addition of PhNHOH and a plot of ΔAbs(422-511) against time. (B) UV-vis spectra of the two forms observed during the reaction and a zoomed-in picture of the Q band region. (C) Reaction of the ferrous wt swMb^{II}-PhNO product with ferricyanide. Conditions: 100 mM sodium phosphate pH 7.4, (A-B) [Mb] = 4.8 μM, [PhNHOH] = 800 μM; (C) [Mb^{II}-PhNO] = 2.4 μM, [ferricyanide] = 200 μM

2.3.3.2 X-ray crystal structure of wt swMb^{II}-PhNO

The X-ray crystal structure of PhNO bound to wt swMb^{II} was solved to 1.75 Å resolution at our home source (**Figure 2.17**). Data collection and refinement statistics are shown in **Table 2-7**. The diffraction data was obtained from crystals of ferric Mb^{III} that were soaked with PhNHOH for 30 min (see section 2.2.8.4). The resulting PhNO ligand was determined to be *N*-bound to the Fe which matches our UV-vis findings. As expected, the hydrophobic portion of the ligand is oriented towards the hydrophobic interior of the distal pocket in this protein.

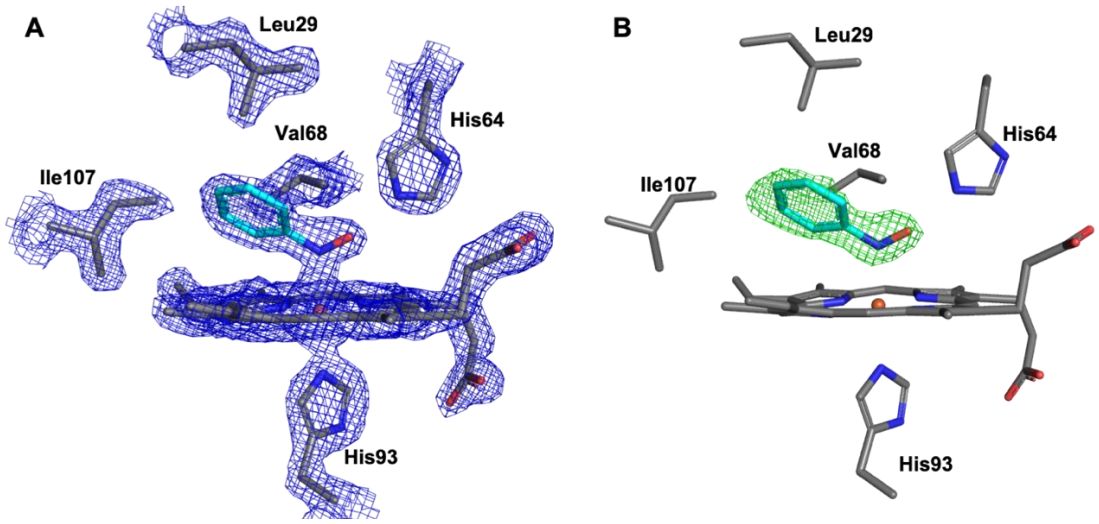

Figure 2.17. The final model and (A) $2F_o$-F_c omit map contoured at 1 σ, and (B) the F_o-F_c omit map contoured at 3 σ, of the heme active site of the ferrous wt swMb^{II}-PhNO derivative.

2.3.4 Interactions of ferric Hb with RNHOH (R = Ph, Me, t-Bu)

2.3.4.1 UV-vis spectroscopy of Hb with RNHOH (R = Ph, Me, t-Bu)

UV-vis spectroscopy was used to monitor the reaction between ferric Hb^{III}-H_2O and the arylhydroxylamine PhNHOH (**Figure 2.18**). The Soret band shifted from 406 nm to 422 nm and in the Q band region, two new peaks at 540 nm and 560 nm appeared (**Figure 2.18B**). The reaction was essentially complete after ~25 min (**inset of Figure 2.18A**). The changes in the spectra indicate that a ferrous derivative with a bound ligand likely formed. Interestingly, if the reaction was allowed to react for a longer period of time (~1 h), the solution within the cuvette became cloudy as a precipitate began to form possibly indicating degradation through irreversible hemichrome (bis-his coordinated heme) formation (see later).[74]

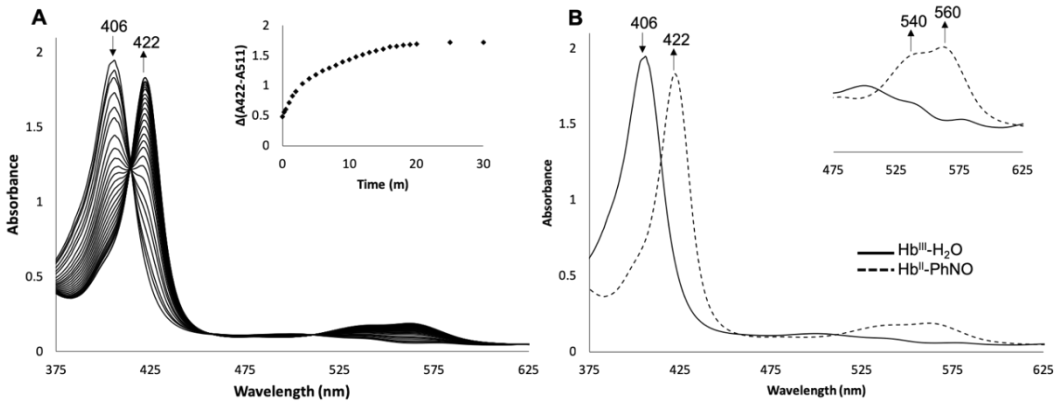

Figure 2.18. Reactions of ferric Hb^{III}-H_2O with PhNHOH. (A) Changes after addition of PhNHOH and a plot of ΔAbs(422-511) against time. (B) UV-vis spectra of the two forms observed during the reaction and a zoomed in picture of the Q band region. Conditions: 100 mM sodium phosphate pH 7.4, [Hb] = 3 μM, [PhNHOH] = 1.6 mM

UV-vis spectroscopy was used to monitor the related reaction between ferric Hb^{III}-H_2O and MeNHOH (**Figure 2.19**). Over time, the Soret band at 405 nm shifted to 420 nm. In the Q band region, new peaks at 540 nm and 572 nm appeared (**inset of Figure 2.19B**). These shifts are indicative of the formation of a ferrous derivative with an Fe-bound ligand. However, the reaction never reached completion as can be seen in the Soret band region which still had partial 405 nm and partial 420 nm character. After approximately 1 h, the reaction reached its maximum extent of formation. Even after multiple days, the reaction did not ever reach completion (**inset of Figure 2.19A**). This may be an indication that MeNHOH was only reacting with either the α or β subunit and not both.

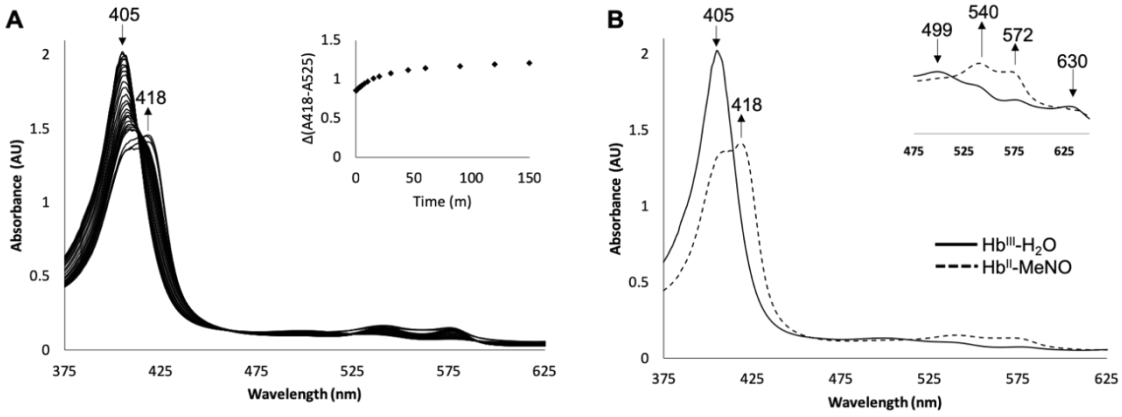

Figure 2.19. Reactions of ferric Hb^{III}-H_2O with MeNHOH. (A) Changes after addition of MeNHOH and a plot of ΔAbs(418-525) against time. (B) UV-vis spectra of the two forms observed during the reaction and a zoomed-in picture of the Q band region. Conditions: 100 mM sodium phosphate pH 7.4, [Hb] = 3 μM, [MeNHOH] = 1.6 mM

UV-vis spectroscopy was used to monitor the reaction between ferric Hb^{III}-H_2O and *t*-BuNHOH (**Figure 2.20**). Only very subtle changes were observed during this reaction in the Soret band region. The peak at 406 nm decreased and slightly shifted to 409

nm. The largest differences were observed in the Q band region. The peaks at 500 and 630 nm were replaced by peaks at 533 and 565 nm as well as a local minimum at 560 nm (**inset of Figure 2.20**). This pattern is consistent with the formation of a hemichrome containing a bis-histidyl coordinated ferric center.[75]

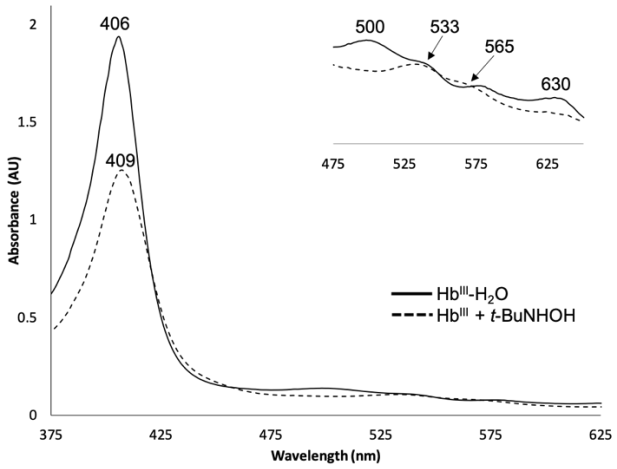

Figure 2.20. UV-vis spectra of the reaction between ferric Hb^{III}-H$_2$O and *t*-BuNHOH as well as a zoomed-in picture of the Q band region. Conditions: 100 mM sodium phosphate pH 7.4, [Hb] = 3 μM, [*t*-BuNHOH] = 1.6 mM

2.3.4.2 The X-ray crystal structure of the product resulting from reacting ferric Hb^{III} with PhNHOH

Although UV-vis spectroscopy of the product generated from ferric Hb^{III} and PhNHOH revealed the formation of the ferrous Hb^{II}-PhNO complex, attempted crystallization resulted in an unexpected degradation to ferric β-hemichrome. The X-ray crystal structure of the product [α-$Fe^{III}(H_2O)$][β-$Fe^{III}(His)_2$-SNO]$_{\{PhNO\}}$was solved to 1.89 Å resolution from diffraction data collected at the SSRL (**Figure 2.21**). Data collection and refinement statistics are shown in **Table 2-7**. The diffraction data was obtained from crystals grown in 3.2 M Na/K phosphate buffer at pH 6.81 (see Section 2.2.8.5). Differences were observed between the α and β active sites. In both α subunits, water was bound to the Fe at the active site. The α1 active site is shown in **Figure 2.22**.

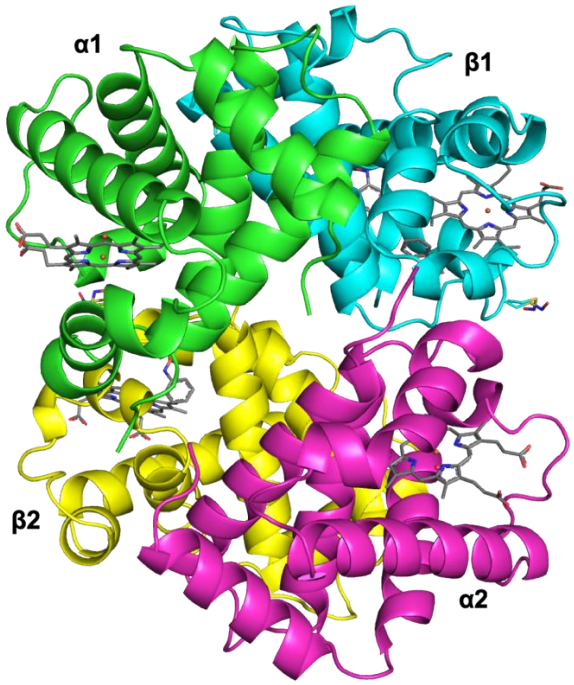

Figure 2.21. The overall 1.89 Å resolution X-ray crystal structure of [α-$Fe^{III}(H_2O)$][β-$Fe^{III}(His)_2$-SNO]$_{\{PhNO\}}$ formed from the reaction between ferric Hb and PhNHOH.

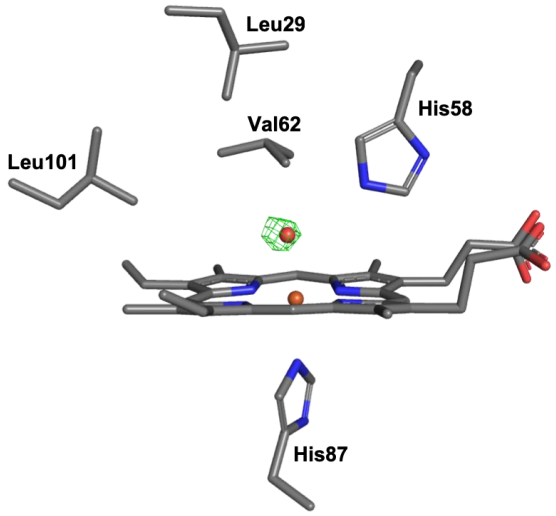

Figure 2.22. The heme model and F_o-F_c omit map (contoured at 2σ) of water in the α1 active site of [α-$Fe^{III}(H_2O)$][β-$Fe^{III}(His)_2$-SNO]$_{\{PhNO\}}$.

In both β subunits, the heme is shifted towards the outside of the pocket, allowing for the formation of a hemichrome (**Figure 2.23A-B**). The movement of the heme out of the pocket left room behind the heme on the inside of the pocket, and two PhNO molecules were observed to sit in this area (**Figure 2.23C-D**).

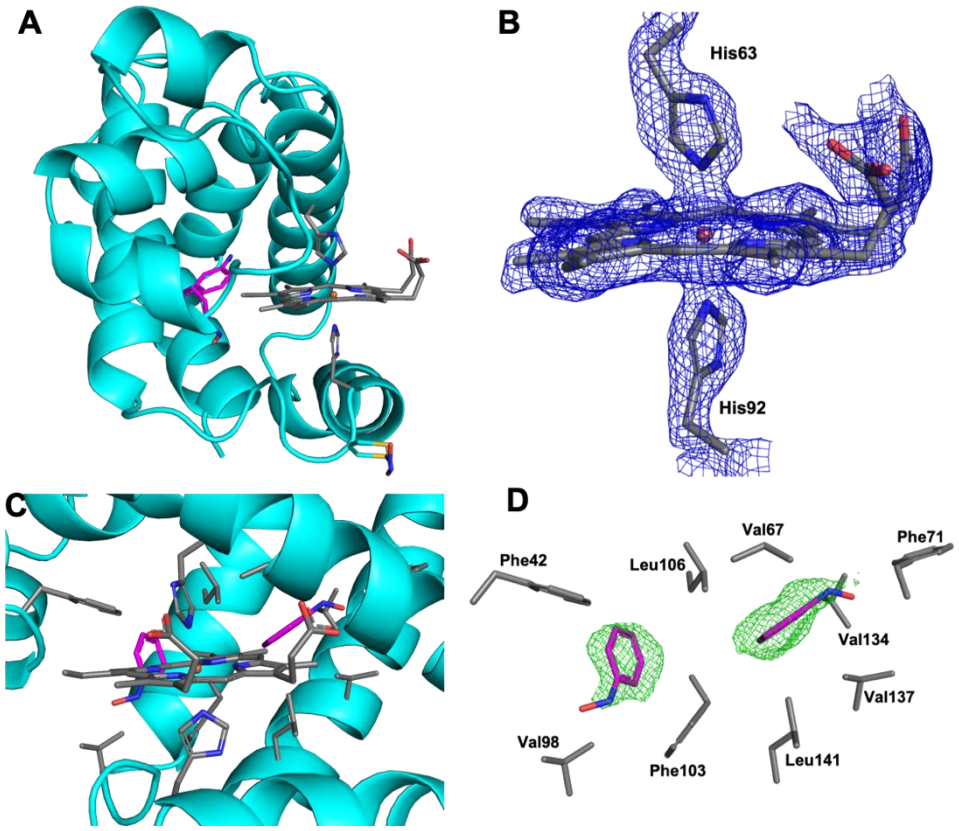

Figure 2.23. (A) Overall view of the β1 chain, (B) the $2F_o$-F_c map (contoured at 0.5 σ) of the hemichrome formed in the β1 subunit, (C) active site of the β1 subunit and (D) the F_o-F_c omit map (contoured at 1.5 σ) of PhNO in the β1 subunit.

In both β subunits, one propionate group is fixed through H-bonding with nearby βLys66, but the orientation of the other propionate group differs between the two subunits (**Figure 2.24**). In β1, the other propionate group is flexible, but in β2, the other propionate has only one orientation, stabilized by H-bonding with a fixed water molecule (bottom right of **Figure 2.24**). The propionate groups in both α subunits are stabilized through H-bonding interactions with fixed waters, Lys61 and His45 (top of **Figure 2.24**). Similar stabilization interactions were observed previously for ferric R-state Hb^{III}-H_2O.[76]

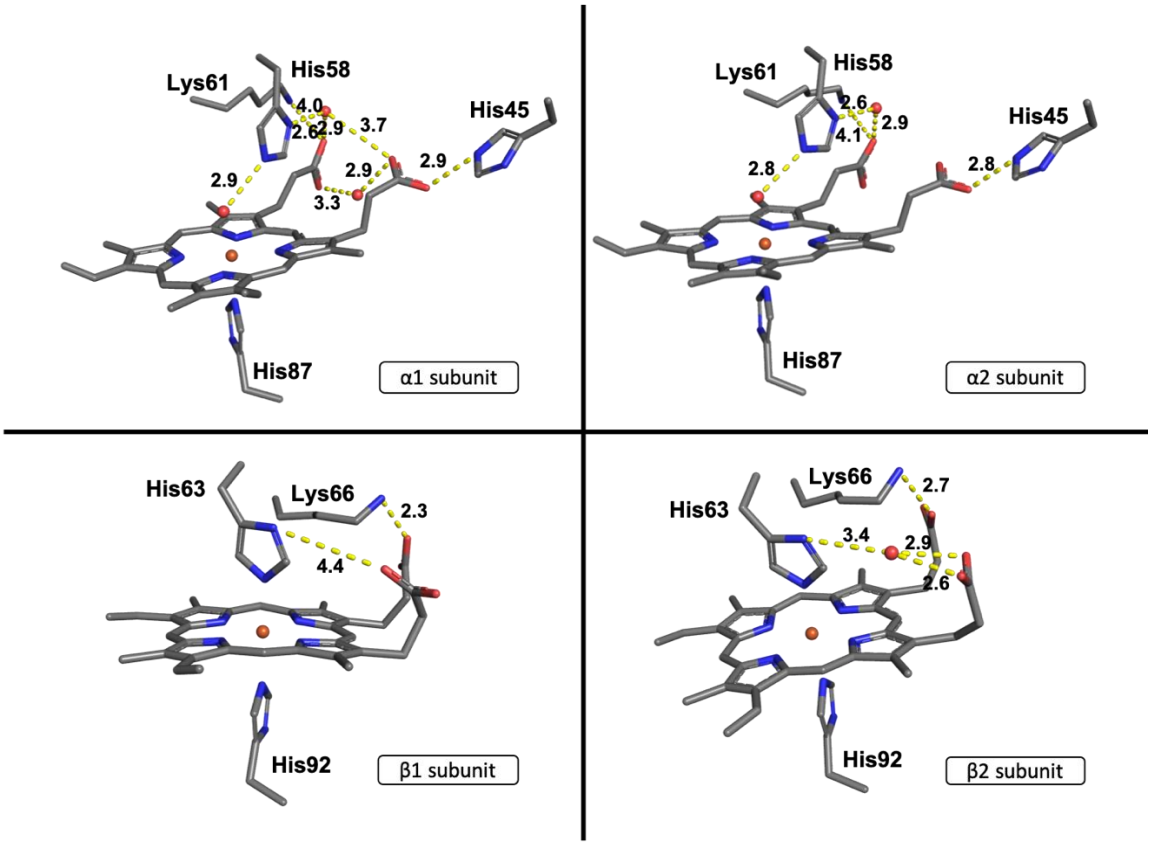

Figure 2.24. [α-$Fe^{III}(H_2O)$][β-$Fe^{III}(His)_2$-SNO]$_{\{PhNO\}}$ propionate interactions.

Table 2-4 summarizes the stereochemical parameters of the hemichromes in this structure. The parameters measured include the tilt angle between the heme plane and the proximal (θ_p) and the distal (θ_d) histidine imidazole planes and the dihedral angle between the two imidazole planes (ω) (Figure 2.25), as well as the bond angle Nε_{2im}-Fe-Nε_{2im}, and selected distance measurements. These parameters are within the reported ranges for hemichromes in other X-ray crystal structures.[77, 78]

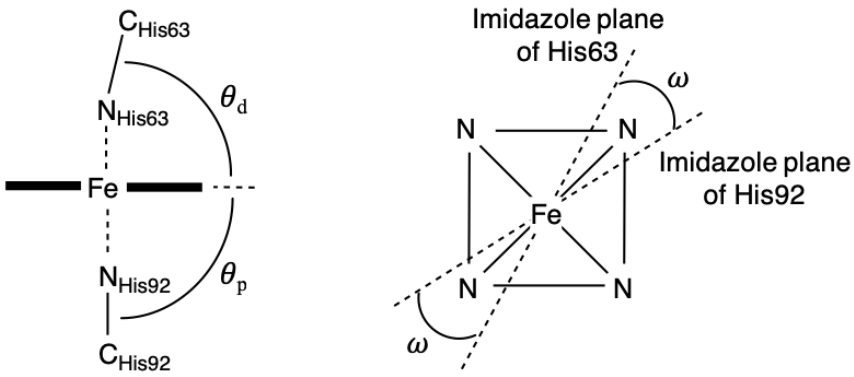

Figure 2.25. Hemichrome measurements, θ_p, θ_d and ω.

Table 2-4. [α-$Fe^{III}(H_2O)$][β-$Fe^{III}(His)_2$-SNO]$_{\{PhNO\}}$ hemichrome parameters

	θ_p (°)	θ_d (°)	Nε_{2im}-Fe-Nε_{2im} (°)	ω (°)	Fe-Nε_{2im} (Å)		Cα_{prox}- Cα_{dist} (Å)
					Prox.	Dist.	
β1	90	80	177	72	2.2	2.1	12.7
β2	90	79	176	67	2.2	2.1	12.7

Additionally, in both β subunits, the βCys93 sidechains were found to be nitrosated (**Figure 2.26**), resulting in *S*-nitrosothiol (SNO) derivatives. The -SNO group was modeled in place of the terminal -SH of Cys93 in two different conformations at 50% occupancy each (**Figure 2.26**) and each of these is stabilized through H-bonding interactions (**Figure 2.27**). In both subunits, one -SNO conformation is stabilized by a αThr8 residue from the neighboring asymmetric unit. The other conformation is stabilized through a water H-bonded to the backbone C=O of a βGlu90 residue of the same subunit.

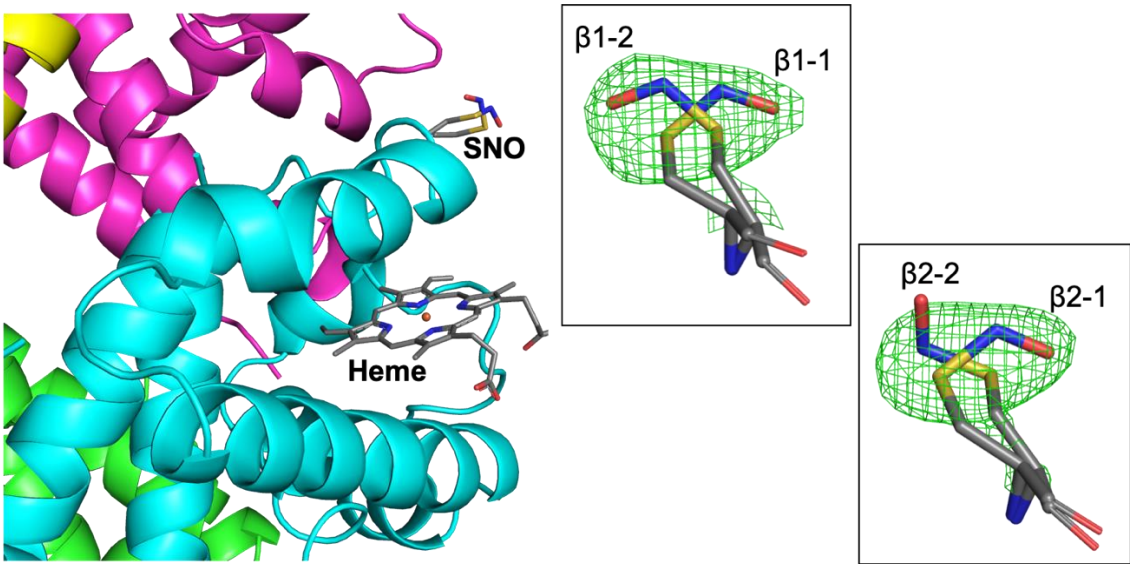

Figure 2.26. The environment surrounding the -SNO moieties in the overall $[\alpha\text{-}Fe^{III}(H_2O)][\beta\text{-}Fe^{III}(His)_2\text{-}SNO]_{\{PhNO\}}$ crystal structure (left) and the F_o-F_c omit maps (contoured at 2 σ) for the SNO groups in both β subunits (right).

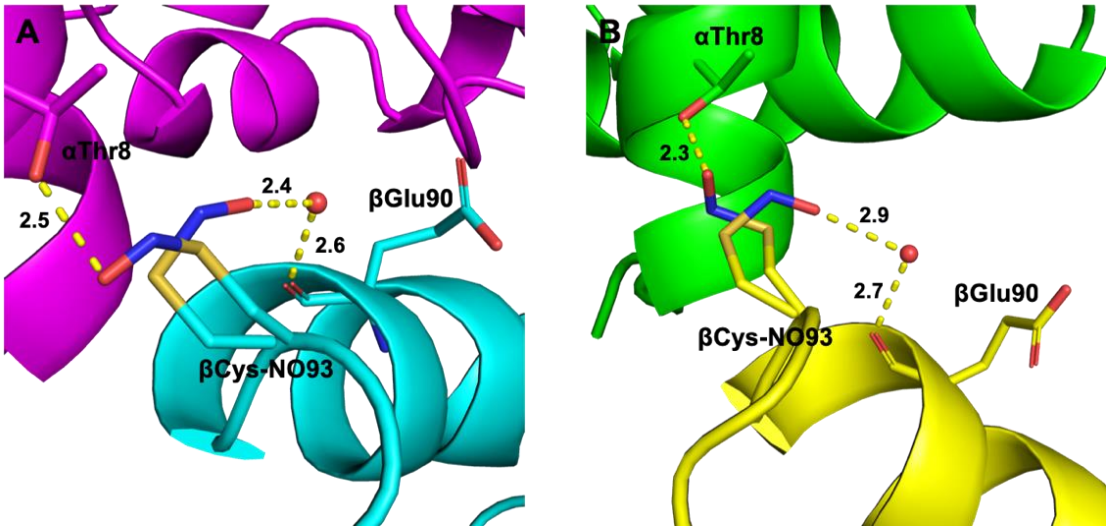

Figure 2.27. H-bonding interactions between the βCys93-NO groups and the backbone C=O of βGlu90 and αThr8 of a symmetry mate in the (A) β1 and (B) β2 subunits.

Table 2-5 displays the geometrical measurements for the SNO groups of the *S*-nitrosated ferric β-hemichrome. Based on computational studies performed by others to predict bond lengths and bond angles of all the possible SNO species (**Table 2-2**)[69-73], these measurements are in agreement with calculations performed by Zhao and Houk,[69] that show within this crystal structure, the nitrosated Cys93 is most likely the thionitroxide radical species (Cys-S-NH-O•).

Table 2-5. [α-$Fe^{III}(H_2O)$][β-$Fe^{III}(His)_2$-SNO]$_{\{PhNO\}}$ SNO parameters. Bond distances are measured in Å and angles are measured in °.

	N-O	**S-N**	**C-S**	**∠SNO**	**∠CSN**	**∠CCS**	**∠CSNO**
β1-1	1.23	1.63	1.79	121	97	111	78
β1-2	1.21	1.63	1.80	116	92	111	88
β2-1	1.23	1.61	1.79	118	99	119	67
β2-2	1.21	1.61	1.80	114	90	111	76

2.3.4.3 The X-ray crystal structure of the product resulting from reacting ferric Hb^{III} with MeNHOH

Crystallization resulted in the formation of the [α-$Fe^{III}(H_2O)$][β-Fe^{II}(MeNO)] derivative. The X-ray crystal structure of this product was solved to 1.93 Å resolution from diffraction data collected at our home source (**Figure 2.28**). The structure was solved to 1.93 Å resolution from diffraction data collected at our home source. Data collection and refinement statistics are shown in **Table 2-7**. The diffraction data was obtained from crystals grown in 3.2 M Na/K phosphate pH 6.30 in trays set at 2 h (See section 2.2.8.5). Differences were observed between the α and β active sites. In both α subunits, water was bound to the Fe at the active site and in both β subunits, MeNO was N-bound to the iron. The fact that the MeNO only reacted with one subunit is consistent with the UV-vis spectroscopy data obtained (see **Figure 2.19**).

We then probed whether X-ray irradiation of the crystal altered the identity of the compound as it is common for Fe to undergo photoradiation. After X-ray data collection, the crystal was dissolved in buffer (0.1 M sodium phosphate at pH 7.4), and a UV-vis spectrum was obtained (**Figure 2.29**). Two peaks were seen in the Soret region at 406 and 420 nm which is consistent with the solution UV-vis spectrum which suggested that MeNO only reacted with one subunit (**Figure 2.19**). The X-ray crystal structure confirms this, showing that MeNO only reacted with the β subunits.

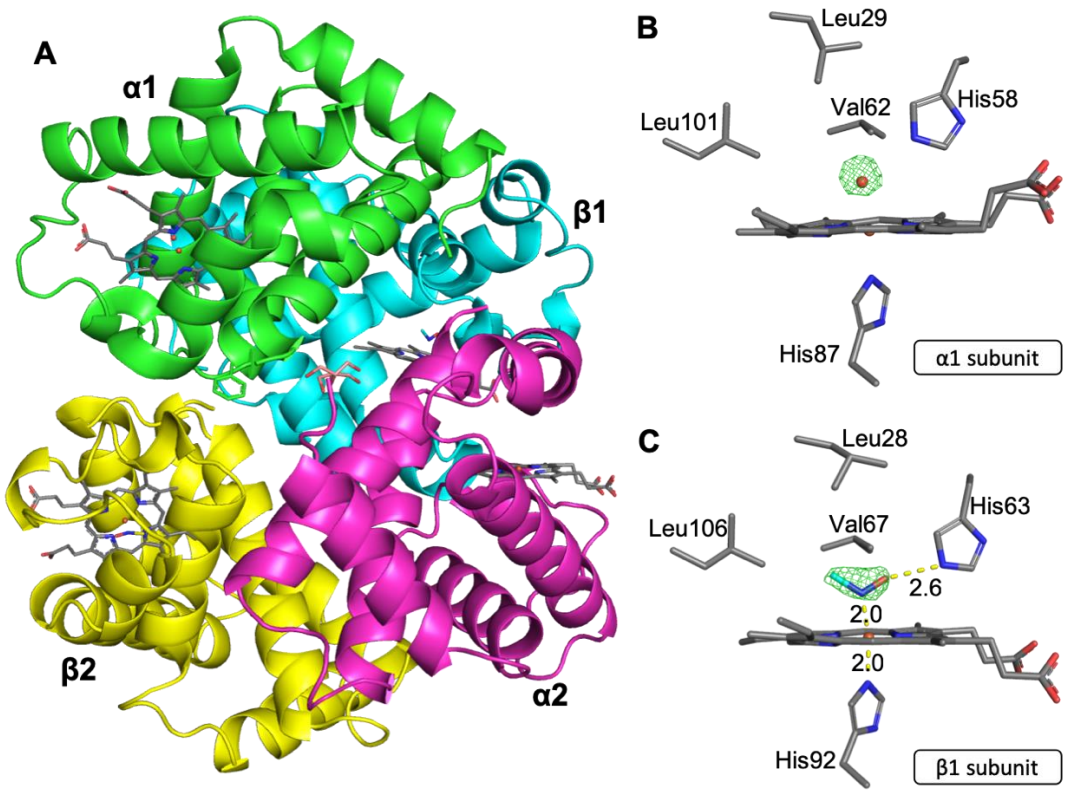

Figure 2.28. X-ray crystal structure of the [α-$Fe^{III}(H_2O)$][β-Fe^{II}(MeNO)] Hb derivative. (A) Overall tetrameric form. Final model of the active site and F_o-F_c omit maps (contoured at 2 σ) of the α1 subunit (B) and β1 subunit (C).

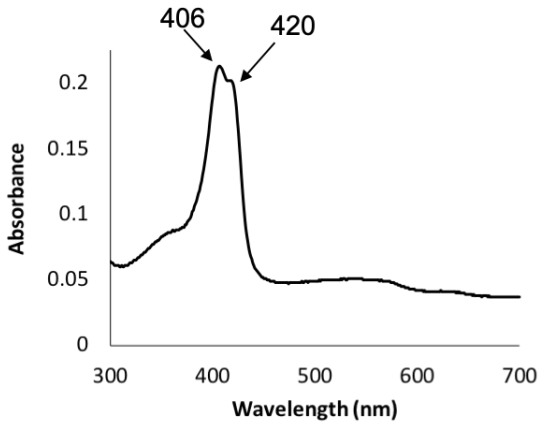

Figure 2.29. UV-vis spectroscopy of the dissolved crystal of the [α-$Fe^{III}(H_2O)$][β-Fe^{II}(MeNO)] Hb derivative after X-ray diffraction data collection.

2.3.4.4 The X-ray crystal structure of the product resulting from reacting ferric Hb^{III} with t-BuNHOH

Crystallization resulted in the formation of the $[\alpha\text{-}Fe^{III}(H_2O)][\beta\text{-}Fe^{III}(His)_2]_{\{t\text{-}BuNHOH\}}$ derivative. The X-ray crystal structure of *t*-BuNHOH in complex with human Hb was solved to 2.20 Å resolution from diffraction data collected at our home source (**Figure 2.30**). Data collection and refinement statistics are shown in **Table 2-7**. The diffraction data was obtained from crystals grown in 3.2 M Na/K phosphate buffer at pH 6.30 (see Section 2.2.8.5). Differences were observed between the α and β active sites. In both α subunits, water was bound to the Fe at the active site. The α1 active site is shown in **Figure 2.31**.

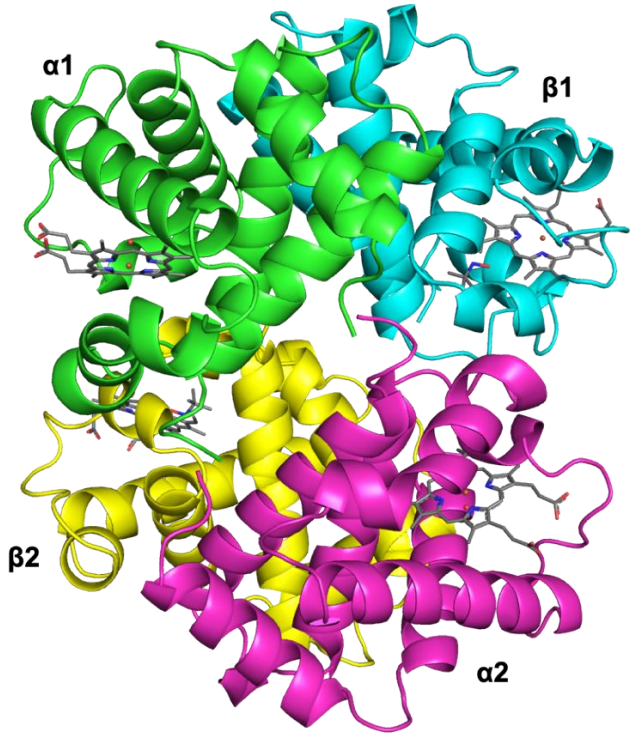

Figure 2.30. Overall X-ray crystal structure of the $[\alpha\text{-}Fe^{III}(H_2O)][\beta\text{-}Fe^{III}(His)_2]_{\{t\text{-}BuNHOH\}}$ Hb derivative at 2.20 Å resolution.

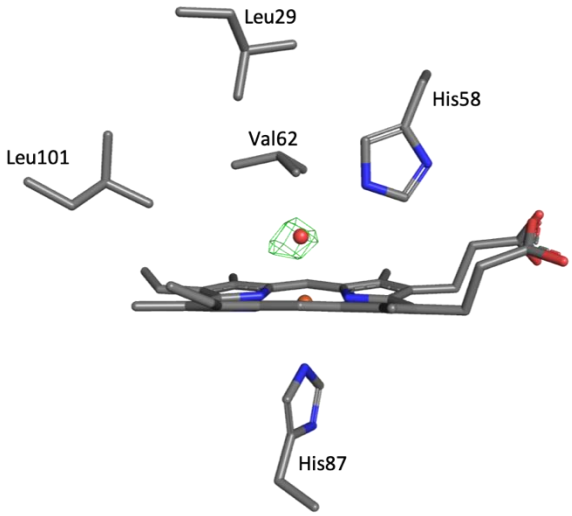

Figure 2.31. Final model and F_o-F_c omit map (contoured at 1.75 σ) of water in the α1 subunit active site of [α-$Fe^{III}(H_2O)$][β-$Fe^{III}(His)_2$]$_{\{t\text{-BuNHOH}\}}$.

In both β subunits, the heme is shifted towards the outside of the pocket, allowing for the formation of a hemichrome (**Figure 2.32A-B**). The movement of the heme out of the pocket left room behind the heme on the inside of the pocket and a single *t*-BuNHOH was modeled into the new electron density in this area (**Figure 2.32C-D**).

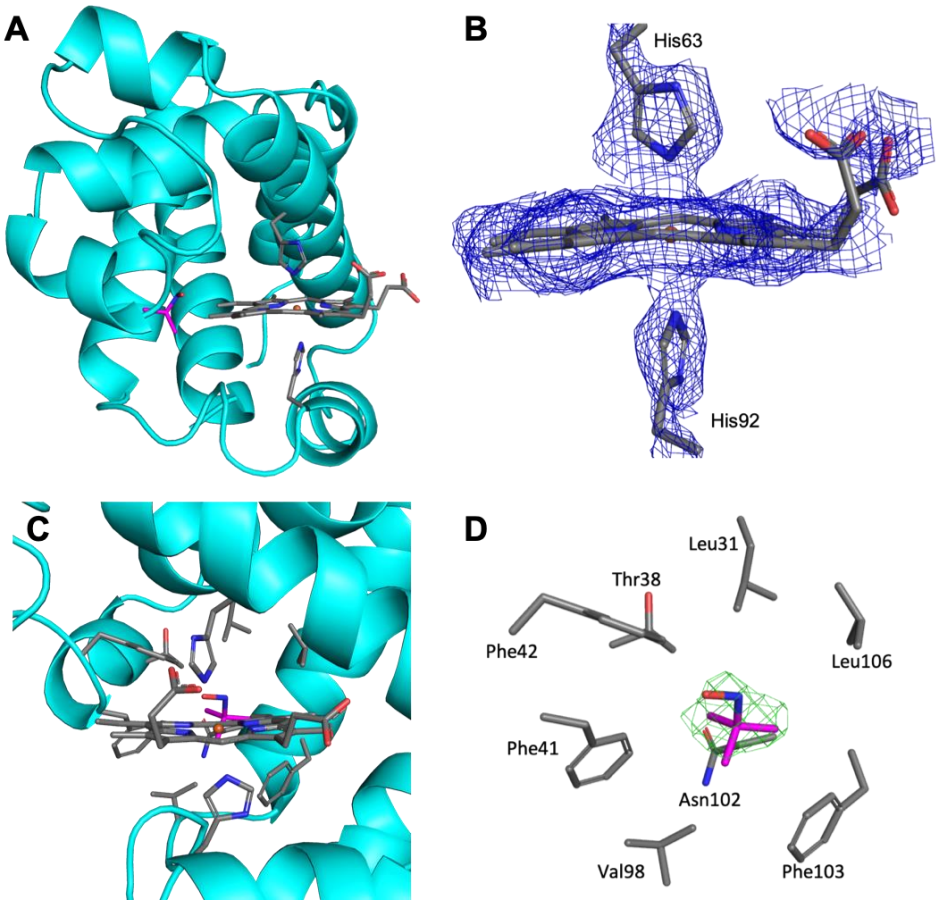

Figure 2.32. (A) Overall view of the β1 chain, (B) the $2F_o$-F_c map (contoured at 0.3 σ) of the hemichrome formed in the β1 subunit, (C) the active site of the β1 subunit and (D) the F_o-F_c omit map (contoured at 1.5 σ) of *t*-BuNHOH molecule in the β1 subunit.

In both β subunits, the propionate groups are fixed through H-bonding with the nearby Lys66 and Lys59 residues (**Figure 2.33, bottom**). In the β1 subunit, however, the H-bonding interactions appear to be much weaker than those in the β2 subunit. The propionate groups in both α subunits are stabilized through H-bonding interactions with fixed waters and the nearby His58 and His45 residues (**Figure 2.33, top**). Similar stabilization of the propionate groups was seen for ferric R-state Hb^{III}-H_2O.[76]

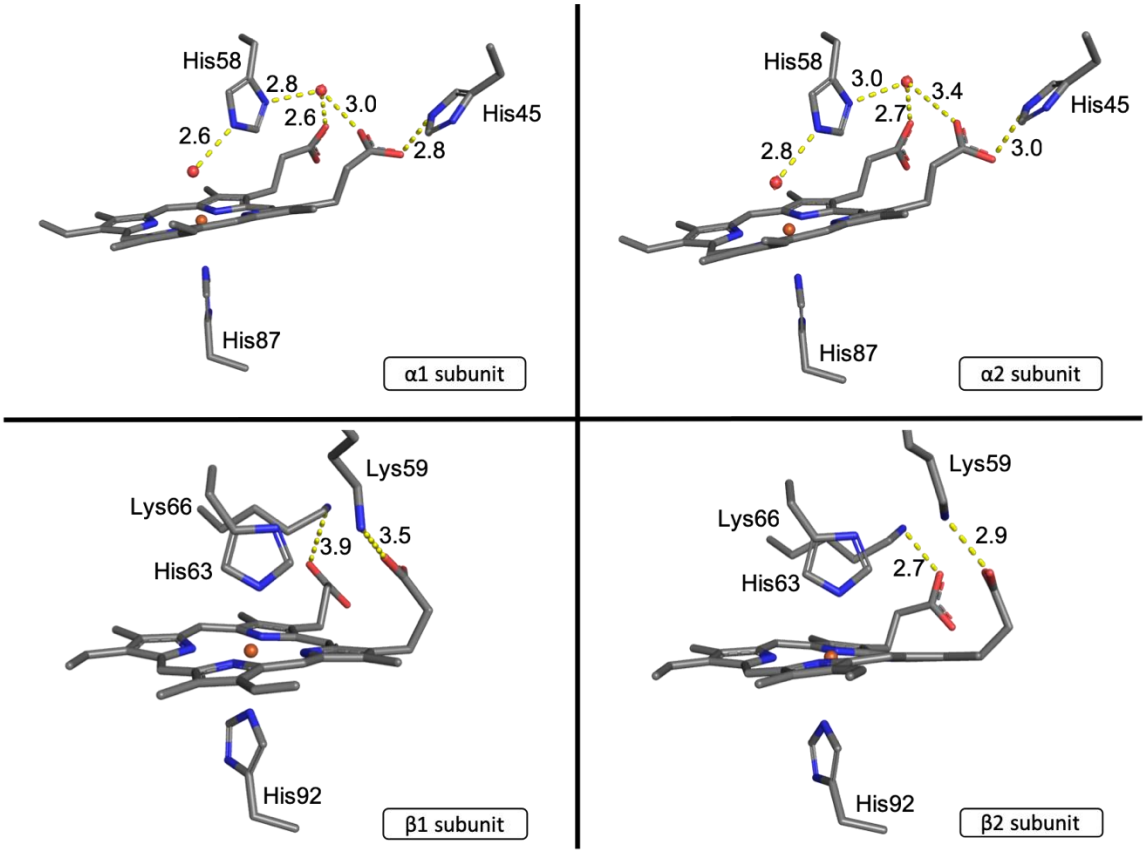

Figure 2.33. [α-$Fe^{III}(H_2O)$][β-$Fe^{III}(His)_2$]$_{\{t\text{-BuNHOH}\}}$ propionate interactions.

Table 2-6 summarizes the geometrical parameters of these β-hemichromes from the reaction between ferric Hb^{III}-H_2O and *t*-BuNHOH. See section 2.3.5.2 and **Figure 2.25** for a description of the parameters measured. These parameters are within the reported ranges for other heme-based hemichromes.[77, 78]

Table 2-6. [α-$Fe^{III}(H_2O)$][β-$Fe^{III}(His)_2$]$_{\{t\text{-BuNHOH}\}}$ hemichrome parameters

	θ_p (°)	θ_d (°)	$N\varepsilon_{2im}$-Fe-$N\varepsilon_{2im}$ (°)	ω (°)	Fe-$N\varepsilon_{2im}$ (Å)		$C\alpha_{prox}$- $C\alpha_{dist}$ (Å)
					Prox.	Dist.	
β1	79	84	174	78	2.4	2.4	13.0
β2	87	80	178	70	2.6	2.4	12.9

2.3.5 Interactions of swMb and Hb with AmphNHOH

2.3.5.1 UV- vis spectroscopy of swMb with AmphNHOH

UV-vis spectroscopy was used to monitor the reaction between ferric wt swMb^{III}-H_2O and AmphNHOH (**Figure 2.34**). The Soret band of the ferric wt Mb^{III}-H_2O at λ_{max} 409 nm shifted slowly to 423 nm over a 24 h period, and new peaks in the Q band region at 543 and 576 nm also appeared (**Figure 2.34B**). These shifts are indicative of the formation of a ferrous Mb^{II}-RNO derivative. The reaction does not go to completion and in fact is only ~22% complete over this time period (calculated using OriginPro). Other ferrous Mb^{II}-RNO complexes display similar absorption bands.[1,79] Once formed, this ferrous nitrosoalkane derivative is fairly stable in solution, showing only mild decomposition over time for the Mb products (~12% decomposition over 7 d) as judged by UV-vis spectroscopy.

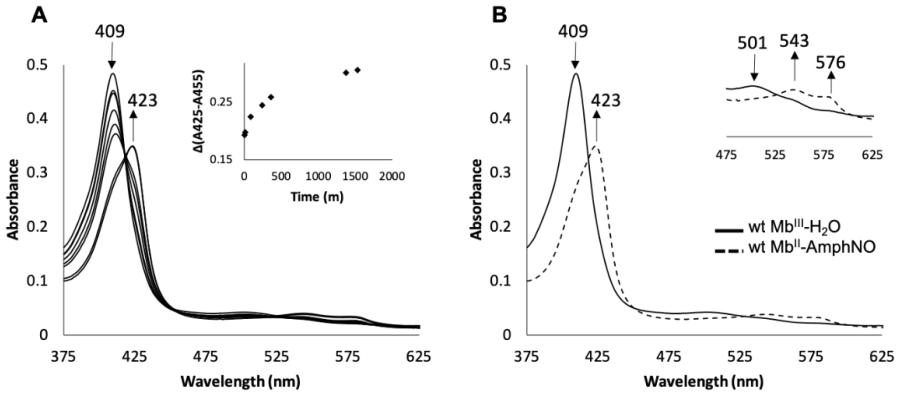

Figure 2.34. Reaction of ferric wt swMb^{III}-H_2O with AmphNHOH. (A) Changes after addition of AmphNHOH and a plot of ΔAbs(425-555) against time. (B) UV-vis spectra of the two forms observed during the reaction and a zoomed-in picture of the Q band region. Conditions: 0.1 M phosphate buffer at pH 7.4, [Mb] = 2 μM, final [AmphNHOH] = 80 μM.

Additionally, the reactions of two other mutant ferric swMbs (H64Q and H64V) were evaluated with AmphNHOH using UV-vis spectroscopy (**Figure 2.35**). For ferric H64Q Mb^{III}-H_2O, the peak in the Soret region shifted from 409 nm to 424 nm and the peak in the Q band region at 503 nm disappeared as two peaks at 543 nm and 561 nm appeared (**Figure 2.35A**). Similarly, for ferric H64V Mb^{III}, the peak in the Soret region shifted from 395 nm to 425 nm and the peak in the Q band region at 504 nm disappeared as two peaks at 541 nm and 572 nm appeared (**Figure 2.35B**). The reaction was essentially complete after ~30 min for the H64Q Mb mutant and ~60 min for the H64V Mb mutant.

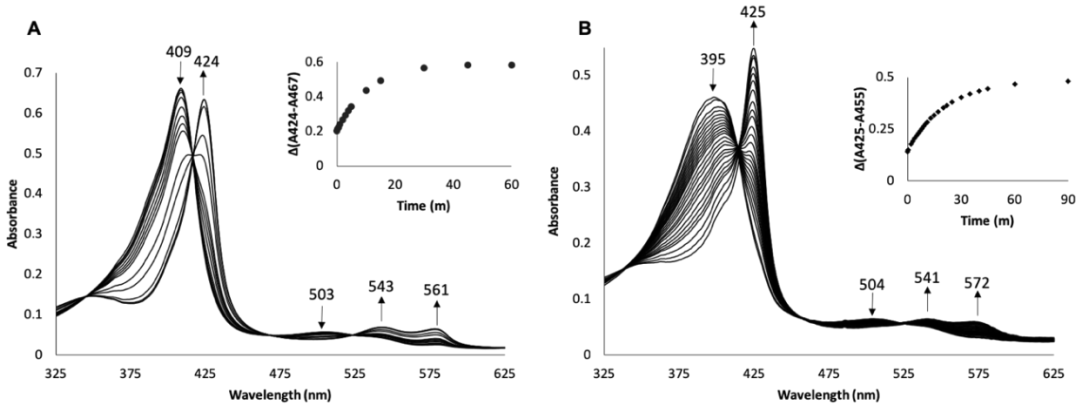

Figure 2.35. UV-vis spectral changes during the reaction of AmphNHOH with ferric (A) H64Q and (B) H64V Mb mutants. A plot of ΔAbs(424-467) against time for the H64Q mutant (A) and ΔAbs(425-455) against time for the H64V mutant (B). Conditions: 0.1 M phosphate buffer at pH 7.4, [Mb] = 2 μM, final [AmphNHOH] = 80 μM.

To test the chemical reversibility of the reaction between these ferric Mb^{III} mutants and AmphNHOH, the oxidant potassium ferricyanide was added to the ferrous product Mb^{II}-AmphNO in buffer (0.1 M sodium phosphate at pH 7.4). The original peaks in the Soret region and in the Q band region reappeared, indicating a return their respective ferric

precursors (**Figure 2.36**). The time it took for the products to convert back to their ferric form varied. For wt Mb, the reaction was complete in ~40 min. The reaction was much quicker for the H64Q mutant (10 min) and especially for the H64V mutant (5 min).

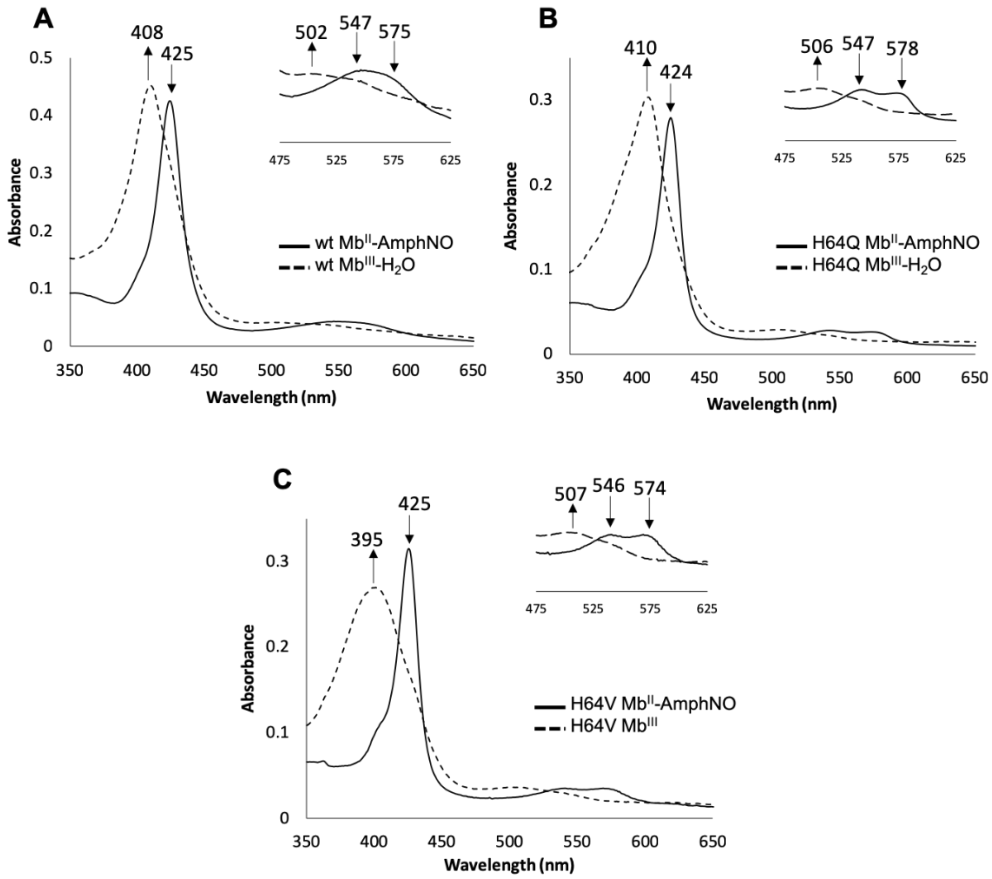

Figure 2.36. UV-vis spectroscopy of the reactions of ferrous (A) wt Mb^{II}-AmphNO, (B) H64Q Mb^{II}-AmphNO, and (C) H64V Mb^{II}-AmphNO with ferricyanide as well as a zoomed-in picture of the Q band region. Conditions: 100 mM sodium phosphate at pH 7.4, [Mb-AmphNO] = 2.4 μM, [ferricyanide] = 200 μM

2.3.5.2 UV-vis spectroscopy of ferric Hb with AmphNHOH

The reaction of excess AmphNHOH with ferric Hb^{III}-H_2O in phosphate buffer at pH 7.4 results in spectral shifts (**Figure 2.37**) analogous to that of Mb. The Soret band shifts from 406 nm to 421 nm, and new bands at 541 and 559 nm appear, with a ~77% conversion occurring over a 4 h period (calculated using OriginPro). Once formed, this ferrous nitrosoalkane derivative is fairly stable in aerobic solution, showing no visible decomposition for the Hb derivative even after 3 d as judged by UV-vis spectroscopy. This experiment was also carried out under anaerobic conditions and similar results were seen. The reaction does reach completion faster under aerobic conditions, however. Under anaerobic conditions, the product is stable even after 6 d as judged by UV-vis spectroscopy. The reversal of this reaction using the oxidant potassium ferricyanide was attempted, however the reaction appeared to be irreversible.

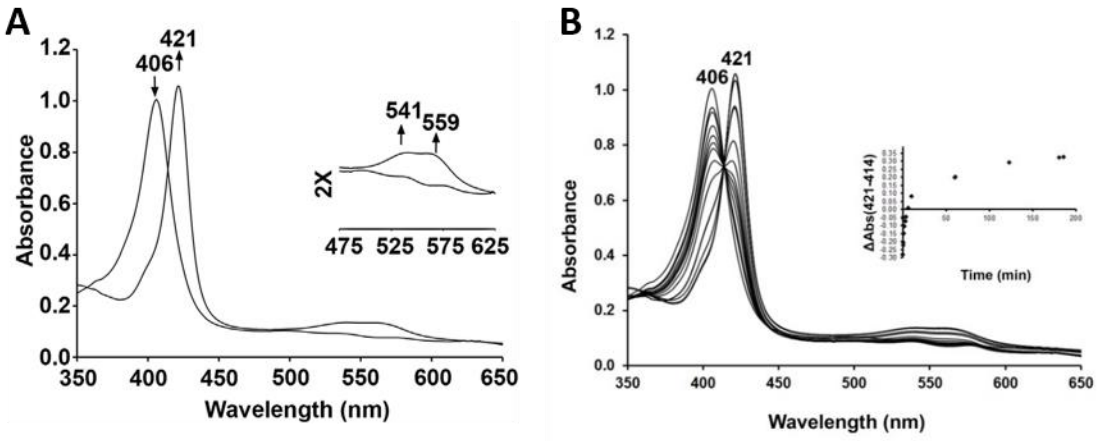

Figure 2.37. UV-vis spectral changes during the reaction of ferric Hb^{III}-H_2O with AmphNHOH. (A) Spectra of the initial and final readings as well as a zoomed-in picture of the Q band region. (B) Time course and a plot of ΔAbs(421-414) against time. Conditions: 0.1 M phosphate buffer at pH 7.4, [Hb] = 12.5 μM, final [AmphNHOH] = 100 μM.

2.3.5.3 The X-ray crystal structure of the product resulting from reacting ferric Hb with AmphNHOH

Crystallization resulted in the formation of the [α-$Fe^{III}(H_2O)$][β-Fe^{II}(AmphNO)] derivative. The X-ray crystal structure of this product was solved to 2.15 Å resolution from diffraction data collected at our home source (**Figure 2.38**). Data collection and refinement statistics are shown in **Table 2-7**. The diffraction data was obtained from crystals grown in 3.2 M Na/K phosphate buffer at pH 6.47 (see Section 2.2.8.5). Like that of the [α-$Fe^{III}(H_2O)$][β-Fe^{II}(MeNO)] structure described earlier, differences were observed between the α and β active sites. In both α subunits (**Figure 2.38B**), water was bound to the iron at the active site, and AmphNO is *N*-bound to the Fe in both β subunits (**Figure 2.38C**). The hydrophobic portion of the AmphNO ligand is, as predicted, oriented towards the interior hydrophobic region of the active site pocket.

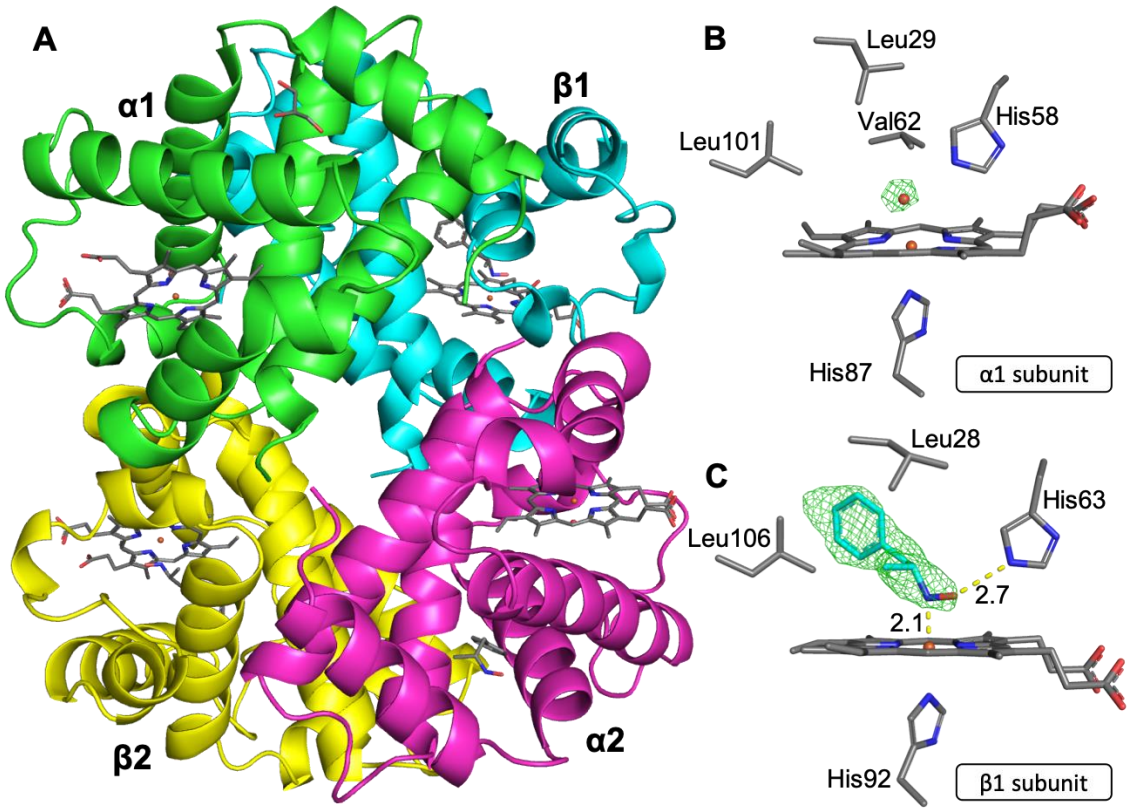

Figure 2.38. X-ray crystal structure of the [α-$Fe^{III}(H_2O)$][β-Fe^{II}(AmphNO)] Hb derivative. (A) Overall tetrameric structure. Final model of the active site and F_o-F_c omit maps of (B) the α1 subunit (contoured at 3 σ) and (C) the β1 subunit (contoured at 2 σ).

In order to determine the quaternary state of the full Hb tetramer, a comparison of the β2 FG and α1 C interface of representative structures was made (**Figure 2.39**). Based on this overall of the signature "switch" region, this [α-$Fe^{III}(H_2O)$][β-Fe^{II}(AmphNO)] structure (green in **Figure 2.39**) most closely matches that of R-state Hb (magenta in **Figure 2.39**).

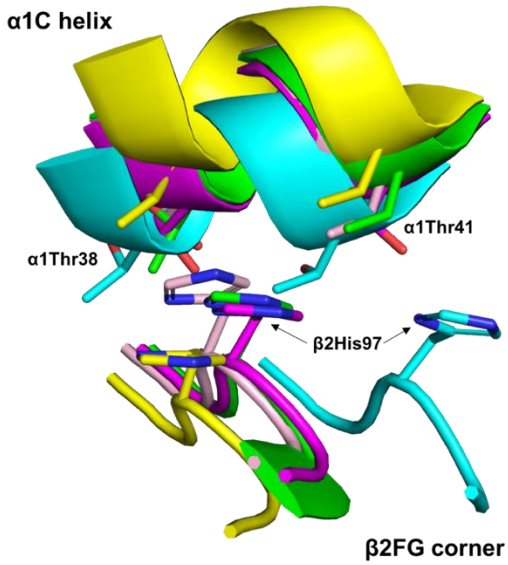

Figure 2.39. Comparison of the α1β2 interface of representative Hb structures. Analysis of the representative key residues show that the [α-$Fe^{III}(H_2O)$][β-Fe^{II}(AmphNO)] structure presented in this work is in the R-state. Green: [α-$Fe^{III}(H_2O)$][β-Fe^{II}(AmphNO)] (this work), Cyan: T-state deoxyHb (PDB id: 1B86), Magenta: R-state Hb(CO) (PDB id: 1AJ9), Yellow: R2-state Hb(CO) (PDB id: 1BBB), Light Pink: R3-state Hb(CO) (PDB id: 1YZI)

We further verified the Fe oxidation state the crystal by performing UV-vis on the dissolved crystal (**Figure 2.40**) after X-ray diffraction data collection. The spectrum displayed two peaks in the Soret band at 405 and 421 nm. The UV-vis spectrum of the precursor ferric Hb^{III}-H_2O has a λ_{max} at 406 nm and in solution, upon reaction with AmphNHOH, the λ_{max} shifts to 421 nm (see above). This supports the notion that the α subunit has a ferric center bound with water (corresponding to the peak at 405 nm) and that the β subunit has ferrous AmphNO moiety (corresponding to the peak at 421 nm).

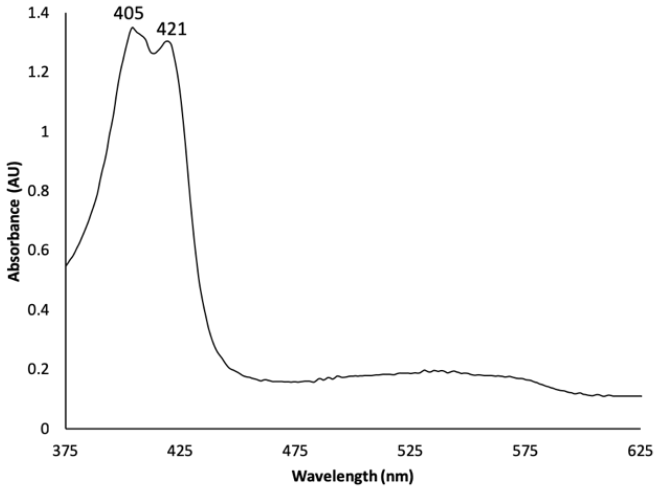

Figure 2.40. UV-vis spectroscopy of the dissolved crystal of [α-$Fe^{III}(H_2O)$][β-Fe^{II}(AmphNO)] after X-ray diffraction data collection.

Table 2-7. X-ray data collection and refinement statistics

	H64V Mb^{III}-NO_2	**H64Q Mb^{II}-ACM**	**Hb-CAMNO[g]**	**wt Mb^{II}-PhNO**	**Hb-PhNO[h]**
PDB ID	6CF0			6M9N	6M9O
Data collection[a]	MicroMax 007HF	MicroMax 007HF	MicroMax 007HF	MicroMax 007HF	SSRL, Beamline 9-2
Wavelength	1.54	1.54	1.54	1.54	0.98
Space group	*P6*	*P6*	$P12_11$	$P12_11$	$P4_1$
Cell dimensions	90.15, 90.15, 45.32 90.00, 90.00, 120.00	90.29, 90.29, 45.26 90.00, 90.00, 120.00	53.33, 82.68, 62.59 90.00, 100.02, 90.00	34.53, 30.05, 64.62 90.00, 104.55, 90.00	53.26, 53.26, 194.71 90.00, 90.00, 90.00
Resolution (Å)	78.07-1.64	45.26-1.76	49.41-1.75	50.00-1.75	32.58 – 1.89
I/σ[I]	10.07 (2.88)	24.79 (9.06)	9.41 (2.22)	29.1 (2.57)	23.1 (3.42)
No. of reflections					
Observed	20847	22224	79263	103408	84905
Unique	1537	21041 (2046)	48509 (3140)	13162 (632)	43077 (4284)
Multiplicity	4.7	1.8 (1.4)	1.6 (1.4)	3.1 (3.0)	2.0 (2.0)
Completeness (%)	99.94 (100.00)	99.8 (98.3)	90.10 (58.90)	99.7 (99.2)	100 (100)
R_{merge}[b]	0.060 (0.224)	0.024 (0.058)	0.050 (0.206)	0.036 (0.347)	0.050 (0.161)
$CC_{1/2}$	0.995	0.999	0.995	0.900	0.989
Refinement statistics					
No. of protein atoms	1214	1262	4501	1203	4384
R factor[c]	0.165	0.150	0.153	0.229	0.201
R_{free}[d]	0.193	0.178	0.205	0.276	0.248
RMSD Bond length (Å)	0.024	0.019	0.017	0.012	0.015
RMSD Bond angles (°)	2.25	1.99	1.96	1.578	1.64
Overall Mean B Factor ($Å^3$)	17.58	14.43	15.93	21.52	38.45
Ramachandran plot (%)[e]					
most favored residues	96.69	98.01	98.56	96.77	98.00
outliers	0.00	0.00	0.00	0.00	0.00

(a) Values in parentheses correspond to the highest resolution shells. (b) $R_{merge} = \Sigma|I-\langle I\rangle|/\Sigma(I)$, where I is the individual intensity observation and $\langle I\rangle$ is the mean of all measurements of I. (c) $R = \Sigma||F_o|-|F_c||/\Sigma|F_o|$, where F_o and F_c are the observed and calculated structure factors, respectively. (d) R_{free} was calculated by using 5% of the randomly selected diffraction data which were excluded from the refinement. (e) As calculated using *MOLPROBITY*. The full identities of the X-ray crystal structures: (g) $[\alpha\text{-}Fe^{II}][\beta\text{-}Fe^{II}\text{-}SNO]_{\{CAMNO\}}$, (h) $[\alpha\text{-}Fe^{III}(H_2O)][\beta\text{-}Fe^{III}(His)_2\text{-}SNO]_{\{PhNO\}}$

Table 2-7. X-ray data collection and refinement statistics (cont'd)

	Hb-MeNO[g]	**Hb-*t*-BuNHOH**[h]	**Hb-AmphNO**[i]
PDB ID			6M9P
Data collection[a]	MicroMax 007HF	MicroMax 007HF	MicroMax 007HF
Wavelength	1.54	1.54	1.54
Space group	$P4_1$	$P4_1$	$P4_1$
Cell dimensions	53.46, 53.46, 191.38 90.00, 90.00, 120.00	53.26, 53.26, 192.55 90.00, 90.00, 120.00	53.34, 53.34, 190.65 90.00, 90.00, 90.00
Resolution (Å)	46.67-1.91	40.99-2.2	40.85-2.15
I/σ[I]	24.85 (5.65)	12.46 (0.89)	14.22 (4.60)
No. of reflections			
Observed	77535	49286	37504
Unique	40716 (3626)	26843 (2533)	26737 (2436)
Multiplicity	1.9 (1.7)	1.8 (1.5)	1.4 (1.0)
Completeness (%)	98.46 (87.25)	98.95 (94.27)	93.0 (85.0)
R_{merge}[b]	0.041 (0.149)	0.085 (0.876)	0.043 (0.025)
$CC_{1/2}$	0.996	0.987	0.982
Refinement statistics			
No. of protein atoms	4372	4298	4335
R factor[c]	0.185	0.211	0.216
R_{free}[d]	0.241	0.288	0.287
RMSD Bond length (Å)	0.016	0.017	0.021
RMSD Bond angles (°)	1.85	1.94	1.530
Overall Mean B Factor ($Å^3$)	32.36	54.55	27.05
Ramachandran plot (%)[e]			
most favored residues	98.40	90.29	94.0
outliers	0.65	1.62	1.1

(a) Values in parentheses correspond to the highest resolution shells. (b) $R_{merge} = \Sigma|I-\langle I\rangle|/\Sigma(I)$, where I is the individual intensity observation and $\langle I\rangle$ is the mean of all measurements of I. (c) $R = \Sigma||F_o|-|F_c||/\Sigma|F_o|$, where F_o and F_c are the observed and calculated structure factors, respectively. (d) R_{free} was calculated by using 5% of the randomly selected diffraction data which were excluded from the refinement. (e) As calculated using *MOLPROBITY*. The full identities of the X-ray crystal structures: (g) [α-$Fe^{III}(H_2O)$][β-Fe^{II}(MeNO)], (h) [α-$Fe^{III}(H_2O)$][β-$Fe^{III}(His)_2$]$_{\{t\text{-BuNHOH}\}}$, (i) [α-$Fe^{III}(H_2O)$][β-Fe^{II}(AmphNO)]

2.4 Discussion

2.4.1 Interaction of H64V swMb with nitrite

The X-ray crystal structure of ferric H64V swMb^{III}-NO_2 revealed that the nitrite ligand was N-bound to the Fe center (**Figure 2.41A**). A similar result was obtained by a previous lab member, Dr. Jun (Eva) Yi, using H64V hhMb (**Figure 2.41B**).[5] Based on the Fe-N(NO_2) distances, the *N*-binding mode is much more defined in the sw derivative (2.1 Å) than in the hh derivative (2.6 Å). In wt Mb, a H-bond is typically provided by the distal H64 residue, but in both ferric H64V Mb^{III}-NO_2 structures described here, the nitrite in the active site pocket is stabilized through a H-bonding network provided by fixed waters, which essentially take the place of the now-absent H64 residue.

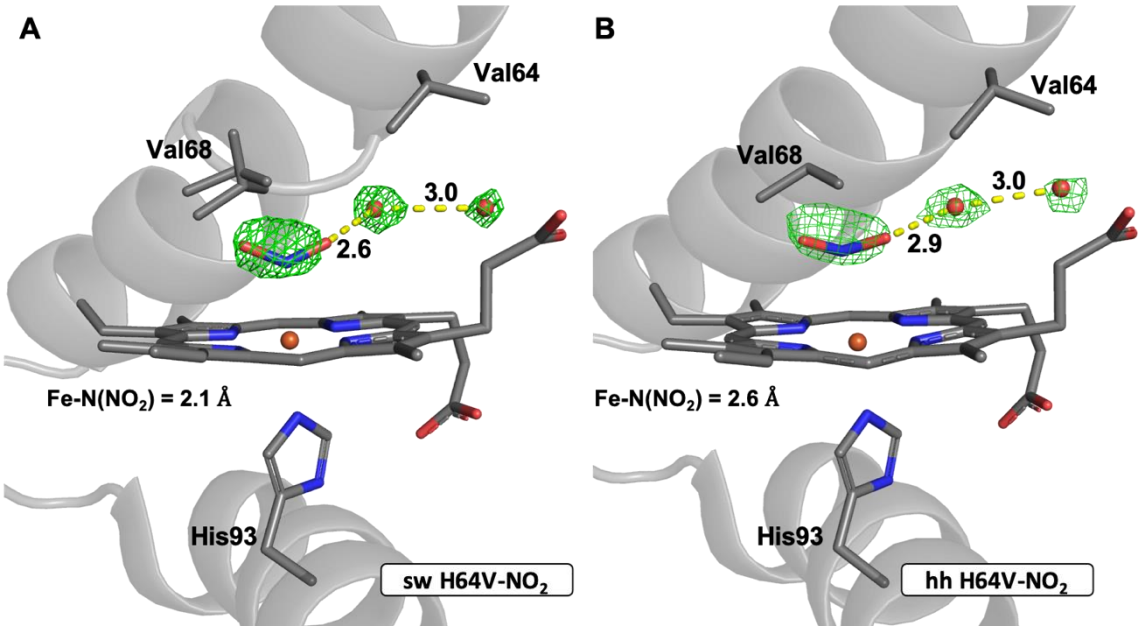

Figure 2.41. Comparison of the ferric H64V Mb^{III}-NO_2 X-ray crystal structures obtained from (A) sw (this work) and (B) hh (PDB id: 3HEP).

The H64V Mb mutant is most closely related to the H64A mutant as both mutations lack a H-bond at position 64. The UV-vis spectrum of H64V swMb in reaction with nitrite (**Figure 2.5**) is similar to that from the reaction of H64A swMb and nitrite.[4] However, the X-ray crystal structure of ferric H64A swMb^{III}-NO_2, obtained by former lab member Dr. Bing Wang, displayed an *O*-bound NO_2 moiety unlike the ferric H64V swMb^{III}-NO_2 in which the NO_2 was *N*-bound. This can be rationalized by the observation that the crystal structure of the precursor ferric H64A swMb^{III}-H_2O adduct contains an Fe-bound H_2O ligand[80]; thus, the *O*-bound nitrite appears to essentially replace another *O*-bound ligand (H_2O). In contrast, however, the ferric H64V swMb^{III} structure does not reveal an Fe-bound H_2O ligand[6], implying there may be a lower affinity for an added *O*-bound ligand such as nitrite in the *O*-nitrito form.

2.4.2 Analysis of the reactions of swMb and Hb with Mtz and CAM

2.4.2.1 Importance of H-bonding

Our results, summarized in **Table 2-1**, suggest that a distal pocket H-bond is necessary for the reaction of both CAM and Mtz with ferric Mb^{III} since neither CAM nor Mtz reacted with the H64A or H64V mutants. Mtz did react with ferric wt, H64Q and V68A/I107Y Mb^{II} suggesting that Mtz does not have a preference for a certain amino acid at position 64 but does require a H-bond in this location. Interestingly, CAM does not react with wt or V68A/I107Y Mb but does in fact react with the H64Q mutant. These results suggest that CAM has a preference for Gln over His in position 64. Since CAM is a larger substrate than Mtz (**Figure 2.4**), it likely requires a more flexible amino acid like Gln to allow CAM to enter the pocket.

2.4.2.2 Analysis of the reaction of ferric H64Q swMb^{III} with Mtz

Based on the UV-vis studies of the reaction of ferric H64Q Mb^{III}-H_2O and Mtz (**Figure 2.7C**), Mtz was predicted to be bound at the Fe-center of Mb in solution. However, after crystallization and solution of the X-ray crystal structure of this product, it was found that it was acetamide (ACM) that was bound instead. The reaction between Mb and Mtz was carried out under reducing conditions using sodium dithionite. Interestingly, sodium dithionite by itself can reductively activate Mtz, eventually leading to ring fission generating hydroxyethyl oxamic acid and ACM.[81] Based on the X-ray crystal structure obtained, Mtz was likely cleaved by dithionite during the extended crystallization time period,[81] and the crystals obtained were those from the contributing [Mb+ACM] reaction.

In the final structure (**Figure 2.9**), ACM was modeled as *O*-bound based on the crystal structure of a synthetic model obtained by a previous lab member, Dr. Nan Xu.[82]

2.4.2.3 Analysis of the reaction between ferrous deoxyHb^{II} with CAMNO

Prior to this work, there were no reported X-ray crystal structures of any heme protein in complex with CAM or its derivatives. Our original goal was to obtain such a complex containing a direct Fe-CAMNO interaction. Presented in this chapter is the heme-protein crystal structure of Hb with an unbound CAMNO molecule in the crystal (**Figure 2.10 and Figure 2.13**). The structure contains a weakly interacting H_2O in the active site of the α subunit (**Figure 2.10B**) and no distal Fe-bound ligand in the β subunit active site (**Figure 2.10C**). This crystal was grown under anaerobic conditions and as shown by the analysis in **Figure 2.11**, the tetrameric structure is in the T-state. I note that the X-ray crystal structure of T-state deoxyHb (PDB id: 4HHB) also has a weakly interacting water in the α subunit and no Fe-bound ligand in the β subunit.[83] The overall RMSD between ferrous T-state deoxyHb^{II} and the [α-Fe^{II}][β-Fe^{II}-SNO]$_{\{CAMNO\}}$ structure is 0.381 Å indicating that CAMNO had very little effect on the overall protein structure. A primary important difference between the two structures is that in our [α-Fe^{II}][β-Fe^{II}-SNO]$_{\{CAMNO\}}$ structure, the βCys93 residues have been nitrosated (**Figure 2.14**).

The crystal structure presented here is the first to show that CAMNO is capable of nitrosating Hb at the βCys93 residue. UV-vis studies show that CAMNO does react with Hb at the Fe center (our original intent), most likely forming an *N*-bound ligand (**Figure 2.8**). Additionally, it is already known that CAMNO can displace O_2 from Hb.[26] Further discussion of S-nitrosation is in section 2.4.7.

2.4.3 Analysis and comparison of the structures of the products from the reactions of ferric wt swMb^{III} and Hb^{III} with PhNHOH

Presented here is the structural demonstration of the interaction between swMb and PhNHOH yielding an *N*-bound Fe^{II}-PhNO adduct. The only other crystal structure of a Mb-PhNO adduct is that from hhMb (PDB id: 2NSS) obtained by a former lab member Dr. Daniel Copeland. The two overall structures are very similar (RMSD of 0.452 Å), but with very slight differences in their active sites (**Figure 2.42**). For the residues in the active sites of the two structures, His64 is the residue that differs the most; a ~70° rotation (∠ swCε_1-Cδ_2-hhCε_1) is observed. Due to this rotation in His64, the distance between the nitrosobenzene-O and His-Nε differs between the two (2.2 Å in swMb and 2.8 Å in hhMb). The orientation of the Fe-bound PhNO is similar in these two structures, with the hydrophobic phenyl group oriented towards the hydrophobic interior of the distal pocket. A unique feature of the previously determined ferrous hhMb^{II}-PhNO structure was the presence of a second PhNO molecule (modeled in two conformations with 50% occupancy each) in the Xe1 pocket on the proximal side of the heme (bottom left side of **Figure 2.42**). Identified crystallographically in 1984,[84] these Xe pockets (x4) have long been predicted to act as additional dioxygen storage sites and to participate in ligand migration.[85]

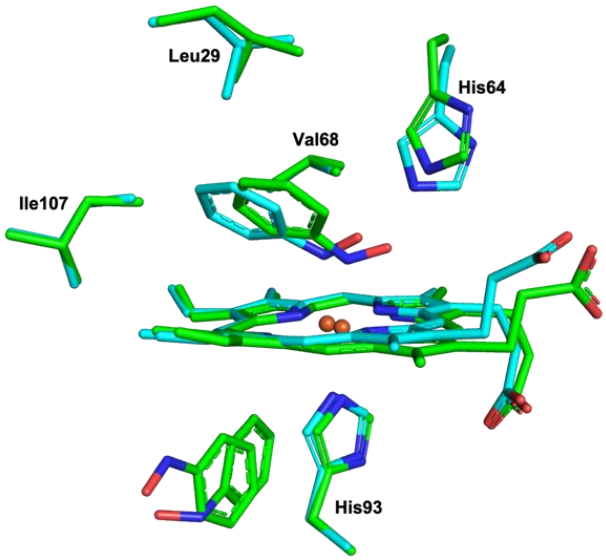

Figure 2.42. Comparison of the active sites of ferrous swMb^{II}-PhNO (cyan, this work) and hhMb^{II}-PhNO (green, PDB id: 2NSS).

Only one other crystal structure of a heme protein in complex with PhNO has been reported, namely that of ferrous legHb^{II}-PhNO, published in 1982.[86] LegHb is found in leguminous plant nodules and is a monomeric protein. A comparison of the active site of our ferrous swMb^{II}-PhNO structure was made with ferrous legHb^{II}-PhNO (**Figure 2.43**). The orientation of PhNO is opposite in the two structures. In ferrous swMb^{II}-PhNO, the phenyl group is oriented towards the inner, hydrophobic portion of the pocket, whereas in ferrous legHb^{II}-PhNO, the phenyl group is oriented towards the outer, hydrophilic portion of the pocket. The likely reason for this difference is the position and orientation of the distal histidine. In swMb, the PhNO is stabilized through a H-bond with His64. However, this is not possible in the legHb structure. In ferrous legHb^{II}-PhNO, His63 is oriented away from the heme pocket, making it very unlikely that PhNO would be able to form a H-bond with His63. In the X-ray crystal structure of ferrous legHb^{II}-O_2 (PBD id: 2GDM), the His63

residue is in a position closer to that of swMb His64. It is likely that in order for PhNO to enter the heme pocket and bind to the Fe center, legHb His63 had to rotate towards the exterior of the pocket. The rotation of His63 also creates a "larger" active site which may account for some of the reason why PhNO can be oriented towards the exterior of the pocket.

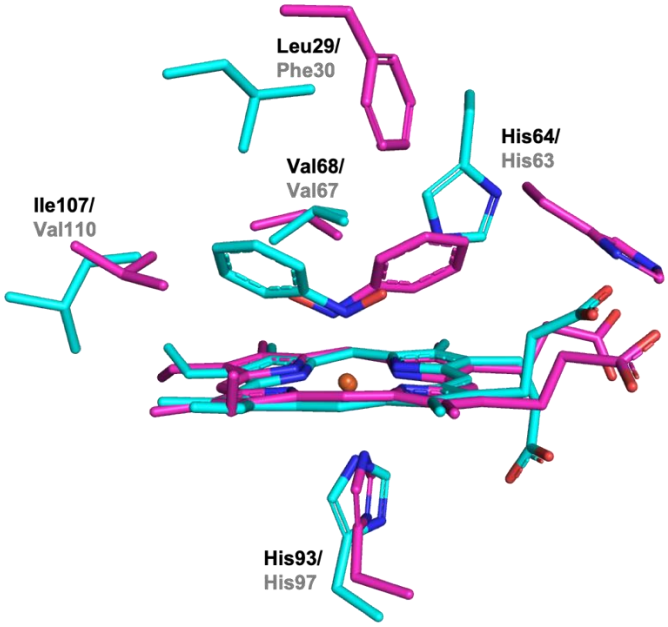

Figure 2.43. Overlay of the active sites of ferrous swMb^{II}-PhNO (cyan, this work) and legHb^{II}-PhNO (magenta, PDB id: 1LH7). Residue identifiers are labeled black for Mb and grey for legHb.

Unlike the reaction of ferric Mb^{III} with PhNHOH to generate ferrous Mb^{II}-PhNO, the reaction of ferric Hb^{III} with PhNHOH did not result in crystal containing an Fe-bound PhNO ligand. Instead, our crystallization conditions enhanced the formation of a hemichrome in the Hb β subunit (**Figure 2.23**). *This unplanned result turned out to be quite advantageous, as it provided us with a physiologically important structure we could*

not have otherwise obtained. The [α-$Fe^{III}(H_2O)$][β-$Fe^{III}(His)_2$-SNO]$_{\{PhNO\}}$ structure was compared to a ferric Hb^{III}-H_2O crystal structure in order to assess the effects that the hemichrome formation had on the structure of the protein (**Figure 2.44**). The overall structures are quite similar (RMSD of 0.207 Å). However, large differences exist in the β subunits. Formation of a hemichrome causes large movements in the F helix (residues β85-100) as the proximal His92 residue is drawn further out of the pocket to stay coordinated to the heme Fe (**Figure 2.23A**). Additionally, there is a large shift (4.5 Å Fe_1-Fe_2) of the heme towards the outside of the pocket (**Figure 2.23B**). Further discussion of hemichrome formation is presented in section 2.4.8.

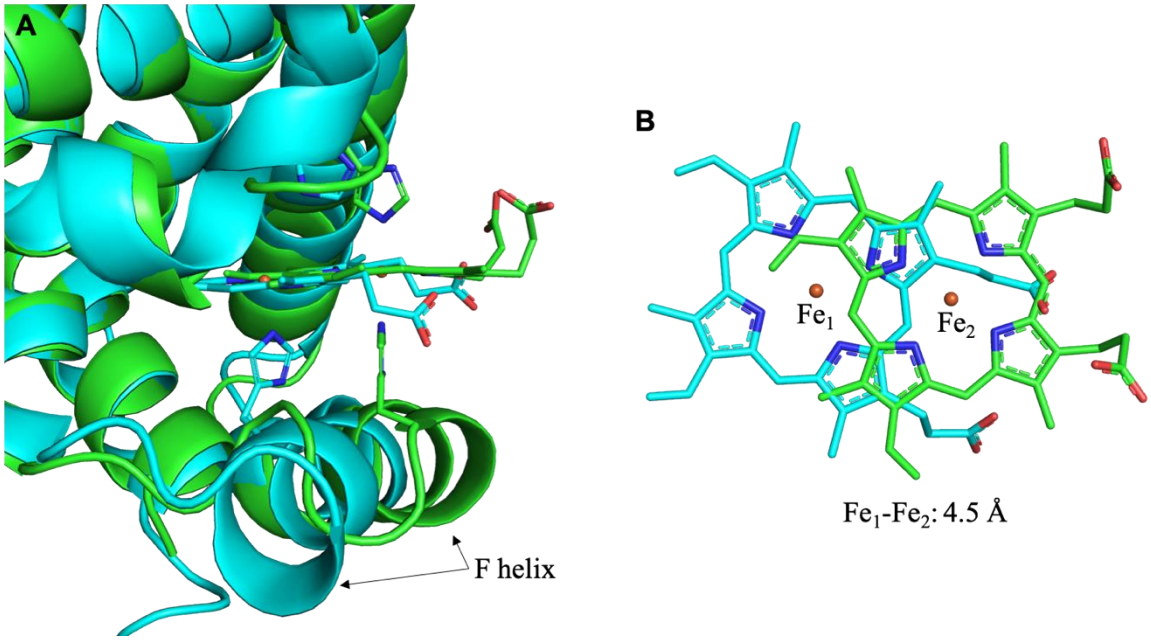

Figure 2.44. Overlay of the β1 active site (A) and hemes (B) of a ferric Hb^{III}-H_2O (PDB id: 3P5Q; cyan) and [α-$Fe^{III}(H_2O)$][β-$Fe^{III}(His)_2$-SNO]$_{\{PhNO\}}$ (green, this work).

Not only did the reaction of ferric Hb^{III}-H_2O with PhNHOH result in a hemichrome formation, but our crystal structure is the first to show that the biologically relevant PhNHOH/PhNO species can serve as an "NO donor" to nitrosate Hb at the βCys93 position. UV-vis studies show that PhNHOH does react initially with Hb at the Fe center, most likely forming an *N*-bound ligand such as that seen in swMb. We note that the nitrosation of the βCys93 residue induces flexibility in the C-terminal residues βLys144, Tyr145 and His146 of this structure, as was seen in a previously reported crystal structure of nitrosated Hb obtained by a different reaction.[87] Further discussion of *S*-nitrosation is in section 2.4.7.

2.4.4 Analysis of the [α-Fe^{III}(H$_2$O)][β-Fe^{II}(MeNO)] crystal structure

Presented here is the X-ray crystal structure of [α-Fe^{III}(H$_2$O)][β-Fe^{II}(MeNO)] formed through the *oxidative* pathway from reaction of ferric Hb^{III}-H$_2$O with MeNHOH (**Figure 2.28**). The only other reported X-ray crystal of MeNO in complex with Hb was published by a former lab member Dr. Jun (Eva) Yi.[88] In her work, the Hb-MeNO adduct was formed through the *reductive* pathway from reaction of ferric Hb^{III}-H$_2$O with dithionite and MeNO$_2$. Comparing these two structures, the overall RMSD is 0.204 Å. In Dr. Yi's structure, MeNO is *N*-bound to the heme-Fe in both the α and β subunits ([α-Fe^{II}(MeNO)][β-Fe^{II}(MeNO)]), but in my structure, MeNO is only *N*-bound to the heme-Fe in the β subunits and a water is bound in the α subunits ([α-Fe^{III}(H$_2$O)][β-Fe^{II}(MeNO)]) (**Figure 2.45**). Due to this observation, it is not surprising that there are very minor differences in the β active sites (**Figure 2.45B**), but larger differences exist in the α active sites (**Figure 2.45A**). In my structure, a water is held in place through H-bonding with αHis58 (2.9 Å). In Dr. Yi's structure, the αHis58 residue swings out of the pocket ~16° (∠ Nε$_2$-C$_\beta$-Nε$_2$) to accommodate MeNO, which is still held in place by a H-bond with αHis58 (2.7 Å).

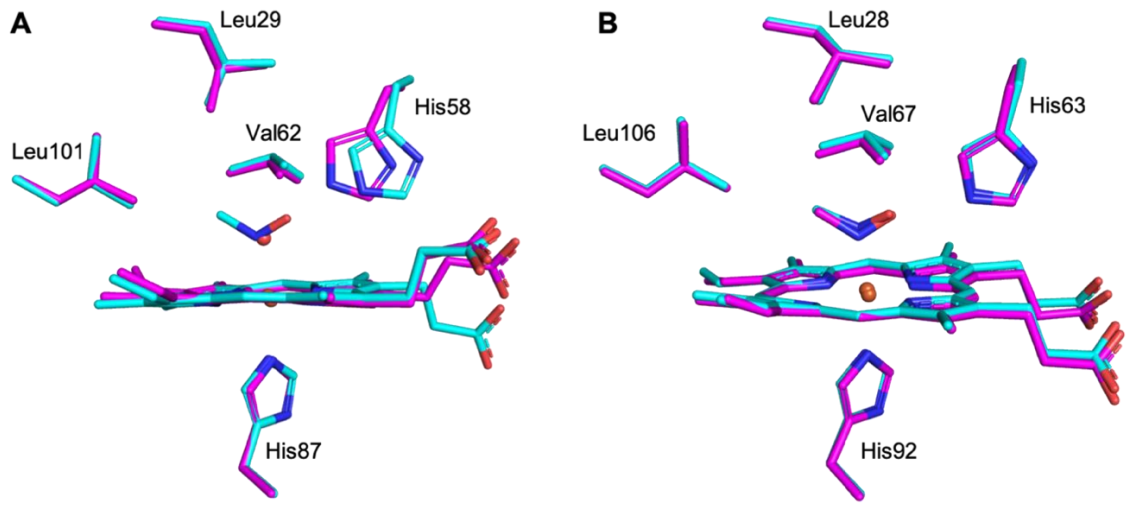

Figure 2.45. Overlay of the heme sites of the α1 subunits (A) and β1 subunits (B) of the products formed from the reaction of ferric Hb^{III}-H_2O with dithionite and $MeNO_2$ (cyan, PDB id: 4M4A) or with MeNHOH (magenta, this work).

The MeNO binding differences in these two structures can be explained by examining their UV-vis spectra. The reaction of ferric Hb^{III}-H_2O with dithionite and $MeNO_2$ goes to completion.[88] However, the reaction between ferric Hb^{III}-H_2O and MeNHOH does not go to completion, even after multiple days (**Figure 2.19**). Therefore, it explains the observation that in Dr. Yi's structure, MeNO is bound to Fe in both the α and β subunits and in my structure, MeNO is only bound to Fe in the β subunits.

2.4.5 Analysis of the [α-Fe^{III}(H$_2$O)][β-Fe^{III}(His)$_2$]$_{\{t\text{-BuNHOH}\}}$ crystal structure

Hemichromes formed in the β subunits of ferric Hb^{III}-H$_2$O upon reaction with *t*-BuNHOH (**Figure 2.32**). In many respects, the structure of the product was very similar to that formed from the PhNHOH reaction, but without *S*-nitrosation. To determine the effect that hemichrome formation had on the overall protein structure, the [α-Fe^{III}(H$_2$O)][β-Fe^{III}(His)$_2$]$_{\{t\text{-BuNHOH}\}}$ crystal structure was compared to a ferric Hb^{III}-H$_2$O crystal structure (**Figure 2.46**). The overall RMSD between the two structures is 0.229 Å, indicating that the two structures have high similarity. The main differences that exist between the two structures are within the β subunits. As can be seen in **Figure 2.46A**, hemichrome formation caused the F-helix (residues β85-100) to move as His92 was pulled further into the solvent channel to remain coordinated to the heme-Fe. The formation of a hemichrome also caused, similar to that seen from the PHNHOH reaction, a large shift of the heme (4.4 Å Fe$_1$-Fe$_2$) out of the active site pocket (**Figure 2.46B**). Further discussion of hemichrome formation is presented in section 2.4.8.

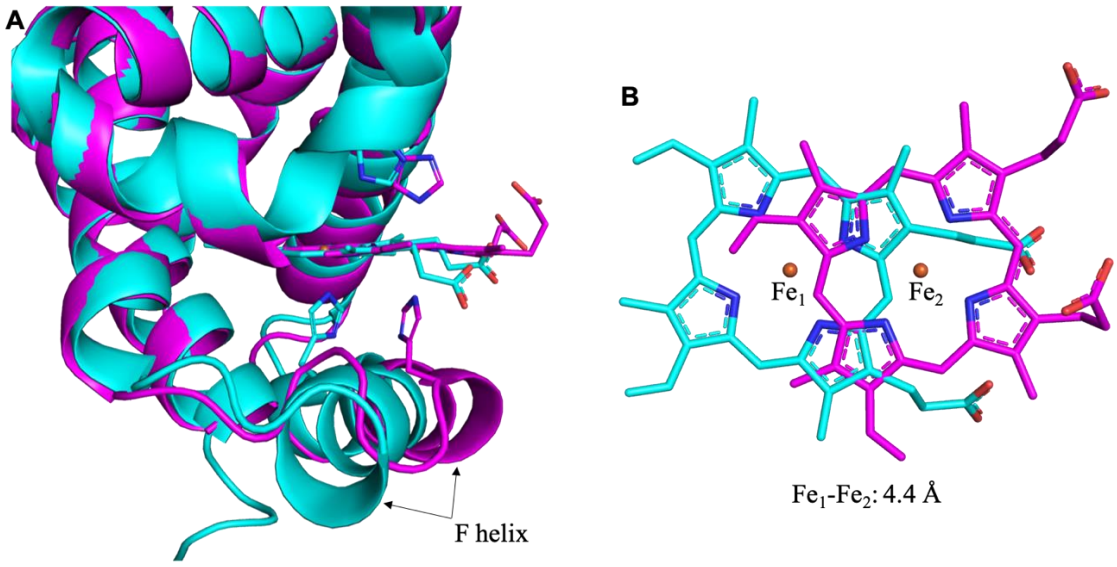

Figure 2.46. Overlay of the β1 active site (A) and hemes (B) of a ferric Hb^{III}-H_2O (PDB id: 3P5Q; cyan) and $[\alpha\text{-}Fe^{III}(H_2O)][\beta\text{-}Fe^{III}(His)_2]_{\{t\text{-}BuNHOH\}}$ (magenta, this work). This representation is similar to that shown for $[\alpha\text{-}Fe^{III}(H_2O)][\beta\text{-}Fe^{III}(His)_2\text{-}SNO]_{\{PhNO\}}$ in **Figure 2.44**.

2.4.6 Analysis of the Mb- and Hb-AmphNO interactions

2.4.6.1 E-helix movement allows for AmphNO binding

Here we present the first X-ray crystal structure of the interaction between the bulky ligand, AmphNHOH, and human Hb. It was previously predicted that due to its smaller active site cavity, Hb would be unable to accommodate bulky ligands such as AmphNHOH/AmphNO in its active site.[44, 45] To better understand how Hb was in fact able to accommodate AmphNHOH, our [α-$Fe^{III}(H_2O)$][β-Fe^{II}(AmphNO)] structure was aligned with that of ferric Hb^{III}-H_2O (PDB id: 3P5Q) as shown in **Figure 2.47** and **Figure 2.48**. The overall RMSD of the two structures is 0.283 Å. The only significant differences observed between the structures are in the β subunits, more specifically in the E helix and EF corner regions. Within the active sites of the β subunits, very subtle differences are observed. The largest difference between the two active sites is the position of Val67, which was displaced by 3.5 Å (**Figure 2.47**). Val67 is part of the E helix and is not the only residue to undergo changes upon AmphNO binding to Fe (**Figure 2.48**). The E helix partially unravels, specifically between residues 65-76, inducing large shifts (1.5-8 Å in Cα), and allowing for the accommodation of the phenyl moiety of AmphNO which would otherwise clash with the Val67 residue.

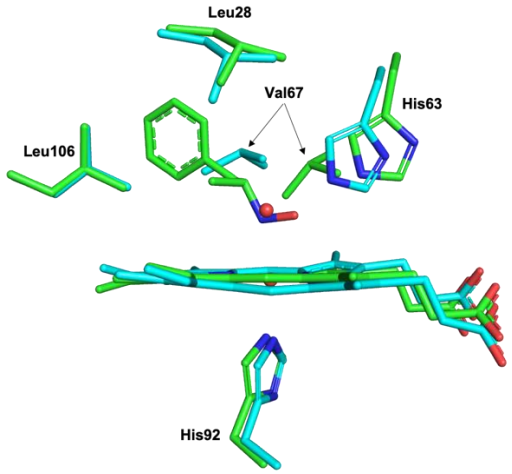

Figure 2.47. Overlay of the β1 active sites of ferric Hb^{III}-H_2O (cyan, PDB id: 3P5Q) and [α-$Fe^{III}(H_2O)$][β-Fe^{II}(AmphNO)] (green, this work).

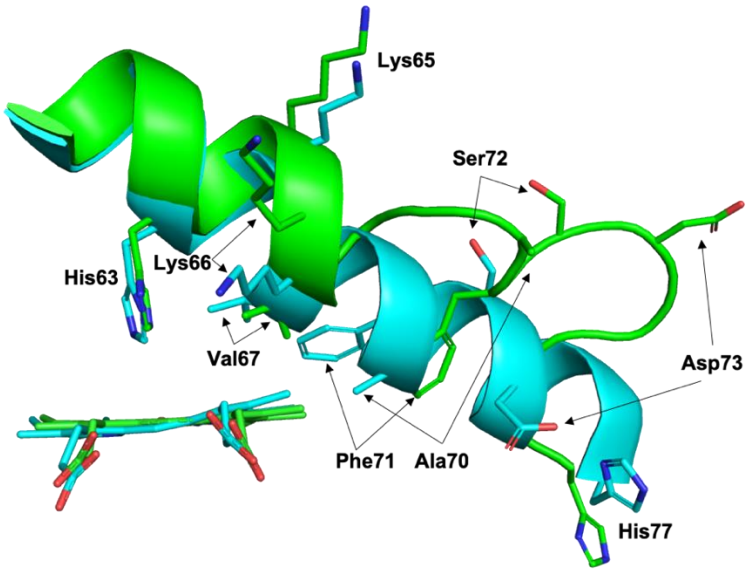

Figure 2.48. Overlay of the β1 E helix of ferric Hb^{III}-H_2O (cyan, PDB id: 3P5Q) and [α-$Fe^{III}(H_2O)$][β-Fe^{II}(AmphNO)] (green, this work).

2.4.6.2 Comparison of the structures of the β subunit of [α-$Fe^{III}(H_2O)$][β-Fe^{II}(AmphNO)] Hb and ferrous H64A $swMb^{II}$-AmphNO

We previously published the X-ray crystal structure of H64A Mb-AmphNO[43] and have been unsuccessful to date in crystallizing any other (wt or mutant) ferrous $swMb^{II}$-AmphNO complexes. Despite this, the X-ray crystal structure of [α-$Fe^{III}(H_2O)$][β-Fe^{II}(AmphNO)] presented here, provides us with very useful structural insight into the likely crystal structures of wt and other mutant swMb-AmphNO complexes. Alignment of the [α-$Fe^{III}(H_2O)$][β-Fe^{II}(AmphNO)] β chain with both ferric wt $swMb^{III}$-H_2O (RMSD = 1.183 Å, PDB id: 2MBW) and ferrous H64A $swMb^{II}$-AmphNO (RMSD = 1.368 Å, PDB id: 5KD1), allowed us to further analyze the binding of AmphNO to Fe at the active sites of these heme proteins (**Figure 2.49**).

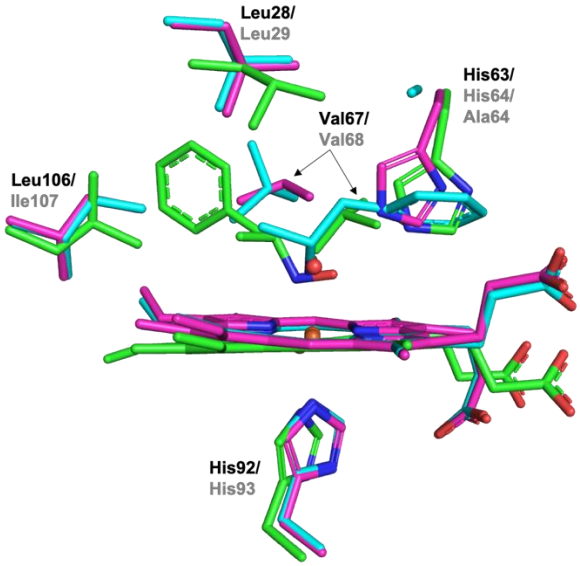

Figure 2.49. Overlay of the active sites of ferric wt $swMb^{III}$-H_2O (magenta, PDB id: 2MBW), ferrous H64A $swMb^{II}$-AmphNO (cyan, PDB id: 5KD1) and the β1 active site of [α-$Fe^{III}(H_2O)$][β-Fe^{II}(AmphNO)] (green, this work). Residue identifiers are labeled black for Hb and grey for Mb.

Just as that noted in the comparison of the β1 active site of [α-$Fe^{III}(H_2O)$][β-Fe^{II}(AmphNO)] with ferric Hb^{III}-H_2O (Figure 2.47), the only significant difference in the active sites observed between ferrous H64A $swMb^{II}$-AmphNO, ferric wt $swMb^{III}$-H_2O and the β1 active site of [α-$Fe^{III}(H_2O)$][β-Fe^{II}(AmphNO)], was the position of the Val67/Val68 residues (Figure 2.49). The position of Val67 in the Hb structure is 2.6 Å (Cα) shifted from that of Val68 in both wt Mb and the H64A Mb mutant. A closer look at the E helix region (**Figure 2.50**) reveals that partial unraveling only occurred in the β1 subunit of the Hb structure. H64A Mb lacks a bulky residue at position 64 (analogous to H63 in Hb), therefore it was unnecessary for the E helix to unravel to accommodate Fe-bound AmphNO in the active site. Due to this lack of E helix movement, however, Val68 (analogous to Val67 in Hb) did not shift, which resulted in the orientation of the AmphNO phenyl group pointing towards the exterior of the active site pocket rather than towards the inside as observed in [α-$Fe^{III}(H_2O)$][β-Fe^{II}(AmphNO)].

From the UV-vis spectroscopy results, it was evident that AmphNO does bind to the Fe centers of active sites of wt, H64Q and H64V Mb. From the structural comparison in **Figure 2.50**, it appears that in order for AmphNO to bind in both wt and H64Q Mb, the E-helix likely shifts and partially unravels to move the distal Val similar to what was observed in [α-$Fe^{III}(H_2O)$][β-Fe^{II}(AmphNO)]. H64V Mb is more closely related to H64A Mb and therefore, AmphNO likely binds to the heme-Fe without movement of the E-helix, and the orientation of AmphNO will likely match the orientation observed in ferrous H64A Mb^{II}-AmphNO.

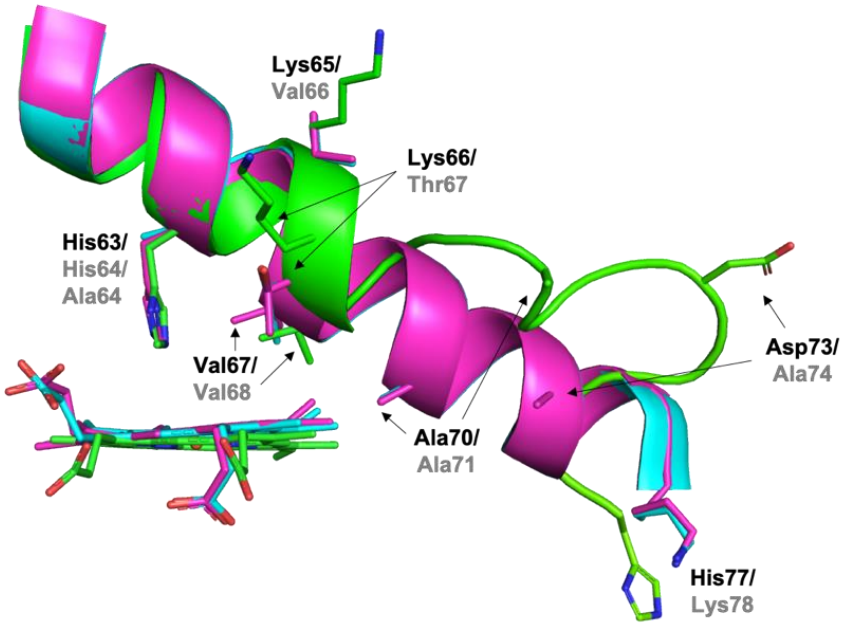

Figure 2.50. Overlay of the E helix region of ferric wt swMb^{III}-H_2O (magenta, PDB id: 2MBW), ferrous H64A swMb^{II}-AmphNO (cyan, PDB id: 5KD1) and the β1 subunit of [α-Fe^{III}(H_2O)][β-Fe^{II}(AmphNO)] (green, this work). Residue identifiers are labeled black for Hb and grey for Mb. This is a supplementary comparison to that shown in **Figure 2.48**.

2.4.6.3 An AmphNHOH molecule in the α Xe2 pocket

As with Mb, Xe pockets have long been predicted to be binding sites in Hb, contributing to ligand migration through the protein. Savino et al, identified 12 Xe sites in tetrameric Hb using X-ray crystallography.[89] Molecular dynamics studies have mapped the possible cavities throughout Hb and shown the potential for ligands to reach the distal pocket by traveling through tunnels that match up with the Xe sites.[90] Within the α subunits of our [α-$Fe^{III}(H_2O)$][β-Fe^{II}(AmphNO)] crystal structure, we have shown for the first time, the presence of a bulky ligand in one of these Xe pockets.

Although water, and not an AmphNHOH derivative, was observed in the active site of the α subunits, molecules were found in the Xe2 pocket of both α subunits. In the α1 subunit, a glycerol molecule was modeled in (**Figure 2.51A-C**) and in the α2 subunit (**Figure 2.51D-F**), an AmphNHOH molecule was modeled in to this site. The Xe2 pocket is surrounded by primarily hydrophobic residues, thus it is interesting that both glycerol and AmphNHOH were found in these sites. Glycerol interacts with a nearby fixed water and both the sidechain and mainchain of the Trp14 residue (**Figure 2.51C**). In the case of the AmphNHOH moiety, it is stabilized in this pocket through H-bonding with a nearby water which further H-bonds with the backbone C=O of the Gly18 and Trp14 residues (**Figure 2.51F**).

Our UV-vis spectroscopy studies on the interaction of Hb with AmphNHOH[43] imply that AmphNO binds with both the α and β subunits, however this was not observed in our crystal structure. One of the possible pathways for ligands to travel to/from the distal pocket is through the Xe2 site.[90] In our crystal structure, we have captured the AmphNHOH

in a temporary position as it was either traveling to or from the distal site where it can bind to the Fe-center.

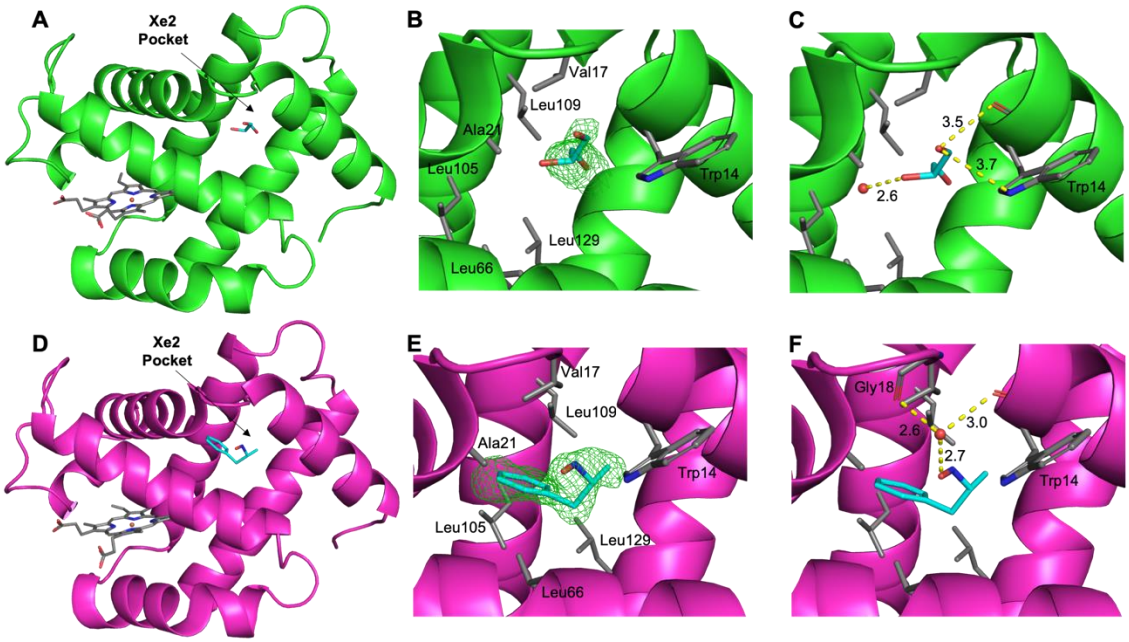

Figure 2.51. The crystal structure of the α1 subunit (A-C) and α2 subunit (D-F) from the [α-$Fe^{III}(H_2O)$][β-Fe^{II}(AmphNO)] Hb derivative. (A) The α1 chain displaying glycerol in the Xe2 pocket, (B) the F_o-F_c omit map (contoured at 2 σ) and (C) the nearest interactions in the α1 Xe2 pocket. (D) The α2 chain displaying AmphNHOH in the Xe2 pocket, (E) the F_o-F_c omit map (contoured at 2 σ) and (F) the nearest interactions in the α2 Xe2 pocket.

2.4.7. SNO formation in the Hb products

S-nitrosation, namely the generation of S-nitrosothiols (SNOs) through the interaction of cysteines and NO, has been well-established as being important for the normal function of the human body.[91, 92] Additionally, abnormal levels of SNOs have been associated with diseases such as diabetes, arthritis, strokes and even cancer.[92, 93] Furthermore, NO's participation in vasodilation is thought to be supplemented by S-nitrosation of Hb, where this may provide an additional route by which NO is transported from the lungs to the veins and arteries.[94] S-nitrosation of proteins typically occurs at the site of exposed cysteine residues and there are a total of six cysteines per Hb tetramer, but only one that is accessible for S-nitrosation, namely the βCys93 residue.[95] Consistent with this, in the structures presented above, S-nitrosation of Hb occurred only at the βCys93 sites.

There are currently a total of 28 *S*-nitrosated protein structures that have been deposited in the PDB. Of those, only one is of an *S*-nitrosated heme protein, namely that of SNO-Mb from blackfin tuna.[96] A Hb-SNO structure was previously reported[87]; however, the structure was later reanalyzed and the "-SNO moiety" was determined to be the Cys-S-N$^{\bullet}$-O radical.[97] Presented in this work is the crystal structure of [α-$Fe^{III}(H_2O)$][β-$Fe^{III}(His)_2$-SNO]$_{\{PhNO\}}$ displaying the presence of a thionitroxide radical (Cys-S-NH-O$^{\bullet}$) at the βCys93 position (**Figure 2.14**) and of [α-Fe^{II}][β-Fe^{II}-SNO]$_{\{CAMNO\}}$ displaying the presence of both the *trans*-SNO and thionitroxide radical at the βCys93 position (**Figure 2.26**).

The mechanism by which NO is thought to be transported by Hb is linked with the allostery of the protein.[91] In the T-state, the βCys93 residue is surface exposed, making it

easily accessible for S-nitrosation to produce SNO-Hb. Upon oxygenation, Hb transitions from the T to the R-state which moves the βCys93 residue into an internal inaccessible position, protecting the NO from being released. Finally, deoxygenation of SNO-Hb causes the protein to transition from the R-state back to the T-state, exposing the βCys93 residue and allowing the NO to be transferred to another protein. In this work, I was able to obtain a crystal structure of SNO-Hb in both the T and R-states. Of the two structures obtained, $[\alpha\text{-}Fe^{II}][\beta\text{-}Fe^{II}\text{-}SNO]_{\{CAMNO\}}$ is in the T-state and $[\alpha\text{-}Fe^{III}(H_2O)][\beta\text{-}Fe^{III}(His)_2\text{-}SNO]_{\{PhNO\}}$ is in a modified R-state.

It is clear how βCys93 was nitrosated in the $[\alpha\text{-}Fe^{II}][\beta\text{-}Fe^{II}\text{-}SNO]_{\{CAMNO\}}$ structure since in the T-state, the βCys93 residue is solvent exposed. The reason $[\alpha\text{-}Fe^{II}][\beta\text{-}Fe^{II}\text{-}SNO]_{\{CAMNO\}}$ was in the T-state is because the reaction took place anaerobically. However, it is important to note that SNOs cannot generally form under anaerobic conditions.[98] This likely indicates the presence of traces of O_2 during this reaction, which assisted in the SNO formation. The $[\alpha\text{-}Fe^{III}(H_2O)][\beta\text{-}Fe^{III}(His)_2\text{-}SNO]_{\{PhNO\}}$ crystal structure resulted from an aerobic reaction which generally favors the R-state. In the typical R-state, βCys93 is an internal residue, but in our $[\alpha\text{-}Fe^{III}(H_2O)][\beta\text{-}Fe^{III}(His)_2\text{-}SNO]_{\{PhNO\}}$ structure, due to hemichrome formation (see Section 2.4.8), the βCys93 residue becomes solvent exposed, making it possible for S-nitrosation to take place.

This work also showed for the first time that both the biologically relevant compounds PhNHOH and CAMNO are both capable of nitrosating Hb at the βCys93 position.

2.4.8. Hemichrome formation

Hemichrome formation in physiology is significant, as hemichromes have been shown to lead to Heinz body formation in red blood cells leading to hemolysis and furthermore, hemolytic anemia.[99,100] Additionally, accumulation of hemichromes has been shown to contribute to thalassemias.[101] Typically in tetrameric Hb, hemichromes are only formed in either the α or the β chains, but not both.[77] In horse Hb, a hemichrome forms only in the α subunits[102] and in arctic fish Hb, a hemichrome forms only in the β subunits.[78] Consistent with this notion of a single subunit (α or β) hemichrome formation, the reaction of ferric adult human Hb^{III}-H_2O with PhNHOH (**Figure 2.23**) or *t*-BuNHOH (**Figure 2.32**) produced hemichrome derivatives only in the β subunits. Although Mb has a more rigid distal pocket than Hb,[74] hemichromes have in fact also been observed in Mb.[103] Observation of hemichromes only in the β chains of human tetrameric Hb is likely due to increased flexibility in the β chains of human Hb as compared to swMb and the α chains of human Hb. In general, there are two types of hemichromes, reversible (hemichrome I) and irreversible (hemichrome II). Without the addition of an exogenous ligand, over a period of seven months, human Hb only half converts to hemichrome I.[100] This indicates that the hemichromes formed under our relatively short time periods are not an artifact of normal Hb degradation, but that the hemichrome formation is in fact caused by the addition of the PhNHOH and *t*-BuNHOH reagents. Although the reaction of both PhNHOH and *t*-BuNHOH with human Hb resulted in β subunit hemichrome formation, there are only slight differences between the resulting structures (RMSD = 0.360 Å).

As shown in **Figure 2.44** ([α-$Fe^{III}(H_2O)$][β-$Fe^{III}(His)_2$-SNO]$_{\{PhNO\}}$) and **Figure 2.46** ([α-$Fe^{III}(H_2O)$][β-$Fe^{III}(His)_2$]$_{\{t\text{-BuNHOH}\}}$), the hemes in the β subunits of both structures

are laterally displaced out of the heme pockets, in addition to that observation of large movements in the proximal F helix (residues β85-100) regions, in order to accommodate hemichrome formation. The β-hemes in both structures have translated and rotated, ~4.4 – 4.5 Å (Fe_1-Fe_2) and 30°, respectively, out of the heme pocket resulting in bis-coordination of the Fe by both the distal and proximal His residues. A comparison of the β subunits of ferric Hb^{III}-H_2O, [α-$Fe^{III}(H_2O)$][β-$Fe^{III}(His)_2$-SNO]$_{\{PhNO\}}$ and [α-$Fe^{III}(H_2O)$][β-$Fe^{III}(His)_2$]$_{\{t\text{-BuNHOH}\}}$, is shown in **Figure 2.52**.

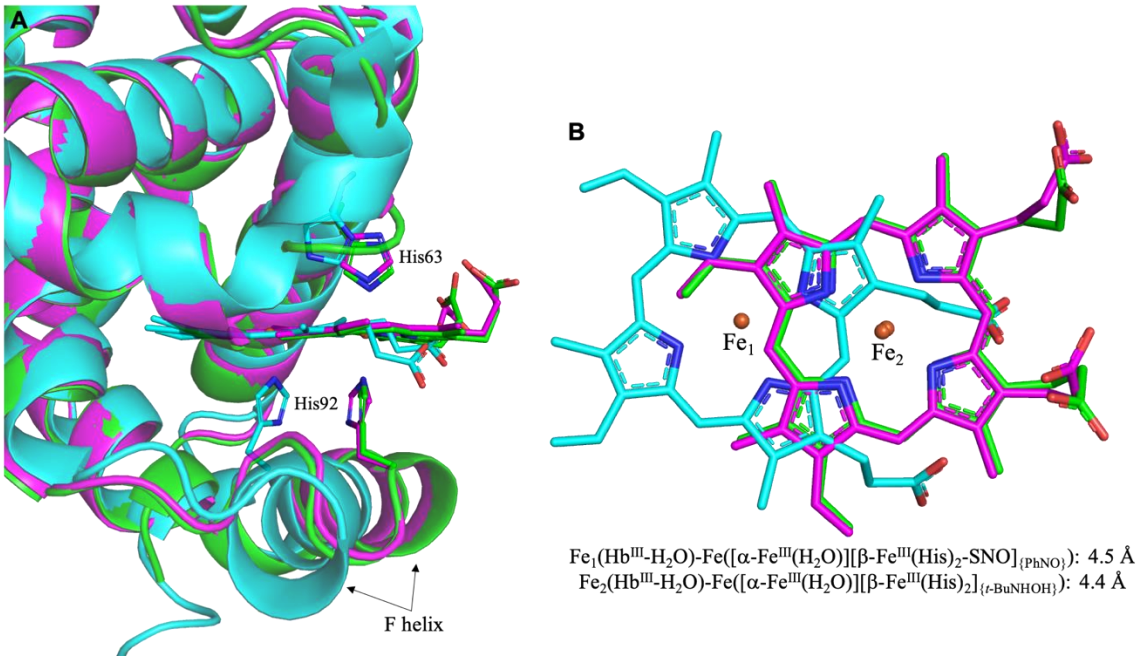

Figure 2.52. Overlay of the β1 active sites (A) and hemes (B) of ferric Hb^{III}-H_2O (cyan, PDB ID: 3P5Q), [α-$Fe^{III}(H_2O)$][β-$Fe^{III}(His)_2$-SNO]$_{\{PhNO\}}$ (green, this work) and [α-$Fe^{III}(H_2O)$][β-$Fe^{III}(His)_2$]$_{\{t\text{-BuNHOH}\}}$ (magenta, this work).

In order to determine the quaternary state of the full Hb tetramer, a comparison of the β2FG and α1C interface, referred to as the signature "switch" region, is made.[68] The comparison is made using representative X-ray crystal structures in the R (PDB id: 1AJ9),

RR3 (PDB id: 3D17), R3 (PDB id: 1YZI), RR2 (PDB id: 1MKO) and R2 (PDB id: 1BBB) conformations. The quaternary structures of both [α-$Fe^{III}(H_2O)$][β-$Fe^{III}(His)_2$-SNO]$_{\{PhNO\}}$ and [α-$Fe^{III}(H_2O)$][β-$Fe^{III}(His)_2$]$_{\{t\text{-}BuNHOH\}}$ appear to be closest to the R conformation. In the case of [α-$Fe^{III}(H_2O)$][β-$Fe^{III}(His)_2$-SNO]$_{\{PhNO\}}$, it has an RMSD of (i) 0.7 Å with the R conformation, (ii) 1.0 Å with both the RR3 and R3 conformations, and (iii) 1.2 and 1.7 Å with the RR2 and R2 conformations, respectively. For [α-$Fe^{III}(H_2O)$][β-$Fe^{III}(His)_2$]$_{\{t\text{-}BuNHOH\}}$, it has an RMSD of (i) 0.6 Å with the R conformation, (ii) 1.8 Å with the R2 conformation, (iii) 1.4 Å with the R3 conformation, (iv) 1.1 Å with the RR2 conformation, and (v) 0.8 Å with the RR3 conformation. Although the quaternary structures of both [α-$Fe^{III}(H_2O)$][β-$Fe^{III}(His)_2$-SNO]$_{\{PhNO\}}$ and [α-$Fe^{III}(H_2O)$][β-$Fe^{III}(His)_2$]$_{\{t\text{-}BuNHOH\}}$ are similar to the R conformation of Hb, there are significant localized structural differences, primarily in the β subunits as a result of the hemichrome formation. Due to movement of the respective F helices, the βHis97 residues in both [α-$Fe^{III}(H_2O)$][β-$Fe^{III}(His)_2$-SNO]$_{\{PhNO\}}$ and [α-$Fe^{III}(H_2O)$][β-$Fe^{III}(His)_2$]$_{\{t\text{-}BuNHOH\}}$ have moved out of their characteristic classical R-state positions between αThr38 and αThr41 (**Figure 2.53**).

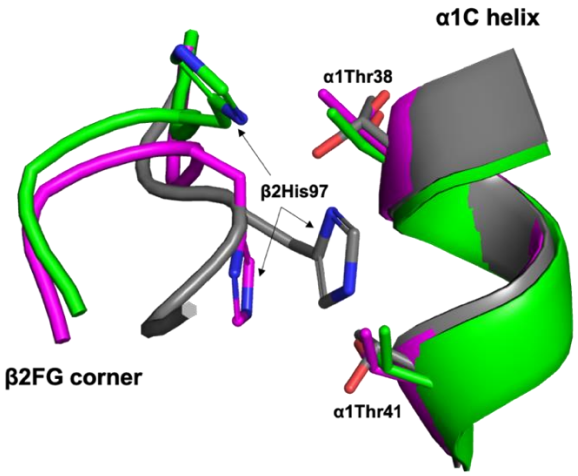

Figure 2.53. Comparison of the signature switch regions of [α-$Fe^{III}(H_2O)$][β-$Fe^{III}(His)_2$-SNO]$_{\{PhNO\}}$ (green, this work), [α-$Fe^{III}(H_2O)$][β-$Fe^{III}(His)_2$]$_{\{t\text{-BuNHOH}\}}$ (magenta, this work) and R-state Hb (grey, PDB id: 1AJ9).

The heme pocket is, in part, formed by the F-helix/FG-corner and C-helix/CD-corner/E-helix/EF-corner, and hemichrome formation caused large movements in these regions. Large backbone movements of the F-helix/FG-corner residues 85-100 occurred in both [α-$Fe^{III}(H_2O)$][β-$Fe^{III}(His)_2$-SNO]$_{\{PhNO\}}$ (1.5 – 6.8 Å) and [α-$Fe^{III}(H_2O)$][β-$Fe^{III}(His)_2$]$_{\{t\text{-BuNHOH}\}}$ (1.4 – 7.1 Å), causing unwinding of residues 93-96 in the F helices as shown in **Figure 2.54**. The surrounding heme environment comprised of residues 39-76 (C-helix/CD-corner/E-helix/EF-corner) also show significant positional differences between the structures (~1-1.5 Å; **Figure 2.55**). Residues 41-46 of the CD-corner, and residues 59, 62, 63, 66, 67, 73-75 of the E-helix moved the most in [α-$Fe^{III}(H_2O)$][β-$Fe^{III}(His)_2$-SNO]$_{\{PhNO\}}$, whereas residues 41-43 and 46 of the CD-corner, and residues 59, 62, 63, 66, 74 and 75 of the E-helix moved the most in [α-$Fe^{III}(H_2O)$][β-$Fe^{III}(His)_2$]$_{\{t\text{-BuNHOH}\}}$.

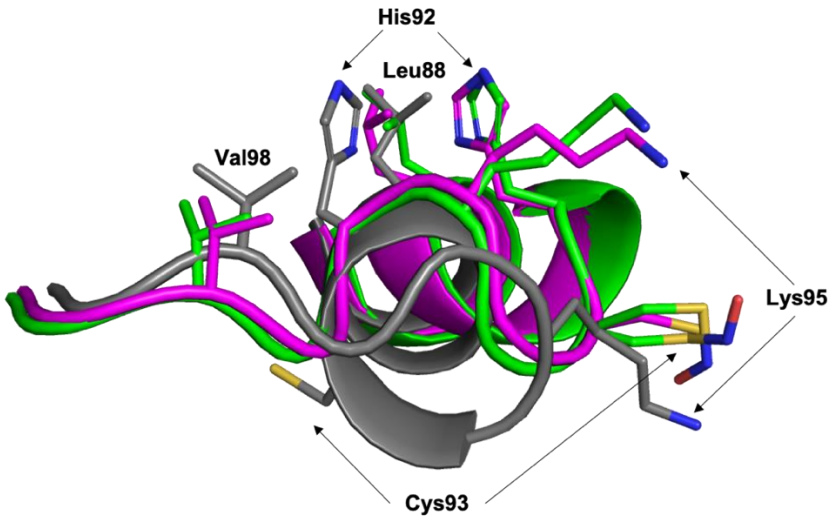

Figure 2.54. Comparison of the F-helix region (residues 85-100) of [α-$Fe^{III}(H_2O)$][β-$Fe^{III}(His)_2$-SNO]$_{\{PhNO\}}$ (green, this work), [α-$Fe^{III}(H_2O)$][β-$Fe^{III}(His)_2$]$_{\{t\text{-}BuNHOH\}}$ (magenta, this work) and R-state Hb (grey, PDB id: 1AJ9).

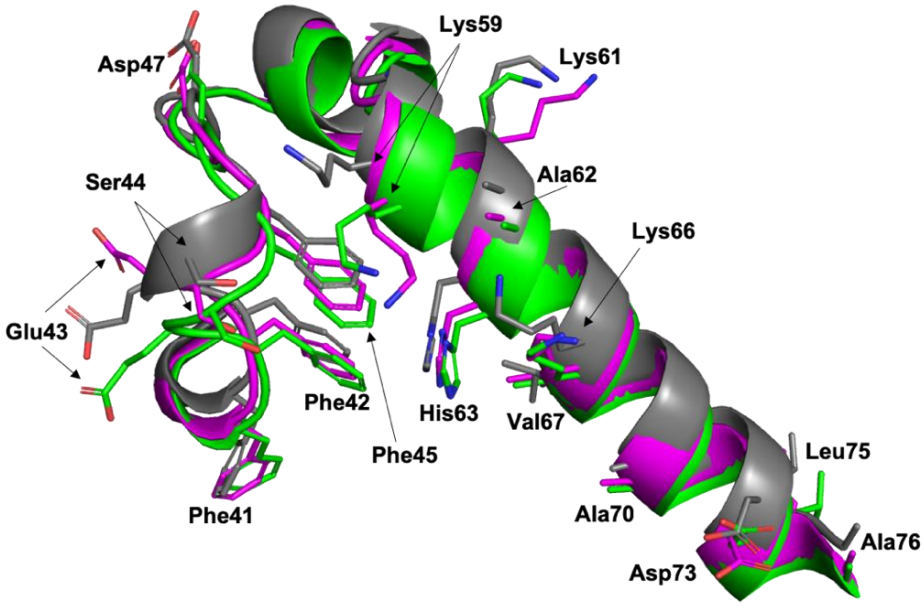

Figure 2.55. Comparison of the C-helix/CD-corner/E-helix/EF-corner (residues 39-76) of [α-$Fe^{III}(H_2O)$][β-$Fe^{III}(His)_2$-SNO]$_{\{PhNO\}}$ (green, this work), [α-$Fe^{III}(H_2O)$][β-$Fe^{III}(His)_2$]$_{\{t\text{-}BuNHOH\}}$ (magenta, this work) and R-state Hb (grey, PDB id: 1AJ9).

In summary, the reaction of PhNHOH and *t*-BuNHOH with Hb resulted in hemichrome formation in the β subunits. Hemichrome formation caused movement of the heme and secondary structures that make up the heme pocket and resulted in a modified R-state structure. More importantly, this movement of the heme out of its natural position within the pocket displays an early stage of heme loss, which eventually can lead to disease states such as anemia.

2.5 Conclusions

Presented in this chapter are the reactions of both Mb and Hb with nitro- and hydroxylamine-containing compounds. The reactions through both the oxidative and reductive pathways were predicted to result in heme-nitroso complexes, and although some did in fact result in heme-nitroso complexes in solution, a variety of other structural features resulted as well which was captured in their X-ray crystal structures, including Xe pocket adducts, S-nitrosation and hemichrome formation.

It was shown that the interaction of ferric H64V swMb^{III} and nitrite results in an N-bound ligand, matching that of the reported ferric H64V hhMb^{III}-nitrite structure. The interactions of wt and mutant ferric swMb^{III}-H_2O with CAM and Mtz stressed the importance of H-bonding contributed by a distal residue, typically His64, to generate ferrous Mb^{II}-nitroso adducts. In the case of CAM, this required a more flexible Gln residue at position 64. Additionally, the reaction between ferric H64Q swMb^{III}-H_2O and Mtz produced an *O*-bound acetamide derivative following the ring cleavage of Mtz.

The X-ray crystal structure of the product of the reaction between AmphNHOH and ferric Hb^{III}-H_2O presented in this paper is the first to demonstrate the ability of Hb to accommodate bulky ligands in its active site. We have shown the importance of the movement of the E-helix in the β subunit of Hb, which creates the necessary space for AmphNO to bind at the Fe-center. Additionally, we have shown the presence of a ligand in the Hb α subunit Xe2 sites. Furthermore, the UV-vis spectroscopy results presented here, in combination with our previously published ferrous H64A Mb^{II}-AmphNO X-ray crystal structure[43], provide strong evidence allowing us to infer what the three-dimensional structures of wt, H64Q and H64V Mb^{II}-AmphNO products would look like. Our data

shows that without a large distal residue such as His at the entry of the active site (e.g., in H64A Mb), no movement of the E-helix is necessary for AmphNO to enter the pocket and bind at the Fe-center. Our studies have shown that bulky ligands can in fact bind to the Fe-center of both Hb and Mb, potentially inhibiting the binding of O_2, leading to some disease states. This raises the question if our observations are limited to AmphNO or if other bulky ligands are also capable of binding at the Fe-center of Hb and/or Mb.

The X-ray crystal structures of ferrous wt Mb^{II}-PhNO and [α-$Fe^{III}(H_2O)$][β-$Fe^{III}(His)_2$-SNO]$_{\{PhNO\}}$ provide the first crystallographic evidence that the oxidation of PhNHOH to PhNO results in binding to Mb and induces large structural changes in Hb. In the case of Mb, PhNO binds to the Fe center, an interaction that likely inhibits the normal oxygen binding ability of Mb. Additionally, in the case of Hb, PhNHOH/PhNO caused the formation of a hemichrome in the β subunits, representing the earliest stages of Hb damage through heme loss. Formation of a hemichrome was also observed in the reaction of Hb with *t*-BuNHOH. The loss of hemes will likely lead to downstream disease states such as anemia. More importantly, the [α-$Fe^{III}(H_2O)$][β-$Fe^{III}(His)_2$-SNO]$_{\{PhNO\}}$ and [α-Fe^{II}][β-Fe^{II}-SNO]$_{\{CAMNO\}}$ structures showed that PhNO and CAMNO are capable of nitrosating the βCys93 of Hb, a result not previously anticipated.

This large body of work presented in this chapter provides hard-to-obtain structural evidence for the wide range of products that can result from the reaction of Mb and Hb with nitro- and hydroxylamine-containing compounds.

2.6 References

[1] Lee, J., Chen, L., West, A. H., and Richter-Addo, G. B. (2002) Interactions of organic nitroso compounds with metals, *Chem Rev 102*, 1019-1066.

[2] Eyer, P., and Ascherl, M. (1987) Reactions of para-substituted nitrosobenzenes with human hemoglobin, *Biol Chem Hoppe Seyler 368*, 285-294.

[3] Antonini, E., and Brunori, M. (1971) Hemoglobin and Myoglobin in Their Reactions with Ligands, In *Frontiers in Biology*, North-Holland, Amsterdam.

[4] Wang, B., Shi, Y., Tejero, J., Powell, S. M., Thomas, L. M., Gladwin, M. T., Shiva, S., Zhang, Y., and Richter-Addo, G. B. (2018) Nitrosyl myoglobins and their nitrite precursors: Crystal structural and quantum mechanics and molecular mechanics theoretical investigations of preferred Fe–NO Ligand orientations in myoglobin distal pockets, *Biochemistry 57*, 4788-4802.

[5] Yi, J., Heinecke, J., Tan, H., Ford, P. C., and Richter-Addo, G. B. (2009) The distal pocket histidine residue in horse heart myoglobin directs the *O*-binding mode of nitrite to the heme iron, *J Am Chem Soc 131*, 18119-18128.

[6] Quillin, M. L., Arduini, R. M., Olson, J. S., and Phillips, G. N. (1993) High-resolution crystal structures of distal histidine mutants of sperm whale myoglobin, *J Mol Biol 234*, 140-155.

[7] Conti, E., Moser, C., Rizzi, M., Mattevi, A., Lionetti, C., Coda, A., Ascenzi, P., Brunori, M., and Bolognesi, M. (1993) X-ray crystal structure of ferric *Aplysia limacina* myoglobin in different liganded states, *J Mol Biol 233*, 498-508.

[8] Suzuki, T. (1986) Amino acid sequence of myoglobin from the mollusc *Dolabella auricularia*, *J Biol Chem 261*, 3692-3699.

[9] Suzuki, T., and Furukohri, T. (1990) Amino acid sequence of myoglobin from the mollusc *Bursatella leachii*, *J Protein Chem 9*, 69-73.

[10] Blaxter, M. L., Ingram, L., and Tweedie, S. (1994) Sequence, expression and evolution of the globins of the parasitic nematode *Nippostrongylus brasiliensis*, *Mol Biochem Parasitol 68*, 1-14.

[11] Romero-Herrera, A. E., Goodman, M., Dene, H., Bartnicki, D. E., and Mizukami, H. (1981) An exceptional amino acid replacement on the distal side of the iron atom in Proboscidean myoglobin, *J Mol Evol 17*, 140-147.

[12] Tada, T., Watanabe, Y.-h., Matsuoka, A., Ikeda-Saito, M., Imai, K., Ni-hei, Y., and Shikama, K. (1998) African elephant myoglobin with an unusual autoxidation behavior: Comparison with the H64Q mutant of sperm whale myoglobin, *Biochim Biophys Acta 1387*, 165-176.

[13] Blaxter, M. L., Vanfleteren, J. R., Xia, J., and Moens, L. (1994) Structural characterization of an *Ascaris* myoglobin, *J Biol Chem 269*, 30181-30186.

[14] Kloek, A. P., Sherman, D. R., and Goldberg, D. E. (1993) Novel gene structure and evolutionary context of *Caenorhabditis elegans* globin, *Gene 129*, 215-221.

[15] Fisher, W. K., Koureas, D. D., and Thompson, E. O. P. (1980) Myoglobins of cartilaginous fishes. 2. Isolation and amino acid sequence of myoglobin of the shark *Mustelus-Antarcticus*, *Aust J Biol 33*, 277-294.

[16] Fisher, W. K., Koureas, D. D., and Thompson, E. O. P. (1981) Myoglobins of cartilaginous fishes. 3. Amino acid sequence of myoglobin of the shark *Galeorhinus-Australis*, *Aust J Biol 34*, 5-10.

[17] Suzuki, T., Suzuki, T., and Yata, T. (1985) Shark myoglobins. 2. Isolation, characterization and amino acid sequence of myoglobin from *Galeohinus-Japonicus*, *Aust J Biol 38*, 347-354.

[18] Møller, J. K. S., and Skibsted, L. H. (2002) Nitric oxide and myoglobins, *Chem Rev 102*, 1167-1178.

[19] Binkerd, E. F., and Kolari, O. E. (1975) The history and use of nitrate and nitrite in the curing of meat, *Fd Cosmet Toxicol 13*, 655-661.

[20] Haldane, J. (1901) The red colour of salted meat, *J Hyg 1*, 115-122.

[21] Maia, L. B., and Moura, J. J. G. (2014) How biology handles nitrite, *Chem Rev 114*, 5273-5357.

[22] Dejam, A., Hunter, C. J., Schechter, A. N., and Gladwin, M. T. (2004) Emerging role of nitrite in human biology, *Blood Cells Mol Dis 32*, 423-429.

[23] Gladwin, M. T., Grubina, R., and Doyle, M. P. (2009) The new chemical biology of nitrite reactions with hemoglobin: R-state catalysis, oxidative denitrosylation, and nitrite reductase/anhydrase, *Acc Chem Res 42*, 157-167.

[24] Helms, C. C., Liu, X., and Kim-Shapiro, D. B. (2016) Recent insights into nitrite signaling processes in blood, *Biol Chem*, 319-329.

[25] Halpert, J. (1981) Covalent modification of lysine during the suicide inactivation of rat liver cytochrome P-450 by chloramphenicol, *Biochem Pharmacol 30*, 875-881.

[26] Eyer, P., Lierheimer, E., and Schneller, M. (1984) Reactions of nitrosochloramphenicol in blood, *Biochem Pharmacol 33*, 2299-2308.

[27] Tsai, T.-H., and Chen, Y.-F. (2003) Pharmacokinetics of metronidazole in rat blood, brain and bile studied by microdialysis coupled to microbore liquid chromatography, *J Chromatogr A 987*, 277-282.

[28] Harrison, J. H., and Jollow, D. J. (1986) Role of aniline metabolites in aniline-induced hemolytic anemia, *J Pharmacol Exp Ther 238*, 1045-1054.

[29] Harrison, J. H., and Jollow, D. J. (1987) Contribution of aniline metabolites to aniline-induced methemoglobinemia, *Mol Pharmacol 32*, 423-431.

[30] Jenkins, F. P., Robinson, J. A., Gellatly, J. B. M., and Salmond, G. W. A. (1972) The no-effect dose of aniline in human subjects and a comparison of aniline toxicity in man and the rat, *Fd Cosmet Toxicol 10*, 671-679.

[31] Singh, H., Purnell, E., and Smith, C. (2007) Mechanistic study on aniline-induced erythrocyte toxicity, *Arh Hig Rada Toksikol 58*, 275-285.

[32] Khan, M. F., Green, S. M., Ansari, G. A. S., and Boor, P. J. (1998) Phenylhydroxylamine: Role in aniline-associated splenic oxidative stress and induction of subendocardial necrosis, *Toxicol Sci 42*, 64-71.

[33] O'Brien, P. J., Wong, W. C., Silva, J., and Khan, S. (1990) Toxicity of nitrobenzene compounds towards isolated hepatocytes: Dependence on reduction potential, *Xenobiotica 20*, 945-955.

[34] U.S. Department of Justice: Drug Enforcement Agency (2017) Drugs of Abuse: A DEA Resource Guide, https://www.dea.gov/sites/default/files/sites/getsmartaboutdrugs.com/files/publications/DoA_2017Ed_Updated_6.16.17.pdf.

[35] Li, L., Everhart, T., Jacob III, P., Jones, R., and Mendelson, J. (2010) Stereoselectivity in the human metabolism of methamphetamine, *Br J Clin Pharmacol 69*, 187-192.

[36] Franklin, M. R. (1974) Complexes of metabolites of amphetamines with hepatic cytochrome P-450, *Xenobiotica 4*, 133-142.

[37] Franklin, M. R. (1974) The formation of a 455 nm complex during cytochrome P-450-dependent *N*-hydroxyamphetamine metabolism, *Mol Pharmacol 10*, 975-985.

[38] Jonsson, J., and Lindeke, B. (1976) On the formation of cytochrome P-450 product complexes during the metabolism of phenylalkylamines, *Acta Pharm Suec 13*, 313-320.

[39] Mansuy, D., Rouer, E., Bacot, C., Gans, P., Chottard, J. C., and Leroux, J. P. (1978) Interaction of aliphatic N-hydroxylamines with microsomal cytochrome P450: Nature of the different derived complexes and inhibitory effects on monoxygenases activities, *Biochem Pharmacol 27*, 1229-1237.

[40] James, R. C., and Franklin, M. R. (1975) Comparisons of the formation of cytochrome P-450 complexes absorbing at 455 nm in rabbit and rat microsomes, *Biochem Pharmacol 24*, 835-838.

[41] Mansuy, D., Beaune, P., Chottard, J. C., Bartoli, J. F., and Gans, P. (1976) The nature of the "455 nm absorbing complex" formed during the cytochrome P450 dependent oxidative metabolism of amphetamine, *Biochem Pharmacol 25*, 609-612.

[42] Beckett, A. H., and Bélanger, P. M. (1975) Metabolic incorporation of oxygen into primary and secondary aliphatic amines and the consequences in carbon-nitrogen bond cleavage, *J Pharm Pharmacol 27*, 547-552.

[43] Wang, B., Powell, S. M., Guan, Y., Xu, N., Thomas, L. M., and Richter-Addo, G. B. (2017) Nitrosoamphetamine binding to myoglobin and hemoglobin: Crystal structure of the H64A myoglobin-nitrosoamphetamine adduct, *Nitric Oxide 67*, 26-29.

[44] Ricoux, R., Boucher, J.-L., Mansuy, D., and Mahy, J.-P. (2000) Formation of iron(II)–nitrosoalkane complexes: A new activity of microperoxidase 8, *Biochem Biophys Res Commun 278*, 217-223.

[45] Ricoux, R., Lukowska, E., Pezzotti, F., and Mahy, J.-P. (2004) New activities of a catalytic antibody with a peroxidase activity, *Eur J Biochem 271*, 1277-1283.

[46] Atamna, H., Paler-Martínez, A., and Ames, B. N. (2000) *N*-*t*-butyl hydroxylamine, a hydrolysis product of α-phenyl-*N*-*t*-butyl nitrone, is more potent in delaying senescence in human lung fibroblasts, *J Biol Chem 275*, 6741-6748.

[47] Gan, Y., Zhang, W., Huang, H., Xia, X., and Cheng, Y. (2006) Industrial synthesis of N-methylhydroxylamine hydrochloride by electrochemical reduction of nitromethane, *Chin J Chem Eng 14*, 649-653.

[48] Stolze, K., and Nohl, H. (1995) Reactions of reducing xenobiotics with oxymyoglobin. Formation of metmyoglobin, ferryl myoglobin and free radicals: An electron spin resonance and chemiluminescence study, *Biochem Pharmacol 49*, 1261-1267.

[49] Hirao, H., Thellamurege, N. M., Chuanprasit, P., and Xu, K. (2013) Importance of H-abstraction in the final step of nitrosoalkane formation in the mechanism-based inactivation of cytochrome P450 by amine-containing drugs, *Int J Mol Sci 14*, 24692.

[50] Taxak, N., Desai, P. V., Patel, B., Mohutsky, M., Klimkowski, V. J., Gombar, V., and Bharatam, P. V. (2012) Metabolic-intermediate complex formation with cytochrome

P450: Theoretical studies in elucidating the reaction pathway for the generation of reactive nitroso intermediate, *J Comput Chem 33*, 1740-1747.

[51] Springer, B. A., and Sligar, S. G. (1987) High-level expression of sperm whale myoglobin in *Escherichia coli*, *Proc Natl Acad Sci USA 84*, 8961-8965.

[52] Ikeda-Saito, M., Hori, H., Andersson, L. A., Prince, R. C., Pickering, I. J., George, G. N., Sanders, C. R., Lutz, R. S., McKelvey, E. J., and Mattera, R. (1992) Coordination structure of the ferric heme iron in engineered distal histidine myoglobin mutants, *J Biol Chem 267*, 22843-22852.

[53] Safo, M. K., and Abraham, D. J. (2003) X-ray crystallography of hemoglobins, *Methods Mol Med 82*, 1-19.

[54] Eyer, P., and Schneller, M. (1983) Reactions of the nitroso analogue of chloramphenicol with reduced glutathione, *Biochem Pharmacol 32*, 1029-1036.

[55] Corbett, M. D., and Chipko, B. R. (1978) Synthesis and antibiotic properties of chloramphenicol reduction products, *Antimicrob Agents Chemother 13*, 193-198.

[56] Mourad, M. S., Varma, R. S., and Kabalka, G. W. (1985) Reduction of alpha,beta-unsaturated nitro compounds with boron hydrides: A new route to N-substituted hydroxylamines, *J Org Chem 50*, 133-135.

[57] Phillips, G. N., Arduini, R. M., Springer, B. A., and Sligar, S. G. (1990) Crystal structure of myoglobin from a synthetic gene, *Proteins 7*, 358-365.

[58] Otwinowski, Z., and Minor, W. (1997) Processing of X-ray diffraction data collected in oscillation mode, *Methods Enzymol 276*, 307-326.

[59] Winn, M. D., Ballard, C. C., Cowtan, K. D., Dodson, E. J., Emsley, P., Evans, P. R., Keegan, R. M., Krissinel, E. B., Leslie, A. G. W., McCoy, A., McNicholas, S. J.,

Murshudov, G. N., Pannu, N. S., Potterton, E. A., Powell, H. R., Read, R. J., Vagin, A., and Wilson, K. S. (2011) Overview of the CCP4 suite and current developments, *Acta Cryst D67*, 235-242.

[60] McCoy, A. J., Grosse-Kunstleve, R. W., Adams, P. D., Winn, M. D., Storoni, L. C., and Read, R. J. (2007) Phaser crystallographic software, *J Appl Crystallogr 40*, 658-674.

[61] Murshudov, G. N., Vagin, A. A., and Dodson, E. J. (1997) Refinement of macromolecular structures by the maximum-likelihood method, *Acta Cryst D53*, 240-255.

[62] Emsley, P., and Cowtan, K. (2004) Coot: Model-building tools for molecular graphics, *Acta Cryst D60*, 2126-2132.

[63] Chen, V. B., Arendall, W. B., 3rd, Headd, J. J., Keedy, D. A., Immormino, R. M., Kapral, G. J., Murray, L. W., Richardson, J. S., and Richardson, D. C. (2010) MolProbity: all-atom structure validation for macromolecular crystallography, *Acta Cryst D66*, 12-21.

[64] Schrodinger, L. (2015) *The PyMOL Molecular Graphics System, Version 2.0*.

[65] Read, R. J., and Schierbeek, A. J. (1988) A phased translation function, *J Appl Crystallogr 21*, 490-495.

[66] Moriarty, N. W., Draizen, E. J., and Adams, P. D. (2017) An editor for the generation and customization of geometry restraints, *Acta Cryst D73*, 123-130.

[67] Moriarty, N. W., Grosse-Kunstleve, R. W., and Adams, P. D. (2009) Electronic ligand builder and optimization workbench (eLBOW): A tool for ligand coordinate and restraint generation, *Acta Cryst D65*, 1074-1080.

[68] Baldwin, J., and Chothia, C. (1979) Haemoglobin: The structural changes related to ligand binding and its allosteric mechanism, *J Mol Biol 129*, 175-220.

[69] Zhao, Y.-L., and Houk, K. N. (2006) Thionitroxides, RSNHO•: The structure of the SNO moiety in "S-Nitrosohemoglobin", a possible NO reservoir and transporter, *J Am Chem Soc 128*, 1422-1423.

[70] Bartberger, M. D., Houk, K. N., Powell, S. C., Mannion, J. D., Lo, K. Y., Stamler, J. S., and Toone, E. J. (2000) Theory, spectroscopy, and crystallographic analysis of S-nitrosothiols: Conformational distribution dictates spectroscopic behavior, *J Am Chem Soc 122*, 5889-5890.

[71] Yi, J., Coppens, P., Powell, D. R., and Richter-Addo, G. B. (2016) Linkage isomerization in nitrosothiols (RSNOs): The X-ray crystal structure of an S-nitrosocysteine and DFT analysis of its metastable MS1 and MS2 isomers, *Comments Inorg Chem 36*, 81-91.

[72] Perissinotti, L. L., Turjanski, A. G., Estrin, D. A., and Doctorovich, F. (2005) Transnitrosation of nitrosothiols: Characterization of an elusive intermediate, *J Am Chem Soc 127*, 486-487.

[73] Baciu, C., and Gauld, J. W. (2003) An assessment of theoretical methods for the calculation of accurate structures and SN bond dissociation energies of S-nitrosothiols (RSNOs), *J Phys Chem A 107*, 9946-9952.

[74] Rifkind, J. M., Abugo, O., Levy, A., and Heim, J. (1994) Detection, formation, and relevance of hemichromes and hemochromes, In *Methods in Enzymology*, pp 449-480, Academic Press.

[75] Winterbourn, C. C. (1990) Oxidative reactions of hemoglobin, In *Methods in Enzymology*, pp 265-272, Academic Press.

[76] Yi, J., Thomas, L. M., Musayev, F. N., Safo, M. K., and Richter-Addo, G. B. (2011) Crystallographic trapping of heme loss intermediates during the nitrite-induced degradation of human hemoglobin, *Biochemistry 50*, 8323-8332.

[77] Vergara, A., Verde, C., di Prisco, G., and Mazzarella, L. (2008) Bis-histidyl ferric adducts in tetrameric haemoglobins, In *Dioxygen Binding and Sensing Proteins: A Tribute to Beatrice and Jonathan Wittenberg* (Bolognesi, M., di Prisco, G., and Verde, C., Eds.), pp 93-105, Springer Milan, Milano.

[78] Vergara, A., Franzese, M., Merlino, A., Vitagliano, L., Verde, C., di Prisco, G., Caroline Lee, H., Peisach, J., and Mazzarella, L. (2007) Structural characterization of ferric hemoglobins from three antarctic fish species of the suborder *Notothenioidei*, *Biophys J 93*, 2822-2829.

[79] Mansuy, D., Chottard, J. C., and Chottard, G. (1977) Nitrosoalkanes as Fe(II) ligands in the hemoglobin and myoglobin complexes formed from nitroalkanes in reducing conditions, *Eur J Biochem 76*, 617-623.

[80] Vojtěchovský, J., Chu, K., Berendzen, J., Sweet, R. M., and Schlichting, I. (1999) Crystal structures of myoglobin-ligand complexes at near-atomic resolution, *Biophys J 77*, 2153-2174.

[81] Dingsdag, S. A., and Hunter, N. (2018) Metronidazole: An update on metabolism, structure–cytotoxicity and resistance mechanisms, *J Antimicrob Chemother 73*, 265-279.

[82] Xu, N., Guan, Y., Nguyen, N., Lingafelt, C., Powell, D. R., and Richter-Addo, G. B. (2019) Interactions of acetamide and acrylamide with heme models: Synthesis, infrared spectra, and solid state molecular structures of five- and six-coordinate ferric porphyrin derivatives, *J Inorg Biochem 194*, 160-169.

[83] Fermi, G., Perutz, M. F., Shaanan, B., and Fourme, R. (1984) The crystal structure of human deoxyhaemoglobin at 1.74 Å resolution, *J Mol Biol 175*, 159-174.

[84] Tilton, R. F., Kuntz, I. D., and Petsko, G. A. (1984) Cavities in proteins: Structure of a metmyoglobin xenon complex solved to 1.9 angstrom, *Biochemistry 23*, 2849-2857.

[85] Tetreau, C., Blouquit, Y., Novikov, E., Quiniou, E., and Lavalette, D. (2004) Competition with xenon elicits ligand migration and escape pathways in myoglobin, *Biophys J 86*, 435-447.

[86] Kuranova, I. P., Teplyakov, A. V., Obmolova, G. V., Voronova, A. A., Popov, A. N., Kheiker, D. M., and Arutyunyan, E. G. (1982) X-ray diffraction study of leghemoglobin in complexes with nitrosobenzene, nicotinic acid, and acetate, fluoride, and cyanide ions, *Bioorg Khim 8*, 1625-1636.

[87] Chan, N.-L., Rogers, P. H., and Arnone, A. (1998) Crystal structure of the S-nitroso form of liganded human hemoglobin, *Biochemistry 37*, 16459-16464.

[88] Yi, J., Ye, G., Thomas, L. M., and Richter-Addo, G. B. (2013) Degradation of human hemoglobin by organic C-nitroso compounds, *Chemical Communications 49*, 11179-11181.

[89] Savino, C., Miele, A. E., Draghi, F., Johnson, K. A., Sciara, G., Brunori, M., and Vallone, B. (2009) Pattern of cavities in globins: The case of human hemoglobin, *Biopolymers 91*, 1097-1107.

[90] Mouawad, L., Maréchal, J.-D., and Perahia, D. (2005) Internal cavities and ligand passageways in human hemoglobin characterized by molecular dynamics simulations, *Biochim Biophys Acta 1724*, 385-393.

[91] Singel, D. J., and Stamler, J. S. (2004) Chemical physiology of blood flow regulation by red blood cells: The role of nitric oxide and S-nitrosohemoglobin, *Annu Rev Physiol 67*, 99-145.

[92] Foster, M. W., McMahon, T. J., and Stamler, J. S. (2003) S-nitrosylation in health and disease, *Trends Mol Med 9*, 160-168.

[93] Lancaster, J. R. (2008) Protein cysteine thiol nitrosation: Maker or marker of reactive nitrogen species-induced nonerythroid cellular signaling?, *Nitric Oxide 19*, 68-72.

[94] Jia, L., Bonaventura, C., Bonaventura, J., and Stamler, J. S. (1996) S-nitrosohaemoglobin: A dynamic activity of blood involved in vascular control, *Nature 380*, 221.

[95] Reischl, E., Dafre, A. L., Franco, J. L., and Wilhelm Filho, D. (2007) Distribution, adaptation and physiological meaning of thiols from vertebrate hemoglobins, *Comp Biochem Physiol C Toxicol Pharmacol 146*, 22-53.

[96] Schreiter, E. R., Rodríguez, M. M., Weichsel, A., Montfort, W. R., and Bonaventura, J. (2007) S-nitrosylation-induced conformational change in blackfin tuna myoglobin, *J Biol Chem 282*, 19773-19780.

[97] Chan, N.-L., Kavanaugh, J. S., Rogers, P. H., and Arnone, A. (2004) Crystallographic analysis of the interaction of nitric oxide with quaternary-T human hemoglobin, *Biochemistry 43*, 118-132.

[98] Smith, B. C., and Marletta, M. A. (2012) Mechanisms of S-nitrosothiol formation and selectivity in nitric oxide signaling, *Curr Opin Chem Biol 16*, 498-506.

[99] Winterbourn, C. C., and Carrell, R. W. (1974) Studies of hemoglobin denaturation and heinz body formation in the unstable hemoglobins, *J Clin Invest 54*, 678-689.

[100] Blumberg, W. E., and Peisach, J. (1971) Low-spin compounds of heme proteins, *Bioinorg Chem 100*, 271-291.

[101] Ferru, E., Pantaleo, A., Mannu, F., Carta, F., and Turrini, F. (2010) May band 3 hyper-phosphorylation have a functional role in microcyte formation in heterozygous thalassemias?, *Blood Cells Mol Dis 45*, 65-66.

[102] Robinson, V. L., Smith, B. B., and Arnone, A. (2003) A pH-dependent aquomet-to-hemichrome transition in crystalline horse methemoglobin, *Biochemistry 42*, 10113-10125.

[103] Arnold, E. V., Bohle, D. S., and Jordan, P. A. (1999) Reversible and irreversible hemichrome generation by the oxygenation of nitrosylmyoglobin, *Biochemistry 38*, 4750-4756.

Chapter 3. *Clostridioides difficile* nitroreductase

3.1 Introduction

Clostridioides difficile (formerly *Clostridium difficile*) is an anaerobic bacterium that colonizes the lower intestinal tract in humans and other mammals. *C. difficile* infection (CDI) caused by pathogenic strains can result in diarrhea, severe colitis or even death.[1] Reported cases of CDI in the United States alone exceeded 250,000 with 14,000 deaths in 2013[2], with these numbers rising to ~500,000 with ~29,000 deaths in 2015.[3] CDI occurrences are not only increasing in the US, but across the globe with many cases seen in Canada, Europe, Asia, India and many other areas of the world.[4] Concerns about rising CDI have prompted the Centers for Disease Control (CDC) to label *C. difficile* as an urgent threat[2] and for the White House to declare the reduction of CDI occurences a top priority.[5] One of the reasons for the increase in CDI occurrence is the frequent use of antibiotics which creates an imbalance in the intestinal microflora and allows *C. difficile* to thrive and colonize the gut.[6] Another possible reason is the emergence of the NAP1/BI/027 family of *C. difficile* strains. As of 2009, this family accounted for ~61% of all clinical isolates.[7] R20291 is an epidemic and hypervirulent strain, part of the NAP1/B1/027 family, and was responsible for the Stokes Mandeville outbreaks in the United Kingdom in 2003 and 2004.[8]

---

*Reproduced in part from, with permission, from "Crystal structures of two nitroreductases from hypervirulent *Clostridium difficile* and functionally related interactions with the antibiotic metronidazole" B. Wang*, S.M. Powell*, N. Hessami, F.Z. Najar, L.M. Thomas, E.A. Karr, A.H. West, G.B. Richter-Addo. *Nitric Oxide.* **2016**, 60, 32-39 © Elsevier Inc.[11]

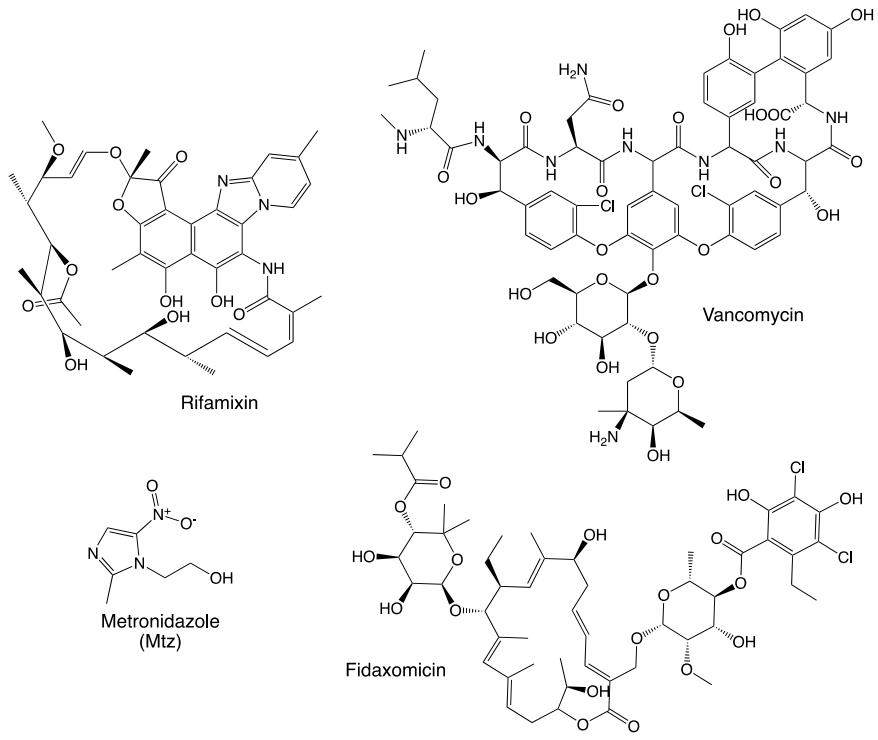

Figure 3.1. Some of the more commonly prescribed drugs for CDI treatment.

There are currently a variety of treatment options available for CDI (**Figure 3.1**). Metronidazole (Mtz) is a common and relatively low-cost nitro-containing drug prescribed for treatment of CDI.[9, 10] Vancomycin, a glycopeptide, is also commonly prescribed for CDI, however it is more often prescribed for severe and recurring cases of CDI.[12] Fidaxomicin is a narrow-spectrum antibiotic designed specifically for the treatment of CDI and has shown similar levels of efficacy as vancomycin, but has not yet been widely accepted as a treatment option.[13] Rifamixin is prescribed to complement vancomycin in cases of recurrent CDI.[12] Apart from antibiotics, fecal microbiota transplant (FMT) has recently become more accepted as a treatment option for CDI, however there are many unanswered questions regarding how to properly choose a donor or how to properly administer FMT, preventing FMT from becoming a widely accepted first-line treatment

option.[14] Despite the multitude of treatment options available for CDI treatment, Mtz remains the number one recommended treatment for CDI.[15]

Mtz typically functions as a prodrug and is metabolized by a class of nitroreductase (NR) enzymes to produce toxic metabolites that kill the pathogen. NRs are a family of FMN-dependent, NAD(P)H-linked proteins widely distributed in bacteria that typically exist as homodimers with protomers varying in size (23-30 kDa).[16] Unlike myoglobin and hemoglobin which require the use of a metal, NRs function via either a two-electron (Type I) or one-electron (Type II) reduction pathway based on their response to oxygen (**Figure 3.2**).

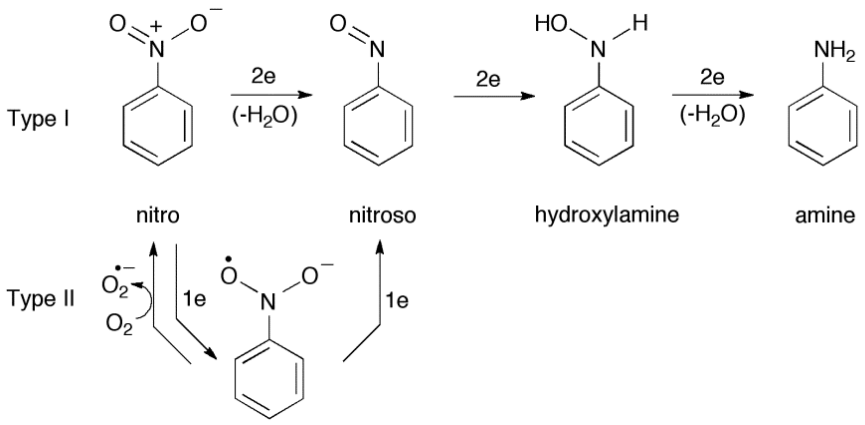

Figure 3.2. Reduction pathways of nitro compounds by Type I (air-insensitive) and Type II (air-sensitive) NRs.[16]

A rising concern is the emergence of Mtz-resistant *C. difficile* strains. There are many reports that cite the failure of treatments for CDI with Mtz[9, 17-20], however recent reports show an increased failure.[21] A mutation resulting in a truncation of a NR was found in both a resistant strain and a sensitive strain of *C. difficile* with reduced susceptibility to Mtz, implicating NRs in Mtz resistance.[22] Mtz resistance has been associated with NRs in

Bacterocides fragilis, the most-commonly found bacterium in clinical specimen,[23-25] and *Helicobacter pylori*, the bacteria responsible for stomach ulcers.[26, 27]

Interestingly, although NRs are thought to be the primary enzymes responsible for Mtz metabolism in *C. difficile*, no NRs from the hypervirulent R20291 strain had been characterized prior to our work in this area. Further, only three NR crystal structures from the less-virulent *C. difficile* 630 strain had been deposited in the Protein Data Bank (PDB; with PDB id: 3GFA, 3EO8, and 3H4O/3KOQ), but no manuscripts describing these structures have been published. Importantly, in addition to lack of structural information of any NR from the hypervirulent *C. difficile* R20291 strain, no functional assays for the reaction of nitro substrates (e.g., Mtz) with NR from any *C. difficile* strain had been reported.

In this work, I determined one of the first two X-ray crystal structures of a NR (CDR20291_0767; NR_0767) from the hypervirulent *C. difficile* R20291 strain. I also investigated the reaction of nitro-containing compounds (**see Mtz in Figure 3.1 and Figure 3.3**) with this NR, and the results confirm the functional role of these proteins in the reductive metabolism of nitro-drugs by NRs in *C. difficile*.

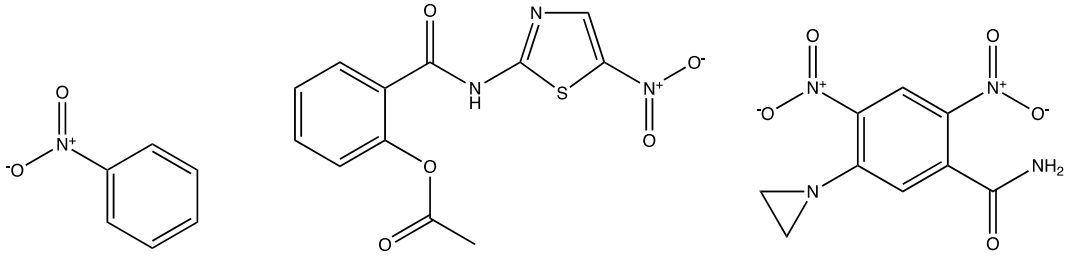

Figure 3.3. Structures of the nitro-containing compounds used in the NR redox-assay.

3.2 Material and Methods

3.2.1 Cloning

A putative NR gene (CDR20291_0767) was identified from the annotated genome sequence of hypervirulent *C. difficile* and confirmed by a BLAST search[28] against the conserved domain database.[29] The recombinant plasmid pSGC-0767 containing the NR gene was constructed by our collaborators at Albert Einstein College of Medicine (AECOM). The plasmid also contained an N-terminal 6-His tag extension to facilitate its purification.

3.2.2 Expression and purification

The plasmid pSGC-0767 was transformed into *E. coli* BL21 (DE3) competent cells. The NR (NR_0767) was expressed by autoinduction in ZY media supplemented with kanamycin (50 μg/mL), $MgSO_4$ (1 mM), glycerol (0.5% w/v), glucose (0.05% w/v), α-lactose (0.2% w/v), 100 μM vitamin B_{12}, and trace metals.[30] Autoinduction was performed at 37 °C for 5 h and then adjusted to 22 °C and left to incubate overnight.

Following centrifugation, the yellow cell pellets were harvested and transferred into a COY anaerobic chamber (3% H_2 in nitrogen). All purification procedures were performed in the anaerobic chamber. The collected cells were resuspended in binding buffer (50 mM Tris, 500 mM NaCl, 5 mM β-mercaptoethanol (βME), 20 mM imidazole, pH 8.0) that contained appropriate amounts of DNase, RNase and PMSF and then was sonicated on ice. After centrifugation, the supernatant was loaded onto a Ni-NTA affinity column (MCLAB) equilibrated with binding buffer. The column was then washed with wash buffer (binding buffer with 50 mM imidazole). The bound His-tagged protein was then eluted from the

column with elution buffer (binding buffer with 250-500 mM imidazole). Following Ni column elution, fractions containing the protein (as determined by SDS-PAGE) were combined.

The pooled protein was concentrated using an Amicon ultra filter with a cutoff of 10 kDa (Millipore). The concentrated sample was applied to a gel filtration Superdex 200 increase 10/300 GL column set up on an ÄKTA Pure system (GE Healthcare) inside a COY anaerobic chamber. The column was equilibrated with gel filtration buffer (50 mM Tris, pH 7, 150 mM NaCl, 1 mM EDTA and 2 mM β-ME at pH 8.0). The elution profile of the protein was recorded by monitoring the absorption at 280 nm using the ÄKTA. The molecular mass of NR_0767 was estimated against the elution profiles of the standard proteins; conalbumin (75 kDa), ovalbumin (44 kDa), carbonic anhydrase (29 kDa), and ribonuclease A (13.7 kDa). Fractions containing the pure NR, as judged by SDS-PAGE, were pooled and concentrated to 10 mg/mL. The protein concentration was determined using a Bradford Standard Assay.

Purification procedures were also performed in open air for comparison.

3.2.3 Redox assay of NR activity

Titration experiments for the reduction and re-oxidation of the FMN cofactors of NR_0767 were performed under anaerobic conditions as previously described.[31] All buffers were purged with nitrogen gas for at least 30 min prior to being moved into the anaerobic chamber. A sealable quartz cuvette (Starna cells) with a septum was used. After each titration, the cuvette was sealed, and the absorption spectra read using a Hewlett Packard 8453 spectrophotometer.

For the reaction between NR_0767 and Mtz, ~18 μM of NR in 3 mL of 50 mM Tris buffer at pH 8.0 was reduced by the addition of 7 sequential aliquots of 2 μL of a stock solution of 12.5 mM dithionite in buffer in order to obtain the spectrum of the reduced form. Re-oxidation of the NR was performed by first reducing the protein followed by the addition of 8 sequential aliquots of 1 μL of a stock solution of 20 mM Mtz in buffer.

A similar procedure was followed for the reaction of NR_0767 with other nitro-containing substrates: nitrobenzene (NB), CB-1954 and nitazoxanide (NTZ) (**Figure 3.3**). For the reaction of NR_0767 and NB, 1 μL of 500 mM NB was added to reduced NR (~18 μM in 2.5 mL buffer). For the reaction with CB-1954, 1 μL of 50 mM CB-1954 was added to reduced NR (~18 μM in 2.5 mL buffer). And for the reaction with NTZ, 1 μL of 50 mM NTZ was added to reduced NR (~18 μM in 2.5 mL buffer).

3.2.4 Crystallization

Broad-screen crystallization trials for NR were carried out with a Mosquito robot (TTP Labtech) in the University of Oklahoma Macromolecular Crystallography Laboratory (MCL). The sitting drop vapor diffusion method was used by mixing 300 nL of protein (4-14 mg/mL) with 300 nL of well solution to form the drop. Each crystallization well contained 60 μL of well solution. Crystallization was carried out in MRC 2 subwell plates (Swissci).

Two peaks resulted from gel-filtration; one colorless (corresponding to a dimer) and one yellow (corresponding to a protomer). Fractions corresponding to these peaks were pooled separately and separate drops were set for each set of fractions. Only the yellow pooled fractions yielded crystals. These yellow rod-shaped crystals (~400 mm in length) formed after three days in well B3 (0.2 M diammonium hydrogen citrate, 20% PEG 3350) of an MCSG2 (Microlytic Inc.) broad screen. The crystals were briefly dipped in a cryosolution made of the crystallization well solution plus 15% glycerol, then immediately mounted on the goniometer for X-ray data collection.

3.2.5 X-ray data collection, data processing, structure solution and refinement

X-ray diffraction data of NR was collected at our home source in the MCL using a Rigaku MicroMax 007HF microfocus X-ray generator equipped with a Dectris Pilatus 200 K silicon pixel detector.

The data was collected at 100 K with Cu Kα radiation (λ = 1.54178 Å) from the generator operated at the working condition 40kV/30 mA. The data were processed using HKL3000.[32] The structure factors were calculated using the CCP4 program suite.[33] The

three-dimensional structure of the full-length NR was solved by molecular replacement in PHASER (PHENIX) using a NR from *Parabacteroides distasonis* (PDB id: 3M5K) as a model.[34] All refinements were performed by phenix.refine. The model was rebuilt using COOT.[35] The MolProbity server was used for structure validation.[36]

The initial 10 cycles of restrained refinement were run with phenix.refine, and the R factor decreased from 0.29 to 0.25. Ligands and water were added to the model according to the F_o-F_c electron density maps in the subsequent refinement cycles. Two FMN cofactors and two imidazoles (based on the electron density map, and the fact that imidazole was in the Ni column elution buffer) were introduced into the model using phenix.ligandfit. A total of 311 water molecules were sequentially added using COOT. The first 7 N-terminal residues of both protomer 1 and 2 were omitted because of the lack of electron density. The final R factor and R_{free} are 0.18 and 0.23, respectively. The atomic coordinates and structure factors have been deposited in the PDB (PDB id: 5J6C).

3.3 Results

3.3.1 Protein characterization

The nitroreductase (CDR20291_0767; NR_0767) was expressed in high yield (~50 mg/L) in *E. coli*. The protein was obtained in high purity (>90%) as shown by SDS-PAGE. The protein band seen on the gel was just below the 25 kDa marker matching the calculated NR mass of 23 kDa (**Figure 3.4A**). The gel filtration profile displayed two peaks (**Figure 3.4B**). The first peak corresponds to the dimer, but the fractions were colorless due to the absence of the FMN cofactor. The second peak was yellow and corresponded to a monomer. The two sets were pooled separately for crystallization. Interestingly, the monomeric form that was present in solution resulted in a dimeric form after crystallization. Additionally, the dimeric form present in solution did not yield any crystal growth.

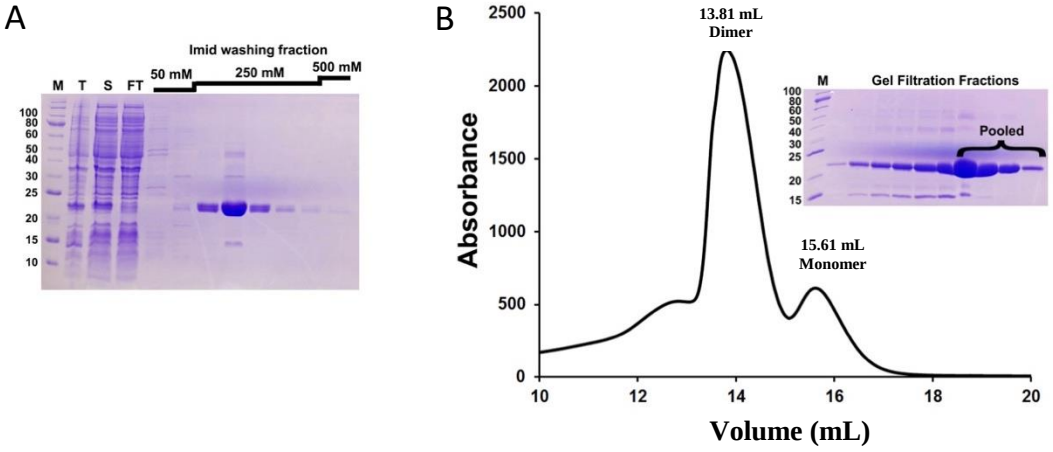

Figure 3.4. Purification of NR_0767 was performed in two steps – a Ni-NTA column followed by gel filtration. (A) The SDS-PAGE gel after the Ni column. (B) Gel filtration chromatograph and SDS-PAGE. The colorless fractions pooled for crystallography are indicated in the gel.

Initially, NR was purified anaerobically due to the anaerobic nature of *C. difficile*, but we determined that this protein can also be purified aerobically. Minimal differences were seen between the anaerobic and aerobic purifications (**Figure 3.5**). Crystallization of the protein was therefore carried out aerobically.

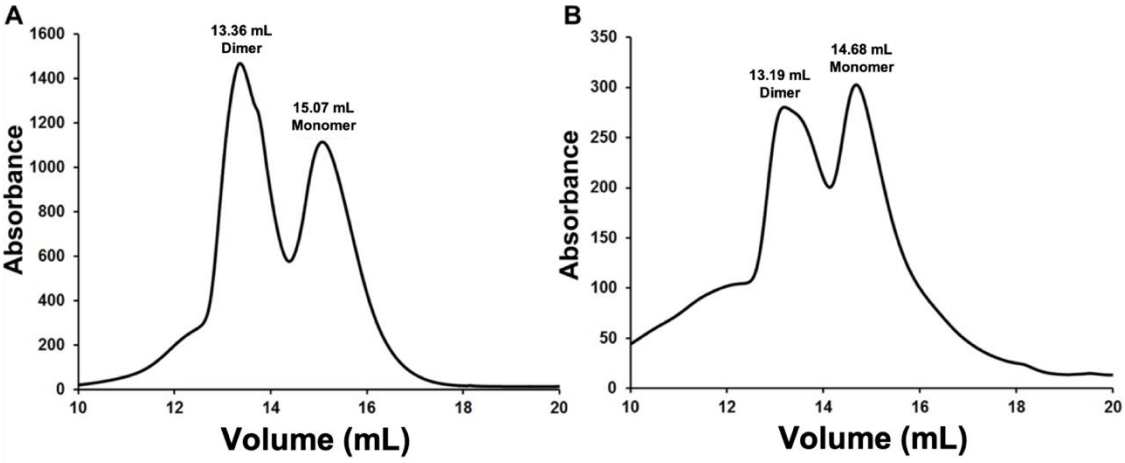

Figure 3.5. Size exclusion chromatograph of NR_0767 comparing outcomes of (A) aerobic and (B) anaerobic purification.

3.3.2 Reduction of nitro-drugs by NR

The NR was reduced anaerobically using dithionite, with a corresponding color change from yellow (oxidized FMN, left in Figure 3.6) to colorless (reduced FMN, right in Figure 3.6). Oxidized NR has a typical absorption spectrum of a flavoprotein with absorbance peaks at 370 nm and 450 nm.[37]

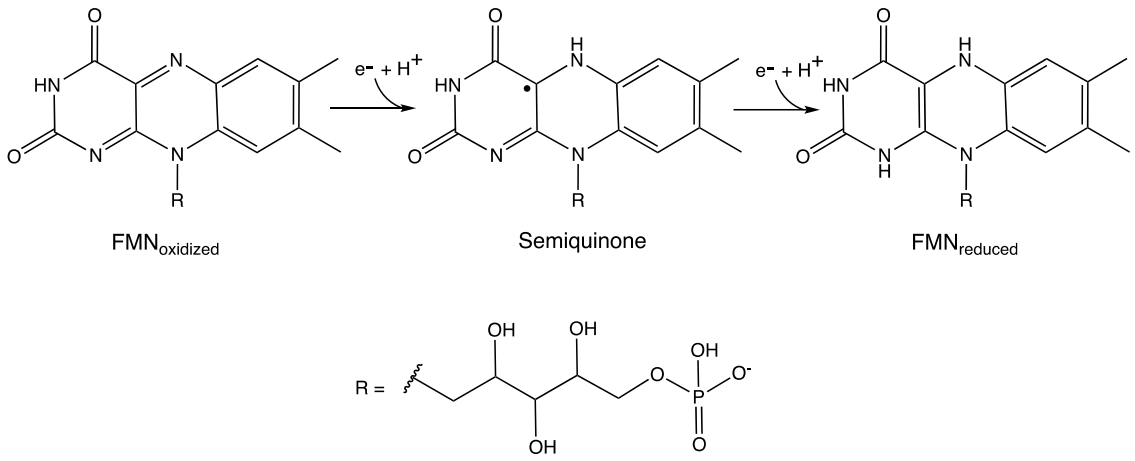

Figure 3.6. Oxidation state of the NR co-factor, flavin mononucleotide (FMN).

Upon dithionite addition, these peaks decreased in intensity (**Figure 3.7**). Reduced NRs are susceptible to reaction with oxygen, and even small amounts of air leaking into the cuvette will cause changes in the spectra due to re-oxidation of the reduced FMN.

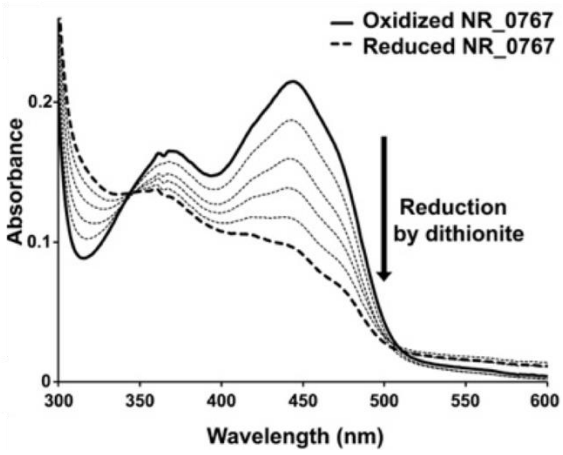

Figure 3.7. Reduction of NR showing absorbance changes of the oxidized FMN cofactor upon addition of dithionite. Conditions: 50 mM Tris buffer, pH 8, [NR] = 18 µM, each addition is 2 µL of 12.5 mM dithionite.

The reduced NR (in the absence of excess dithionite) was anaerobically re-oxidized by the addition of the nitro-containing drug (**Figure 3.8**), with a corresponding color change from colorless (reduced FMN) back to yellow (oxidized FMN). The absorbance at 450 nm increased as the reduced protein (lowest dashed line) became oxidized (top thick line).

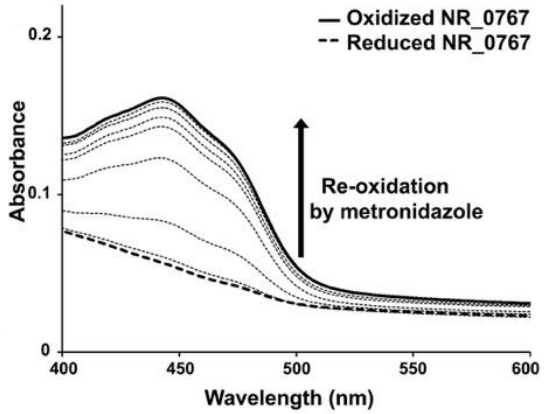

Figure 3.8. Re-oxidation of NR by Mtz, showing the increase in intensity of the peak due to oxidized NR. Conditions: 50 mM Tris buffer, pH 8, [NR] = 18 µM, each addition is 1 µL of 20 mM Mtz.

The same redox assay was performed using three other nitro-containing compounds to further establish the nitroreduction capability of this protein (**Figure 3.9**). NB is a simple nitro-containing compound, CB-1954 is an anticancer drug, and NTZ is an antiviral drug. In all three cases, after the addition of the nitro-substrate, a return of the peak at 450 nm was observed. These results show that NR_0767's ability to reduce nitro-containing substrates is not unique to Mtz and further confirms its identity as a NR protein.

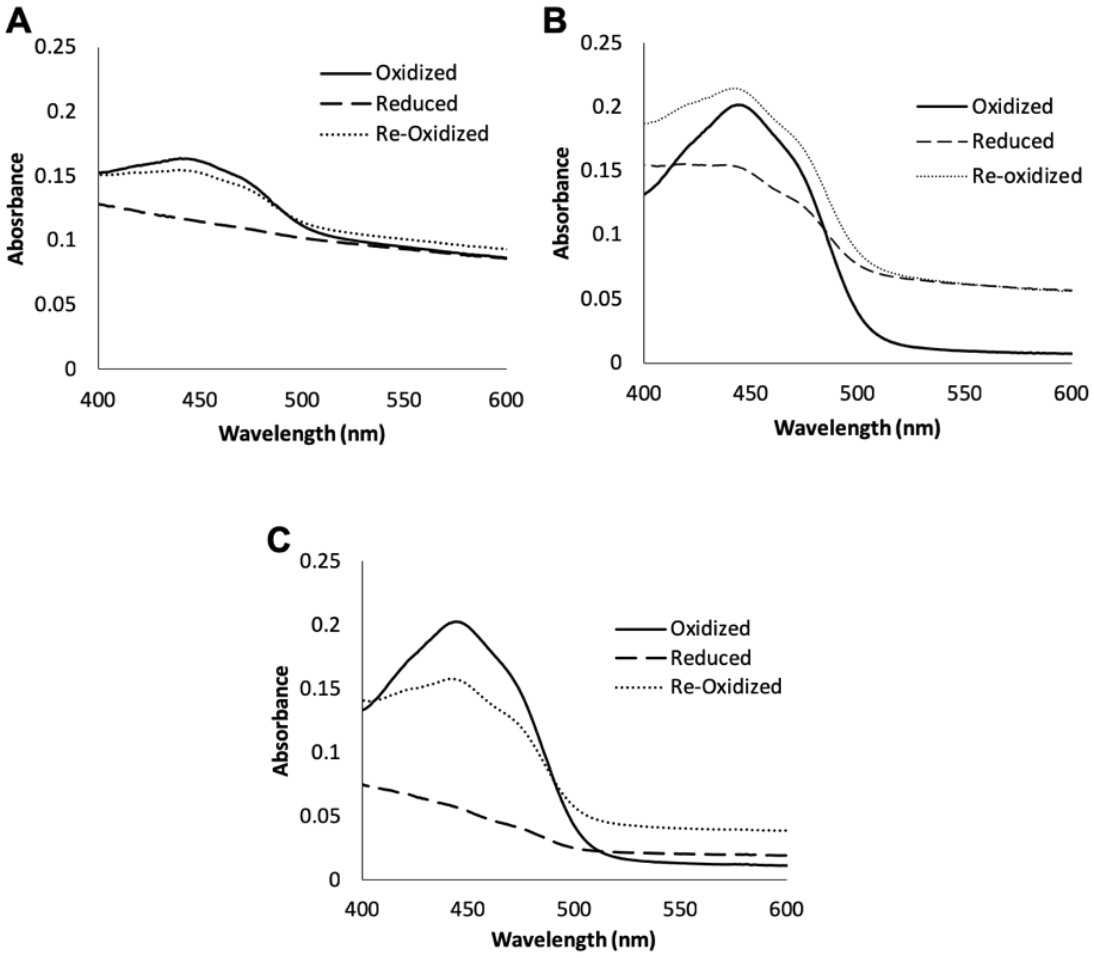

Figure 3.9. Re-oxidation of NR_0767 by NB (A), CB-1954 (B) and NTZ (C) showing the increase in intensity of the peak due to oxidized NR. Conditions: 50 mM Tris buffer pH 8, [NR] = 18 µM; reduced spectrum is after addition of 2 µL of 12.5 mM dithionite; oxidized spectrum is after addition of 2 µL of 500 mM NB (A), 1 µL of 50 mM CB-1954 (B), and 1 µL of 50 mM NTZ (C).

Having purified this NR from the hypervirulent *C. difficile* strain and having established its NR activity, we then proceeded to crystallize and determine its three-dimensional structure by X-ray crystallography.

3.3.3 Overall structure of NR from hypervirulent C. difficile R20291

After three days, yellow rod-shaped crystals (~450 mm in length) formed in well B3 (0.2 M diammonium hydrogen citrate, 20% PEG 3350) of an MCSG2 (Microlytic Inc.) broad screen. **Figure 3.10** shows the crystal used for data collection.

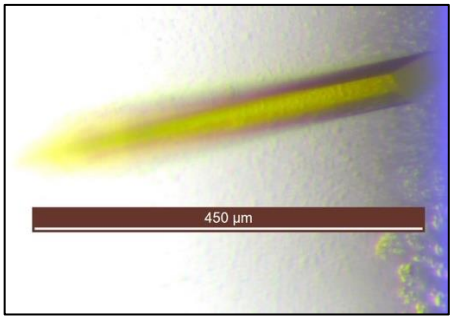

Figure 3.10. Crystal of NR_0767 used for X-ray data collection.

The structure of NR was solved to 2.1 Å resolution and represents one of the first two NR crystal structures from the hypervirulent *C. difficile* R20291 strain. The second structure, NR_0684, was obtained by my lab colleague Dr. Bing Wang. Data collection and refinement statistics are shown in **Table 3-1**. Including the N-terminal 6-His tag and the 16 extra linker residues, the cloned NR has a total of 201 amino acids per protomer. As mentioned in the experimental section 3.2.5, the first seven N-terminal residues of both protomer 1 and 2 were omitted due to lack of electron density.

Table 3-1. Data Collection and refinement statistics

	NR_0767
PDB ID	5J6C
Data collection[a]	MicroMax 007HF
Space group	$P2_12_12$
Wavelength (Å)	1.54
Cell dimensions (Å)	67.91, 70.73, 87.88
Resolution (Å)	50.00 – 2.10
$I/\sigma[I]$	12.64 (2.18)
No. of reflections	
Observed	86479
Unique	25340 (1260)
Multiplicity	3.4 (3.1)
Completeness (%)	99.3 (99.4)
R_{merge}[b]	0.109 (0.454)
$CC_{1/2}$	0.814
Refinement statistics	
No. of protein atoms	2898
R factor[c]	0.18
R_{free}[d]	0.23
RMSD Bond length (Å)	0.007
RMSD Bond angles (°)	0.906
Overall Mean B Factor (Å^3)	25.42
Ramachandran plot (%)[e]	
most favored residues	98.3
outliers	0.00

(a) Values in parentheses correspond to the highest resolution shells. (b) $R_{merge} = \Sigma|I-\langle I\rangle|/\Sigma(I)$, where I is the individual intensity observation and $\langle I\rangle$ is the mean of all measurements of I. (c) $R = \Sigma||F_o|-|F_c||/\Sigma|F_o|$, where F_o and F_c are the observed and calculated structural factors, respectively. (d) R_{free} was calculated by using 5% of the randomly selected diffraction data which were excluded from the refinement. (e) As calculated using *MOLPROBITY*.

The crystal structure revealed that the NR is a homodimer (**Figure 3.11**) with each protomer binding one equivalent of FMN. The NR adopts the classic NR α+β fold[31, 38] within each protomer, with the FMN cofactors located near the interface of the protomers.

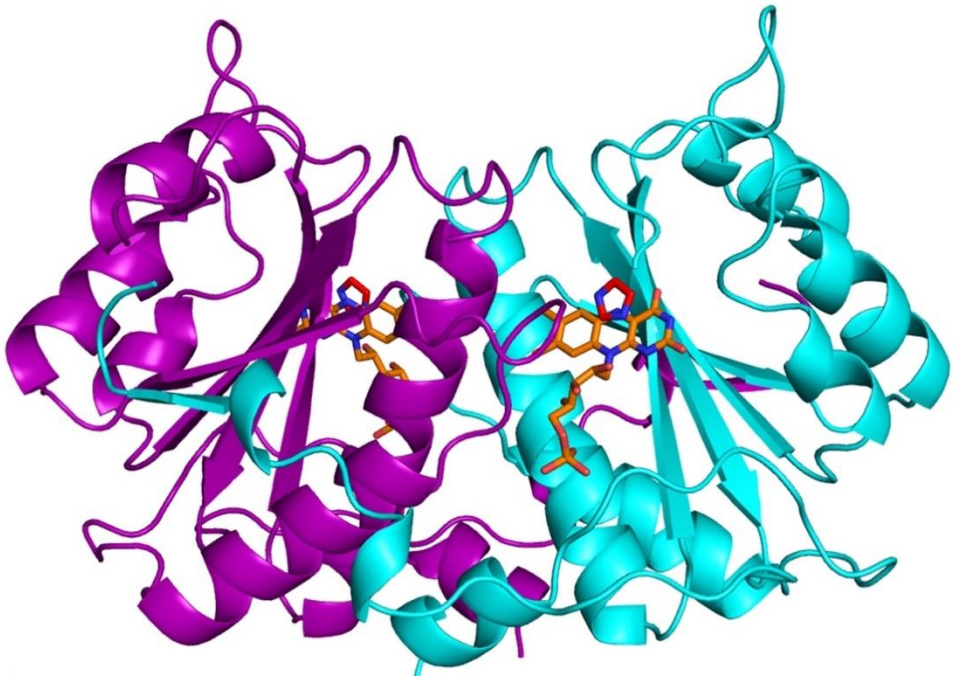

Figure 3.11. Overall structure of NR _0767. Protomer 1 is drawn in purple, protomer 2 is drawn in cyan, FMN in orange and imidazole in red.

Each protomer consists of a β-sheet in the central core surrounded by α-helices (**Figure 3.12**). The five-strand β sheet (β5β1β2β4β3) arrangement is formed from four antiparallel β strands (β1β2β4β3) complemented by a fifth β strand (β5) from the partner protomer.

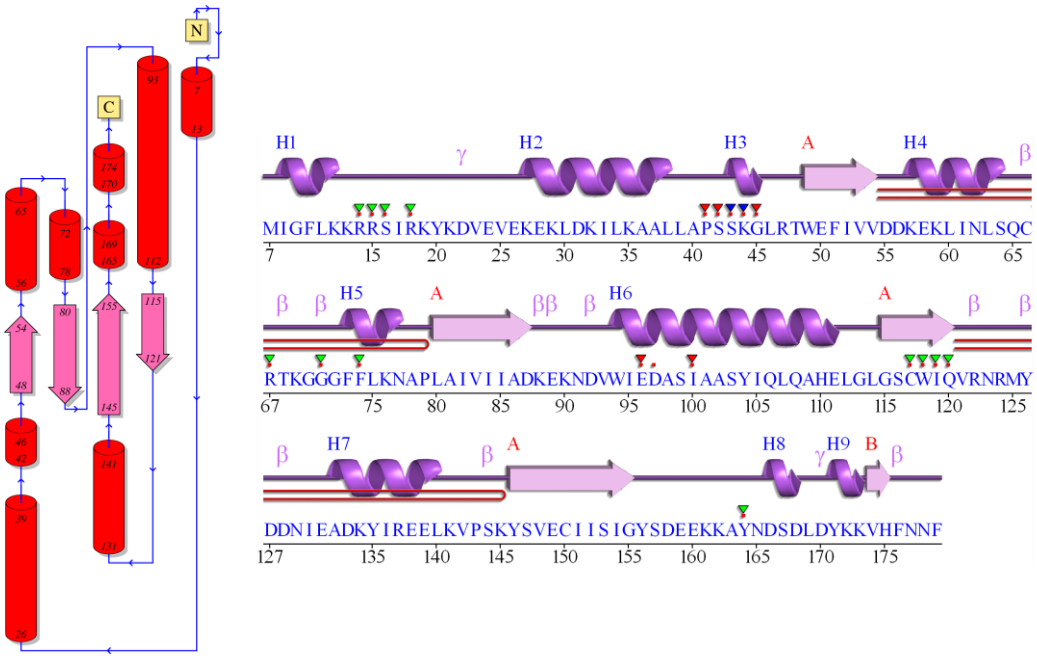

Figure 3.12. PDBsum display of the secondary structure of a single monomer of NR.[39]

A blastp search was used to identify homologs of NR_0767 using its amino acid sequence.[40] Twelve total homologs were found across *B. fragilis, G. metallireducens, D. hafniense, G. sulfurreducens, V. harveyi, B. subtilis, P. distasonis, M. smegmatis* and *P. gingivalis*. The resulting potential homologs all showed <30% sequence identity when compared to NRs from the hypervirulent *C. difficile* strain R20291. Similar results were also obtained from 3D structural comparisons employing the Dali server.[41] The potential homologs are annotated as either NRs or NAD(P)H:FMN oxidoreductases. Most of the homologs have a very similar overall protein fold (avg. RMSD 1.5-2.8 Å and Z score 21-15; calculated using the Dali server) as NR_0767 even with low sequence identities.

3.3.4 FMN and substrate binding sites

Each protomer contains an FMN cofactor located near the dimer interface (**Figure 3.11**). The FMN binding site is accessible to solvent and several water molecules are involved in the interactions with the FMN cofactors and the residues above and below the FMN. The FMN binding site in protomer 1 (**Figure 3.13A**) is stabilized primarily by residues from this protomer, with interactions from only one residue (S43) of protomer 2. The other FMN (**Figure 3.13B**) is stabilized primarily by residues from protomer 2, with interactions from three residues (S42, S43, and K44) of protomer 1. Each of the FMN sites accommodates an imidazole molecule (present in the purification buffers) above the isoalloxazine group through a π-π stacking interaction (centroid to centroid distance of 3.8-3.9 Å from the imidazole ring to the isoalloxazine group). In protomer 1, S43 interacts with the imidazole through a water network, but in protomer 2, S43 is directly involved in a H-bond between O_γ(S43) and N_3(imid). The observed interaction between S43 and imidazole implies a likely role for S43 in substrate stabilization.

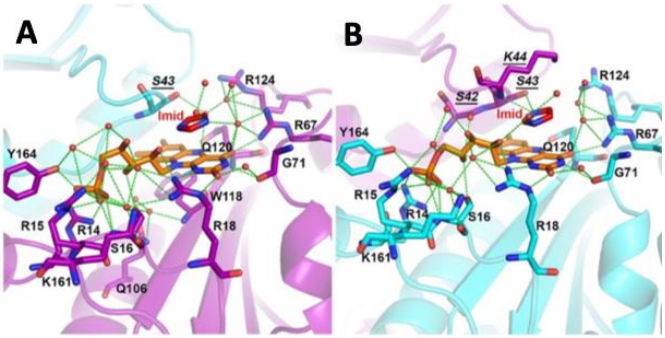

Figure 3.13. FMN binding sites of NR_0767, including the imidazoles in red. Protomer 1 (A) is drawn in purple, protomer 2 (B) is drawn in cyan, and FMN in orange. The underlined residues represent those from the partner protomers in these homodimeric structures.

3.4 Discussion

3.4.1 Type I vs. type II NR

The ability to aerobically purify NR_0767 allowed us to initially hypothesize that this NR functions as a Type I (oxygen insensitive) NR. The UV-vis spectral results of reduction and re-oxidation of the NR (**Figure 3.7**, **Figure 3.8, Figure 3.9**) display no absorbance at 600 nm that would have been indicative of a semiquinone state (**middle of** Figure 3.6) generated by one-electron reduction of the FMN cofactor.[37] This further supports our hypothesis that this NR functions as a Type I NR and follows a two-electron reduction pathway with nitro-containing species.

We are currently unsure of the identity of the primary organic product(s) resulting from the nitro-containing drug reduction by this *C. difficile* NR. Based on literature precedent,[42] we speculate that the nitro-drug is reduced to an initial nitroso derivative that readily converts under our experimental conditions to the bioactive hydroxylamine product. We are pursuing the isolation and identification of the primary and secondary products following the methods of Çelik, et al.[43], however our efforts using both GC-MS and LC-MS have been unsuccessful thus far.

3.4.2 Comparison of overall NR fold

The crystal structure of a second NR from *C. difficile* R20291 (CDR20291_0684; NR_0684) has also been solved in our lab by Dr. Bing Wang. Using a blastp search, NR_0767 and NR_0684 have 24% sequence identity over 186 amino acids.[40] Despite the low sequence identity, the overall folds of the two proteins are quite similar (**Figure 3.14**). The RMSD is 2.3 Å for protomer 1, and 2.9 Å for protomer 2. The core of the protomers and the dimer interface overlay quite well. The largest difference between the two structures is a result of the unique segment in NR_0684, which does not align with NR_0767 in either protomer 1 or 2. We are currently unsure of the importance of this unique structural feature.

Figure 3.14. Overlay of the X-ray crystal structures of NR_0684 (green) and NR_0767 (this work, purple).

3.4.3 Potential substrate binding site

Our NR_0767 structure shows a loop area (between α2 and β1) above the isoalloxazine ring of FMN; this loop area is also present in some other NRs.[38, 42, 44] S43 of NR_0767 (**underlined in Figure 3.13**) is located in this loop. This loop appears to play an important role in the interaction and stabilization of the imidazole. A structural comparison between our NR and an *E. coli* NR complex with bound nitrofurazone (PDB id: 1YKI)[42] showed that the position of the imidazole in NR_0767 overlaps with the semicarbazone "tail" of nitrofurazone in the *E. coli* NR (**Figure 3.15**). The comparison suggests that the position of the imidazole in our NR is a potential substrate binding site for Mtz when it reacts with NRs, since Mtz also contains an imidazole ring. Thus, the loop between α2 and β1 (residues 44-53) may play a significant role in accommodating substrates such as Mtz.

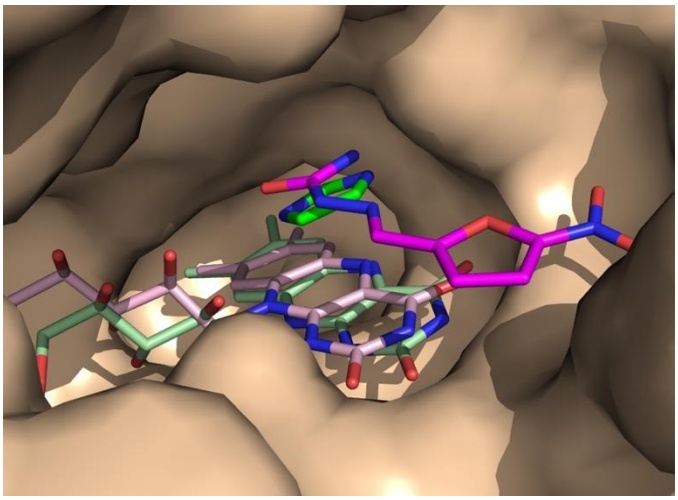

Figure 3.15. Superposition of the FMN binding sites of NR_0767 from *C. difficile* R20291 and a NR (PDB accession code 1YKI) from *E. coli*. The FMN and imidazole from NR_0767 are represented in light green and green, respectively. The FMN and nitrofurazone from the *E. coli* NR complex are represented in light magenta and magenta, respectively.

Sequence alignments (**Figure 3.16**) of the two *C. difficile* NRs shown above, with NRs from *H. pylori* and *E. coli* show that the two ends of this loop area are well conserved, leaving the center area of the loop variable. The variable region of this loop may help explain the differences in substrate binding specificity between NRs.

We are currently pursuing a co-crystal structure of NR_0767 with a nitro-containing drug. However, efforts thus far have been unsuccessful.

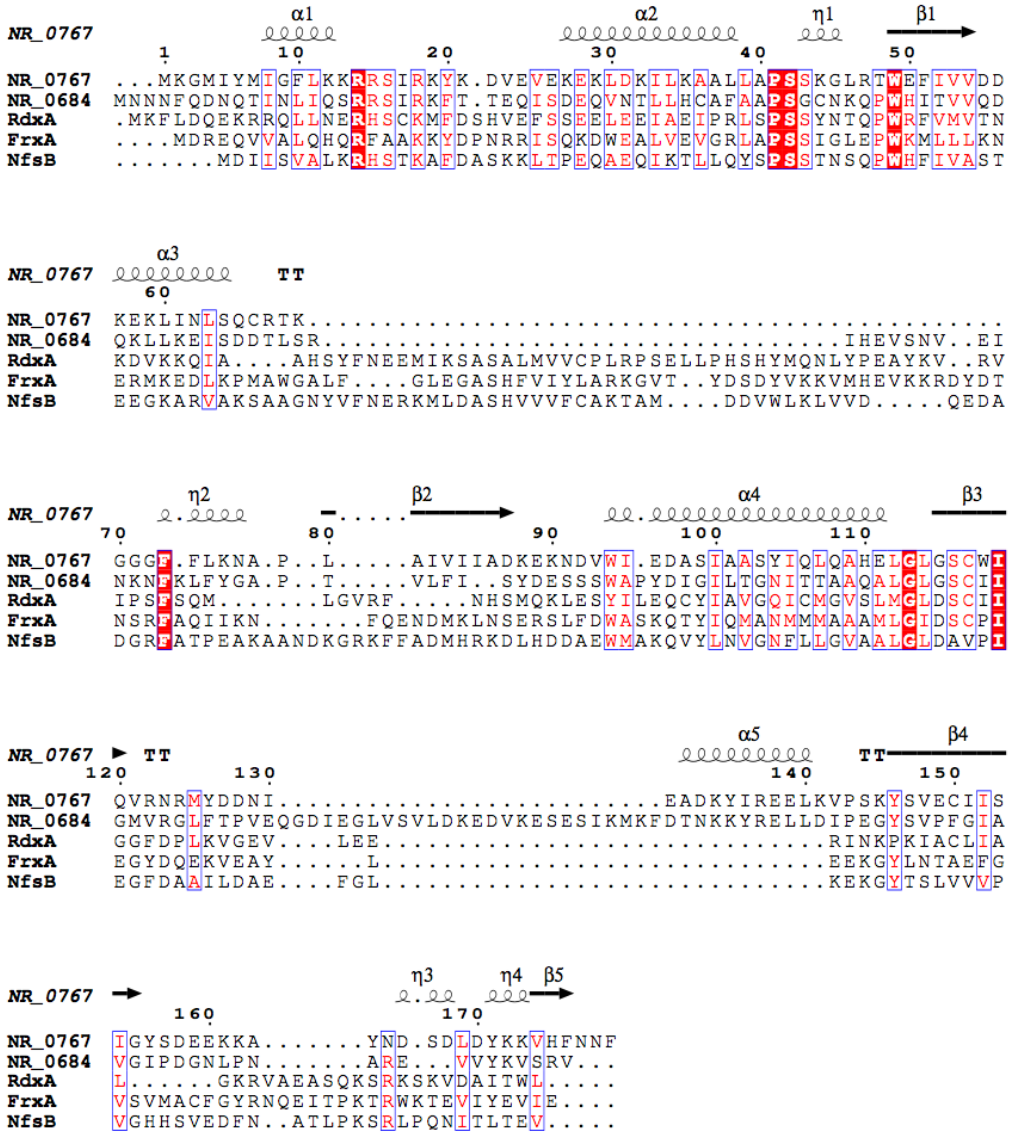

Figure 3.16. Sequence alignment of NRs from three different strains. NR_0767 and NR_0684, from *C. difficile* R20291; RdxA and FrxA, two NRs from *H. pylori*; and NfsB, a NR from *E. coli*. Secondary structure was assigned according to our NR_0767 coordinates. The sequence alignment was produced with ClustalO[45] and displayed with ESPript.[46]

3.4.4 Importance of Cys117

As mentioned in the introduction, Mtz resistance has been associated with NRs in *H. pylori*.[26, 27] The primary NRs in *H. pylori* are RdxA and FrxA, however, only RdxA has been linked with *H. pylori* Mtz susceptibility.[38] Like *C. difficile* NR_0767, RdxA forms a dimer and within each protomer, forms the classic NR α+β fold and the FMN cofactors are located near the interface of the protomers. The RMSD between NR_0767 and RdxA is 3.211 Å (**Figure 3.17**) and their sequence identity is 32% (see **Figure 3.16** for alignment).

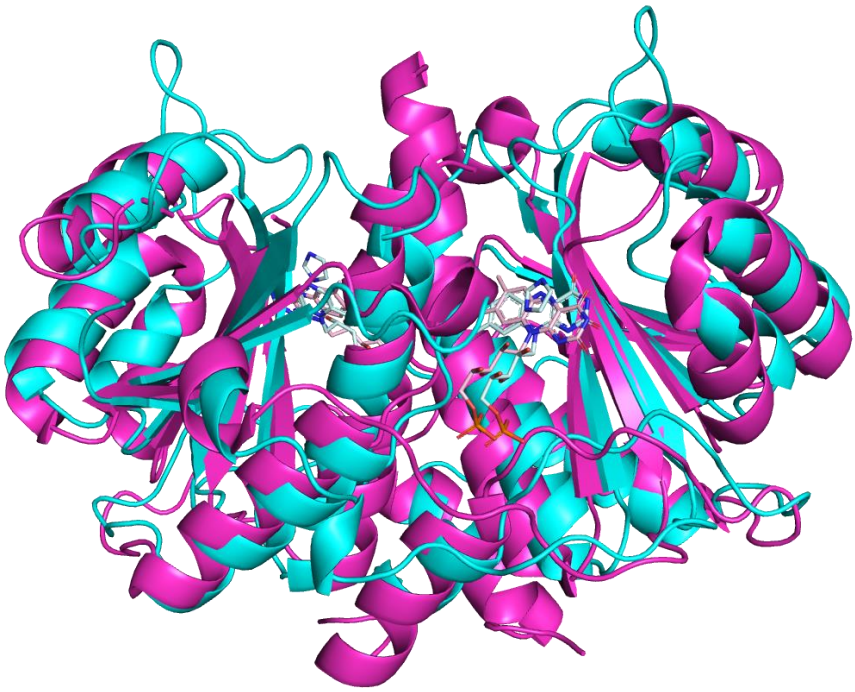

Figure 3.17. Overlay of the X-ray crystal structures of *H. pylori* RdxA (PDB id: 3QDL) and *C. difficile* NR_0767 (this work, cyan).

Martínez-Julvez, et al. reported the importance of Cys159 which is proximal to FMN in the active site.[38] They found that mutations at this site drastically reduced Mtz reduction. It was predicted that due to its proximity (3.8 Å) to N1 of FMN, which can be

protonated once FMN is fully reduced (right of **Figure 3.6**), that Cys159 is involved in the protonation of FMN and thus directly involved in Mtz reduction. NR_0767 also possesses a Cys at this site (Cys117) which is at a similar distance from N1 (3.6 Å) as Cys159 in RdxA is (**Figure 3.18**). Mutagenesis studies need to be performed to confirm the importance of Cys117 in NR_0767, however, based on the structural comparisons with RdxA, it is likely that Cys117 plays a role in NR_0767 Mtz metabolism.

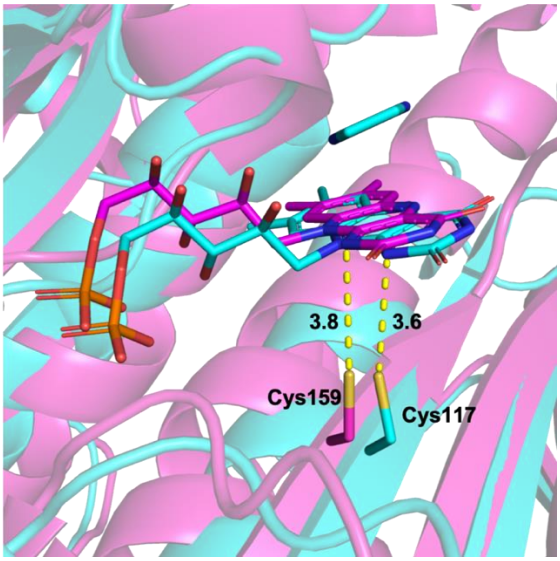

Figure 3.18. Overlay of the FMN active site and proximal Cys of *H. pylori* RdxA (PDB id: 3QDL) and *C. difficile* NR_0767 (this work, cyan).

3.5 Conclusions

In this chapter, I have reported the expression, purification and structural characterization of one of the first two *C. difficile* NRs from the hypervirulent R20291 strain. Redox assays with Mtz, NB, NTZ and CB-1955 show that NR_0767 does indeed function as a nitroreductase and more specifically, a Type I nitroreductase. Based on structural comparisons, we have established the likely importance of the loop between α2 and β1 (residues 44-53) in substrate specificity and Cys117 in Mtz reduction. Additionally, our group's work with NR_0767 and NR_0684 was the first reported observation of the interactions of Mtz and NRs from any *C. difficile* strain.

3.6 References

[1] Poutanen, S. M., and Simor, A. E. (2004) *Clostridium difficile*-associated diarrhea in adults, *Can Med Assoc J 171*, 51-58.

[2] Centers for Disease Control and Prevention (2013) Antibiotic resistance threats in the United States, http://www.cdc.gov/drugresistance/threat-report-2013/pdf/ar-threats-2013-508.pdf.

[3] Lessa, F. C., Mu, Y., Bamberg, W. M., Beldavs, Z. G., Dumyati, G. K., Dunn, J. R., Farley, M. M., Holzbauer, S. M., Meek, J. I., Phipps, E. C., Wilson, L. E., Winston, L. G., Cohen, J. A., Limbago, B. M., Fridkin, S. K., Gerding, D. N., and McDonald, L. C. (2015) Burden of *Clostridium difficile* infection in the United States, *N Engl J Med 372*, 825-834.

[4] Burke, K. E., and Lamont, J. T. (2014) *Clostridium difficile* infection: A worldwide disease, *Gut and Liver 8*, 1-6.

[5] The White House (2015) National action plan for combating antibiotic-resistant bacteria, Washington, D. C., https://www.cdc.gov/drugresistance/pdf/national_action _plan_for_ combating_antibotic-resistant_bacteria.pdf.

[6] Voth, D. E., and Ballard, J. D. (2005) *Clostridium difficile* toxins: mechanism of action and role in disease, *Clin Microbiol Rev 18*, 247-263.

[7] Knight, D. R., Elliott, B., Chang, B. J., Perkins, T. T., and Riley, T. V. (2015) Diversity and evolution in the genome of *Clostridium difficile*, *Clin Microbiol Rev 28*, 721-741.

[8] Healthcare Commission (2006) Investigation into outbreaks of *Clostridium difficile* at Stoke Mandeville Hospital, Buckinghamshire Hospitals NHS Trust, (Inspection,

Commission for Healthcare Audit and Inspection), London, United Kingdom. http://www.buckinghamshirehospitals.nhs.uk/healthcarecommision/HCC-Investigation-into-the-Outbreak-of-Clostridium-difficile.pdf.

[9] Leffler, D. A., and Lamont, J. T. (2009) Treatment of *Clostridium difficile*-associated disease, *Gastroenterology 136*, 1899-1912.

[10] McFarland, L. V. (2016) Therapies on the horizon for *Clostridium difficile* infections, *Expert Opin Investig Drugs 25*, 541-555.

[11] Wang, B., Powell, S. M., Hessami, N., Najar, F. Z., Thomas, L. M., Karr, E. A., West, A. H., and Richter-Addo, G. B. (2016) Crystal structures of two nitroreductases from hypervirulent *Clostridium difficile* and functionally related interactions with the antibiotic metronidazole, *Nitric Oxide 60*, 32-39.

[12] Ünal, C. M., and Steinert, M. (2016) Novel therapeutic strategies for *Clostridium difficile* infections, *Expert Opin Ther Targets 20*, 269-285.

[13] Bagdasarian, N., Rao, K., and Malani, P. N. (2015) Diagnosis and treatment of *Clostridium difficile* in adults: A systematic review, *J Am Med Assoc 313*, 398-408.

[14] Borody, T. J., Paramsothy, S., and Agrawal, G. (2013) Fecal microbiota transplantation: Indications, methods, evidence, and future directions, *Gastroenterol Rep 15*, 337.

[15] World Health Organization (2017) WHO Model List of Essential Medicines, 20th ed.

[16] Roldán, M. D., Pérez-Reinado, E., Castillo, F., and Moreno-Vivián, C. (2008) Reduction of polynitroaromatic compounds: the bacterial nitroreductases, *FEMS Microbiol Rev 32*, 474-500.

[17] Musher, D. M., Aslam, S., Logan, N., Nallacheru, S., Bhaila, I., Borchert, F., and Hamill, R. J. (2005) Relatively poor outcome after treatment of *Clostridium difficile* colitis with metronidazole, *Clin Infect Dis 40*, 1586-1590.

[18] Nair, S., Yadav, D., Corpuz, M., and Pitchumoni, C. S. (1998) *Clostridium difficile* colitis: factors influencing treatment failure and relapse--a prospective evaluation, *Am J Gastroenterol 93*, 1873-1876.

[19] Baines, S. D., O'Connor, R., Freeman, J., Fawley, W. N., Harmanus, C., Mastrantonio, P., Kuijper, E. J., and Wilcox, M. H. (2008) Emergence of reduced susceptibility to metronidazole in *Clostridium difficile*, *J Antimicrob Chemother 62*, 1046-1052.

[20] Huang, H., Weintraub, A., Fang, H., and Nord, C. E. (2009) Antimicrobial resistance in *Clostridium difficile*, *Int J Antimicrob Agents 34*, 516-522.

[21] Jin, S. J., Seo, K. H., and Wi, Y. M. (2018) The effect of concomitant use of systemic antibiotics in patients with *Clostridium difficile* infection receiving metronidazole therapy, *Epidemiol Infect 146*, 558-564.

[22] Lynch, T., Chong, P., Zhang, J., Hizon, R., Du, T., Graham, M. R., Beniac, D. R., Booth, T. F., Kibsey, P., Miller, M., Gravel, D., Mulvey, M. R., and Canadian Nosocomial Infection Surveillance, P. (2013) Characterization of a stable, metronidazole-resistant *Clostridium difficile* clinical isolate, *PLoS ONE 8*, e53757.

[23] Gal, M., and Brazier, J. S. (2004) Metronidazole resistance in *Bacteroides* spp. carrying nim genes and the selection of slow-growing metronidazole-resistant mutants, *J Antimicrob Chemother 54*, 109-116.

[24] Reysset, G. (1996) Genetics of 5-nitroimidazole resistance in *Bacteroides* species, *Anaerobe 2*, 59-69.

[25] Schapiro, J. M., Gupta, R., Stefansson, E., Fang, F. C., and Limaye, A. P. (2004) Isolation of metronidazole-resistant *Bacteroides fragilis* carrying the nimA nitroreductase gene from a patient in Washington State, *J Clin Microbiol 42*, 4127-4129.

[26] Sisson, G., Jeong, J. Y., Goodwin, A., Bryden, L., Rossler, N., Lim-Morrison, S., Raudonikiene, A., Berg, D. E., and Hoffman, P. S. (2000) Metronidazole activation is mutagenic and causes DNA fragmentation in *Helicobacter pylori* and in *Escherichia coli* containing a cloned *H. pylori* rdxA^{+} (nitroreductase) gene, *J Bacteriol 182*, 5091-5096.

[27] Jeong, J. Y., Mukhopadhyay, A. K., Dailidiene, D., Wang, Y., Velapatino, B., Gilman, R. H., Parkinson, A. J., Nair, G. B., Wong, B. C., Lam, S. K., Mistry, R., Segal, I., Yuan, Y., Gao, H., Alarcon, T., Brea, M. L., Ito, Y., Kersulyte, D., Lee, H. K., Gong, Y., Goodwin, A., Hoffman, P. S., and Berg, D. E. (2000) Sequential inactivation of rdxA (HP0954) and frxA (HP0642) nitroreductase genes causes moderate and high-level metronidazole resistance in *Helicobacter pylori*, *J Bacteriol 182*, 5082-5090.

[28] Altschul, S. F., Madden, T. L., Schäffer, A. A., Zhang, J., Zhang, Z., Miller, W., and Lipman, D. J. (1997) Gapped BLAST and PSI-BLAST: a new generation of protein database search programs, *Nucleic Acids Res 25*, 3389-3402.

[29] Marchler-Bauer, A., Derbyshire, M. K., Gonzales, N. R., Lu, S., Chitsaz, F., Geer, L. Y., Geer, R. C., He, J., Gwadz, M., Hurwitz, D. I., Lanczycki, C. J., Lu, F., Marchler, G. H., Song, J. S., Thanki, N., Wang, Z., Yamashita, R. A., Zhang, D., Zheng, C., and Bryant, S. H. (2015) CDD: NCBI's conserved domain database, *Nucleic Acids Res 43*, D222-226.

[30] Studier, F. W. (2005) Protein production by auto-induction in high density shaking cultures, *Protein Expr Purif 41*, 207-234.

[31] Chauviac, F.-X., Bommer, M., Yan, J., Parkin, G., Daviter, T., Lowden, P., Raven, E. L., Thalassinos, K., and Keep, N. H. (2012) Crystal structure of reduced MsAcg, a putative nitroreductase from *Mycobacterium smegmatis* and a close homologue of *Mycobacterium tuberculosis* Acg, *J Biol Chem 287*, 44372-44383.

[32] Otwinowski, Z., and Minor, W. (1997) Processing of X-ray diffraction data collected in oscillation mode, *Methods Enzymol 276*, 307-326.

[33] Winn, M. D., Ballard, C. C., Cowtan, K. D., Dodson, E. J., Emsley, P., Evans, P. R., Keegan, R. M., Krissinel, E. B., Leslie, A. G. W., McCoy, A., McNicholas, S. J., Murshudov, G. N., Pannu, N. S., Potterton, E. A., Powell, H. R., Read, R. J., Vagin, A., and Wilson, K. S. (2011) Overview of the CCP4 suite and current developments, *Acta Cryst D67*, 235-242.

[34] Adams, P. D. (2010) PHENIX: a comprehensive Python-based system for macromolecular structure solution, *Acta Cryst D66*, 213-221.

[35] Emsley, P., and Cowtan, K. (2004) Coot: model-building tools for molecular graphics, *Acta Cryst D60*, 2126-2132.

[36] Chen, V. B., Arendall, W. B., 3rd, Headd, J. J., Keedy, D. A., Immormino, R. M., Kapral, G. J., Murray, L. W., Richardson, J. S., and Richardson, D. C. (2010) MolProbity: all-atom structure validation for macromolecular crystallography, *Acta Cryst D66*, 12-21.

[37] Macheroux, P. (1999) UV-visible spectroscopy as a tool to study flavoproteins, In *Flavoprotein Protocols* (Chapman, S., and Reid, G., Eds.), pp 1-7, Humana Press.

[38] Martínez-Julvez, M., Rojas, A. L., Olekhnovich, I., Espinosa Angarica, V., Hoffman, P. S., and Sancho, J. (2012) Structure of RdxA - an oxygen-insensitive nitroreductase essential for metronidazole activation in *Helicobacter pylori*, *FEBS J 279*, 4306-4317.

[39] de Beer, T. A. P., Berka, K., Thornton, J. M., and Laskowski, R. A. (2014) PDBsum additions, *Nucleic Acids Res 42*, D292-D296.

[40] Altschul, S. F., Gish, W., Miller, W., Myers, E. W., and Lipman, D. J. (1990) Basic local alignment search tool, *J Mol Biol 215*, 403-410.

[41] Holm, L., and Rosenström, P. (2010) Dali server: conservation mapping in 3D, *Nucleic Acids Res 38*, W545-549.

[42] Race, P. R., Lovering, A. L., Green, R. M., Ossor, A., White, S. A., Searle, P. F., Wrighton, C. J., and Hyde, E. I. (2005) Structural and mechanistic studies of *Escherichia coli* nitroreductase with the antibiotic nitrofurazone: Reversed binding orientations in different redox states of the enzyme, *J Biol Chem 280*, 13256-13264.

[43] Çelik, A., Yetiş, G., Ay, M., and Güngör, T. (2016) Modification of existing antibiotics in the form of precursor prodrugs that can be subsequently activated by nitroreductases of the target pathogen, *Bioorg Med Chem Lett 26*, 4057-4060.

[44] Chang, C., Xu, X., Zheng, H., Savchenko, A., Edwards, A., Joachimiak, A., Midwest Center for Structural Genomics. (2006) deposited with the PDB (PDB access code 2H0U).

[45] Sievers, F., Wilm, A., Dineen, D., Gibson, T. J., Karplus, K., Li, W., Lopez, R., McWilliam, H., Remmert, M., Söding, J., Thompson, J. D., and Higgins, D. G. (2011) Fast, scalable generation of high-quality protein multiple sequence alignments using Clustal Omega, *Mol Syst Biol 7*, 539.

[46] Robert, X., and Gouet, P. (2014) Deciphering key features in protein structures with the new ENDscript server, *Nucleic Acids Res 42*, W320-W324.

Chapter 4. Cytochrome P450 BM3-HD

4.1 Introduction

Cytochromes P450 (P450s) belong to a very large superfamily within the even larger family of mono-oxygenases.[1] The primary reaction of P450s is O-atom insertion into a C-H bond and this is accomplished with the help of a heme prosthetic group (**Figure 4.1**). In its ferric resting state, water binds to the axial (sixth) position (**1 in Figure 4.1**). Binding of a ligand to the pocket (away from the Fe) causes the water to be released, beginning the catalytic cycle which requires the entry of O_2.

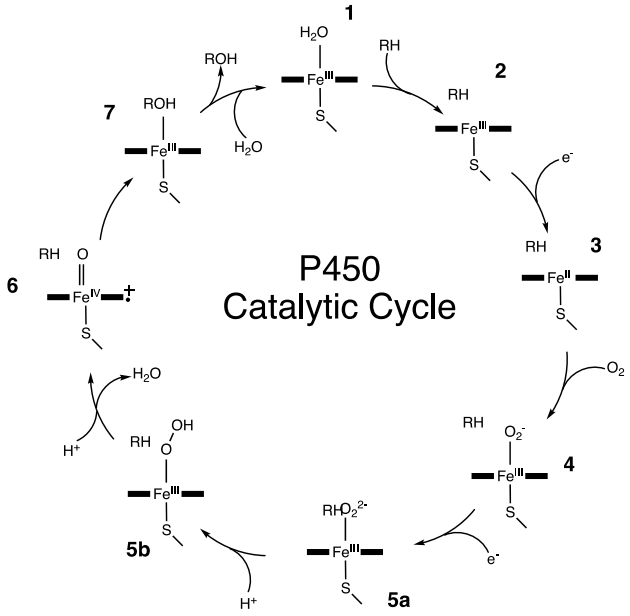

Figure 4.1. Cytochrome P450 oxygenase mechanism.[2] The intermediates are numbered.

P450s perform a large variety of functions such as steroid production and fatty acid metabolism. However, they are best known for their role in drug metabolism as the vast majority of human P450s are located within the liver.[2] P450s are responsible for ~74% of

all xenobiotic metabolism within the human body.[2] All P450s contain a heme domain and a reductase partner that shuttles electrons from NAD(P)H to the heme center. The type of reductase/redox partner defines what class the P450s are within. There are ten total classes of P450 systems, however mammalian P450s all fall into class I or II.[1] Class I P450s partner with a redoxin to shuttle electrons from a membrane-bound NAD(P)H-dependent reductase creating a three-protein system (**Figure 4.2A**), while class II P450s contain a membrane-bound NADPH–cytochrome-P450 reductase (CPR), creating a two-protein system (**Figure 4.2B**).[3] Most human P450s are considered to be class II.

The difficulty in studying mammalian P450s is that they are membrane-bound and therefore difficult to solubilize. In 1981, a bacterial P450 system was discovered in *Bacillus megaterium*.[4] This P450, termed BM3 (CYP102A1), conveniently possesses both the P450 heme and reductase domains in a single polypeptide, and is classified as a class VIII P450 (**Figure 4.2C**).[1] Additionally, P450 BM3 is not membrane bound and is therefore much easier to solubilize. Not long after its discovery, it was reported that P450 BM3 functions like a Type II system and since that time, P450 BM3 has been used as a model system for human P450s.[5]

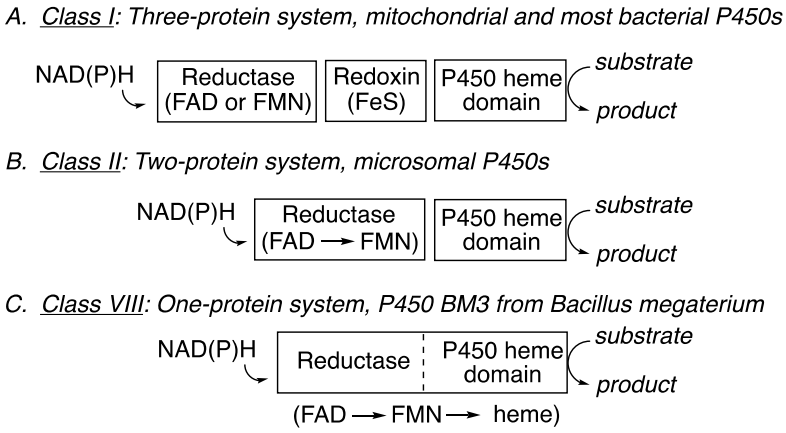

Figure 4.2. Classes of P450 systems.

Full-length P450 BM3 is a 119 kDa protein, but for the purposes of this study that focuses on ligand binding, only the P450 BM3 heme domain (BM3-HD) was used. The heme domain of BM3 is 55 kDa and corresponds to residues 1-455.[4, 6] Unlike myoglobin (Mb) and hemoglobin (Hb), the proximal ligand to the heme in P450 BM3-HD is a cysteine rather than a histidine. The overall structure and active site of P450 BM3-HD in complex with palmitoleic acid are shown in **Figure 4.3**. An important structural feature is the I-helix which houses Thr268. The I-helix helps to make up the substrate binding region and Thr268 is an important residue in oxygen binding and activation, thus making it important for substrate binding as well.[7] In addition to Thr 268, both Ala264 and Phe87 have been shown to contribute to the substrate specificity of P450 BM3-HD, while Arg47, Ala82 and Val78 have been shown to act as "gatekeepers" along the substrate entrance to the heme pocket.[8, 9] Additionally, the active site volume of P450 BM3-HD (~500 $Å^3$) is much larger than that of Mb (~50 $Å^3$) and Hb (~50 $Å^3$), allowing for a much greater diversity of substrates (based on size) that can bind within the active site.

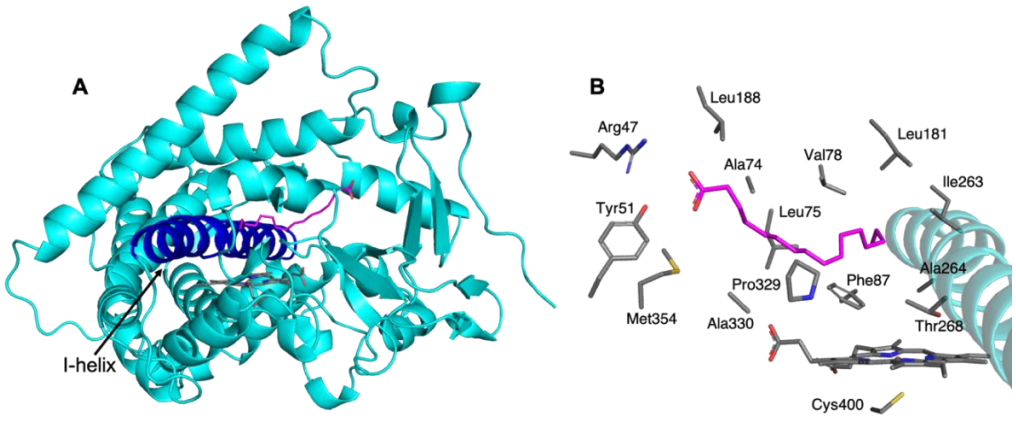

Figure 4.3. (A) Overall structure and (B) active site of BM3 heme domain with bound palmitoleic acid (PDB id: 1FAG). Palmitoleic acid is shown in magenta and the I-helix is shown in blue in (A).

UV-vis spectroscopy has historically been used as a powerful tool to study interactions of P450s with substrates, as the heme chromophore has characteristic absorptions for the various ferric and ferrous liganded states.[10] In fact, P450s get their name from their characteristic absorbance band at 450 nm in the Soret region when the ferrous form is bound to CO.[11, 12] Ligands can bind to either the amino acid residues in the heme active site (Type I) or can coordinate directly with the heme-Fe (Type II) as shown in **Figure 4.4A**. Type I difference spectra have a characteristic maximum at 390 nm and minimum at 420 nm, while Type II difference spectra display a characteristic minimum at 415 nm or lower and a maximum between 425 and 440 nm in (**Figure 4.4B)**.[2] Many inhibitors of P450s bind in a Type II fashion, including N-containing compounds which bind through their N-atoms to the heme-Fe. In doing so, they block the binding of O_2, halting the catalytic cycle (Step between intermediates 3 and 4 in **Figure 4.1**).[8] In this chapter, I present a spectroscopic investigation of the reactions between P450 BM3-HD and three N-containing sets of ligands, namely *C*-nitroso compounds, imidazoles and hydrazines.

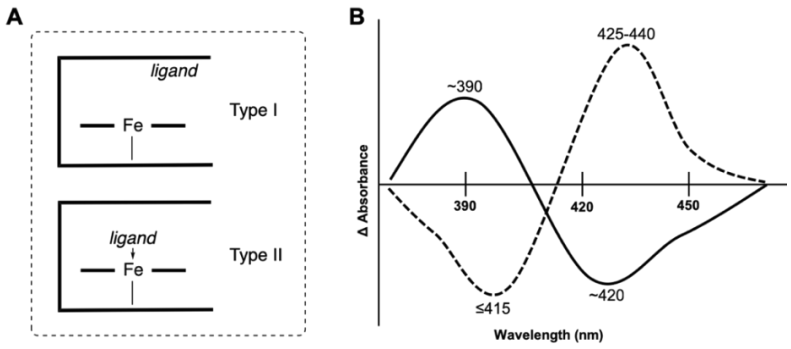

Figure 4.4. (A) Ligands can bind to P450s in a Type I or Type II binding mode. (B) The difference spectra of Type I (solid line) have a λ_{max} at ~390 nm and λ_{min} of ~420 nm, while Type II (dashed line) have a λ_{min} 415 nm or lower and λ_{min} of 425-440 nm.

C-nitroso compounds (RNO, R = alkyl or aryl) are formed from the oxidative metabolism of their hydroxylamine precursors or from the reductive metabolism of their nitro precursors.[13] It is known that these RNOs can inhibit P450s by binding at their Fe centers, preventing further binding of O_2.[14-16] The inhibitory complexes that form are characterized by a ~455 nm peak in the Soret region. RNOs can cause an accumulation of prescription drugs in the liver during multi-drug treatments, as the first RNO-metabolite of one drug will bind to P450 forming a complex which further inhibits any reactions with a second drug.[14] In 1976, Mansuy published a study describing the formation of heme-RNO complexes in rat liver microsomes when treated with nitroalkanes.[17] However, there are no reported studies involving P450 BM3-HD and RNOs. Additionally, there are no crystal structures in the Protein Data Bank (PDB) of any P450-nitrosoalkane complexes. The RNO ligands used in this study are shown in **Figure 4.5**.

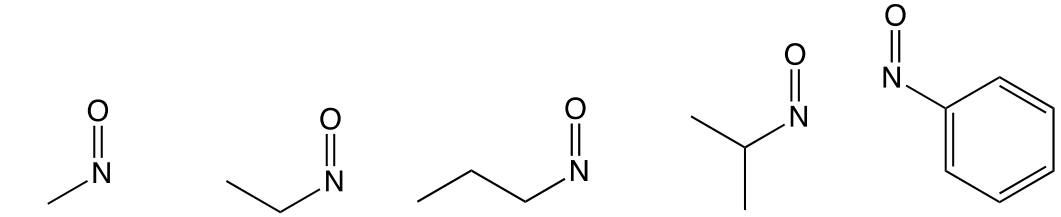

Figure 4.5. RNO ligands used in this study.

Imidazoles have a high affinity for heme proteins. Due to this, imidazole groups are a common moiety in P450-targetted drugs.[18, 19] For example, ketoconazole is an imidazole-based inhibitor of $P450_{17\alpha}$ (CYP17A) used in treatment of prostate cancer.[20] Miconazole and clotrimazole are imidazole-based inhibitors of aromatase (CYP19A) used for breast cancer therapy.[19] There are no published studies of P450 BM3-HD with simple

imidazoles. There are, however, many X-ray crystal structures of other P450s with imidazoles, but there is only one structure of P450 BM3-HD in complex with any simple imidazole (PDB id: 4KF2) and it is a double mutant of P450 BM3-HD.[9] The imidazoles used in my work are shown in **Figure 4.6**.

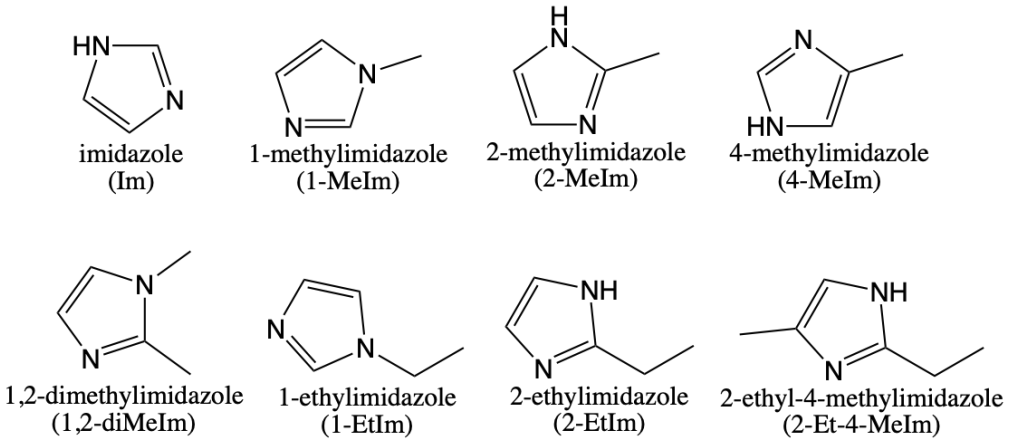

Figure 4.6. Imidazole-based ligands used in this study.

Hydrazines are of interest due to their ability to cause adverse health effects in humans such as cancer, liver damage, hemolytic anemia and reticulocytosis.[21, 22] They are components of isoniazid, an antibiotic prescribed for tuberculosis, and of hydralazine, a medication used to treat high blood pressure and heart failure. Additionally, hydrazines are environmental toxins and are used in rocket fuels, plastic foams and farming chemicals. Hydrazines are toxic to humans both through inhalation and ingestion. In Mb and Hb, reaction with hydrazines causes damage to the protein and in the case of Hb, can lead to formation of Heinz bodies.[23] However, due to the larger site of the P450 active site, P450s can interact with hydrazines without damage occurring in the protein, but they can still inhibit the activity of these proteins.[24] There is currently only one crystal structure of the product formed between any P450 and a hydrazine, namely of P450cam in complex with

a phenyl group after reaction with phenyldiazene (PDB id: 1CP4).[25] There is also only one reported study of P450 BM3-HD with hydrazines.[26] The focus of this study will be the arylhydrazines ($ArNHNH_2$, Ar = aryl) shown in **Figure 4.7**.

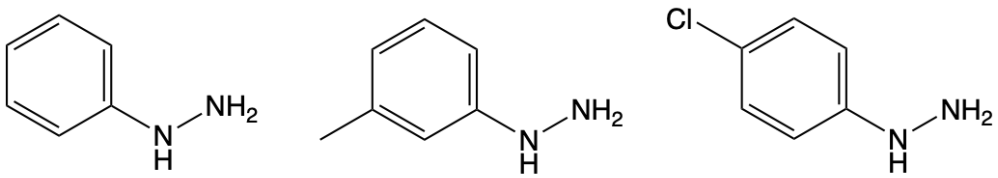

phenylhydrazine (PhHZ) | 3-methylphenylhydrazine (3-MePhHZ) | 4-chlorophenylhydrazine (4-ClPhHZ)

Figure 4.7. Arylhydrazine ligands used in this study.

The goal of this chapter is to fill the gaps in knowledge surrounding the interactions of P450 BM3-HD with *C*-nitroso compounds, imidazoles and hydrazines. This work was performed primarily using UV-vis spectroscopy to probe these interactions.

4.2 Materials and Methods

4.2.1 Cloning and Expression of P450 BM3 Heme Domain (P450 BM3-HD)

Plasmids containing only the heme domain of P450 BM3 (BM3-HD) were a generous gift from Dr. Thomas Poulos from University of California at Irvine. These plasmids were transformed into either *E. coli* DH5α or BL21 (DE3) cells and subsequently expressed in LB media.

Expression trials were performed to optimize the expression of P450 BM3-HD based on literature precedent.[27-30] Expression was carried out at varying temperatures (28 – 37 °C) for varying times (15 – 48 h). The amount of ampicillin in the starting LB (100 or 120 μg/mL) and the amount of IPTG to add (0.5 mM or 1 mM) to induce expression was varied. The point at which to add isopropyl β-D-1-thiogalactopyranoside (IPTG) also varied (OD_{600} = 0.5 – 1.0). I also tested the addition of more ampicillin at the time when IPTG was added. Additionally, attempts were made to increase the heme content of the expressed protein by adding aminolevulinic acid (ALA), the heme precursor, to the growth media. Ultimately, it was found that the best conditions for expression of P450 BM3-HD was to use LB supplemented with 120 μg/mL ampicillin and to grow the cells until OD_{600} reached 0.6 – 0.7, at which point 0.5 mM IPTG and 120 μg/mL ampicillin were added. The temperature was adjusted to 30 °C and cells were left to grow for 15-18 h before being harvested. After harvesting, cell pellets were stored at -80°C until needed.

4.2.2 Purification of P450 BM3-HD

Frozen cell pellets were thawed and resuspended in Buffer A (30 mM potassium phosphate pH 7.4, 0.1 mM EDTA, 10 mM βME). The cells were lysed using an Emulsiflex. Following lysis, multiple methods of purification were tested[27-30] to yield high purity P450 BM3-HD. The efforts are summarized below.

The first purification attempts included an initial streptomycin sulfate precipitation step and dialysis prior to any chromatography, but these steps were later found to be unnecessary as they did not improve yield or purity. Different combinations of DEAE anion exchange, Q-sepharose anion exchange and S-200 gel filtration columns were used to achieve high purity. The column chromatography was performed in the University of Oklahoma Protein Production Core (PPC) on a GE ÄKTA FPLC. Following each chromatography step, SDS-PAGE gels were run to evaluate purity and to select which fractions to pool for the subsequent step. In addition to SDS-PAGE gels, the ÄKTA was equipped with a second UV-vis detector set to 420 nm which assisted in the selection of fractions containing the target protein. The final pure protein was concentrated to ~25 mg/mL using its extinction coefficient at 418 nm (95 $mM^{-1}cm^{-1}$).[31]

To increase heme content, heme reconstitution was performed following purification.[32, 33] Dithiothreitol (DTT; 20 mM) was added to concentrated P450 BM3-HD, and dissolved hemin (2.5 mg in minimal 0.1 M KOH diluted with ddH_2O to 1.5 mL) was added dropwise and left to stir at room temperature for ~24 h. The sample was centrifuged to remove any excess hemin and the pellet was discarded. The supernatant contained the final ferric P450 BM3-HD used for all further experiments.

4.2.3 UV-vis studies of P450 BM3-HD with N-containing ligands

UV-vis spectroscopy, using a Hewlett Packard 8453 spectrophotometer, was used to monitor the aerobic reactions of P450 BM3-HD with the three different sets of N-containing ligands.

4.2.3.1 C-nitroso compounds

The interactions of ferric P450 BM3-HD with *C*-nitroso compounds (RNO where R = alkyl or aryl, **Figure 4.5**; nitrosomethane (MeNO), nitrosoethane (EtNO), 1-nitrosopropane (PrNO), 2-nitrosopropane (*i*-PrNO), and nitrosobenzene (PhNO)) were studied following the methods of a former lab member, Dr. Daniel Copeland.[34] Reduction of the Fe-center of ferric P450 BM3-HD followed by reaction with the nitro-precursors (RNO_2; R = alkyl or aryl), yields their respective nitroso products (RNOs). Initially, 2.4 mL of buffer (100 mM sodium phosphate, pH 7.4) and 25 μL ferric P450 BM3-HD (25 mg/mL) were mixed in a quartz cuvette (Starna cells). 50 μL sodium dithionite (1 M) was added and immediately followed by the addition of 25 μL nitro-substrate (1 M; ~2000x excess). Reaction time of zero was set at the addition of nitro-substrate.

4.2.3.2 Imidazoles

Ferric P450 BM3-HD and its interaction with the imidazoles (**Figure 4.6**; imidazole (Im), 1-methylimidazole (1-MeIm), 2-methylimidazole (2-MeIm), 4-methylimidazole (4-MeIm), 1,2-dimethylimidazole (1,2-diMeIm), 1-ethylimidazole (1-EtIm), 2-ethylimidazole (2-EtIm), and 2-ethyl-4-methylimidazole (2-Et-4-MeIm)) were studied. 2.5 mL of buffer (100 mM sodium phosphate, pH 7.4) and 20 μL ferric P450 BM3-HD (25

mg/mL) were mixed in a quartz cuvette (Starna cells) for an initial spectral reading. 10 μL imidazole-substrate (1 M, ~1000x excess) was then added to the cuvette and a final reading was taken.

4.2.3.3 Arylhydrazines

Ferric P450 BM3-HD and its interaction with arylhydrazines (Ar-$NHNH_2$, Ar = aryl; **Figure 4.7**; phenylhydrazine (PhHZ), 3-methylphenylhydrazine (3-MePhHZ), and 4-chlorophenylhydrazine (4-ClPhHZ)) were studied. 2.5 mL of buffer (100 mM sodium phosphate, pH 7.4) and 20 μL ferric P450 BM3-HD (25 mg/mL) were mixed in a quartz cuvette (Starna cells) for an initial spectral reading. Time zero was set at the addition of 2 μL hydrazine-substrate (0.5 M, ~100x excess) to the cuvette. Readings were taken at different time points during the reaction to monitor formation of products.

4.2.4 Crystallization Attempts

Efforts were made to obtain a crystal of ferric P450 BM3-HD using a variety of crystallization conditions. Initial efforts followed the methods of Li, et. al (0.05 M HEPES pH 7.0, 2.0-3.0 M ammonium sulfate, 2-6% MPD).[27] Conditions were also optimized around published conditions from crystal structures in the PDB – 3BEN (11% PEG 3350, 200 mM $MgCl_2$, 7.5% glycerol, 100 mM MES pH 6.0), 2J1M/2J4S (0.04-0.05 M Zn acetate, 15-20% PEG 3350, 14% DMSO) and 2IJ2 (100 mM cacodylate pH 6.0, 160 mM $MgCl_2$, 18% PEG 3350). A number of broad screens were also tested – MCSG1-4, Wizard, CSHT, MIDAS and Morpheus. Finally, I attempted co-crystallization with MeNO, EtNO, iPrNO and imidazole. None of these conditions have yielded crystals thus far.

4.3 Results

4.3.1 Expression and purification of P450 BM3-HD

P450 BM3-HD was successfully overexpressed in *E. coli* BL21 cells (**Figure 4.8**). The sample taken following induction (I) has a much thicker band at ~50 kDa than the sample taken prior to induction (uninduced; U). The position of this band matches the calculated molecular weight of P450 BM3-HD of 53.2 kDa.

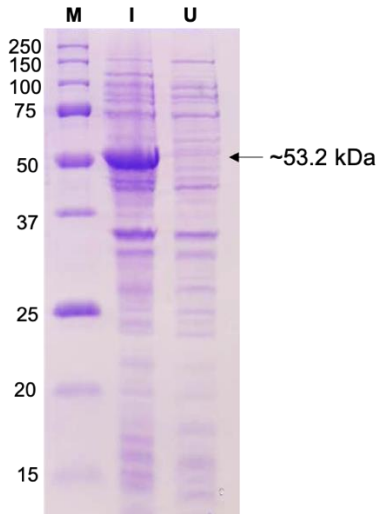

Figure 4.8. SDS-PAGE gel of P450 BM3-HD following induction with IPTG. The induced (I) lane shows the overexpression of P450 BM3-HD (52.3 kDa) compared to the uninduced (U) sample.

After optimizing the expression conditions, I moved on to optimizing the purification strategy. Initial attempts included a streptomycin sulfate precipitation followed by dialysis to remove any excess streptomycin sulfate, and separation using a Q-sepharose anion exchange column and finally an S-200 gel filtration column.[27] As is shown in **Figure**

4.9, the purity of the protein was very poor following the final purification step. Additional efforts were made to increase protein purity.

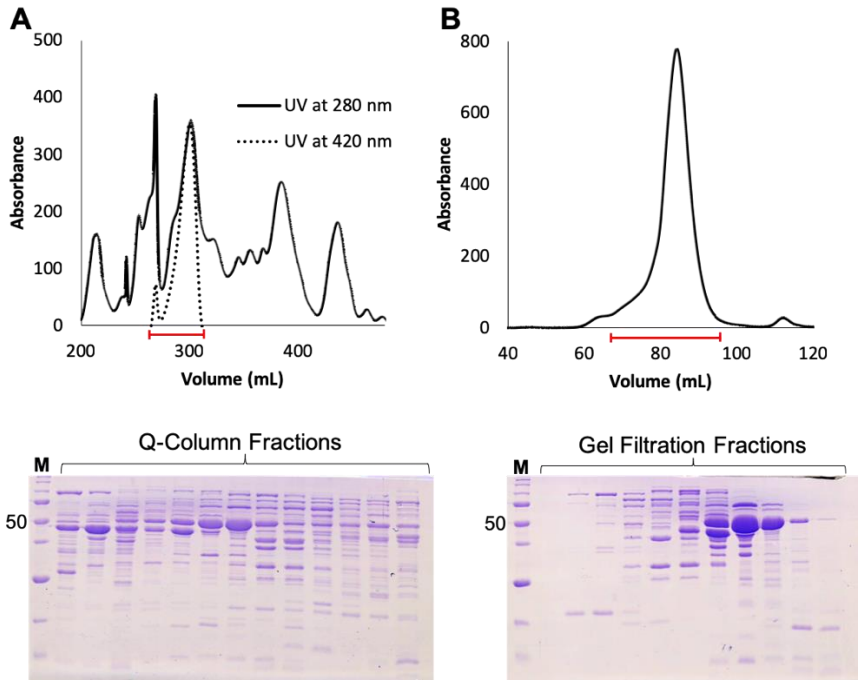

Figure 4.9. P450 BM3-HD purification chromatographs of the (A) Q-column and (B) S-200 gel filtration. Red bars along the x-axis of the chromatographs indicate where fractions were pulled from. Below each chromatograph is its corresponding SDS-PAGE.

Following the methods of Di Nardo, et. al,[30] the streptomycin sulfate step was eliminated and the use of a DEAE column was added. The final purification strategy consisted of separation using a DEAE anion exchange column, buffer exchange to remove salt, a Q-sepharose anion exchange column and finally an S-200 gel filtration column. As shown in **Figure 4.10**, this purification strategy improved the purity of the resulting P450 BM3-HD.

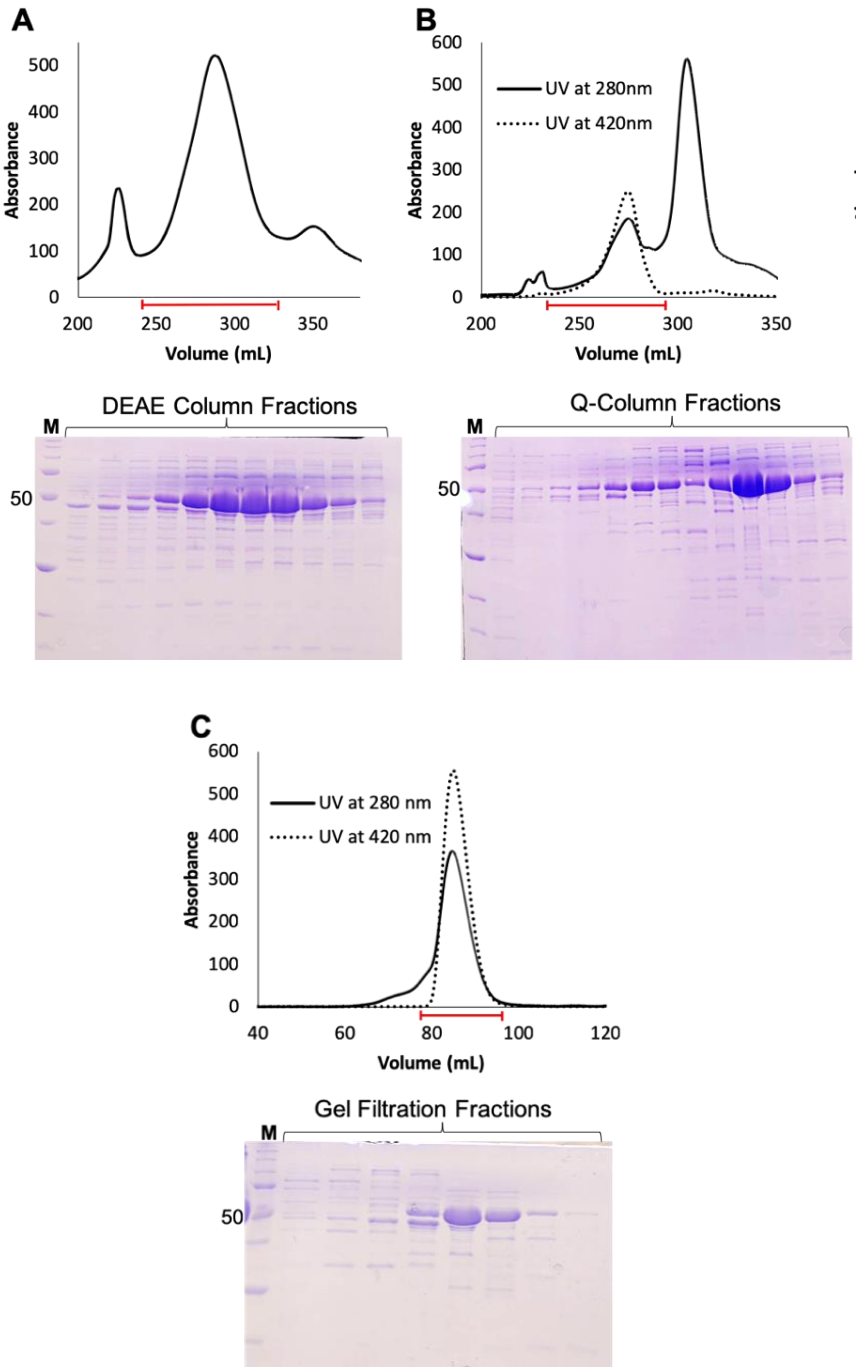

Figure 4.10. P450 BM3-HD purification chromatographs of the (A) DEAE column, (B) Q-column, and (C) S-200 gel filtration. Red bars along the x-axis of the chromatographs indicate where fractions were pulled from. Below each chromatograph is its corresponding SDS-PAGE.

4.3.2 Reactivity with C-nitroso compounds

UV-vis spectroscopy was used to monitor the reactions of ferric P450 BM3-HD with MeNO, EtNO, PrNO, *i*-PrNO, and PhNO. In all cases, an initial spectral reading of ferric P450 BM3-HD was taken and a peak at 419 nm in the Soret band was observed which verified the presence of the oxidized ferric form. After the simultaneous addition of sodium dithionite and the RNO_2 precursor, a decrease at 419 nm and the appearance of a new peak at 452 nm was observed (**Figure 4.11**). The appearance of a peak at 452 nm indicates the reduction of both the heme and the RNO_2 to its respective ferrous Fe^{II}-RNO form, specifically, the formation of an *N*-bound Fe^{II}-RNO derivative. PhNO was also tested; however, no differences were observed in the spectra even after 60 min of reaction.

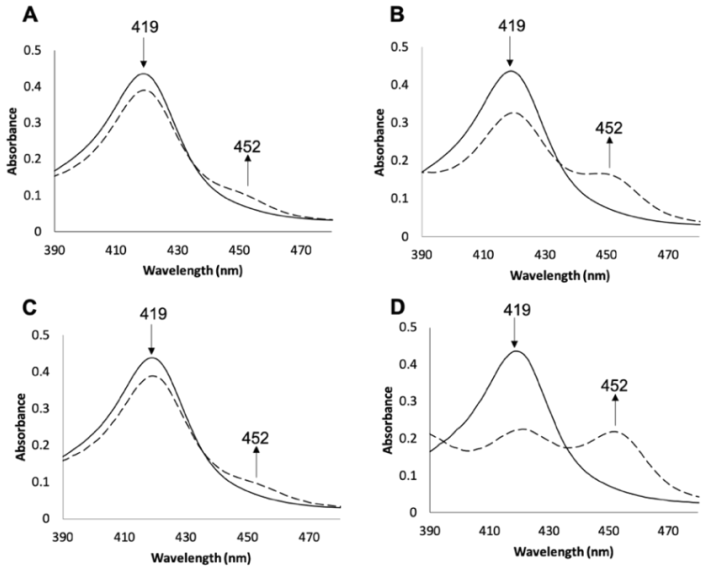

Figure 4.11. UV-vis spectroscopy of ferric P450 BM3-HD (solid line) in reaction with RNO_2 precursors, resulting in ferrous P450 BM3-HD-RNO complexes. The result at 60 min is shown as a dashed line. (A) MeNO, (B) EtNO, (C) PrNO, (D) *i*-PrNO. Conditions: 100 mM sodium phosphate buffer pH 7.4, [P450 BM3 HD] = 4.8 μM, [dithionite] = 20 mM, [substrate] = 10 mM

4.3.3 Reactivity with imidazoles

UV-vis spectroscopy was used to monitor the reactions of ferric P450 BM3-HD with Im, 1-MeIm, 2-MeIm, 4-MeIm, 1,2-diMeIm, 1-EtIm, 2-EtIm, and 2-Et-4-MeIm. The UV-vis spectrum of P450 BM3-HD with Im is shown in **Figure 4.12A**. Upon addition of Im, a shift in the Soret band from 418 nm to 421 nm was observed. Similar shifts were seen for the reaction of ferric P450 BM3-HD with 1-MeIm, 4-MeIm, and 1-EtIm. No reactions were observed for all the 2-substituted imidazoles presumably due to the steric clashes between the imidazole-substituents and the porphyrins rings.[35]

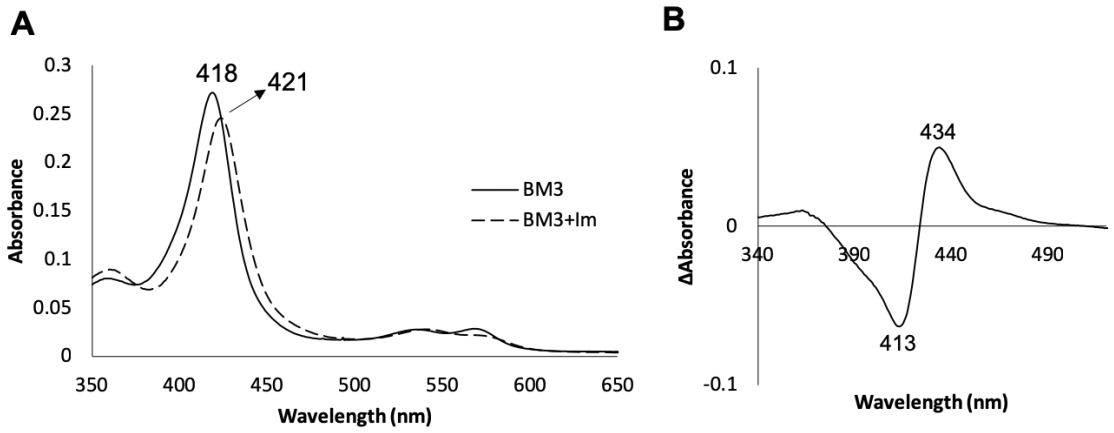

Figure 4.12. UV-vis spectrum of ferric P450 BM3-HD with Im (A), as well as the calculated difference spectrum (B). Conditions: 100 mM sodium phosphate buffer pH 7.4, [P450 BM3 HD] = 3.8 μM, [substrate] = 4 mM

To determine the type of binding between the imidazoles and ferric P450 BM3-HD, a difference spectrum was calculated. As shown in **Figure 4.12B**, for Im, a λ_{max} was observed at 434 nm and λ_{min} was observed at 413 nm. These peaks are indicative of Type II binding. Similar peaks were observed in the difference spectra for 1-MeIm, 4-MeIm, and

1-EtIm as shown in **Table 4-1**. These results are consistent with literature that imidazoles should bind P450s in the Type II binding mode.[36]

Table 4-1. Difference spectra peaks for P450 BM3-HD with imidazoles.

	Im	**1-MeIm**	**4-MeIm**	**1-EtIm**
λ_{min}	413	413	414	413
λ_{max}	434	433	434	433

4.3.4 Reactivity with arylhydrazines

UV-vis spectroscopy was used to monitor the reactions of ferric P450 BM3-HD with PhHZ, 3-MePhHZ and 4-ClPhHZ. The UV-vis spectrum of P450 BM3-HD in reaction with PhHZ is shown in **Figure 4.13**. Immediately after the addition of PhHZ, a shift is seen in the Soret band from 418 nm to 421 nm (**Figure 4.13A**). Similar to that seen with the imidazoles, after a difference spectrum was calculated, a λ_{max} at 434 nm and λ_{min} at 413 nm was observed. This pattern in the difference spectrum indicates Type II binding. Unlike the imidazoles, however, the reactions do not stop after this first step. Over time, a disappearance of the peak at 421 nm, and an appearance of a peak at 480 nm was evident (**Figure 4.13B**). Similar shifts were seen for both 3-MePhHZ and 4-ClPhHZ.

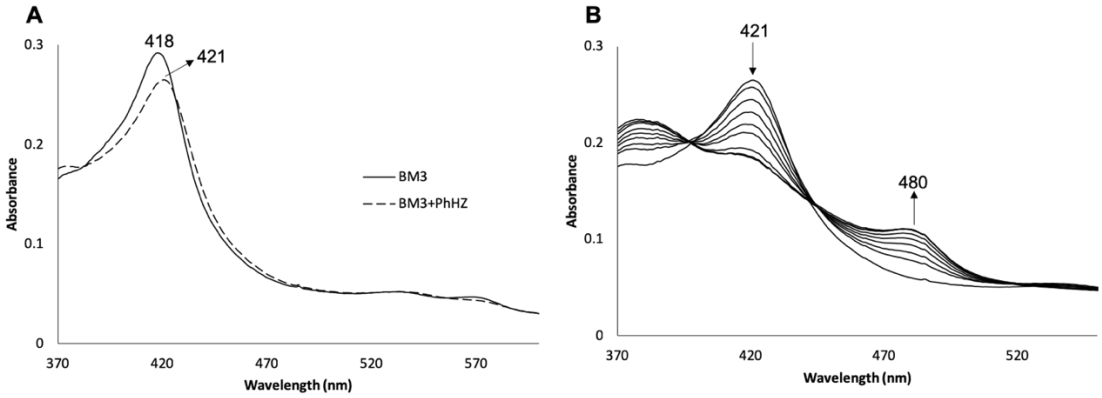

Figure 4.13. UV-vis spectrum of ferric P450 BM3-HD with PhHZ. (A) The spectrum after the initial addition of PhHZ and (B) the changes in the spectrum over time. Conditions: 100 mM sodium phosphate buffer pH 7.4, [P450 BM3 HD] = 3.8 μM, [substrate] = 400 μM

The time that it took for the peak at 421 nm to begin decreasing varied between ligands (**Figure 4.14**). For PhHZ, the shift toward 480 nm began at ~40 min (**Figure 4.14A**) and the reaction reached its peak at ~150 min. After ~150 min however, the absorbance at 480 nm began to decrease, indicating instability of the product. For 3-MePhHZ, the shift toward 480 nm began at ~30 min and the reaction reached its peak at ~180 min (**Figure 4.14B**). The product appeared to be stable as there was very little decrease in the absorbance at 480 nm up to ~300 min. For 4-ClPhHZ, the shift toward 480 nm began at ~10 min and the reaction reached its peak at ~80 min (**Figure 4.14C**). This product appeared stable as well as there was very little decrease in the 480 nm peak up to ~180 min.

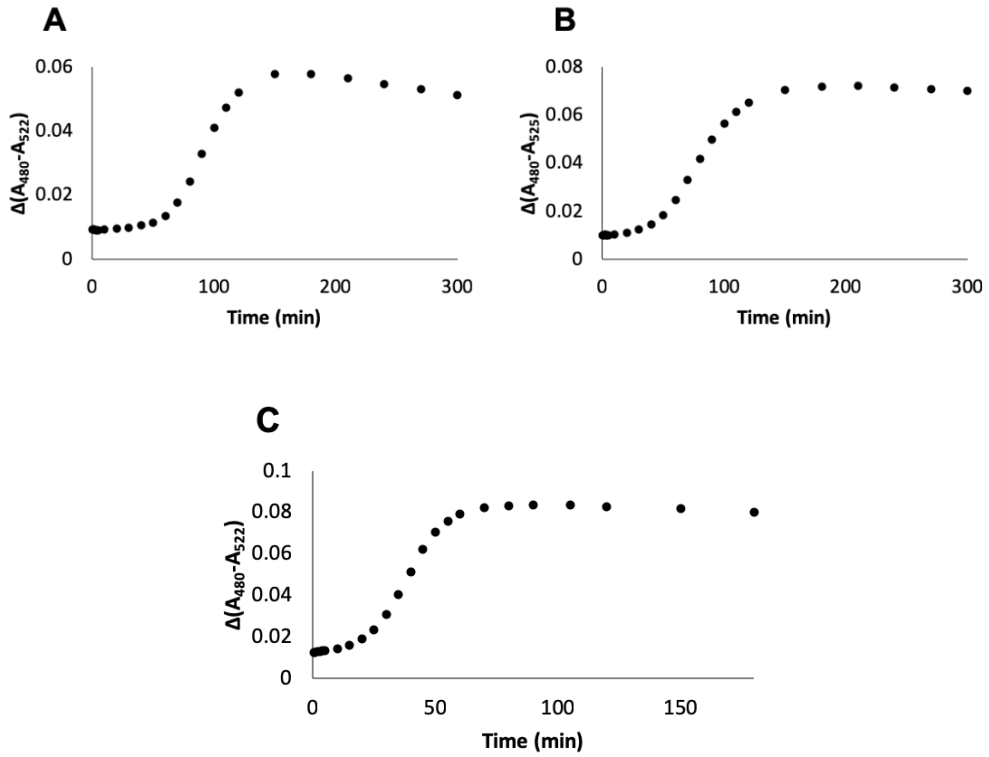

Figure 4.14. Time course of the reactions of ferric P450 BM3-HD with (A) PhHZ, (B) 3-MePhHZ and (C) 4-ClPhHZ. Plots are displayed as ΔAbs versus time.

4.3.5 Crystallization

Crystallization efforts of the ferric P450 BM3-HD protein have not yet, in my hands, yielded crystals. **Figure 4.15** shows the resulting hanging drops of four of the many conditions attempted. The lack of crystal formation is likely due to insufficient purity of the final sample which could not be improved to >90% (**Figure 4.10C**).

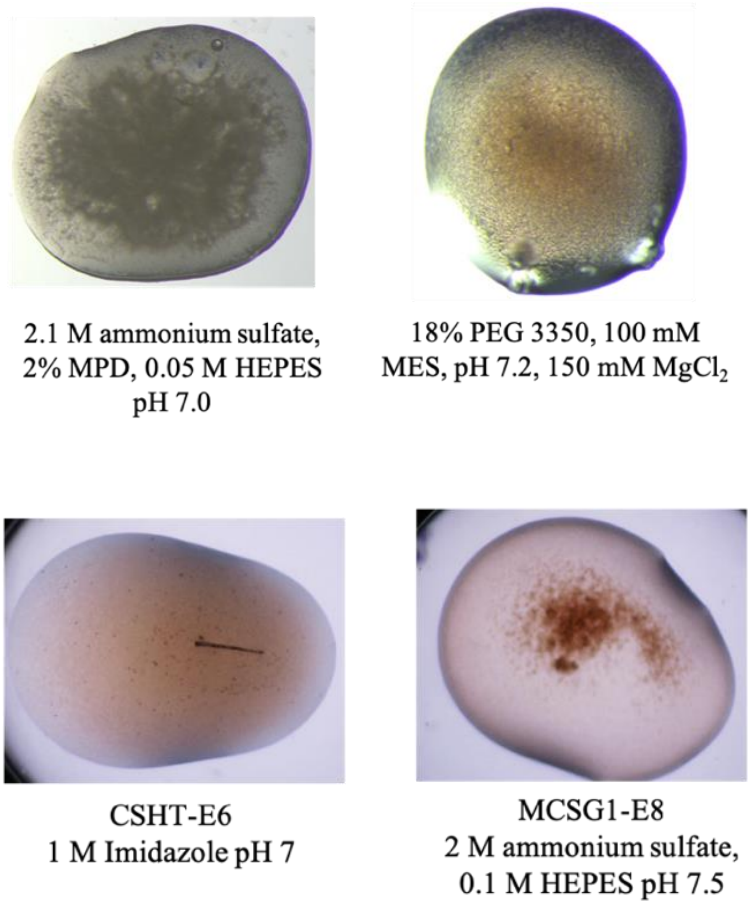

Figure 4.15. Various crystallization conditions resulting in P450 BM3-HD precipitation, but without crystal formation.

4.4 Discussion

4.4.1 Relationship of C-nitroso ligand sterics and extent of complex formation

As can be seen in **Figure 4.11**, the RNOs reacted with ferric P450 BM3-HD to varying degrees. To determine the difference in RNO reactivity with ferric P450 BM3-HD, the extent of formation was calculated based on the disappearance of the peak at 419 nm. It was calculated as the change in absorbance at 419 nm divided by the initial absorbance at 419 nm and multiplied by 100 (Δ419/419). The results are displayed in **Figure 4.16**.

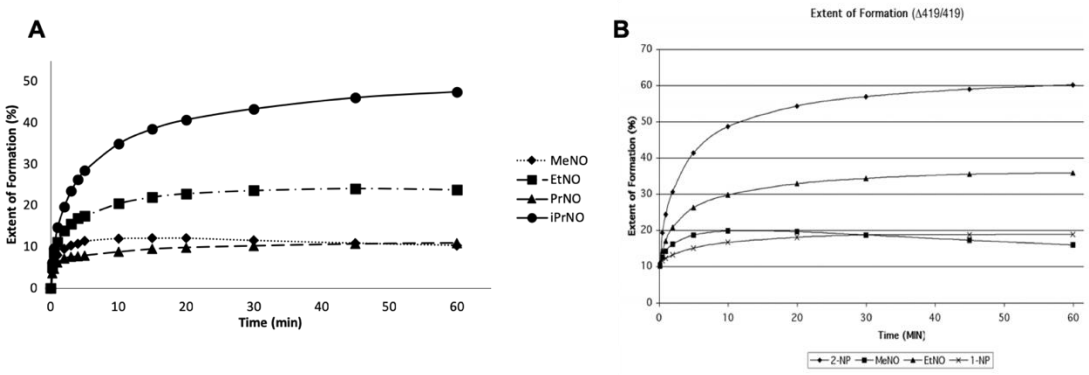

Figure 4.16. Extent of formation for the reactions of ferric P450 BM3-HD with RNOs from (A) this work and (B) related work by Dan Copeland.[34]

Over a one-hour period, the extent of formation with MeNO was 11%, EtNO was 24%, PrNO was 11% and *i*-PrNO was 48%. Since I was following the methods of Dan Copeland, my results (**Figure 4.16A**) were compared with his (**Figure 4.16B**). Copeland's results for extent of formation at the one-hour time point were similar to my work (MeNO was 16%, EtNO was 36%, PrNO was 19% and i-PrNO was 60%). His values were

consistently higher than mine, which could be attributed to minor differences in starting conditions such as initial protein concentration.

As the alkyl group increases in size from methyl → ethyl → isopropyl, the extent of formation with ferric P450 BM3-HD increases as well. The exception to this steric trend is PrNO, which reached a maximum extent of formation matching that of MeNO. The same trend was observed in Copeland's work. This exception to this trend can be explained by an examination of the P450 BM3-HD active site and by computationally "docking" the respective RNO ligand as *N*-bound to the Fe-center in the previously determined X-ray structure of this protein. The predicted structures of the ferrous P450 BM3-HD-RNO complexes were constructed in Pymol and are displayed in **Figure 4.17**. The orientations of the artificially placed RNOs were fixed, guided by other reported hemoprotein-RNO crystal structures.[37] MeNO, EtNO and *i*-PrNO, were readily modeled in the active site as *N*-bound ligands, with the alkyl groups oriented towards the hydrophobic interior of pocket leaving the O-atom of each RNO ligand to H-bond with the nearby Thr268 (**Figure 4.17A, B, D)**. For PrNO, the terminal methyl group clashes with both Phe87 and Ala264 (**Figure 4.17C**; closer than the sum of Van der Waals radii[38]), making it difficult for the *n*-propyl chain to find a stable position in the active site. I note that Phe87 has been shown to influence substrate specificity in P450 BM3-HD[8, 9] and this could explain why the extent of formation for PrNO is so low relative to the other longer-chain RNOs tested.

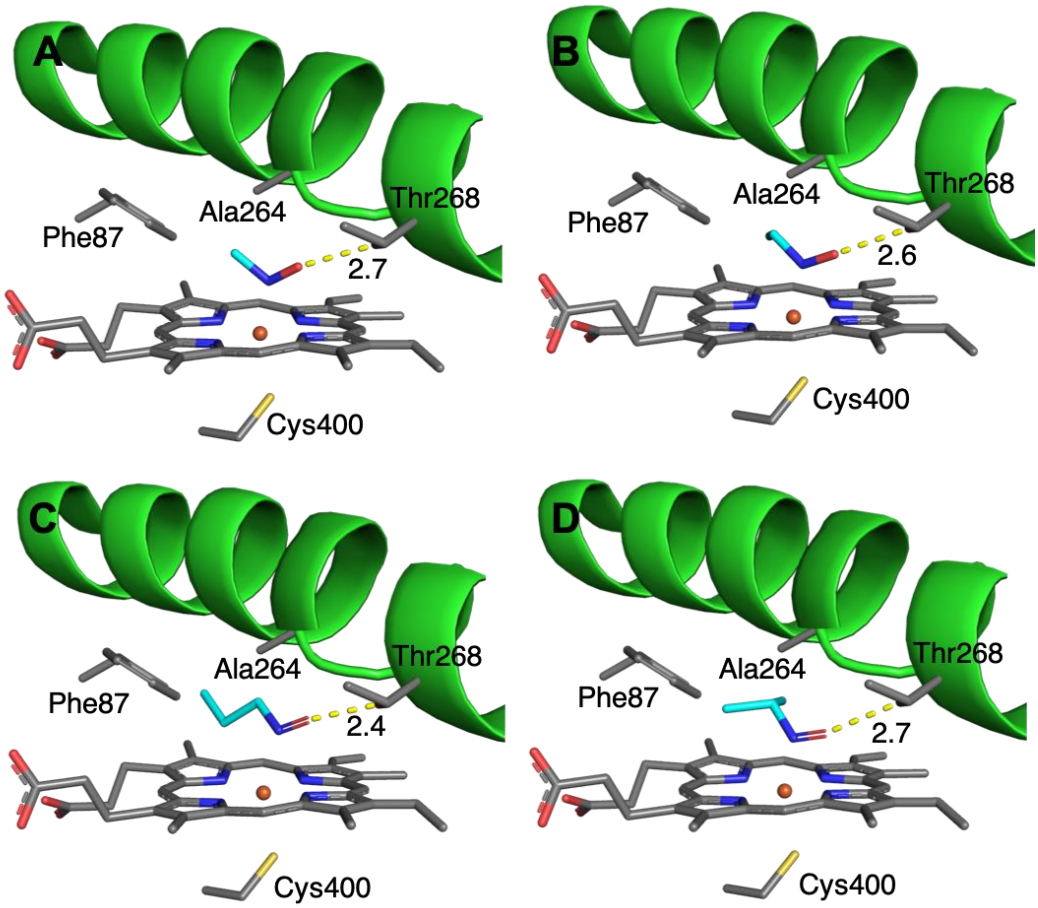

Figure 4.17. Predicted ferrous P450 BM3-HD-RNO interactions modeled into the P450 BM3-HD active site using the protein structure from PDB id: 1FAG. (A) MeNO, (B) EtNO, (C) PrNO, (D) *i*-PrNO.

The trends observed for the extent of formation for the ferrous P450 BM3-HD-RNO derivatives are also comparable to the work performed by Mansuy with rat liver microsomal P450's (**Figure 4.18**).[17] In my work, following the methods of Copeland, I calculated the extent of formation based on the disappearance of the starting material peak at 419 nm. This was attributed to the fact that calculating the extent of formation based on the appearance of the product peak at 452 nm would likely result in an inaccurate

comparison since each of the four ligand complexes would have a different extinction coefficient. However, in Mansuy's work, he calculated the extent of formation using the difference between the product peak at 455 nm and an isosbestic point at 490 nm (ΔAbs 455-490 nm) as shown in **Figure 4.18B**. In order to compare my results to Mansuy's, I recalculated the extent of formations using a similar method (**Figure 4.18A**). While minor differences exist, the overall trends observed in **Figure 4.16A** still hold up after using a different method to calculate the extent of formation.

Three ligands overlap between Mansuy's work and my work; MeNO, EtNO, and *i*-PrNO. The extent of formation trend for Mansuy's work is EtNO > *i*-PrNO > MeNO. This trend is somewhat similar to that presented in this work (*i*-PrNO > EtNO > MeNO), but with a difference in the relative position of *i*-PrNO. Unlike P450 BM3-HD, which has a bulky Phe at position 87 (**Figure 4.17**), the equivalent residue in microsomal P450s is typically a much less bulky residue such as Gly.[8] By replacing Phe with Gly, this weakens the hydrophobic interactions between *i*-PrNO and the active site pocket, causing *i*-PrNO to be less stable in the pocket of microsomal P450s and thus lower its extent of formation. The fact that the trends are somewhat similar between P450 BM3-HD and microsomal P450s shows that P450 BM3-HD is a suitable model for other P450s.

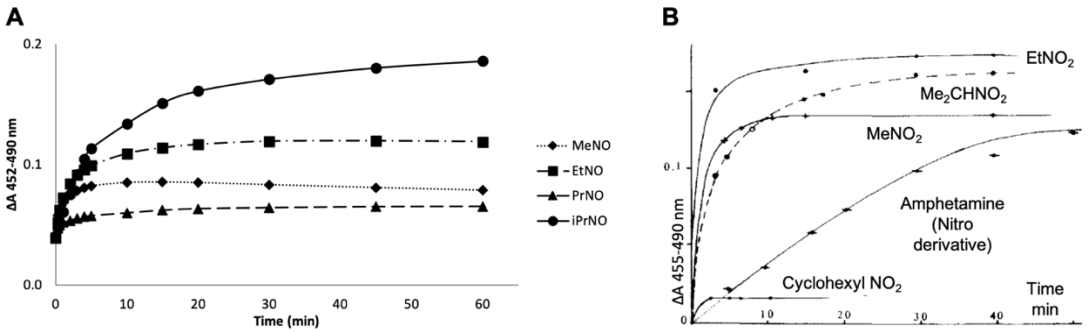

Figure 4.18. Comparison of appearance of the product peak for (A) P450 BM3-HD and (B) Mansuy's work with rat liver microsomes in reaction with nitro-compounds.[17]

It should also be noted that there was no reaction between ferric P450 BM3-HD and nitrobenzene ($PhNO_2$) under our conditions. P450-PhNO complexes have been reported previously, however, the complexes were formed through the reaction of PhNO directly under anaerobic conditions or through the reaction of PhNHOH with a reducing agent.[39, 40]

4.4.2 P450 BM3-HD-imidazole complexes

Imidazoles, more specifically 1- and 4-substituted imidazoles, have long been known to be inhibitors of P450s. The first reported study of the interactions of alkylimidazoles with microsomal P450s was published in 1974.[41] Prior to my current work, there were no reports describing the interactions of ferric P450 BM3-HD with alkylimidazoles using UV-vis spectroscopy.

In my work, ferric P450 BM3-HD was reacted with Im, 1-MeIm, 2-MeIm, 4-MeIm, 1,2-diMeIm, 1-EtIm, 2-EtIm, and 2-Et-4-MeIm. Curiously, no reaction occurred upon addition of 2-substituted imidazoles under our reaction conditions. Rogerson, et al. reported that sterics play a large part in the interaction of imidazoles with P450s, therefore 2-substituted imidazoles are likely to have reduced or no reactions with P450s.[35] With the 1- and 4-substituted imidazoles, shifts in the Soret λ_{max} from 418 to 421 nm were observed for the complexes (**Figure 4.12A**), matching literature values for imidazole-based fatty acids in their interactions with ferric P450 BM3-HD.[8]

The difference UV-vis spectra were also calculated for each successful reaction (**Figure 4.12B**). The λ_{max} and λ_{min} were consistently observed at ~434 and ~413 nm, respectively (**Table 4-1**). These values match that of Type II difference spectra indicating that the products are N-bound to the heme-Fe.[8, 36, 41] Interestingly, although imidazoles are known to be potent inhibitors of most P450s, they are weak inhibitors of P450 BM3-HD, which has been attributed to P450 BM3-HD's more rigid active site residues, as determined by solid-state NMR.[8, 42] There is currently only one crystal structure of P450 BM3-HD with a simple imidazole and it is not with wild-type (wt) P450 BM3-HD, but with a mutant F87V form of P450 BM3-HD.[9] As can be seen in **Figure 4.19**, the mutation of Phe to Val

allows for the binding of Im to the heme-Fe. Based on the overlay of wt and F87V P450 BM3-HD, the distance between the nearest carbons of F87 and Im is 1.7 Å which is likely to cause clashing, leaving Im unstable in the active site. This could explain the difficulty in obtaining ferrous P450 BM3-HD-imidazole crystal structures.

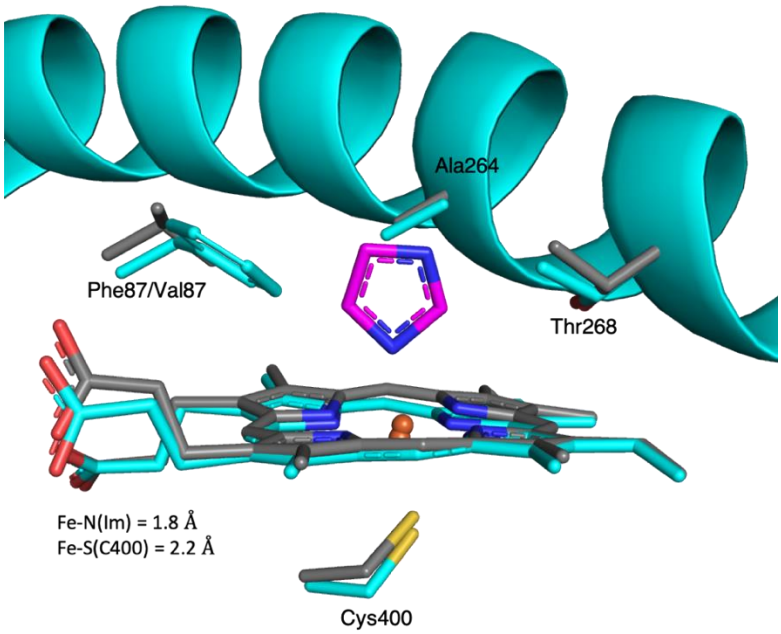

Figure 4.19. Overlay of the active sites and I-helix of wt P450 BM3-HD-palmitoleic acid (cyan; PDB id: 1FAG) and F87V P450 BM3-HD-Im (grey; PDB id: 4KF2). Palmitoleic acid is not shown for ease of viewing and Im is shown in magenta.

Locuson, et al. published a study in 2007 discussing the "incomplete" heme coordination of imidazoles with P450 3A4 and 2C9 after observing that their calculated difference spectra consistently had a significant shoulder at ~390 nm (**Figure 4.20A**).[36] Typically, N-containing ligands such as imidazoles react with the heme-Fe and help to stabilize low-spin Fe, but a shoulder at ~390 nm likely indicates that there is still some

high-spin Fe remaining after the reaction is complete. The same trend was observed for all reactions of ferric P450 BM3-HD with imidazoles (**Figure 4.20B**), however the shoulder for ferric P450 BM3-HD is drastically reduced as compared to that of P450 3A4. Therefore, it is likely that there is a much smaller amount of high-spin Fe present.

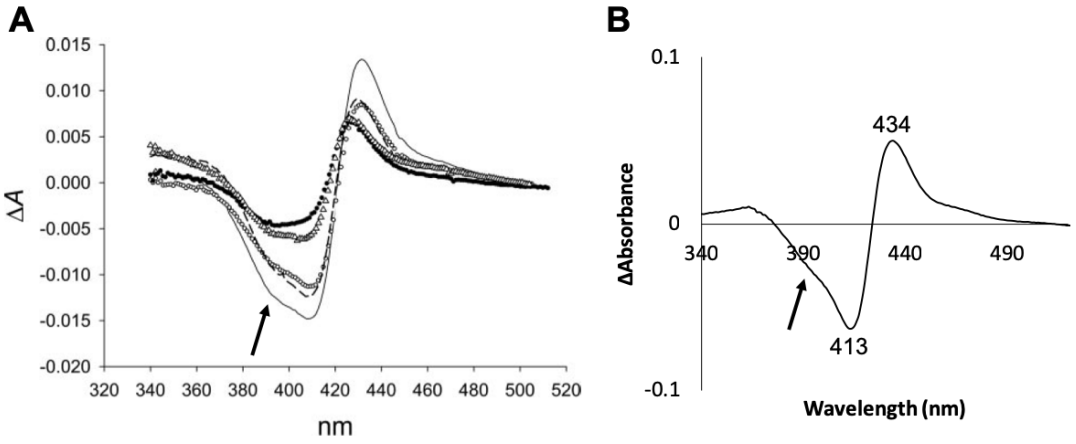

Figure 4.20. (A) Calculated difference spectrum of the reaction between P450 3A4 and imidazole-based ligands.[36] The Im reaction is indicated with a solid line. (B) Calculated difference spectrum of the reaction between P450 BM3-HD and Im. Arrows indicate a shoulder at ~390 nm.

4.4.3 Formation of σ-bonded aryl-iron complexes

As was observed for the interaction of ferric P450 BM3-HD with imidazoles, upon addition of arylhydrazines, the Soret peak shifted from 418 to 421 nm (**Figure 4.13A**) indicating ligand binding at the heme-Fe (**first step in Figure 4.21**). Under aerobic conditions, as more oxygen (from air) enters the reaction, an aryl radical is formed which can react with the now oxidized ferric heme-Fe.[43] This was observed in my UV-vis spectral studies as the peak at 421 nm decreased simultaneously with an increase in a 480 nm peak (**Figure 4.13B**). A λ_{max} from 470-480 nm is indicative of a σ-bonded aryl-iron complex (**second step in Figure 4.21**)[23], therefore it is likely that the identity of the products in the above UV-vis spectral studies are σ-bonded aryl-iron complexes as well. Similar results were produced in microsomal P450's in their reaction with PhHZ, further justifying P450 BM3-HD as a model P450.[44]

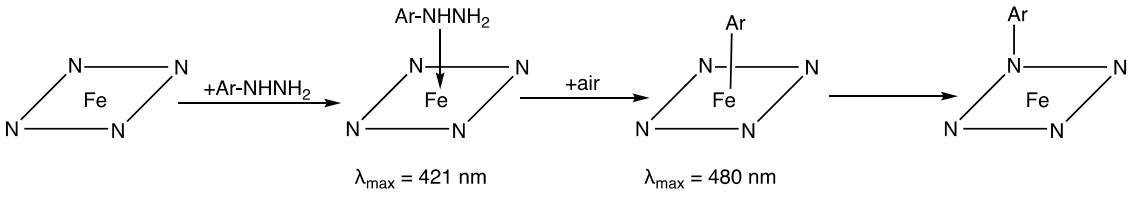

Figure 4.21. Reaction mechanism of P450 BM3-HD with arylhydrazines (NH_2NH-Ar).

Since the UV-vis spectral shifts match those of other previously published studies, it can be inferred what the identities of the ferric P450 BM3-HD-aryl complexes are. The first crystal structure of a hemoprotein-aryl derivative was published in 1984, and describes a Mb-phenyl complex resulting from the reactions of Mb with PhHZ.[45] More recently, Dr. Bing Wang of our lab published four crystal structures of H64A and H64Q Mb after

reaction with 3-MePhHZ and 4-ClPhHZ.[46] Only one ferric P450-aryl crystal structure has been reported which is a $P450_{cam}$-phenyl structure resulting from reaction with phenyldiazene.[25] The structure of P450 BM3-HD-aryl would likely resemble that of $P450_{cam}$ as their active site makeups are similar (**Figure 4.22**). Additionally, based on Dr. Wang's recent work, it is known that the aryl-carbon that will bind to the Fe is the carbon that was initially bonded to the hydrazine group.[46]

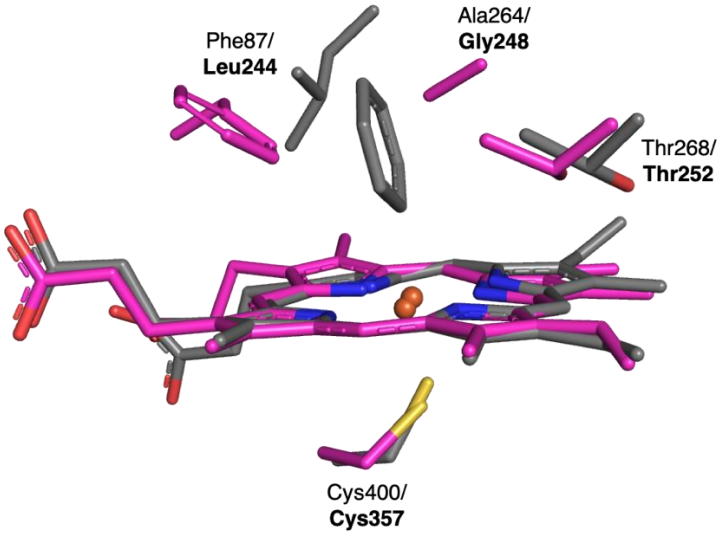

Figure 4.22. Alignment of $P450_{cam}$-phenyl (grey; PDB id: 1CP4) with wt P450 BM3-HD (pink; PDB id: 1FAG). Residues are listed as P450 BM3-HD/$P450_{cam}$.

If further oxidation of the Fe^{III} to Fe^{IV} were to occur, this would induce a shift of the aryl group from the heme-Fe to one of the heme N-atoms (**final step in Figure 4.21**).[23] Unique to P450s is that the Fe to nitrogen shift can take place within the active site pocket without damage to the protein itself, making arylhydrazines useful probes for active site chemistry.[23] Various studies have been published with various P450s to identify which of the four heme N-atoms the aryl group migrates to, by isolating the modified porphyrin and

subjecting it to HPLC separation. In the case of P450 BM3-HD, upon reaction with phenylhydrazine, a N_B:N_A:N_C:N_D ratio of 2:9:2:1 was obtained (see **Figure 4.23A** for naming scheme).[26] This indicates that the area distal to N_A in the active site is likely the most open for ligand binding (**Figure 4.23B**). Looking at the published X-ray crystal structure of P450 BM3-HD in complex with 1,2-ethanediol and polyethylene glycol (PEG) (PDB id: 4ZFA)[47], the volume above the heme correlates very well with the HPLC results as the largest cavity is above N_A (**Figure 4.23C**).

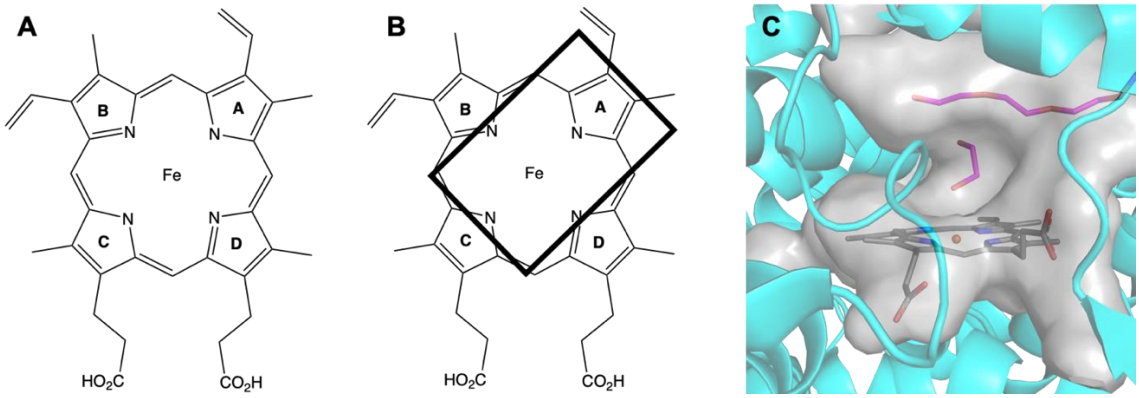

Figure 4.23. (A) Heme pyrrole nomenclature. (B) HPLC results suggest that the area distal to N_A in P450 BM3-HD is likely the most open for substrate binding. This area is indicated by a box (modified from Tuck, et al[26]). (C) The interior cavities (grey) of P450 BM3-HD with 1,2-ethanediol and PEG (PDB id: 4ZFA) is shown.

In my studies, I used PhHZ, 3-MePhHZ and 4-ClPhHZ. In the future, porphyrin isolation and HPLC (as done by Swanson, et al.[48]) could be used to identify the porphyrin-N migration ratios for these three ligands. The ratio would likely vary between the three ligands as the bulk and location of the aryl-substituent changes.

4.4.4 Future Work

4.4.4.1 FTIR spectroscopy with P450 BM3-HD and RNOs

Since attempts at crystallizing ferric P450 BM3-HD have thus far not been successful, a different method must be used to monitor the structural changes occurring in ferric P450 BM3-HD upon ligand binding. Fourier Transform Infrared (FTIR) spectroscopy can be used to detect changes in secondary structure. This is done by monitoring the amide I (1700-1600 cm^{-1}), amide II (1600-1500 cm^{-1}) and amide III (1220-1320 cm^{-1}) bands.[49] The amide I band corresponds to C=O stretching which is weakly coupled with C-N stretching and N-H bending, the amide II band corresponds to C-N stretching which is strongly coupled with N-H bending and the amide III band corresponds to N-H in-plane-bending and C-N stretching vibrations.[49, 50] Most commonly, the amide I and III bands are used to diagnose structural changes as the amide II band is not very sensitive to these changes.[50] Additionally, for heme proteins, the porphyrin vinyl groups have a signal at ~1640 cm^{-1} (C=C stretch) which overlaps with the amide I band, but the signal between ~1740 and 1725 cm^{-1} (propionate C=O stretch) can be seen.[51]

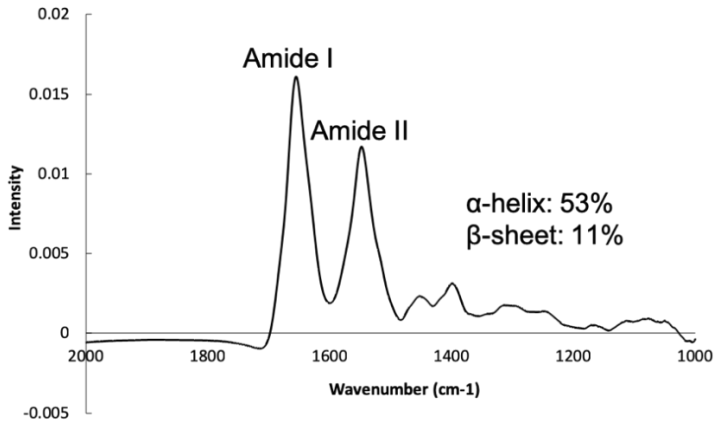

Figure 4.24. FTIR spectrum of ferric P450 BM3-HD. Conditions: 0.2 mM P450 BM3-HD in 100 mM sodium phosphate at pH 7.4

For this study, structural changes upon binding of RNOs to ferric P450 BM3-HD would be measured. The reaction between ferric P450 BM3-HD and RNOs would be carried out using their RNO_2 precursors similar to the UV-vis studies performed (See Section 4.2.3.1). If binding does not occur or the RNO_2 is in excess, signals would be observed at 1600-1530 cm^{-1} and 1390-1300 cm^{-1} for alkyl RNO_2 and at 1550-1490 cm^{-1} and 1355-1315 cm^{-1} for aromatic RNO_2.[52] If the RNO_2 is reduced to RNO and binds to ferric P450 BM3-HD, signals should be seen at or below ~1550 cm^{-1} corresponding to ferrous Fe^{II}-RNO.[51] A preliminary FTIR spectrum of ferric P450 BM3-HD has been obtained using a Bruker Tensor-II equipped with an attenuated total reflectance (ATR) cell (**Figure 4.24**). The secondary structure breakdown matches with the PDBsum results (54% alpha, 12% beta).[53]

4.4.4.2 Extension to human P450s

Our goal is to eventually extend these studies to human P450s. CYP1A2, 2A6 and 3A4 are located in the liver and are some of the major contributors known to metabolize xenobiotics. Combined, these three P450s are responsible for ~50% of the total 74% of xenobiotic metabolism performed by P450s in the body.[2] This makes CYP1A2, 2A6 and 3A4 the most relevant for us to work with.

We were gifted the plasmids for P450s 1A2, 2A6 and 3A4 from Dr. Peter Guengerich at Vanderbilt University. In collaboration with my lab colleague, Viridiana Herrera, we successfully cloned the non-transmembrane portion of all three P450s and added a His-tag following published procedures.[54-56] All three P450s were successfully expressed. Initial efforts were made to purify the proteins using Ni-NTA columns which showed promising results. However, in order to improve the purification and the solubility of the proteins, detergent screening needs to be completed. Thus far, the only detergent that has been screened is triton and only minimal improvements in solubility were observed.

4.5 Conclusions

In this chapter, I have presented a spectroscopic analysis of the interaction of the heme domain of cytochrome P450 BM3-HD with *C*-nitroso compounds, imidazoles and arylhydrazines. It has been shown that *C*-nitroso compounds bind to ferric P450 BM3-HD in the *N*-binding mode and that the alkyl group size affects the extent of formation of the resulting complexes. Imidazoles were shown to bind ferric P450 BM3-HD in a Type II manner and, based on published work, are likely *N*-bound. Additionally, Phe87 likely plays a role in the binding of both *C*-nitroso compounds and imidazoles. Finally, the binding of arylhydrazines to ferric P450 BM3-HD was discussed. Initially, arylhydrazines interact with ferric P450 BM3-HD in a Type II manner, but under aerobic conditions, the aryl radical that forms, binds to the heme-Fe forming a σ-bonded aryl-iron complex. This work shows that P450 BM3-HD works well as a model system for P450 interactions with *C*-nitroso compounds, imidazoles and arylhydrazines.

4.6 References

[1] Hannemann, F., Bichet, A., Ewen, K. M., and Bernhardt, R. (2007) Cytochrome P450 systems - biological variations of electron transport chains, *Biochim Biophys Acta 1770*, 330-344.

[2] Guengerich, F. P. (2015) Human cytochrome P450 enzymes, In *Cytochrome P450: Structure, Mechanism, and Biochemistry* (Ortiz de Montellano, P. R., Ed.) 4 ed., Kluwer Academic/Plenum Publishers, New York.

[3] Munro, A. W., and Lindsay, J. G. (1996) Bacterial cytochromes P-450, *Mol Microbiol 20*, 1115-1125.

[4] Narhi, L. O., and Fulco, A. J. (1986) Characterization of a catalytically self-sufficient 119,000-dalton cytochrome P-450 monooxygenase induced by barbiturates in *Bacillus megaterium*, *J Biol Chem 261*, 7160-7169.

[5] Munro, A. W., Leys, D. G., McLean, K. J., Marshall, K. R., Ost, T. W. B., Daff, S., Miles, C. S., Chapman, S. K., Lysek, D. A., Moser, C. C., Page, C. C., and Dutton, P. L. (2002) P450 BM3: the very model of a modern flavocytochrome, *Trends Biochem Sci 27*, 250-257.

[6] Ruettinger, R. T., Wen, L. P., and Fulco, A. J. (1989) Coding nucleotide, 5' regulatory, and deduced amino acid sequences of P-450BM-3, a single peptide cytochrome P-450:NADPH-P-450 reductase from *Bacillus megaterium*, *J Biol Chem 264*, 10987-10995.

[7] Yeom, H., Sligar, S. G., Li, H., Poulos, T. L., and Fulco, A. J. (1995) The role of Thr268 in oxygen activation of cytochrome P450BM-3, *Biochemistry 34*, 14733-14740.

[8] Haines, D. C., Chen, B., Tomchick, D. R., Bondlela, M., Hegde, A., Machius, M., and Peterson, J. A. (2008) Crystal structure of inhibitor-bound P450BM-3 reveals open conformation of substrate access channel, *Biochemistry 47*, 3662-3670.

[9] Butler, C. F., Peet, C., Mason, A. E., Voice, M. W., Leys, D., and Munro, A. W. (2013) Key mutations alter the cytochrome P450 BM3 conformational candscape and remove inherent substrate bias, *J Biol Chem 288*, 25387-25399.

[10] Luthra, A., Denisov, I. G., and Sligar, S. G. (2011) Spectroscopic features of cytochrome P450 reaction intermediates, *Arch Biochem Biophys 507*, 26-35.

[11] Klingenberg, M. (1958) Pigments of rat liver microsomes, *Arch Biochem Biophys 75*, 376-386.

[12] Omura, T., and Sato, R. (1962) A new cytochrome in liver microsomes, *J Biol Chem 237*, PC1375-PC1376.

[13] Lee, J., Chen, L., West, A. H., and Richter-Addo, G. B. (2002) Interactions of organic nitroso compounds with metals, *Chem Rev 102*, 1019-1066.

[14] Delaforge, M., Jaouen, M., and Mansuy, D. (1983) Dual effects of macrolide antibiotics on rat liver cytochrome P-450, *Biochem Pharmacol 32*, 2309-2318.

[15] Mansuy, D., Rouer, E., Bacot, C., Gans, P., Chottard, J. C., and Leroux, J. P. (1978) Interaction of aliphatic N-hydroxylamines with microsomal cytochrome P450: Nature of the different derived complexes and inhibitory effects on monoxygenases activities, *Biochem Pharmacol 27*, 1229-1237.

[16] Bensoussan, C., Delaforge, M., and Mansuy, D. (1995) Particular ability of cytochromes P450 3A to form inhibitory P450-iron-metabolite complexes upon metabolic oxidation of aminodrugs, *Biochem Pharmacol 49*, 591-602.

[17] Mansuy, D., Beaune, P., Chottard, J. C., Bartoli, J. F., and Gans, P. (1976) The nature of the “455 nm absorbing complex” formed during the cytochrome P450 dependent oxidative metabolism of amphetamine, *Biochem Pharmacol 25*, 609-612.

[18] Hackett, J. C., Kim, Y.-W., Su, B., and Brueggemeier, R. W. (2005) Synthesis and characterization of azole isoflavone inhibitors of aromatase, *Bioorg Med Chem 13*, 4063-4070.

[19] Recanatini, M., Cavalli, A., and Valenti, P. (2002) Nonsteroidal aromatase inhibitors: Recent advances, *Med Chem Res 22*, 282-304.

[20] Owen, C. P., Shahid, I., Lee, W.-Y., and Ahmed, S. (2010) Synthesis and biochemical evaluation of a range of (4-substituted phenyl)sulfonate derivatives of 4-hydroxybenzyl imidazole-based compounds as potent inhibitors of 17α-hydroxylase/17,20-lyase (P45017α) derived from rat testicular microsomes, *Bioorg Med Chem Lett 20*, 5345-5348.

[21] Choudhary, G., and Hansen, H. (1998) Human health perspective of environmental exposure to hydrazines: A review, *Chemosphere 37*, 801-843.

[22] Jonen, H. G., Werringloer, J., Prough, R. A., and Estabrook, R. W. (1982) The reaction of phenylhydrazine with microsomal cytochrome P-450. Catalysis of heme modification, *J Biol Chem 257*, 4404-4411.

[23] Ortiz de Montellano, P. R. (1995) Arylhydrazines as probes of hemoprotein structure and function, *Biochimie 77*, 581-593.

[24] Ortiz de Montellano, P. R. (1984) The inactivation of cytochrome P-450, In *Annual Reports in Medicinal Chemistry* (Bailey, D. M., Ed.), Chapter 20. pp 201-211, Academic Press.

[25] Raag, R., Swanson, B. A., Poulos, T. L., and Ortiz de Montellano, P. R. (1990) Formation, crystal structure, and rearrangement of a cytochrome P-450cam iron-phenyl complex, *Biochemistry 29*, 8119-8126.

[26] Tuck, S. F., Peterson, J. A., and Ortiz de Montellano, P. R. (1992) Active site topologies of bacterial cytochromes P450101 (P450cam), P450108 (P450terp), and P450102 (P450BM-3). In situ rearrangement of their phenyl-iron complexes, *J Biol Chem 267*, 5614-5620.

[27] Li, H. Y., Darwish, K., and Poulos, T. L. (1991) Characterization of recombinant *Bacillus megaterium* cytochrome P-450 BM-3 and its two functional domains, *J Biol Chem 266*, 11909-11914.

[28] Sevrioukova, I., Truan, G., and Peterson, J. A. (1996) The flavoprotein domain of P450BM-3: Expression, purification, and properties of the flavin adenine dinucleotide- and flavin mononucleotide-binding subdomains, *Biochemistry 35*, 7528-7535.

[29] Sevrioukova, I., Truan, G., and Peterson, J. A. (1997) Reconstitution of the fatty acid hydroxylase activity of cytochrome P450BM-3 utilizing its functional domains, *Arch Biochem Biophys 340*, 231-238.

[30] Di Nardo, G., Dell'Angelo, V., Catucci, G., Sadeghi, S. J., and Gilardi, G. (2016) Subtle structural changes in the Asp251Gly/Gln307His P450 BM3 mutant responsible for new activity toward diclofenac, tolbutamide and ibuprofen, *Arch Biochem Biophys 602*, 106-115.

[31] Quaroni, L. G., Seward, H. E., McLean, K. J., Girvan, H. M., Ost, T. W. B., Noble, M. A., Kelly, S. M., Price, N. C., Cheesman, M. R., Smith, W. E., and Munro, A. W.

(2004) Interaction of nitric oxide with cytochrome P450 BM3, *Biochemistry 43*, 16416-16431.

[32] Wagner, G. C., Perez, M., Toscano, W. A., and Gunsalus, I. C. (1981) Apoprotein formation and heme reconstitution of cytochrome P-450cam, *J Biol Chem 256*, 6262-6265.

[33] Wagner, G. C., Gunsalus, I. C., Wang, M. Y., and Hoffman, B. M. (1981) Cobalt-substituted cytochrome P-450cam, *J Biol Chem 256*, 6266-6273.

[34] Copeland, D. M. A study of the interactions of nitric oxide and nitric oxide containing molecules with heme proteins. Ph.D. Dissertation, University of Oklahoma, Norman, OK, 2006.

[35] Rogerson, T. D., Wilkinson, C. F., and Hetarski, K. (1977) Steric factors in the inhibitory interaction of imidazoles with microsomal enzymes, *Biochem Pharmacol 26*, 1039-1042.

[36] Locuson, C. W., Hutzler, J. M., and Tracy, T. S. (2007) Visible spectra of type II cytochrome P450-drug complexes: Evidence that "incomplete" heme coordination Is common, *Drug Metab Dispos 35*, 614-622.

[37] Yi, J., Ye, G., Thomas, L. M., and Richter-Addo, G. B. (2013) Degradation of human hemoglobin by organic C-nitroso compounds, *Chemical Communications 49*, 11179-11181.

[38] Word, J. M., Lovell, S. C., LaBean, T. H., Taylor, H. C., Zalis, M. E., Presley, B. K., Richardson, J. S., and Richardson, D. C. (1999) Visualizing and quantifying molecular goodness-of-fit: Small-probe contact dots with explicit hydrogen atoms, *J Mol Biol 285*, 1711-1733.

[39] Fukuto, J. M., Brady, J. F., Burstyn, J. N., Van Atta, R. B., Valentine, J. S., and Cho, A. K. (1986) Direct formation of complexes between cytochrome P-450 and nitrosoarenes, *Biochemistry 25*, 2714-2719.

[40] Mansuy, D., Beaune, P., Cresteil, T., Bacot, C., Chottard, J.-C., and Gans, P. (1978) Formation of complexes between microsomal cytochrome P-450-Fe(II) and nitrosoarenes obtained by oxidation of arylhydroxylamines or reduction of nitroarenes *in situ*, *Eur J Biochem 86*, 573-579.

[41] Wilkinson, C. F., Hetnarski, K., Cantwell, G. P., and Di Carlo, F. J. (1974) Structure-activity relationships in the effects of 1-alkylimidazoles on microsomal oxidation in vitro and in vivo, *Biochem Pharmacol 23*, 2377-2386.

[42] Jovanovic, T., and McDermott, A. E. (2005) Observation of ligand binding to cytochrome P450 BM-3 by means of solid-state NMR spectroscopy, *J Am Chem Soc 127*, 13816-13821.

[43] Battioni, P., Mahy, J.-P., Delaforge, M., and Mansuy, D. (1983) Reaction of monosubstituted hydrazines and diazenes with rat-liver cytochrome P450, *Eur J Biochem 134*, 241-248.

[44] Muakkassah, S. F., and Yang, W. C. (1981) Mechanism of the inhibitory action of phenelzine on microsomal drug metabolism, *J Pharmacol Exp Ther 219*, 147-155.

[45] Ringe, D., Petsko, G. A., Kerr, D. E., and Ortiz de Montellano, P. R. (1984) Reaction of myoglobin with phenylhydrazine: A molecular doorstop, *Biochemistry 23*, 2-4.

[46] Wang, B., Thomas, L. M., and Richter-Addo, G. B. (2016) Organometallic myoglobins: Formation of Fe–carbon bonds and distal pocket effects on aryl ligand conformations, *J Inorg Biochem 164*, 1-4.

[47] Geronimo, I., Denning, C. A., Rogers, W. E., Othman, T., Huxford, T., Heidary, D. K., Glazer, E. C., and Payne, C. M. (2016) Effect of mutation and substrate binding on the stability of cytochrome P450BM3 variants, *Biochemistry 55*, 3594-3606.

[48] Swanson, B. A., Dutton, D. R., Lunetta, J. M., Yang, C. S., and Ortiz de Montellano, P. R. (1991) The active sites of cytochromes P450 IA1, IIB1, IIB2, and IIE1. Topological analysis by in situ rearrangement of phenyl-iron complexes, *J Biol Chem 266*, 19258-19264.

[49] Singh, B. R. (1999) Basic aspects of the technique and applications of infrared spectroscopy of peptides and proteins, In *Infrared Analysis of Peptides and Proteins*, pp 2-37, American Chemical Society.

[50] Cai, S., and Singh, B. R. (1999) Determination of the secondary structure of proteins from amide I and amide III infrared bands using partial least-square method, In *Infrared Analysis of Peptides and Proteins*, pp 117-129, American Chemical Society.

[51] Jung, C. (2008) Fourier transform infrared spectroscopy as a tool to study structural properties of cytochromes P450 (CYPs), *Anal Bioanal Chem 392*, 1031-1058.

[52] Brown, J. F. (1955) The infrared spectra of nitro and other oxidized nitrogen compounds, *J Am Chem Soc 77*, 6341-6351.

[53] de Beer, T. A. P., Berka, K., Thornton, J. M., and Laskowski, R. A. (2014) PDBsum additions, *Nucleic Acids Res 42*, D292-D296.

[54] Sandhu, P., Guo, Z. Y., Baba, T., Martin, M. V., Tukey, R. H., and Guengerich, F. P. (1994) Expression of modified human cytochrome P450 1A2 in *Escherichia coli*: Stabilization, purification, spectral characterization, and catalytic activities of the enzyme, *Arch Biochem Biophys 309*, 168-177.

[55] Gillam, E. M. J., Baba, T., Kim, B. R., Ohmori, S., and Guengerich, F. P. (1993) Expression of modified human cytochrome P450 3A4 in *Escherichia coli* and purification and reconstitution of the enzyme, *Arch Biochem Biophys 305*, 123-131.

[56] Nakamura, K., Martin, M. V., and Guengerich, F. P. (2001) Random mutagenesis of human cytochrome P450 2A6 and screening with indole oxidation products, *Arch Biochem Biophys 395*, 25-31.

Appendix: General Scheme of Reactions

Scheme 1. Reductive pathway for the reaction of Mb and Hb with RNO_2 compounds. λ_{max} values are shown below the scheme.

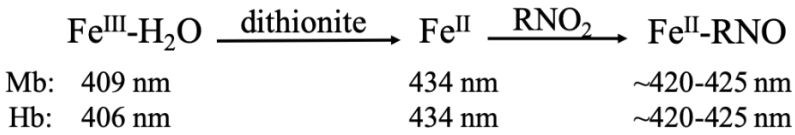

Scheme 2. Oxidative pathway for the reaction of Mb and Hb with RNHOH compounds. λ_{max} values are shown below the scheme.

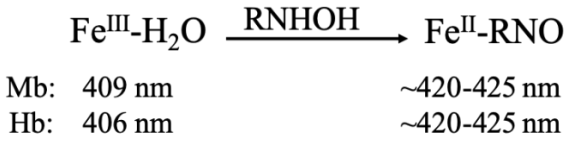

Scheme 3. Reductive pathway for the reaction of NRs with RNO_2 compounds. λ_{max} values are shown below the scheme.

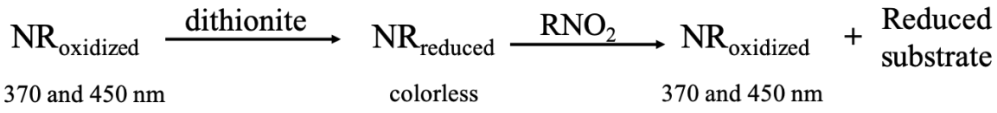

Scheme 4. Reaction of P450 BM3-HD with RNO_2 compounds. λ_{max} values are shown below the scheme.

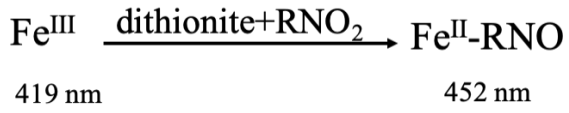

Scheme 5. Reaction of P450 BM3-HD with imidazoles. λ_{max} values are shown below the scheme.

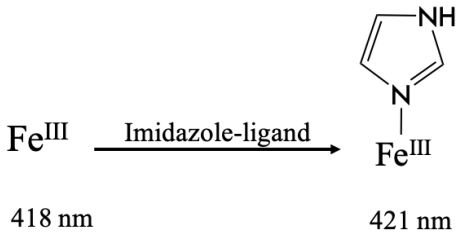

Scheme 6. Reaction of P450 BM3-HD with arylhydrazines. λ_{max} values are shown below the scheme.